Geoengineering Marine Stratocumulus Clouds

Annabel Ka Lai Jenkins

Submitted in accordance with the requirements for the degree of

Doctor of Philosophy

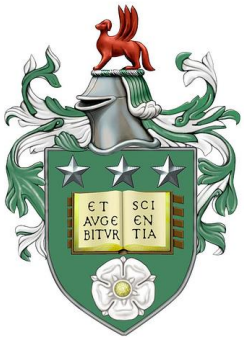

The University of Leeds

School of Earth and Environment

March 2014

Declaration of Authorship

The candidate confirms that the work submitted is her own, except where work which has formed part of jointly authored publications has been included. The contribution of the candidate and the other authors to this work has been explicitly indicated below. The candidate confirms that appropriate credit has been given within the thesis where reference has been made to the work of others.

Jenkins, A. K. L., Forster, P. M. & Jackson, L. S. (2013) The effects of timing and rate of marine cloud brightening aerosol injection on albedo changes during the diurnal cycle of marine stratocumulus clouds. *Atmospheric Chemistry and Physics,* 13, 1659-1673. Work presented in this publication is included in Chapters 3 and 4. The candidate performed all modelling and analysis, and wrote the manuscript. The co-author Piers Forster supervised the work and reviewed the draft manuscript. The co-author Lawrence Jackson provided modelling support and reviewed the draft manuscript.

Jenkins, A. K. L. & Forster, P. M. (2013) The inclusion of water with the injected aerosol reduces the simulated effectiveness of marine cloud brightening. *Atmospheric Science Letters*. Work presented in this publication is included in Chapter 5. The candidate performed all modelling and analysis, and wrote the manuscript. The co-author Piers Forster supervised the work and reviewed the draft manuscript.

Kravitz, B., Forster, P. M., Jones, A., Robock, A., Alterskjær, K., Boucher, O., Jenkins, A. K. L., Korhonen, H., Kristjánsson, J. E., Muri, H., Niemeier, U., Partanen, A.-I., Rasch, P. J., Wang, H. & Watanabe, S. (2013) Sea spray geoengineering experiments in the geoengineering model intercomparison project (GeoMIP): Experimental design and preliminary results. *Journal of Geophysical Research: Atmospheres,* 118, 2013JD020351. The candidate contributed Figure 1 to this publication. The candidate was responsible for collating the data presented in the figure, and for the production of the figure. This figure is reproduced as Figure 1.4 in Chapter 1 of this thesis.

Stuart, G. S., Stevens, R. G., Partanen, A. I., Jenkins, A. K. L., Korhonen, H., Forster, P. M., Spracklen, D. V. & Pierce, J. R. (2013) Reduced efficacy of marine cloud brightening geoengineering due to in-plume aerosol coagulation: parameterization and global implications. *Atmospheric Chemistry and Physics,* 13, 10385-10396. The candidate contributed Section 2.2 (Large-eddy simulation model) to the publication, and the data associated with the large-eddy simulation model shown in the top panel of Figure 3. For this section of the paper, the candidate performed all modelling and analysis, and contributed a draft manuscript section. Work presented in this section of the publication is included in Chapter 7.

Acknowledgements

I would first like to thank my inspirational supervisor Professor Piers Forster. I am grateful not only for the opportunities that he has given me, but for the invaluable guidance, encouragement – and importantly – his unshakeable faith.

I have been fortunate to have benefitted from a Met Office CASE studentship and the kindness and wisdom of my co-supervisor Dr Andy Jones.

I would like to thank the Engineering and Physical Sciences Research Council and the Natural Environment Research Council for their financial support through the Integrated Assessment of Geoengineering Proposals project. I have learnt a great deal from my diverse range of colleagues within this group, and have received caring support from Ros McDonnell.

Within the University of Leeds, I would like to express my gratitude to my Research Support Group of John Marsham and Dominick Spracklen for their contributions in shaping this work. My thanks also to Steven Pickering and Richard Rigby for their valued technical support and to Kirsty Pringle for GLOMAP aerosol data. My heartfelt thanks go to members of the Institute for Climate and Atmospheric Science and particularly to members of the Physical Climate Change Group for their collegiality, humour, and friendship. The moral support of Catherine Scott has been greatly appreciated. I will remain indebted to Lawrence Jackson for his unfailing patience, understanding and encouragement. Indeed, a problem shared is a problem halved.

I wish to additionally thank my wider national and international colleagues, specially noting Dr Douglas Lowe of the University of Manchester, for their positivity and willingness to share their knowledge, skills and passions.

Finally, on a personal note, I would like to thank my faithful friends for keeping my chin up and forgiving my absences. To Kath and Tom for easing the burdens. And lastly, to Steve (for being amazing), and to my family.

Abstract

Marine cloud brightening (MCB) geoengineering has been proposed as a means of ameliorating anthropogenic climate change. High concentrations of nanometre-sized aerosols would be emitted from seagoing vessels, with the intention of increasing the albedo of low-lying marine stratocumulus clouds (MSc) via indirect aerosol effects.

Realistic estimates of the potential effectiveness of MCB are needed to inform policy-making on climate change. However, in spite of increasing model complexity and developments in representing MCB, the relatively coarse resolution of global-scale models prevents implementation details from being captured. This work identified three previously unrepresented implementation details, and examined their importance in achieving realistic estimates of MCB effectiveness. For this, the Weather Research and Forecasting model incorporating aerosol processes (WRF/Chem) was used, allowing clouds to be resolved over a kilometre-scale domain.

Firstly, for a weakly precipitating cloud regime, cloud brightening was found to be sensitive to the timing of MCB aerosol emissions. The largest cloud albedo increase occurred for early morning emissions, with little change occurring for daytime emissions. Timing was less important for the non-precipitating regime where cloud albedo perturbations were generally smaller owing to the absence of a large second indirect (or 'cloud lifetime') effect.

Secondly, near-surface evaporative cooling resulting from the more realistic simulation of MCB emissions as wet droplets rather than the previously assumed dry aerosols reduced aerosol plume heights by up to 30% (40 m), reducing cloud albedo increases by up to one-third.

Finally, aerosol coagulation within the MCB aerosol plume (simulated at sub-metre resolution) resulted in number concentration decreases of up to 50%, consequentially reducing the cloud albedo increases by approximately half for the non-precipitating regime.

These findings suggest that in omitting these details, global-scale model estimates of MCB effectiveness may be exaggerated. The inclusion of these details in global-scale MCB modelling could therefore materially improve the realism of future effectiveness estimates.

Table of Contents

List of Figures

List of Tables

Abbreviations

CAM	Community Atmospheric Model
CBMZ	Carbon Bond Mechanism–Z [gas phase chemical mechanism scheme]
CCN	Cloud Condensation Nuclei
CDR	Carbon Dioxide Removal [form of geoengineering]
DYCOMS-II, RF02	Second Dynamics and Chemistry of Marine Stratocumulus [Field Study], Research Flight Number 02
ECHAM-HAM (and other versions)	Global aerosol-climate model based on the European Centre HAMburg (ECHAM) general circulation model
EMAC	ECHAM/MESSy Atmospheric Chemistry model [combining the ECHAM general circulation model and the Modular Earth Sub-model System (MESSy) interface]
E-PEACE	Eastern Pacific Emitted Aerosol Cloud Experiment
GLOMAP	GLObal Model of Aerosol Processes
HadGAM	[Met Office] Hadley Centre Global Atmospheric Model
HadGEM2(-ES)	[Met Office] Hadley Centre Global Environmental Model (-Earth System)
IPCC	Intergovernmental Panel on Climate Change
LT	Local Time
LW	Longwave [Radiation]
LWP	Liquid Water Path
MCB	Marine Cloud Brightening
MOSAIC	Model for Simulating Aerosol Interactions and Chemistry
MSc	Marine Stratocumulus [Clouds]
N_d	Cloud Droplet Number Concentration
RFP	Radiative Flux Perturbation
RRTMG	Rapid Radiative Transfer Model for Global Circulation Models
SRES	Special Report on Emissions Scenarios
SRM	Solar Radiation Management [form of geoengineering]
SW	Shortwave [Radiation]
TKE	Turbulent Kinetic Energy
WRF/Chem	Weather Research and Forecasting model including aerosol and chemistry processes

Other notation used through this thesis:

[#]xSA	Emission rate of marine cloud brightening aerosols, as a fraction of the maximum rate suggested by (Salter et al., 2008)
CHEM	Simulations including aerosol and chemical processes [Chapter 7] (see also NO_CHEM)
DRY	Simulation cases representing the emission of marine cloud brightening aerosols as dry aerosol particles [Chapter 5] (see also WET)
END	The 5 metre section of the simulation domain space [Figure 7.12; Chapter 7]
NO_CHEM	Simulations where aerosol and chemical processes are suppressed [Chapter 7] (see also CHEM)
NP	Simulated non-precipitating marine stratocumulus cloud base cases produced and used in this work, with NP-Pa representing the case based on North-East Pacific background aerosol conditions, and NP-Ch representing the case based on East China Sea background aerosol conditions (see also PR)
PR	Simulated precipitating marine stratocumulus cloud base case produced and used in this work (see also NP)
WET	Simulation cases representing the emission of marine cloud brightening aerosols as sea water droplets [Chapter 5] (see also DRY)

Chapter 1
Introduction

1.1 Overview

Geoengineering – involving large-scale human intervention into the climate system – has been suggested as a potential means of ameliorating future anthropogenic climate change. This thesis focuses on the marine cloud brightening (MCB) proposal. This proposal intends to increase the albedo of marine stratocumulus (MSc) clouds, thus increasing the proportion of shortwave (SW) radiation reflected back to space, producing a global cooling effect. The increase in cloud albedo is intended to be a response to the emission of aerosols formed from man-made sea water droplets emitted into the marine boundary layer from sea-going vessels.

Estimates of the potential effectiveness of such geoengineering proposals are needed to inform decisions on the response to climate change. It is therefore imperative that these estimates are as realistic as possible. Owing to the considerable risks and moral ambiguities surrounding experimental field-testing, the production of such effectiveness estimates is currently confined to computer model simulations. The ability of global-scale models to capture the response of global-scale climate systems to simulated MCB has led to their predominant use in the research of climatic MCB effects to-date. In spite of developments in representing MCB realistically within these global-scale simulations, the tens of kilometre grid spacing means that they are inherently unable to capture details of the implementation mechanism that occur at scales smaller than this. Importantly, the omission of such details may impair the realism of the resulting effectiveness estimates.

This thesis aims to establish the importance of representing implementation mechanism details that occur at scales smaller than global-scale computer simulations can capture. In order to achieve this, detailed computer simulations, at a cloud-resolving scale, are carried out. The findings presented are thus intended to contribute towards the production of increasingly realistic estimates of MCB effectiveness, but also to illustrate the importance of detailed simulations for geoengineering research more widely.

This opening chapter begins by introducing the field of geoengineering, contextualised in terms of its potential role in responding to anthropogenic climate change. This is followed by an overview of the development of the MCB proposal, with a summary of the approach and key findings of previous MCB literature. This chapter concludes by introducing the aim of this thesis and by presenting an overview of the approach taken herein.

1.2 Anthropogenic Climate Change

Owing to anthropogenic activities, atmospheric concentrations of the greenhouse gas carbon dioxide have risen rapidly from ~280 parts per million in the pre-industrial era to nearly 400 parts per million currently (Dlugokencky and Tans, 2014). These increasing concentrations have led to a perturbation in the net radiative flux at the top of the atmosphere, with this positive downward forcing leading to a warming effect. As such, global mean surface temperatures have risen by approximately 0.7 K over the last century (Trenberth et al., 2007). This is in spite of a hiatus in warming over the past decade (NASA, 2013) possibly caused by increases in ocean heat uptake, low solar activity, and increased aerosol concentrations (Guemas et al., 2013 and references within). This makes it likely that the Northern Hemisphere in the latter half of the Twentieth Century was warmer than it had been in over 1300 years (Jansen et al., 2007). Sea-levels increased by an estimated 1.75 mm yr^{-1} between 1950 and 2000 (Church and White, 2006) while Arctic sea ice extent has reduced such that the September 2012 minimum extent was almost 50% below the 1979−2000 average (National Snow and Ice Data Center, 2013). It has also been suggested that heat waves and extreme rainfall events have increased over the last decade (Coumou and Rahmstorf, 2012).

While the complexity and natural variability of the Earth system makes attribution of climate change challenging, both observational analysis and computer simulations suggest that a substantial anthropogenic influence is highly probable (Forster et al., 2007). Hence, future climate change will depend on both human actions (including the rate of greenhouse gas emissions) and on the sensitivity of the Earth to these changes. In terms of human actions, growth rates of global annual anthropogenic CO_2 emissions have increased from less than 2% in the 1980s and 1990s to over 3% since 2000, with global CO_2 emissions reaching 9.5±0.5 $PgCyr^{-1}$ in 2011 (Peters et al., 2013). These growth rates are in line with the highest projected emissions scenarios used in climate change modelling. There remains some uncertainty in the response of the Earth's temperature to increasing atmospheric CO_2 concentrations (Otto et al., 2013). However, the current lack of emissions abatement means that constraining global mean warming to 2 K above the pre-industrial value by 2100 will become increasingly difficult (Joshi et al., 2011; Rogelj et al., 2012). In addition to global mean temperature increases, other changes may include: sea-level rises of half a metre or more by the end of the century (Jevrejeva et al., 2010; Slangen et al., 2012); an increase in the intensity of tropical storms (Villarini and Vecchi, 2012); and the near total loss of Artic summer sea ice by the 2030s (Wang and Overland, 2012). Ecosystems will also be affected. This includes both vulnerable species with already restricted ranges (e.g. coral reefs), and currently more common species whose ranges may contract (Warren et al., 2013). Finally,

climate change is expected to impact on global human society in several critical areas. These include: global crop productivity (Lobell and Gourdji, 2012); water stress (Arnell et al., 2011); and increasingly frequent extreme events, as described by Rahmstorf and Coumou (2011) and the Intergovernmental Panel on Climate Change (IPCC) (Field et al., 2012).

1.3 Traditional Responses to Climate Change

Traditionally considered pathways for responding to climate change are mitigation and adaptation. Mitigation – which includes reducing anthropogenic greenhouse gas emissions – is generally accepted as the preferred means of limiting climate change (e.g. The Royal Society, 2009). However, as demonstrated by the recently increasing global CO_2 emission rates (and repeated procrastination in formalising effective international agreements on emissions reductions) the potential of mitigation in addressing climate change is currently unfulfilled (Jacobs, 2012).

Adaptation does not directly influence climate change, but is a response to it through changing behaviours that aim to reduce vulnerability. Examples of adaptation include the building of flood defences; the development of drought-tolerant crops; and taking potential future climate conditions into account during infrastructure planning. Owing to the long atmospheric lifetime of CO_2 (up to centuries or longer; Archer et al., 2009) and the high thermal capacity of oceans, anthropogenically-induced climate change will continue for some time, regardless of future mitigation. For example, the sea-level will continue to rise for several hundred years (Meehl et al., 2012). Such 'locked-in' changes mean that future climate change response will require a component of adaptation (e.g. Klein et al., 2007). There are limits to adaptation however. An inability to adapt beyond these limits will lead to, for example, the migration of communities or the extinction of species. (Adger et al., 2009; Dow et al., 2013).

1.4 Geoengineering Overview

The prospect of potential changes to the climate that are beyond the capacity of adaptation has led to the suggestion that geoengineering may be utilised in the future. Geoengineering encompasses a broad range of proposed technological schemes that aim to manipulate the Earth's climate at a large scale in order to reduce the radiative flux imbalances caused by anthropogenic activities. These proposed schemes are broadly referred to as geoengineering. Recent growth and interest in the field of geoengineering has led to high-level reports from The Royal Society (2009) and the United States Government (Centre for Science, Technology, and Engineering, 2011) along with several detailed reviews (Keith, 2000; Vaughan and Lenton, 2011; Caldeira et al., 2013).

All proposed geoengineering technologies are currently immature, with uncertainties both in the design of the technological implementation mechanisms and in the anticipated effects on the climate system (Center for Science, Technology, and Engineering, 2011; Shepherd, 2012). The nomenclature associated with these schemes (and their classification within the mitigation and adaptation spectrum) is also still evolving (e.g. Heyward, 2013; Boucher et al., 2014). As no consensus on these revised classifications has yet been reached, the terminology used here will be consistent with the seminal report by The Royal Society (2009). Thus, under this framework, geoengineering proposals are divided into either carbon dioxide removal (CDR) schemes or solar radiation management (SRM) schemes. The CDR schemes aim to remove carbon dioxide from the atmosphere, with examples of proposed CDR proposals including chemical direct air capture devices or 'CO_2 scrubbers' (e.g. Carbon Engineering Ltd., 2013); ocean fertilisation (e.g. Williamson et al., 2012); and enhanced weathering (e.g. Hartmann et al., 2013). In gradually drawing down atmospheric CO_2 concentrations, these CDR schemes would be akin to reductions in CO_2 emissions, and may even enable negative emissions (The Royal Society, 2009). Responding to climate change by drawing down atmospheric CO_2 concentrations is therefore considered to be relatively safe (The Royal Society, 2009). However, the means of achieving such CO_2 concentration reductions may, in themselves, have potentially dangerous repercussions (for example, impacting the biosphere in the case of ocean fertilisation). CDR schemes would also likely produce only a slow response to climate change.

The SRM schemes aim to reduce the amount of SW solar radiation absorbed by the Earth. Examples of proposed SRM schemes include space-based reflectors (e.g. Angel, 2006); the replication of a volcanic eruption via the addition of sulphate particles to the stratosphere (e.g. Crutzen, 2006; Robock et al., 2009); and the enhancement of surface albedo. Proposals for surface albedo enhancement include the formation of ocean bubbles (e.g. Seitz, 2011); brightening of crops, urban areas and deserts (e.g. Irvine et al., 2011); and the brightening of MSc clouds (e.g. Latham et al., 2012a). As the climate response to SRM would be rapid, SRM has been suggested as a possible means of delaying climate change sufficiently to enable more sustainable climate change responses (e.g. mitigation, adaptation or CDR) to be implemented. This possible capacity to 'buy time' may be particularly important in so-called climate emergency scenarios (Blackstock et al., 2009), although the ability of geoengineering to avoid or reverse a climate tipping-point has been questioned (Lenton, 2013).

While SRM could therefore potentially play a contingency role in responding to climate change, it would likely have serious side-effects. Globally inhomogeneous application of SRM could lead to regional perturbations in, for example, temperature and precipitation (Haywood et al., 2013; Jones et al., 2011a). The resulting creation of regional 'winners' and

'losers' emphasises that decisions on the deployment of SRM geoengineering will be imbued with political sensitivities. Importantly, if SRM were to be used in the absence of mitigation or CDR techniques, atmospheric CO_2 concentrations would continue to rise. As such, ocean acidification (which results from dissolved CO_2) would persist. Global precipitation could reduce in response to the application of SRM owing to reduced rates of surface evaporation (Bala et al., 2008; Jones et al., 2011a). The net primary productivity of plants could increase however, owing to CO_2 fertilisation (Govindasamy et al., 2002). In spite of reduced solar radiation fluxes, further enhancements in photosynthesis could also result from the diffuse radiation caused by the addition of sulphate particles to the stratosphere, as occurred after the eruption of Mount Pinatubo (Gu et al., 2003). Finally, without decreases in atmospheric CO_2 concentrations, SRM would have to continue indefinitely, with sudden cessation causing temperatures to rapidly approach those that would have been reached had SRM never been deployed. Computer simulations of this 'termination effect' suggest that, for the Special Report on Emissions Scenarios (SRES) (IPCC, 2000) 'A2' emission scenario, this temperature recovery could occur at rates of 2 to 4 °C per decade (Matthews and Caldeira, 2007).

1.5 Geoengineering Within Future Climate Change Response Policy

Informed decision-making on climate change response requires a combined consideration of mitigation, adaptation, and the possible auxiliary role of geoengineering (Figure 1.1).

As these climate change response routes are interdependent, it is essential that – alongside ethical and political considerations – realistic estimates of the effectiveness and side-effects of a geoengineering scheme are produced. Being better informed about the realistic potential of geoengineering will prevent 'false hope' and an underestimation of the importance of the strength and timeliness of mitigation and adaptation measures.

In order to protect the Earth from possible irreversible damage, experimental geoengineering research is limited to small-scales in controlled settings (Convention on Biological Diversity, 2010). Because of this, the expense of field-testing, and the difficulty of detecting changes to the climate associated with geoengineering (e.g. Seidel et al., 2014), estimates of global geoengineering effectiveness and side-effects typically utilise computational models (Figure 1.1).

Computer modelling of geoengineering schemes has several benefits. Primarily, computer-based research poses no risk to the climate. Additionally, multiple global simulations can be undertaken over climatically relevant time-scales (up to hundreds of years) and compared against control case scenarios. This allows the effects of geoengineering to be easily

identified, a process which is aided by the availability of output data on a multitude of climate variables. However, computer models have limitations. The degree of realism with which computer models can represent the consequences of geoengineering depends on two aspects. The first is the ability of the model to represent the Earth's climate systems and their response to a modelled geoengineering perturbation. The second is how realistically the geoengineering implementation mechanism is represented within the model.

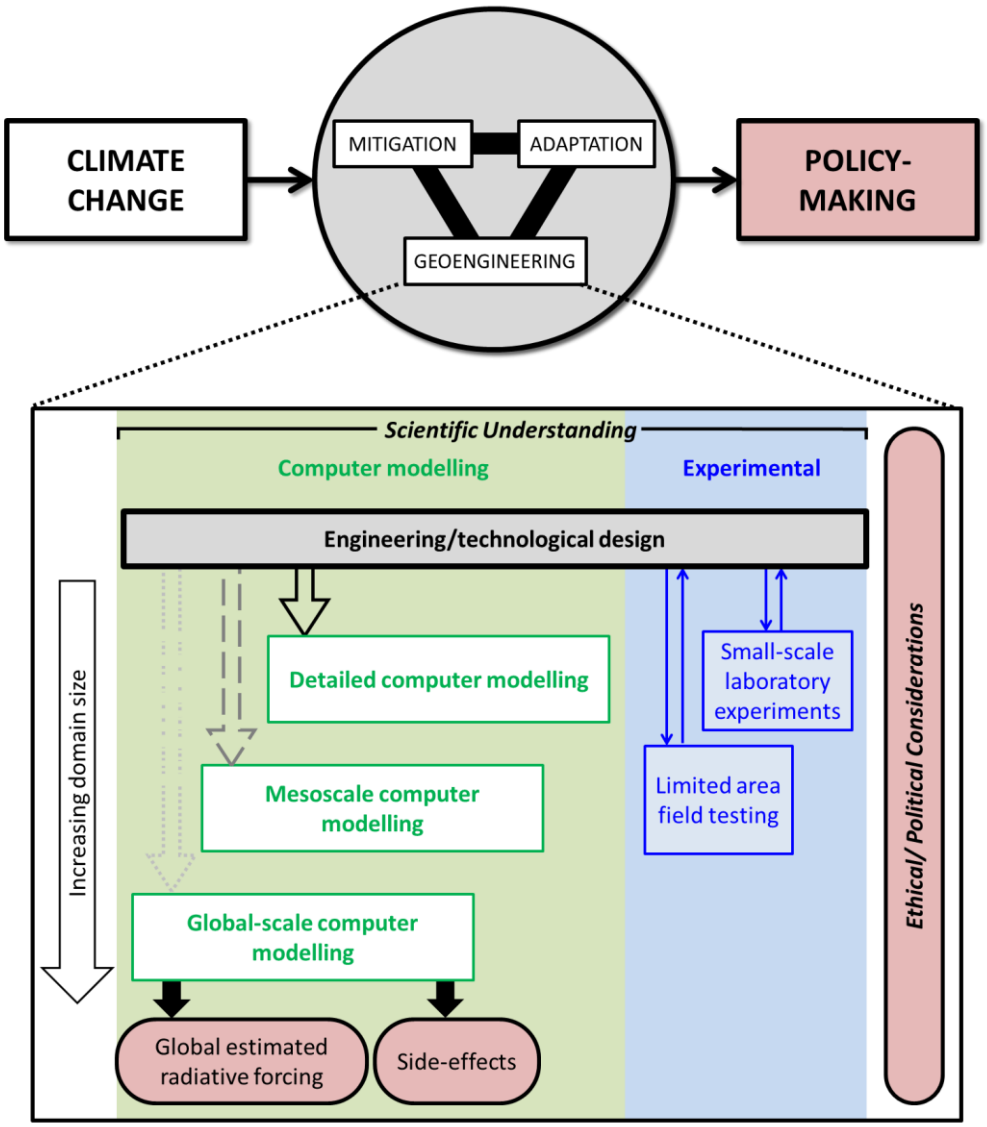

Figure 1.1 *– Schematic indicating considerations necessary for informed policy-making on the response to climate change. Possible research components for the better understanding of geoengineering proposals are detailed.*

The representation of climate systems within computer models is restricted by issues of scale. In reality, climate system processes occur at scales that range over several orders of magnitude. For example, teleconnections can span thousands of kilometres while in-cloud processes may be dominated by the centimetre-scale. Owing to the immense computational intensity associated with numerically representing such a range of processes, it is generally

necessary to simplify the system. This is typically achieved by limiting the resolution of the model and parameterising sub-grid processes.

For global-scale models, capturing such a large domain necessitates a horizontal grid cell spacing of the order of tens of kilometres. While bulk behaviour is represented through parameterisations, processes that occur at scales smaller than these grid cell dimensions cannot be explicitly represented, for example, aerosol-cloud interactions (Boucher et al., 2013). As they are able to capture global-scale climate interactions, these global-scale models are the only means of producing global-scale estimates of the climate's response to geoengineering (Figure 1.1). As such, the simulation of geoengineering proposals has been predominantly carried out using global-scale computer models.

While issues of scale are important for climate processes, they similarly affect the ability of models to realistically represent geoengineering implementation mechanisms. For example, some geoengineering implementation mechanisms are being designed to emit aerosols over meter-scales (e.g. aeroplanes for sulphate particle emissions, and sea-going vessels for cloud brightening sea spray emissions). Their representation within global-scale models is, however, typically simplified, resulting in a uniformly distributed emission over a grid-cell covering tens of square kilometres. This disconnect between the real-life engineering/technological design and its representation within global-scale models means that potentially key processes relating to details of the implementation process are not captured. Importantly, such omission of details may impair the realism of the resulting estimates of effectiveness and side-effects produced by these global scale models.

Better representation of the detailed features of both the climate system and geoengineering implementation mechanisms can be achieved through higher resolution computer modelling. In spite of the advantages of higher resolution computer modelling, the computational costs of increasing the resolution lead to restrictions in domain size. Thus, higher resolution computer modelling is unable to capture large-scale climate interactions and therefore cannot currently produce global estimates of geoengineering effectiveness. However, these higher resolution computer simulations are a powerful tool in examining the importance of capturing the details of geoengineering implementation mechanisms that cannot be represented within global-scale models. Through this enhancement, higher resolution computer simulations of geoengineering can contribute to the development of increasingly realistic estimates of geoengineering effectiveness and side-effects. Such estimates, portraying the highest possible realism, are essential for informed decisions on the response to climate change.

This thesis focuses on illustrating the importance of capturing details of the geoengineering implementation mechanisms in computer simulations. For this, the MCB proposal is considered. The MCB scheme, which proposes the manipulation of aerosol-cloud interactions

in enhancing MSc cloud albedo (Latham, 1990; 2002; Latham et al., 2008; 2012a), was primarily selected for two reasons.

Firstly, the background climate system, comprising of MSc clouds, exhibits characteristics at scales that are well suited to detailed cloud-resolving computer modelling (e.g. Ackerman et al., 2009; Wang et al., 2010; Chen et al., 2011). Secondly, the design of the technological implementation mechanism (in the form of wind-driven sea-going vessels) is fairly well developed, and has been published (Salter et al., 2008). This provides a well-defined basis for assumptions, while exhibiting sufficient ambiguities to enable exploration of sensitivities in the response. The metre-scale of the proposed sea-going vessels also lends itself to detailed computer modelling.

The remainder of this chapter reviews the background of the MCB proposal. This begins with a brief overview of the importance of clouds within the climate and their response to aerosols. An introduction to the MCB proposal is then presented, followed by a summary of MCB research to-date. This chapter ends with a declaration of the specific research objectives that comprise this thesis along with a description of the thesis structure (Section 1.9).

1.6 The Background of Marine Cloud Brightening

1.6.1 The Role of Clouds in the Climate

Clouds cover approximately two-thirds of the Earth's surface (Rossow and Schiffer, 1999; Eastman et al., 2011) and play a significant role in the climate system. Clouds form a crucial part of the hydrological cycle, controlling the amount and location of water stored, transported and deposited as precipitation. Clouds also have an important role in the Earth's energy budget. In addition to the latent heat fluxes associated with water changing states through a cloud's lifecycle, clouds interact with both longwave (LW) and shortwave (SW) radiation.

As clouds lie above (and are often cooler than) the Earth's surface, the amount of LW radiation that is emitted to space from the cloud-top is typically smaller than the amount emitted from the Earth's surface. This positive downward radiative flux effect will act to warm the Earth. However, the optical thickness of clouds acts to reflect incoming SW radiation from the Sun, acting to cool the Earth (a negative radiative flux change). Satellite observations estimate that globally, the annual average LW radiative perturbation caused by all clouds is 31 Wm^{-2}, with an estimated SW radiative perturbation of -48 Wm^{-2} (Ramanathan et al., 1989; Harrison et al., 1990). Thus, globally, clouds produce a cooling effect, with the magnitude of the net downward cloud radiative effect being approximately -17 Wm^{-2} (Harrison et al., 1990).

The net radiative effect of a cloud varies according to its type. For example, high, thin cirrus clouds are much cooler than the surface, but their optical thicknesses are such that their albedo is not markedly higher than the surface below. Thus, reductions to outgoing LW radiation (a global average estimated to be ~5.5 Wm^{-2}) are larger than increases in the reflected SW radiation (estimated to be ~ -4.2 Wm^{-2}). This results in an estimated net global average downward radiative effect of ~1.3 Wm^{-2}, and associated warming (Chen et al., 2000). Conversely, low, thick stratiform clouds have temperatures near to that of the surface, yet optical thicknesses that produce higher albedos than the surface below. Thus, reductions in outgoing LW radiation (estimated to be ~1.2 Wm^{-2}) are small compared to the increases in reflected SW radiation (estimated to be ~ -12.7 Wm^{-2}). This results in an estimated net global average downward radiative effect of ~ -11.5 Wm^{-2}, and associated cooling (e.g. Chen et al., 2000). The cooling efficacy of these low stratiform clouds is particularly evident over oceans, where difference in cloud and surface albedo is greatest, with a typical albedo of around 0.2 to 0.5 for clouds (Painemal and Minnis, 2012) and around 0.07 for the sea-surface (Coakley, 2002).

These estimated cloud radiative effects can be compared with the +2.3 Wm^{-2} [1.1 to 3.3 Wm^{-2}, 90% uncertainty range] estimated radiative forcing associated with anthropogenic activities between pre-industrial times and 2011 (Myhre et al., 2013). Thus, it is evident that even small cloud changes could be significant for the climate. Indeed, these cloud radiative effects are not fixed. As cloud properties are highly sensitive to atmospheric and energetic conditions (Stephens, 2005), any changes in these conditions affect cloud properties, and therefore the cloud radiative effects. In addition to spatial and periodic variations, of climatic interest is how clouds respond to changes associated with increased atmospheric CO_2 concentrations. The magnitude and sign of such cloud changes depend not only on the cloud type and location, but additionally on the nature of the change in conditions caused by the increase in CO_2 concentration.

Initially, increases in atmospheric CO_2 concentrations lead to rapid adjustments in tropospheric radiative heating (Andrews and Forster, 2008; Andrews et al., 2012). In turn, there are rapid adjustments (timescales of days to weeks) in cloud properties (Andrews and Forster, 2008; Andrews et al., 2012). Global-scale computer modelling suggests that these rapid adjustments result in reduced cloud fractions. Owing to perturbations in SW radiative response, these changes are estimated to result in a net positive cloud radiative adjustment (Andrews and Forster, 2008; Andrews et al., 2012; Zelinka et al., 2013).

After these initial rapid cloud adjustments, cloud properties then go on to respond to the longer-term changes to the climate – notably global surface warming. The resulting changes in the radiative properties of the clouds can lead either to positive feedbacks (i.e. that enhance

the warming) or negative feedbacks (i.e. that act to counteract it). These cloud feedbacks are, however, poorly understood (Stephens, 2005) – particularly for low-altitude marine boundary layer clouds (Bony and Dufresne, 2005; Boucher et al., 2013; Webb et al., 2013). Global-scale computer model simulations suggest that in response to surface temperature increases, cloud height and thickness tend to increase, while cloud fraction tends to decrease (Zelinka et al., 2013). Incorporating the various responses of different cloud types across different locations, the changes result in a net positive global mean cloud feedback, largely caused by changes to LW radiative effects (Zelinka et al., 2013). The IPCC state that cloud feedbacks are very likely to be in the range of -0.2 to +2.0 $Wm^{-2}K^{-1}$ (Boucher et al., 2013). Observations cannot yet inform on potential long-term trends, however (Zhou et al., 2013).

1.6.2 A Brief Introduction to Aerosol Indirect Effects

In addition to atmospheric and energetic conditions, cloud properties are also dependent upon the properties and concentrations of available aerosols. This relationship arises from fundamental mechanisms of cloud formation, whereby – for the warm (i.e. liquid phase only) MSc clouds central to the MCB proposal – cloud droplets form when water vapour condenses onto cloud condensation nuclei (CCN). This condensation occurs in the presence of supersaturation (i.e. when the relative humidity exceeds 100%). Supersaturation is dependent upon the speed of updrafts, which are able to transport moisture upwards from the surface. Aerosols that act as CCN can originate from both natural and anthropogenic sources, and typically have compositions that make them hygroscopic. Additionally, owing to the processes associated with condensation, larger aerosols are activated to cloud droplets preferentially to smaller ones (Köhler, 1936). The main source of CCN in the relatively clean marine environment is wind-driven sea spray (Lewis and Schwartz, 2004). However, anthropogenic sources can increase concentrations, particularly close to coasts and downwind of the sources (Lee et al., 2013). Thus, the number, size and composition of available aerosols affects the number and size distribution of formed cloud droplets. These attributes in turn characterise the optical thickness, albedo and SW radiative response of the cloud. This additionally means that changes to the number concentration, size distribution and composition of aerosols may cause a perturbation to the radiative response of the clouds.

While a more detailed review of aerosol-cloud interactions is presented in Chapter 2, briefly, increased aerosol concentrations can alter cloud albedo via both the first and second indirect aerosol effects[1]. In the first indirect aerosol effect, the addition of aerosols – assuming a fixed

[1] While the Fifth IPCC Assessment Report introduces new terminology for describing these effects (Boucher et al., 2013), the terminology used here will remain consistent with the Fourth IPCC Assessment Report (Forster et al., 2007).

liquid water path (LWP; the vertically-integrated liquid water content) – tends to increase the cloud droplet number concentration (N_d). This additionally reapportions the liquid water, forming a higher number of smaller cloud droplets. This reapportionment from a lower number of larger volume droplets to a higher number of smaller volume droplets in turn increases the cross-sectional area of droplets. Owing to the relationship between volume and area, this cross-sectional area increases by a factor of $\left(N_{d\_higher} / N_{d\_lower}\right)^{1/3}$. As a result, the optical thickness of the cloud increases, as does its albedo (Twomey, 1974). The second indirect aerosol effect considers changes to the LWP of the cloud. For a cloud precipitating sufficiently to lose water at the Earth's surface, the reduction in cloud droplet size caused by the addition of aerosols could reduce droplet collision-coalescence (and hence precipitation) sufficiently to cause a net increase in LWP. This resulting LWP increase could boost both the albedo and lifetime of the cloud, reinforcing the first indirect effect (Albrecht, 1989). However, the second indirect aerosol effect is dependent upon highly sensitive cloud processes, background cloud and atmospheric conditions and complex feedbacks (discussed in detail in Chapter 2). Therefore, while the second indirect aerosol effect may lead to albedo increases in certain conditions, the magnitude and even the sign of the second indirect aerosol effect is not well understood.

Crucially, aerosol production processes are closely linked with climatic conditions (Andreae and Rosenfeld, 2008). As such, increases in atmospheric CO_2 concentrations – and the changes to the climate that they induce – can lead to changes in atmospheric aerosol concentrations. These aerosol perturbations can in turn lead to changes in the radiative effect of clouds, further to the rapid responses and feedbacks described in Section 1.6.1.

For example, it has been suggested that the warming caused by increasing atmospheric CO_2 concentrations may enhance the planktonic algae production of dimethyl-sulphide, a precursor of sulphate aerosols that can act as CCN. The hypothesised resulting increases in cloud albedo would act to cool the planet, resulting in a negative feedback response (Charlson et al., 1987). However, subsequent computer simulations suggest that the magnitude of these effects will be dependent upon the spatial distribution of emissions (Woodhouse et al., 2013), and may be very weak (Woodhouse et al., 2010). Other analysis suggests that locally increased wind speeds over the remote Southern Hemisphere oceans since the early 1980s – caused by stratospheric ozone losses and increases in greenhouse gases – have increased the production of sea spray aerosols (Korhonen et al., 2010a). The magnitude of resulting negative radiative forcing, resulting from the associated increase in cloud albedo, is estimated to be sufficient to cancel out 70% of the positive radiative forcing resulting from greenhouse gases in the region.

It is the potential ability of these indirect aerosol effects to alter the radiative response of clouds that has led to the development of the MCB proposal.

1.6.3 The Marine Cloud Brightening Proposal

The MCB proposal aims to increase the albedo of MSc clouds by artificially increasing aerosol concentrations. The envisioned resulting negative radiative forcing would cool the planet and ameliorate climate change (Latham, 1990; Latham, 2002).

The MCB proposal aims to target MSc clouds for three principal reasons. Firstly, these low clouds produce the largest negative radiative effect of all cloud types (owing to the domination of SW related cooling over LW related warming as described in Section 1.6.1). Secondly, the relatively clean background aerosol concentrations in the marine environment are expected to allow a greater albedo enhancement than would occur for more polluted background conditions. Thirdly, as artificially-produced sea water droplets could be a suitable MCB aerosol, the marine environment constitutes an inexhaustible resource.

These low-lying MSc clouds cover up to 15% of the Earth's surface (Rossow and Schiffer, 1999; Eastman et al., 2011).They have a characteristic diurnal cycle (being thickest during the night, and thinning into the day) and tend to form into a cellular structure (with cell diameters being of the order of tens of kilometres). The processes that cause these characteristic properties are detailed in Chapter 2. Persistent MSc cloud decks reside off the west coasts of North America, South America, Africa and Australia (Figure 1.2).

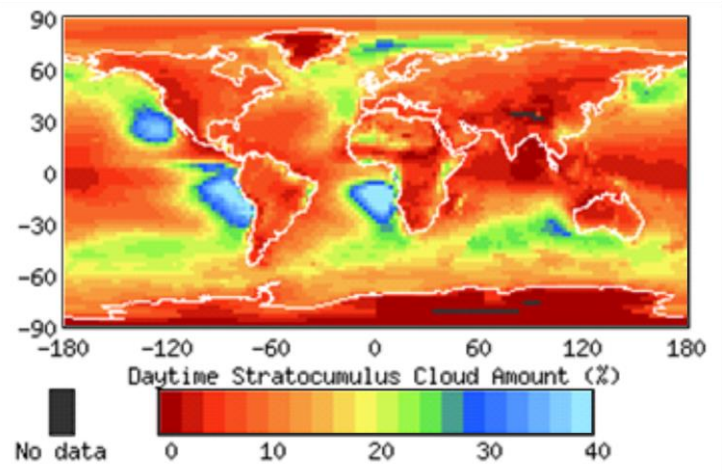

This ISCCP D2 image was obtained from the International Satellite Cloud Climatology Project website http://isccp.giss.nasa.gov maintained by the ISCCP research group at the NASA Goddard Institute for Space Studies, New York, NY on 23 January, 2012. (Rossow and Schiffer, 1999).

Figure 1.2 *– Annual mean daytime stratocumulus cloud amount.*

Global computer simulations have been used to identify the regions which are most susceptible to MCB. While the exact locations vary, there is some agreement that the optimal regions for MCB are these persistent MSc cloud decks, along with regions in the North

Atlantic and Indian Ocean (Rasch et al., 2009; Jones and Haywood, 2012; Partanen et al., 2012). These regions are similarly identified as regions of high susceptibility through the interrogation of observed patterns of SW radiation intensity, N_d, cloud fraction, and wind speed (Salter et al., 2008; Alterskjær et al., 2012).

The aerosols that would be used for MCB are suggested to be monodisperse with dry aerosol diameter of around 200 nm (Latham et al., 2008; Latham et al., 2012a). These aerosols would be small enough to maximise the number of aerosols produced from a given mass of sea water, whilst being large enough to act as CCN. The suggested monodispersivity is intended to delay the onset of precipitation (discussed further in Chapter 2) and hence enhance cloud lifetime.

A design of the implementation mechanism capable of emitting a flux of aerosols for this purpose has been proposed (Salter et al., 2008). This design proposes 300-tonne sea-going vessels, powered by the wind via rotating Flettner rotors approximately 2.4 m in diameter and 20 m in height (represented in the artist's impression; Figure 1.3). These wind-driven rotors would drive the motion of the vessel, allowing submerged turbines to power pumps which would draw-up filtered sea water to be formed into the sea water droplets. In spite of large uncertainties in the cost estimates, it has been suggested that a fleet of such vessels (suggested to be of the order of approximately 1500) would likely compare favourably with other geoengineering schemes (Keith, 2000).

There are design problems yet to be solved, including the development of a suitable aerosol formation system (Latham et al., 2012a; Neukermans et al., 2014). However, the proposal suggests that a maximum sea water pumping rate of 30 kgs^{-1} could be achieved at wind speeds of 6-8 ms^{-1} (Korhonen et al., 2010b). The MCB aerosols (of intended dry diameter ~200 nm) would likely result from the evaporation of formed sea water droplets (Latham et al., 2012a). The diameter of these dry aerosols being approximately one quarter of the diameter of the sea water droplet (Lewis and Schwartz, 2004). Therefore, for a 30 kgs^{-1} sea water mass flux of 800 nm diameter sea water droplets, the resulting aerosol number flux rate would be approximately $1.1x10^{17}$ s^{-1}. The sea water droplets would then be blown through the centre of the hollow rotor at a velocity of 12 ms^{-1} (Salter et al., 2008). Latham et al. (2008) suggest that based on measurements and observations of natural sea salt aerosols, the number fraction of MCB emitted sea salt aerosols reaching the cloud base region would depend on meteorological conditions and could vary between 0.1 and 0.5. Also, given that the spraying process is currently uncertain, the timing and location of the evaporation of the formed sea water droplets in the MCB process is also currently unknown.

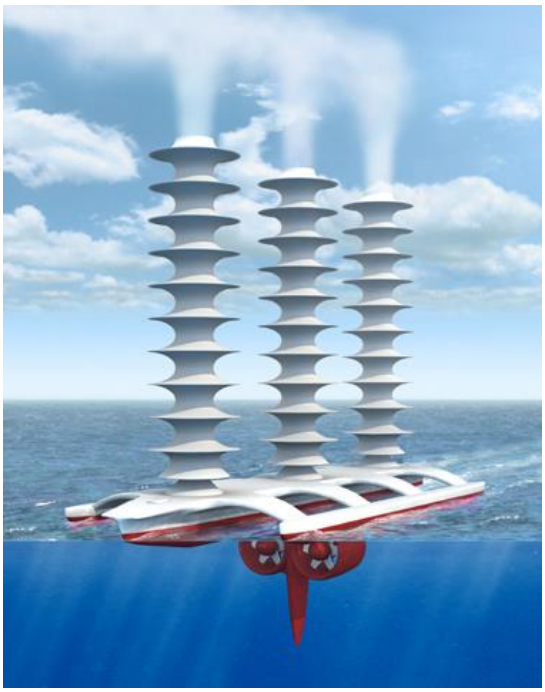

Figure 1.3 *– Artist's impression of a potential cloud brightening vessel (MacNeill, n.d.).*

1.7 Developments in Marine Cloud Brightening Research

As represented in Figure 1.1, realistic estimates of MCB effectiveness and the identification of potential side-effects are essential in order to inform decision-making on the place of MCB in addressing future anthropogenic climate change. These estimates should arise from assumptions based on the engineering design of the MCB scheme.

This section discusses key findings resulting from developments in the computer simulation of MCB to-date.

Mesoscale simulations (Wang et al., 2011a) demonstrate that representing MCB at a resolved cloud dynamics resolution (and thereby allowing details of the aerosol emissions mechanism to be captured) results in responses that could not be simulated at the global scale. These outcomes are discussed further in Section 1.7.4. In spite of the insights that more detailed model simulations afford, and as introduced in Section 1.5, the majority of research into the effects of MCB has been carried out using global-scale models.

Early global computer simulations of MCB avoided simulating the aerosol and aerosol-cloud processes involved in MCB, instead representing the scheme by fixed low-cloud N_d of 375 cm^{-3} or 1000 cm^{-3} (e.g. Latham et al., 2008; Rasch et al., 2009; Jones et al., 2009). This simplification therefore omitted both representation of the possible MCB aerosol emission process, and aerosol-cloud interactions, but allowed patterns of effectiveness and side-effects

to be identified. A summary of key MCB side-effects identified from global computer models is presented in Section 1.7.1.

Subsequently, Korhonen et al. (2010b) developed a wind-speed dependent MCB aerosol emission flux assumption based on the design of the implementation mechanism (Salter et al., 2008). In utilising a global aerosol model and aerosol activation scheme, global N_d changes in response to MCB emissions were estimated for the first time. However, these global aerosol models do not include cloud feedbacks on meteorology, and their use does not typically extend to the estimation of resulting radiative forcings. Key findings associated with the estimation of N_d originating from the use of global climate models are presented in 1.7.2.

The latest global simulations of MCB utilise aerosol-climate models (e.g. Jones and Haywood, 2012; Partanen et al., 2012; Alterskjær and Kristjánsson, 2013). This allows the inclusion of MCB aerosol emission processes, aerosol-cloud interactions, climate feedbacks and the radiative effects of MCB. The representation of the MCB aerosol emission process varies however. While some utilise the wind-speed dependent flux assumption based on Korhonen et al. (2010b) (Jones and Haywood, 2012; Partanen et al., 2012), others simulate the MCB aerosol emissions as fixed increases (Alterskjær et al., 2012; Alterskjær and Kristjánsson, 2013), or multiples of natural sea spray emissions (Hill and Ming, 2012). A summary of estimates of MCB effectiveness based on the use of global aerosol-climate models is presented in Section 1.7.3.

In spite of the importance of understanding and quantifying side-effects, N_d perturbations and the detailed response of clouds, the potential effectiveness of geoengineering schemes are typically quantified using a global mean radiative forcing. Ramaswamy et al. (2001) state that "the radiative forcing of the surface-troposphere system due to the perturbation in or the introduction of an agent (say, a change in greenhouse gas concentrations) is the change in net (down minus up) irradiance (solar plus LW; in Wm^{-2}) at the tropopause after allowing for stratospheric temperatures to readjust to radiative equilibrium, but with surface and tropospheric temperatures and state held fixed at the unperturbed values". It is noted that as the definition of radiative forcing includes only the instantaneous tropospheric albedo changes, it takes into account the first indirect aerosol effect alone. In so doing, it omits the cloud responses associated with: the second indirect aerosol effect (discussed in Section 1.6.2); semi direct cloud effects caused by the absorption of solar radiation by soot (Chapter 2); as well as both the rapid cloud adjustments and cloud feedbacks that result from changes in the troposphere and surface temperatures (Section 1.6.1). In order to account for more of these potential cloud responses, later global MCB modelling studies tend to use an adjusted radiative forcing – the radiative flux perturbation (RFP). Similar to radiative forcing, this holds sea-surface temperature fixed, but allows the meteorology to change, thus allowing

the incorporation of both the first and second indirect effects, along with the semi direct effect, and rapid cloud adjustments (Haywood et al., 2009).

The use of such a radiative forcing measure allows the effectiveness of MCB to be compared against both other geoengineering schemes and climate forcing agents. A summary of the published radiative forcings produced from global-scale MCB simulations is presented in Figure 1.4. Again, for comparison, it is reiterated that – although subject to large uncertainties in some components – the radiative forcing associated with anthropogenic activities between pre-industrial times and 2011 is estimated to be +2.3 Wm^{-2} (Myhre et al., 2013). This figure additionally emphasises the wide range of MCB emission assumptions used in simulating MCB, which complicates the inter-comparison of models.

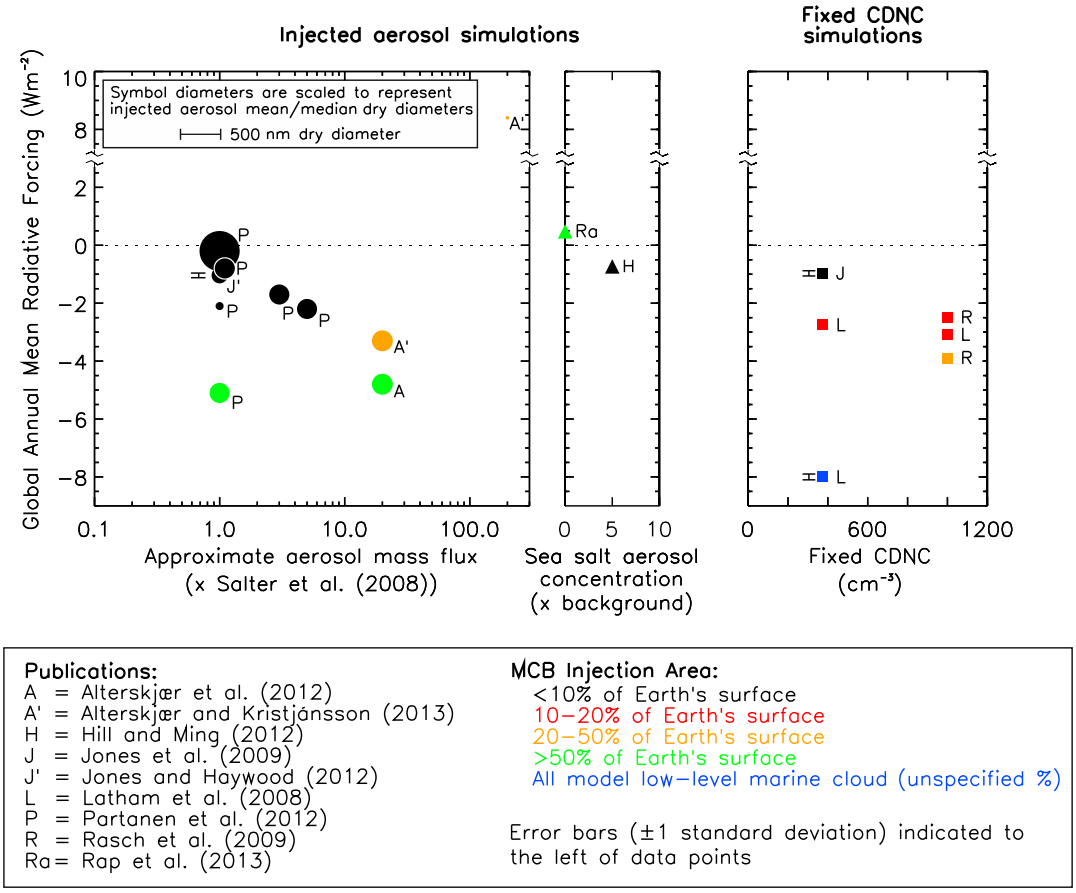

Figure 1.4 *– Summary of radiative forcing estimates from past studies of geoengineering sea salt emissions. Studies are categorised into either emitted aerosol simulations, or fixed cloud droplet number concentration (N_d) simulations. The emitted aerosol simulations are further divided into simulations that introduce sea salt aerosols in relation to the approximate mass fluxes suggested by the Salter et al. (2008) design proposal, or simulations that increase background sea salt aerosol concentrations by a factor. The Rap et al. (2013) paper investigated removal of sea salt emissions from the present day atmosphere. References for each data point are included in the legend. From Kravitz et al. (2013) (including Jenkins).*

1.7.1 The Identification of Side-Effects In Global-Scale Models

While early fixed-N_d global computer simulations omitted any representation of MCB aerosol emissions or aerosol-cloud interactions, they were able to identify key potential climate side-effects, particularly relating to spatially inhomogeneous responses. These patterns of response were typically corroborated by the subsequent global scale modelling that incorporated both MCB aerosol emissions and aerosol-cloud interactions. The subsequent discussion of side-effects first considers temperature responses, then precipitation perturbations, followed by changes to sea-ice extents, ending with the termination effect.

Temperature

MCB-induced temperature decreases were found to be greater local to the MCB target area, through the Tropics, and in the Artic (Jones et al., 2009; Rasch et al., 2009; Hill and Ming, 2012; Jones and Haywood, 2012). The cooling through the Tropics was proposed to result from the strong mixing and primary ocean circulations in the region (Rasch et al., 2009; Hill and Ming, 2012). The Arctic cooling was suggested to originate from an ice-albedo feedback (Jones and Haywood, 2012). In addition to cooling, regions of warming were identified in the North-West Pacific (Rasch et al., 2009; Hill and Ming, 2012) and around Antarctica (Jones et al., 2009; Rasch et al., 2009; Jones and Haywood, 2012). The former was suggested to be caused by teleconnections between the Pacific-North America Oscillation and a MCB induced pseudo-La Niña phase of the El-Nino-Southern Oscillation (Hill and Ming, 2012). The La Niña phase was also shown to occur in the fixed-N_d modelling of Baughman et al. (2012). Warming around Antarctica was suggested to be caused by reduced Antarctic zonal winds resulting from MCB (Jones and Haywood, 2012).

Owing to global-scale interactions occurring outside of the MCB targeted regions, the magnitude of the RFP response was non-linearly related to the extent of MCB application (Jones et al., 2009). The greatest cooling effect resulted from the application of MCB in the South Pacific while temperature changes associated with MCB in the South Atlantic were minor (Jones et al., 2009; Hill and Ming, 2012). Applying MCB to all target areas concurrently produced an RFP that was 25% lower than the sum total for each individual region (Jones et al., 2009). This pattern was also repeated in global mean temperature response (Hill and Ming, 2012).

Precipitation

Precipitation patterns are crucial for future water security, crop growth and maintenance of the biosphere. Like temperature patterns, simulated precipitation patterns were also found to respond to MCB. In initial fixed-N_d simulations (using the Hadley Centre Global Environmental Model, Version 2 (HadGEM2); Jones et al., 2009), precipitation rates

increased in sub-Saharan Africa, Australia, and Northern India, but decreased over Central Asia. Critically precipitation rates also decreased by up to 1 mm day^{-1} relative to the SRES 'business-as-usual' scenario over the Amazon Basin. These patterns were later reproduced in further fixed-N_d representations of MCB (Latham et al., 2012a; Latham et al., 2012b), with the strength of response increasing when emissions were extended over the whole ocean. Similar patterns were found when MCB aerosol emissions and aerosol-cloud interactions were simulated (using the HadGEM2-ES (Earth System) model; Jones and Haywood, 2012), although the magnitude of perturbation was smaller than was initially found. The simulated Amazonian precipitation decreases were found to be a result of MCB applied in the South Atlantic region (Jones et al., 2009; Jones and Haywood, 2012). This corresponds with observations that show that Amazonian precipitation is sensitive to the sea-surface temperature gradient along the Atlantic Ocean (Good et al., 2008). Interrogation of simulated precipitation patterns within the HadGEM model suggests that accuracy is reduced close to steep mountain ranges, and may therefore affect simulation of the Amazonian Basin region (Latham et al., 2012a). Furthermore, reductions in Amazonian precipitation were not present for simulations conducted using other models (Community Climate System Model (Rasch et al., 2009); Geophysical Fluid Dynamics Laboratory AM2.1 General Circulation Model (Hill and Ming, 2012)). Thus, while simulated precipitation outputs in response to MCB may be sensitive to the location of MCB emissions, they may also be sensitive to the model used. Disparities between models may result from, for example, the use of different microphysical parameterisatons. This was suggested to be the reason why the National Center for Atmospheric Research Community Atmosphere Model produced estimates of MCB cloud forcing that were around half of the -8.0±0.1 Wm^{-2} simulated by the Hadley Centre Global Atmospheric Model (HadGAM) (Latham et al., 2008). Inter-model differences are not always significant, however. Similar MCB aerosol emission approaches led to similar radiative forcing outputs for the HadGEM2 model (Jones and Haywood, 2012) and the ECHAM5.5-HAM2 aerosol-climate model (Partanen et al., 2012) for example.

If MCB were to enter the advanced stages of being considered for deployment, multi-model inter-comparisons would be required to determine potential inter-model uncertainties, and to quantify a range of simulated outputs.

Sea-ice Extent

As for temperature and precipitation perturbations, the computer simulation of MCB also produced a spatially inhomogeneous response in sea-ice extent. While MCB resulted in the recovery of mean sea-ice extent, the spatial distribution of coverage differed from the control situation (Rasch et al., 2009; Latham et al., 2012a). The sensitivity of the sea-ice extent response to MCB was also different from the response of precipitation and temperature to

MCB. Thus, the application of MCB could never concurrently return all of the elements of a changed climate to a selected point in time (i.e. present day, or pre-industrial) (Rasch et al., 2009) or achieve multiple climate objectives.

Termination Effect

The termination effect (as introduced in Section 1.4 for SRM geoengineering techniques more widely) has also been investigated for MCB specifically. The fixed-N_d simulation of MCB delayed global mean temperature increases resulting from the SRES 'A1B' emission scenario (IPCC, 2000) by around 25 years. However. its sudden cessation caused temperatures to rapidly recover (a 0.6 K increase) within five to ten years (Jones et al., 2009).

1.7.2 The Estimation of Cloud Droplet Number Concentration Perturbations from Global Aerosol Models

While early fixed-N_d global simulations produced important insights into possible climate responses to MCB, limitations of the models meant that both MCB aerosol emission processes and aerosol-cloud interactions were not captured.

As will be discussed in greater detail in Chapter 2, the formation of cloud droplets depends on several parameters which describe both the background atmospheric and aerosol characteristics, and the characteristics of the emitted MCB aerosols. The background condition parameters include such things as: the aerosol size and number distribution; the maximum supersaturation of water vapour (which is related to the updraft speed within the boundary layer); cloud properties such as cloud thickness; and rate of air that is entrained from above. Potentially important emitted MCB aerosol parameters include the number and size of emitted aerosols and the chemical composition of the particles. Thus, several factors can affect the N_d that may result from an MCB aerosol emission.

This section describes the contribution of global aerosol transport models in MCB modelling. These models require an off-line parameterisation of aerosol activation to calculate N_d. However, the ability to produce global estimates of N_d perturbations resulting from MCB aerosol emission assumptions (Korhonen et al., 2010b) was an important development in MCB modelling.

Such wind-speed dependent MCB emissions in the North Pacific, South Pacific, Indian Ocean, and South Atlantic were simulated in the GLObal Model of Aerosol Processes (GLOMAP) by Korhonen et al. (2010b). Utilising a droplet formation parameterisation (with an assumed vertical velocity distribution), the MCB emissions produced the greatest N_d increase (20%) in the South Pacific. However, the N_d reached only 133 to 177 cm^{-3}, less than half of the 375 cm^{-3} assumed in previous fixed-N_d modelling.

Crucially, in addition to the lower than previously assumed N_d, a 2% reduction in N_d was simulated in response to MCB aerosol emissions in the North Pacific region. Such a N_d reduction would lead to albedo reductions and a warming effect. This N_d reduction was suggested to be caused by a competition effect (Ghan et al., 1998), whereby the larger MCB aerosols would activate preferentially to the smaller background aerosols of the relatively polluted outflow conditions off the West-coast of North America. As the larger MCB aerosols activate preferentially, water condensates on to them, reducing the maximum supersaturation in the cloud region. Under suppressed supersaturation levels, the critical radius of an aerosol necessary for it to activate as a cloud droplet increases. Hence, the smaller background aerosols are no-longer able to activate. Increasing the flux of MCB aerosols five-fold, allowed sufficient new aerosols to activate, eliminating any N_d reductions. Such N_d and albedo decreases were also simulated in the early cloud parcel modelling of Bower et al. (2006) for larger emitted aerosol diameters (>200 nm) into more highly polluted background conditions (N_d of 300 cm^{-3}). However, no reductions occurred for emission into less polluted background conditions (N_d of ~130 cm^{-3}).

A subsequent sensitivity study (using an aerosol activation scheme) considered the effects of various hypothetical combinations of background aerosol concentration, updraft velocity and MCB aerosol size and emission rate on N_d number (Pringle et al., 2012). N_d was generally found to increase asymptotically with MCB aerosol number with MCB aerosols added to already polluted background aerosol concentrations resulting in smaller N_d increases. This corresponds to results anticipated theoretically (Twomey, 1974; Latham et al., 2008), and found in cloud parcel simulations (Bower et al., 2006; Latham et al., 2012a). Increases in N_d were also found to be more sensitive to the number of MCB aerosols emitted than to their size. This included dry diameters of between 100 nm and 500 nm for Pringle et al. (2012) but extended to 4 μm by Bower et al. (2006). Updraft velocity was also found to be important. Smaller MCB aerosols activated to cloud droplets only when the updraft velocities (and hence available moisture) were of sufficient magnitude and updraft-limited conditions could restrict N_d increases regardless of the number and size of MCB aerosols added. However, higher updraft velocities increased supersaturations sufficiently to activate a higher number of MCB aerosols.

These sensitivity simulations also established the conditions necessary for N_d losses. These conditions were found to be a low MCB aerosol concentration (<100-150 cm^{-3}), large MCB aerosol diameter (>250-300 nm), large background aerosol concentrations (≥150 cm^{-3}) and a low cloud updraft velocity (<0.2 ms^{-1}). Low updraft velocities produced low enough supersaturations that preferential activation of the larger MCB aerosols reduced supersaturation to below the critical value needed by the smaller background aerosols to

activate to form cloud droplets. However, the resulting low supersaturations were sufficient to activate further larger MCB aerosols. Hence, as found in the previous global aerosol study of Korhonen et al. (2010b), N_d losses could be overcome by increasing the MCB aerosol emission rate.

Pringle et al. (2012) then went on to depict idealised aerosol concentrations resulting from MCB using baseline aerosol data taken from three different global aerosol models (GLOMAP, EMAC and ECHAM-HAM). These idealised MCB aerosol representations were then used with the same aerosol activation scheme in order to estimate N_d changes resulting from MCB. As occurred for the earlier global-scale computer model representation of MCB, there were disparities in the N_d responses resulting from the different global aerosol models. For example, the background aerosol concentrations in the ECHAM-HAM model were typically less than half of those simulated in the other two models. Hence, while the addition of MCB aerosols resulted in lower N_d concentrations (60-64 cm^{-3}) compared to the GLOMAP model (102-120 cm^{-3}), the percentage increases were larger (130-160% compared to 40-56%). These N_d concentrations were again less than those assumed for the initial fixed-N_d global-scale computer model simulations, and were also less than those found by Korhonen et al. (2010b). However, none of the three models produced a combination of conditions necessary to produce a reduction in N_d. This discrepancy between the findings of Korhonen et al. (2010b) and Pringle et al. (2012) was suggested to result from an overestimated suppression of supersaturation in the former study, owing to the aerosol activation parameterisation used.

1.7.3 The Estimation of Marine Cloud Brightening Effectiveness from Global Aerosol-Climate Models

While the use of global aerosol models allows complex aerosol processes to be simulated, the need to perform aerosol activation calculations off-line prevents climate feedbacks from being captured. Additionally, as this modelling technique does not involve an interactive radiative transfer scheme, the radiative effect of changes to the clouds are typically not estimated.

In the last two years, developments in global-scale computer climate models have included the representation of aerosol transport and aerosol-cloud-radiation interactions. Therefore, this latest generation of global aerosol-climate models can now simulate the MCB aerosol emission processes; interactions between aerosols and clouds; climate feedbacks, and the radiative forcing potential associated with such changes.

Use of the ECHAM5.5-HAM2 aerosol-climate model in simulating MCB aerosol emissions (Partanen et al., 2012) resulted in N_d increases of 74-80% (or N_d values of 194-286 cm^{-3}).

While being larger than previous estimates (Korhonen et al., 2010b; Pringle et al., 2012), these again remain below the initial fixed-N_d assumptions. As for the three global aerosol models used by Pringle et al. (2012), no N_d losses resulted from MCB aerosol emission. This disagreement from the simulation of Korhonen et al. (2010b) was suggested to have been contributed to by lower updraft velocities, higher background aerosol concentrations and lack of cloud feedbacks in the former study. Such a finding reinforces the importance of accurate simulation of such variables as updraft velocity, as demonstrated by the findings of Pringle et al. (2012).

These findings also suggest that the presence of a competition effect associated with MCB that may reduce N_d cannot currently be quantified robustly, and will require further investigation (both computationally and observationally).

For the aerosol activation scheme used by Pringle et al. (2012), only larger (accumulation mode) aerosols resulted in N_d losses. However, use of the Norwegian Earth System model (Alterskjær and Kristjánsson, 2013) found that the emission of large numbers of smaller (Aitken sized) aerosols with modal diameter of 22 nm could also lead to N_d losses and a positive radiative forcing. This was suggested to be caused by the large surface area of the small aerosols producing a large area for condensation of water vapour. While these aerosols took on water, and reduced the maximum supersaturation, they did not grow sufficiently to activate to form cloud droplets. Thus, in the case where supersaturation fell below the critical value needed for activation of background aerosols, N_d reductions resulted. For a mass flux approximately 200 times larger than used by Partanen et al. (2012), covering the ocean between 30°N and 30°S, a positive radiative cloud forcing of 8.4 Wm^{-2} was produced (Alterskjær and Kristjánsson, 2013). It is worth noting that these small aerosols are almost a tenth of the size of those proposed in designs (Salter et al., 2008).

The effect of MCB aerosols on the Earth's radiative budget has so far been considered in terms of the indirect aerosol effects only (i.e. the effect that the aerosols have on clouds). The emission of MCB aerosols into the planetary boundary layer would, however, also result in a direct aerosol effect where the aerosols themselves scatter and absorb SW radiation. The use of aerosol-climate models, that both allow the simulation of the MCB aerosol emission and include interactive radiative transfer calculations, now allows the contribution of this direct aerosol effect to be estimated.

For MCB emissions into similar regions as for the 375 cm^{-3} fixed-N_d simulations of Jones et al. (2009), the ECHAM5.5-HAM2 aerosol-climate model simulated an RFP associated with the indirect effect of -0.7 Wm^{-2} (Partanen et al., 2012). This is just under three-quarters of that found in the fixed-N_d simulation (Jones et al., 2009). There was an additional

contribution of -0.1 Wm^{-2} from the direct aerosol effect, resulting in an overall RFP of -0.8 Wm^{-2}.

Partanen et al. (2012) also found that this total RFP could be increased by increasing the area of MCB emission. As the direct aerosol effect becomes more influential in clear-sky regions, extending the MCB emission area to cover all ice-free ocean led to a net global mean RFP of -3.6 Wm^{-2}, with the contribution of the direct effect increasing to almost 30%. The total RFP could also be increased by increasing the MCB emission number flux, or reducing the size of the emitted aerosol (e.g. from mean dry diameters of 500 nm to 100 nm) while increasing the emission number flux in order to maintain the mass flux. These latter size and number flux changes do not influence the RFP associated with the global mean direct aerosol effect, but have a more significant effect on the indirect aerosol effect.

Further understanding of the importance of indirect and direct effects was produced from investigations using the HadGEM2 Earth System model (Jones and Haywood, 2012). It was found that if the MCB aerosols are targeted to optimise the indirect effect, despite an appreciable contribution from the direct effect, enhancements to the radiative forcing result from meteorological feedbacks with the cloud changes. This produces a RFP of -1.04±0.08 Wm^{-2}. Such meteorological enhancements do not result if the MCB aerosols are targeted to optimise the direct effect, resulting in a RFP of -0.58±0.1 Wm^{-2}. Along with the higher RFP, there is an increased cooling efficiency associated with targeting clouds. This produces a temperature change per unit RFP of 0.52 K/Wm^{-2} compared to 0.22 K/Wm^{-2} when MCB aerosols are emitted to optimise the direct aerosol effect. The poor cooling response for the optimised direct aerosol effect was believed to be caused by reductions in the extent of surface-driven convective clouds in the Tropics in response to surface cooling by the MCB aerosols.

1.7.4 Mesoscale Simulations of Marine Cloud Brightening

As demonstrated in Sections 1.7.1 to 1.7.3, global scale MCB modelling has developed. It now includes a representation of MCB aerosol emissions, aerosol-cloud interactions, climate feedbacks and an estimation of the response of both the radiative balance and a number of climate variables to MCB. As discussed in Section 1.5, these global-scale estimates of the effectiveness and side-effects of MCB are essential in aiding informed decision-making on the place of MCB in response to climate-change.

However, as introduced in Section 1.5, the necessarily coarse resolution of these global-scale models means that they are unable to capture details of the MCB implementation technique. Global-scale models are also currently unable to capture features important to the background cloud conditions (including the process of entrainment of free-tropospheric air and the

resolved dynamics that drive updrafts and hence mesoscale cellular cloud features). In order to assess the possible effects of a more detailed representation of MCB implementation on explicitly resolved cloud dynamics, Wang et al. (2011a) utilised the Weather Research and Forecasting (WRF) cloud-resolving model to simulate MCB at the mesoscale.

Using a double-moment warm-rain microphysical scheme, Wang et al. (2011a) simulated base case conditions that were based on background CCN concentrations of 50, 100 and 200 mg^{-1} (where 100 mg^{-1} is assumed to be a typical marine case, with 1 mg^{-1} approximately equalling 1 cm^{-3}). The horizontal resolution of these simulations was 300 m, and approximately 30 m vertically. The domain size used was 120 km x 60 km, rising 1.5 km vertically. This enabled this study to capture the mesoscale features previously found to be important, particularly for horizontally changing aerosol concentrations (Wang and Feingold, 2009a; Wang and Feingold, 2009b).

The higher resolution of these simulations compared to the global-scale modelling allowed a more detailed representation of the MCB aerosol emission technique. While in global-scale models the aerosols are increased over the grid-cell (covering ~100 km x 100 km), in Wang et al. (2011a) aerosols were introduced into individual grid cells, simulating aerosol emission from individual spraying vessels. This technique, hereinafter described as a point source emission, was found to induce complex dynamical feedbacks in precipitating regimes (Wang and Feingold, 2009b) and a spatially inhomogeneous albedo response. Thus, the albedo was increased along the MCB emission track, but with drier air that is then drawn into adjacent regions resulting in neighbouring albedo decreases. This small-scale inhomogeneity deviates from the inherent uniformity of both MCB aerosol emission and cloud response in global scale models.

These simulations showed that smaller albedo increases were obtained for MCB emissions into higher background aerosol concentrations, as found for N_d changes in previous cloud parcel and global-scale modelling. However, the mesoscale modelling found that this pattern did not continue down to very low background aerosol concentrations (50 mg^{-1}), where the albedo increases were weakened compared to the 100 mg^{-1} background condition. This was the result of precipitation. For the low background aerosol concentrations, small numbers of cloud droplets were formed (<10 mg^{-1}), which grew sufficiently to form rain drops and led to strong precipitation (up to 2 mm day^{-1}). This heavy precipitation removed the emitted MCB aerosols through scavenging before they could reach the cloud. Thus, there was little first indirect aerosol effect and the increase in N_d was insufficient to reduce precipitation via the second indirect aerosol effect.

The background moisture levels were also important. When drier conditions were simulated (9.0 g kg^{-1} in the boundary layer, and 1.5 g kg^{-1} above the cloud-top compared to 9.45 g kg^{-1}

in the boundary and 5.0 g kg^{-1} above the cloud top in the moister simulations), while additional cloud droplets were being formed, they were also evaporating more readily (via processes described more thoroughly in Chapter 2). This offset albedo increases.

As such, significant cloud albedo increases in response to MCB aerosol emissions occurred only for weakly precipitating regimes or conditions of low CCN concentrations (possibly following heavy precipitation). The second indirect aerosol effect (leading to the suppression of precipitation) was suggested as being the most efficient mechanism for increasing albedo in the simulations considered.

In summary, the first part of this chapter has described the concept of MCB, and its potential role in responding to climate change. Decisions on the implementation of MCB would, however, need to be informed by realistic estimates of the scheme's potential effectiveness and side-effects.

The only tool capable of producing such estimates is global-scale computer modelling, which can simulate the large-scale teleconnections and feedbacks needed for capturing global impacts. Such global-scale computer modelling of MCB has developed over time. Increasingly complex models that incorporate an increasing number of climatically-relevant processes, and the improved representation of MCB within these models have both enhanced the realism of simulations. These global-scale simulations have indeed yielded important findings regarding MCB (Section 1.7). However, owing to their grid-spacing of tens of kilometres, they are inherently unable to capture details of the MCB implementation mechanism that occur at scales smaller than this. Hence, global-scale computer modelling of MCB may omit important processes. This omission of MCB implementation mechanism details may therefore impair the realism of the resulting effectiveness estimates.

The simulation of such implementation mechanism details will require higher-resolution computer modelling. But, as the current domain-size limitations of such models prevents them from capturing larger climatic interactions, any findings could only be used to inform future global-scale modelling, rather than provide estimates of MCB effectiveness in themselves.

While there have been numerous global-scale computer simulations of MCB, the importance of capturing these global-sub-grid-scale details has largely been overlooked, with only one previous higher-resolution, mesoscale study having been carried out to-date (Section 1.7.4).

1.8 Research Objectives

This thesis aims to establish the importance of representing details of the implementation mechanism of MCB that occur at scales smaller than global-scale computer simulations can capture. In doing so, this work is intended to inform future global-scale computer modelling of MCB, and, if possible, materially enhance the realism of MCB effectiveness estimates. Additionally, this work could also inform future implementation strategies. For example, as the proposed MCB vessels would potentially sail throughout the night and day, they would encounter the differing cloud and boundary layer conditions that occur over a diurnal cycle. Identifying patterns of MCB effectiveness through the diurnal cycle could thus inform future implementation strategies. While this work focuses on MCB, this central concept may also be applicable to a broader range of proposed geoengineering schemes.

In order to achieve this aim, three case studies are used, each examining a different MCB implementation detail:

Case Study A:

The effect of the timing of MCB aerosol emission through the diurnal cycle of MSc clouds on MCB effectiveness

Case Study B:

The effect of representing the MCB aerosol emission as sea water droplets (rather than as 'dry' aerosols) on resulting MCB effectiveness

Case Study C:

The effect of including aerosol processes that occur within the emission rotor and aerosol plume on the number concentration and size distribution of emitted MCB aerosols, and the resulting effect on the MCB effectiveness

In examining these implementation detail case studies, the cloud-resolving Weather Research and Forecasting model including aerosol and chemistry processes (WRF/Chem) is used. This model is initially configured for use as a cloud-resolving model in order to simulate a range of three idealised MSc cloud conditions. These three conditions are initialised with increasingly polluted background aerosol concentrations. The cloud-resolving model configuration consists of grid cells of 300 m width and a domain size of 9 km x 9 km x 1.5 km (height). These three simulations act as the MSc cloud base cases.

Next, with the model still in the cloud-resolving model configuration, the rapid response of the cloud system to MCB aerosols is investigated for each of the three case studies (Figure 1.5). The cloud-resolving simulations carried out in order to examine the third case study (regarding the inclusion of aerosol processes within the plume) are informed by both simple numerical calculations and additional computer simulations using the WRF/Chem model at higher resolution. These simulations use the model with a grid cell width of 0.5 m

and domain size of 120 m x 40 m, with height of ~60 m. These simulations are designed to capture details of the high aerosol concentrations and characteristic dynamics of the aerosol plume upon emission. These experimental approaches are summarised in Figure 1.5.

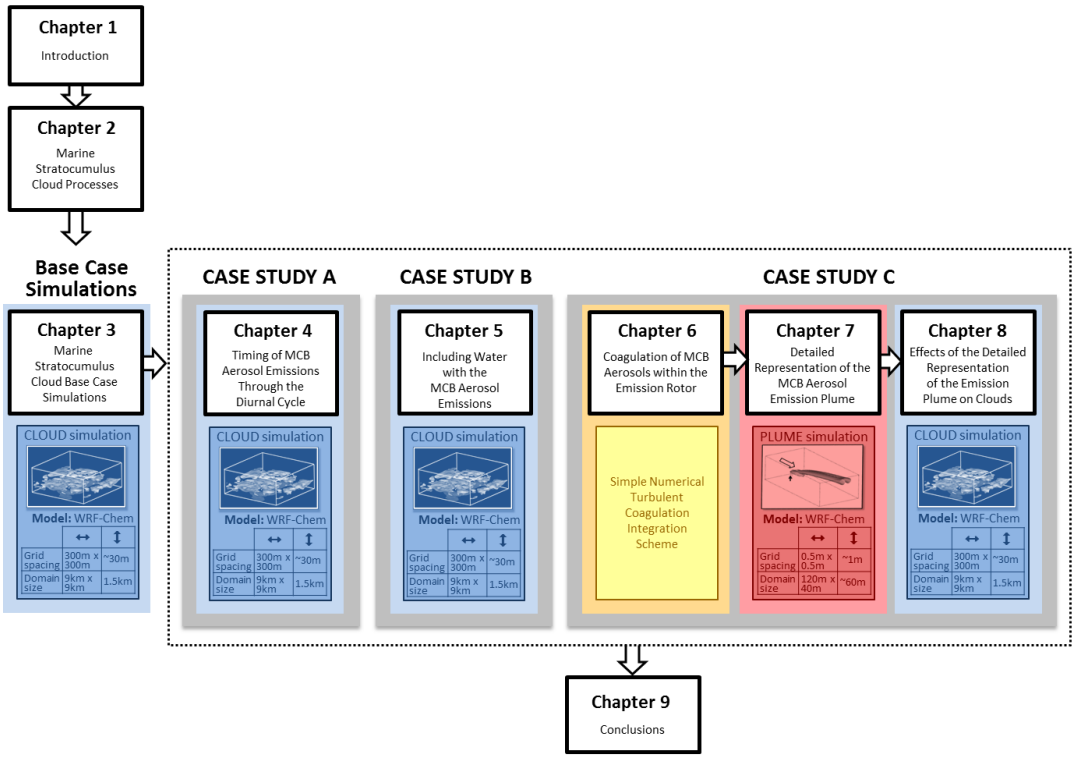

Figure 1.5 *– Overview of the investigative tools used to examine each of the three marine cloud brightening (MCB) implementation detail case studies.*

The ability of cloud-resolving configurations of the WRF model to successfully simulate the characteristic patterns of MSc cloud property variation over a diurnal cycle has been demonstrated in previous studies (Wang et al., 2011a; Chen et al., 2011).

The sub-mesoscale domain size chosen for the cloud simulations allows the rapid cloud system response to the emitted aerosols to be isolated from the subsequent complex, mesoscale feedbacks (Feingold et al., 2010). In spite of omitting these larger, mesoscale feedbacks, previous modelling has shown that useful inferences regarding cloud response and associated dynamical changes to cloud droplet number changes can be obtained from such sub-mesoscale representations (Savic-Jovcic and Stevens, 2008). Similarly, several MSc modelling experiments have been undertaken at domain sizes smaller than those necessary to produce mesoscale features, for example: Stevens et al. (2005a) (3.4 x 3.4 x ~1.5 km); Ackerman et al. (2009) (6.4 x 6.4 x 1.5 km); and Chen et al. (2011) (2.5 x 2.5 x 1.6 km). Limiting the domain size additionally allows simulations to be carried out using the more computationally expensive WRF/Chem model. The incorporation of chemical and aerosol processes in this model has been shown to successfully enhance the ability to examine

realistic aerosol-cloud interactions in MSc cloud fields (Yang et al., 2011b; Saide et al., 2012; George et al., 2013).

Further discussion of the model performance in simulating both resolved cloud features, and the cloud properties perturbations in response to the addition of MCB aerosols, are discussed in Chapters 3, 4, 5 and 8. The ability of the model to simulate detailed aerosol emission plume features (as used in investigating the third case study) is discussed in Chapter 7.

1.9 Thesis Structure

This chapter began by introducing geoengineering as a possible means of ameliorating climate change. Being the focus of this work, the evolution of the MCB proposal and associated research was then presented. This chapter culminated in introducing the focus of this work (encapsulated by three case studies), with an overview of the modelling approaches and thesis structure being presented in Figure 1.5.

Chapter 2 provides an overview of the key processes and characteristics of the target MSc clouds, necessary for understanding the potential cloud changes in response to MCB. Chapter 2 also builds on the fundamental aerosol-cloud interactions – key to the MCB proposal – that were introduced in this chapter, further reviewing these complex relationships in the context of MSc clouds. The cloud-resolving computer model used in this work, along with its setup, are introduced in Chapter 3, which describes the use of the model in forming the three MSc base cases that are the basis of subsequent MCB aerosol emission experiments.

Chapters 4 to 8 constitute the main results of this research. Chapter 4 describes the methodology and results achieved in investigating the first case study (regarding the timing of the aerosol emission through the diurnal cycle). Chapter 5 describes the methodology and results achieved in investigating the second case study (regarding representation of the emitted MCB aerosols as sea water droplets). The third, and final, case study (regarding the consideration of in-rotor and in-plume processes) spans three chapters. Chapter 6 describes the simple numerical integration scheme used to examine in-rotor processes, the results of which inform a plume simulation sensitivity experiment. Chapter 7 describes the experimental design and results associated with the higher-resolution and smaller domain size detailed simulation of the MCB aerosol emission plume. The resulting changes in aerosol number concentration and size distribution are used to inform the cloud-resolving simulations presented in Chapter 8.

This thesis closes with Chapter 9, which summarises the key findings associated with each of the three case studies. This chapter also draws conclusions as to the importance of the detailed computer simulation of MCB in producing increasingly realistic estimates of MCB effectiveness. Included in this chapter are suggestions for future research needs.

Chapter 2
Marine Stratocumulus Cloud Processes

2.1 Introduction

As introduced in Chapter 1, this work focuses on the MCB geoengineering proposal described by Latham et al. (2008) and Salter et al. (2008). This proposal intends to increase the albedo of MSc clouds by intentionally adding aerosols that can act as CCN to the marine boundary layer via sea-going vessels.

The MCB proposal was founded on the theory that adding aerosols to the MSc cloud region could increase cloud albedo. This was suggested to be the result of both creating a larger number of smaller cloud droplets (the First Indirect Aerosol Effect; Twomey, 1977), but also by suppressing precipitating (relating to the Second Indirect Aerosol Effect; Albrecht, 1989). However, research carried out in the last few decades – including campaigns utilising aircraft and ship-based measurements, satellite observations and numerous numerical modelling approaches – suggests that the response of clouds to changes in aerosol concentrations is highly complex, and particularly sensitive to background conditions (Boucher et al., 2013).

This chapter presents a review of the current understanding of MSc clouds and is divided into two main parts. The first part introduces typical MSc characteristics and discusses the roles of key MSc cloud processes in the formation and development of MSc clouds over a diurnal cycle. An appreciation of these fundamental principles is essential as they must be adequately modelled in the computer simulated MSc clouds (Chapter 3) that form the basis of subsequent MCB investigations. The second part of the chapter examines the relationships and dominant feedback processes that exist between cloud processes and aerosols (therefore being of intrinsic importance to the MCB proposal). Accordingly, this chapter closes with a discussion of possible net indirect aerosols effects such as could occur with MCB.

2.2 Typical Marine Stratocumulus Cloud Characteristics

MSc clouds (Figure 2.1) are low, stratus clouds that form below temperature inversions in regions of large-scale subsidence. These temperature inversions typically lie at altitudes of around 1 km (Wood and Bretherton, 2004) and, by limiting the height of convection, restrict the height of the MSc clouds (Klein and Hartmann, 1993). Unlike cumulus-type clouds (that form in response to surface-originating convection), MSc clouds typically form in areas of lower-tropospheric stability associated with cooler sea-surface temperatures. Hence, persistent decks of MSc clouds are located in the mid-latitudes and sub-tropics, over cold water upwelling regions off the west coasts of continents (Klein and Hartmann, 1993), as shown in Figure 1.2 (Chapter 1).

MSc clouds are typically 200-400 m thick, with spatial mean LWP of ~150 g m^{-2}, and N_d that range from less than 10 cm^{-3} (in pristine marine regions) to over 500 cm^{-3} in more polluted regions (Wood, 2012). Precipitation occurs in approximately 20 to 40% of MSc clouds (Bennartz, 2007; Leon et al., 2008; Christensen and Stephens, 2012). Owing to the low altitudes involved, these precipitation processes tend to involve only warm processes (i.e. drizzle and rain). The albedo of MSc cloud decks can range from around 0.3 to 0.7 (Latham et al., 2008).

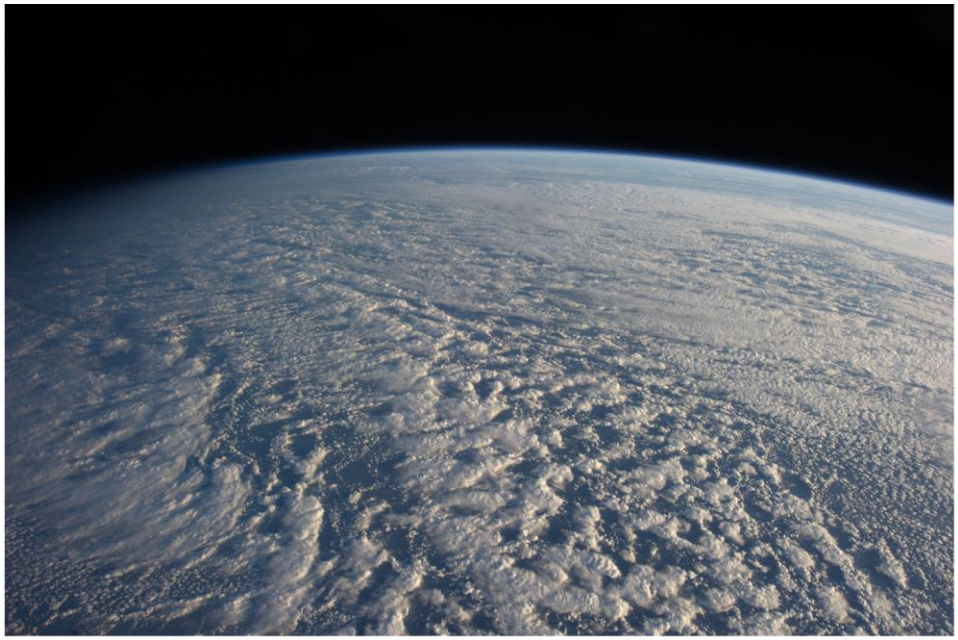

Image courtesy of the Image Science and Analysis Laboratory, NASA-Johnson Space Center. "The Gateway to Astronaut Photography of Earth". Obtained from http://eol.jsc.nasa.gov/scripts/sseop/photo.pl?mission=ISS034&roll=E&frame=016601 on 13th November 2013.

Figure 2.1 *– An example of marine stratocumulus (MSc) clouds, located in the north-west Pacific Ocean, as captured from the International Space Station.*

2.3 Marine Stratocumulus Cloud Processes

Figure 2.2 shows a summary of the physical processes and background conditions that are important in the development of MSc clouds. As introduced in Chapter 1 (Section 1.6.2), warm cloud droplets form when water condenses onto CCN. MSc clouds therefore need both sufficient moisture for such condensation, and an adequate number of aerosols of suitable number concentration, size and composition to act as CCN. As turbulent mixing is a fundamental process in maintaining MSc clouds, this section begins with a description of sources of turbulence within the MSc-topped boundary layer.

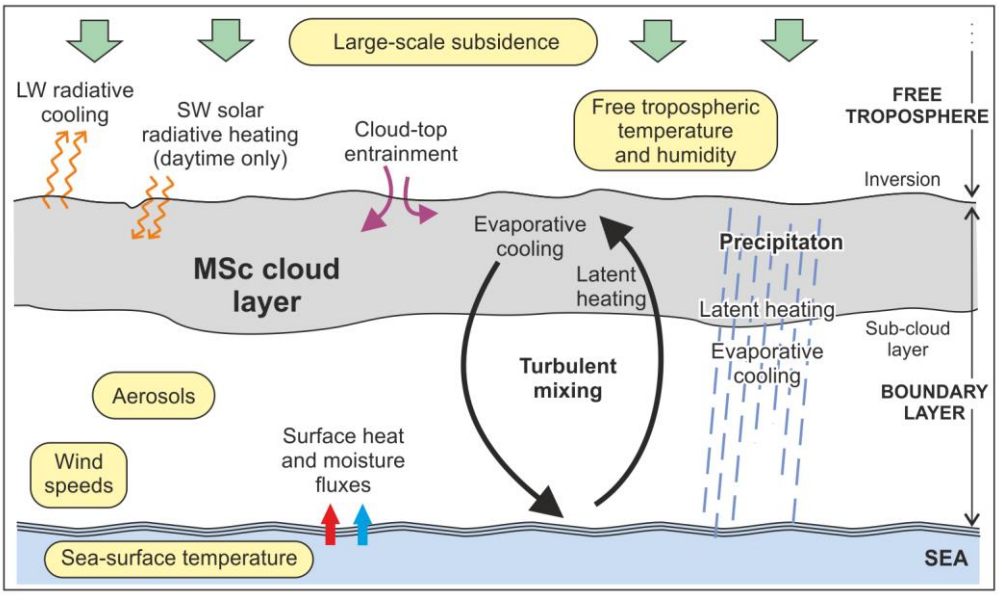

Figure 2.2 *– Summary of the physical processes important for the development of MSc clouds, adapted from Nieuwstadt and Duynkerke (1996). Yellow rounded rectangles show external meteorological and aerosol parameters.*

2.3.1 Sources of Turbulence in the Marine Stratocumulus-Topped Boundary Layer

For the MSc-topped boundary layer, the largest source of turbulence originates from LW radiative cooling at the cloud-top (e.g. Nicholls and Leighton, 1986). This cooling is typically associated with radiative flux perturbations of between 50 and 90 Wm^{-2} and occurs within the upper tens of metres of the cloud (Wood, 2012). This cooling induces negative (downward) buoyancy fluxes in this cloud-top region which results in the creation of turbulence and consequent mixing within the boundary layer.

While this LW cloud-top cooling is the dominant source of MSc-topped boundary layer turbulence, other contributing sources include wind shear across the inversion (e.g. Wang et al., 2008), and sensible and latent heat fluxes at the surface. Upward sensible and latent heat fluxes measured during the second research flight of the Second Dynamics and Chemistry of

Marine Stratocumulus field study (DYCOMS-II) were 16 Wm^{-2} and 93 Wm^{-2} respectively (Ackerman et al., 2009). The magnitude of such surface fluxes will, however, be dependent upon the sea-surface temperature, temperature and humidity of the overlying air, and surface wind speeds. The emission of LW radiation from the Earth's surface additionally contributes to turbulence by warming the MSc cloud base, and thereby inducing positive buoyancy. Finally, additional MSc-topped boundary layer turbulence can result from latent heat processes within the MSc cloud itself. These liquid water fluxes occur as water vapour condenses to form cloud droplets in updrafts, while cloud droplet water in the descending downdrafts evaporates (e.g. Bretherton and Wyant, 1997; Wang et al., 2003).

In a well-mixed (coupled) MSc-topped boundary layer, turbulent mixing is strong enough to mix moisture throughout its depth, from the sea-surface to the cloud layer. MSc-topped boundary layers tend to be well mixed for depths below 750 m to 1000 m becoming more decoupled for deeper boundary layers (Bretherton and Wyant, 1997; Wood and Bretherton, 2004; Bretherton et al., 2010). Transition from MSc to more scattered cumulus clouds occurs as surface warming dominates cloud-top cooling. This tends to occur as the sea-surface warms and the boundary layer deepens towards the equator (Sandu et al., 2010).

2.3.2 The Diurnal Cycle

MSc-topped boundary layers characteristically becomes more decoupled, less well-mixed and more stratified into the daytime (Caldwell et al., 2005). This is the result of cloud-top warming caused by the presence of SW radiation, which acts to offset the cloud-top LW radiative cooling (Nicholls, 1984; Rogers and Koracin, 1992). This daytime radiative offsetting inhibits the cloud-top production of turbulence and hence tends to decouple the cloud and sub-cloud boundary layer (Caldwell and Bretherton, 2009). The presence and strength of decoupling is dependent upon several background conditions – including boundary layer depth and precipitation rates (Sandu et al., 2008). However, the clouds during the day typically exhibit a descent of cloud top (e.g. Blaskovic et al., 1991; Zuidema et al., 2009). This results in a cloud thinning. This daytime thinning – which may also be accentuated by an increase in the height of the cloud base (e.g. Blaskovic et al., 1991; Caldwell et al., 2005) – is concomitant with a decreasing LWP (e.g. Bretherton et al., 2004; Duynkerke et al., 2004), cloud fraction (e.g. Rosenfeld et al., 2006; Caldwell and Bretherton, 2009) and cloud albedo (e.g. Minnis et al., 1992; Comstock et al., 2005). In spite of these daytime cloud changes, as SW radiation diminishes into the night, the nocturnal balance of processes tends to be restored. This results in an increased production of turbulence, leading to the re-coupling of cloud and sub-cloud layers and a recovery in cloud layer properties (Wang et al., 2010). Thus, the daily influence of SW radiation leads to a characteristic diurnal cycle of both dynamic processes and cloud properties in MSc clouds.

2.3.3 Cloud-Top Entrainment

The inversions that cap MSc clouds are characterised by sharp gradients in moisture and temperature, with a drier, warmer free troposphere overlying a wetter and cooler boundary layer below. Temperatures can increase by more than 10 K in a couple of metres, while moisture can decrease by several grams per kilogram of dry air (e.g. Ackerman et al., 2009). These acutely different conditions at the inversion become important because, in addition to producing mixing within the MSc-topped boundary layer, turbulence at the cloud-top also entrains drier, warmer free-tropospheric air into the cloud layer. Typically nocturnal rates of cloud-top entrainment are around 4 mm s^{-1} (Stevens et al., 2003a; Wood and Bretherton, 2004; Caldwell et al., 2005), although they are again dependent upon background conditions. As the rate of entrainment is dependent upon turbulence, it also exhibits a diurnal cycle, decreasing to nearly zero during the day (Caldwell et al., 2005).

The entrainment of free-tropospheric air acts to increase the height of the cloud-top, in opposition to large-scale subsidence. The entrainment of this free-tropospheric air also leads to a complex system of feedbacks, as illustrated schematically in Figure 2.3. Briefly, the entrained free-tropospheric air acts to warm and dry the MSc-topped boundary layer (E1; Figure 2.3), altering the cloud properties by reducing cloud thickness, cloud fraction and LWP. However, as drying of this cloud-top layer reduces the water available for evaporation, evaporative cooling in the cloud-top also reduces, leading to reduced entrainment (E2; Figure 2.3). The warming effect of entrainment also acts to directly stabilise the cloud-top against the turbulence-inducing LW cloud-top radiative cooling (E3; Figure 2.3) which again acts to reduce entrainment.

Thus, while feedbacks associated with both entrainment-induced changes to cloud properties and turbulence act to self-regulate the rate of entrainment, the magnitude of the contribution of each process to the rate of entrainment is not fully understood (Wood, 2012). Understanding cloud-top entrainment – and its effects on clouds – is further complicated by its sensitivity to atmospheric conditions. For example, entrainment rates increase for weaker temperature and humidity gradients across the inversion (e.g. Moeng, 2000). However, particularly warm and dry overlying air will lead to greater drying and warming when entrained into the MSc-topped boundary layer (Ackerman et al., 2004).

As indicated in Figure 2.3, N_d also has an effect on entrainment (E5). As this relationship is relevant to the indirect aerosol effects and the MCB proposal, it is discussed separately in Section 2.4.2.2.

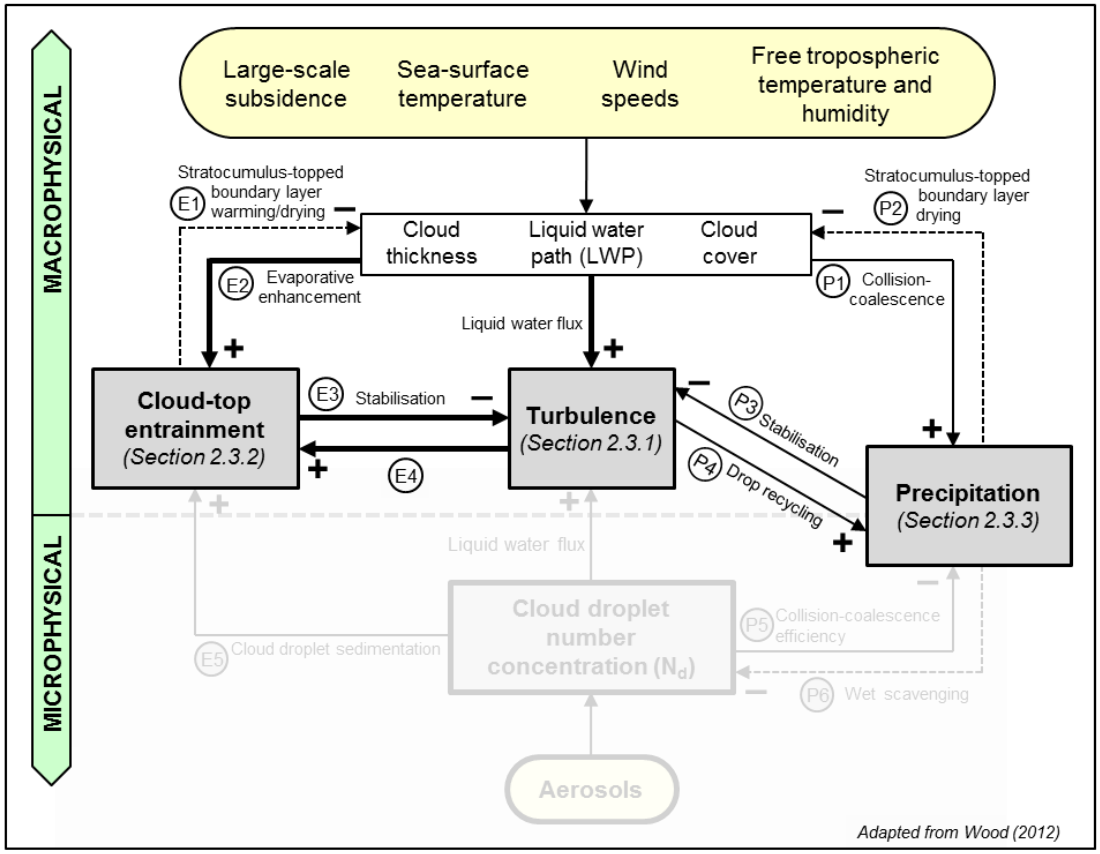

Figure 2.3 *– Conceptual system dynamics diagram illustrating important feedbacks that serve to regulate the thickness, liquid water path (LWP), and cloud cover of MSc clouds. Modified from Figure 26 of Wood (2012). Yellow rounded rectangles show external meteorological and aerosol parameters, as in Figure 2.2. White boxes show key internal variables. Plus and minus signs indicate positive and negative impacts of one variable on another, with the key physical processes accompanying the arrows where necessary. Thick arrows indicate the cloud-radiation-turbulent-entrainment feedback system that constitutes a dominant negative feedback system regulating MSc thickness and cover. Solid lines indicate feedbacks that operate on time scales of typically an hour or less, while dashed lines indicate feedbacks that operate on markedly longer time scales. The thick dotted grey line is used to separate the chart into (top) macrophysical and (bottom) microphysical variables, with precipitation straddling the boundary between the macrophysical and microphysical realms. Circled notations (e.g. E1, P5 etc.) are used for in-text references. Changes associated with changes to the N_d that are faint in this diagram are discussed in Section 2.4.2 in terms of the Second Indirect Aerosol Effect, and represented in Figure 2.7.*

2.3.4 Precipitation

Precipitation occurs when cloud droplets grow sufficiently to form raindrops. Raindrops typically have diameters in excess of ~0.2 mm (American Meteorological Society, 2012). The growth of cloud droplets can occur via condensation, but is largely the result of the collision-coalescence process (Wood, 2012). MSc cloud droplets tend to grow sufficiently to form raindrops when their initial diameters are in excess of 15 to 30 μm (Yum and Hudson, 2002; Rosenfeld et al., 2012). As such, precipitation tends to occur under lower background aerosol

conditions (Bennartz, 2007) which are associated with smaller numbers of larger droplets. As a sufficient number of these cloud droplets must coalescence to form a raindrop, precipitation also depends upon background meteorological conditions (Wang et al., 2010) that effect the cloud thickness and LWP (vanZanten et al., 2005), as indicated in Figure 2.3 (P1).

If precipitation reaches the surface, there may be a resulting loss of LWP (P2; Figure 2.3), although this will depend on dynamical feedbacks that occur in response to precipitation, as will be discussed in this section. As for cloud-top entrainment, precipitation also exhibits a diurnal cycle, decreasing during the day in response to LWP decreases (Leon et al., 2008).

The intensity of precipitation can be described according to the rates at the cloud base, and broadly classified as: light when less than 0.5 mm day^{-1}; moderate when between 0.5 and 2 mm day^{-1}; or heavy when above 2 mm day^{-1} (Wood, 2012).

Precipitation is associated with several complex and interrelated processes within the MSc-topped boundary layer including latent heat fluxes, dynamics, stability and moisture distributions. For example, the formation of raindrops causes latent heating within the cloud, producing a warming of approximately 30 Wm^{-2} for surface rain rates of 1 mm day^{-1} (Wood, 2012). This effect counters the LW radiative cooling, stabilising the MSc-topped boundary layer (P3; Figure 2.3) and reducing turbulent production. Reduced turbulence in turn reduces the amount by which droplets are recycled within the cloud layer, thus reducing the opportunity for collision-coalescence, leading to decreases in the precipitation rate (P4; Figure 2.3) (Feingold et al., 1996). As the precipitation falls from the cloud, it evaporates, leading to evaporative cooling and the addition of moisture in the sub-cloud layer (Feingold et al., 1999). Around 80% of the precipitation evaporates within 150−250 m of the cloud base for the light to moderate precipitation rates of between 0.2 to 0.8 mm day^{-1} at cloud base (Wood, 2005). The resulting changes to the temperature and moisture profiles of the MSc-topped boundary layer induce a dynamical response, and hence affect the subsequent structure of the clouds. A simplified schematic representation of possible cases is shown in Figure 2.4.

Light precipitation that evaporates entirely within the sub-cloud layer produces a thin layer of evaporatively cooled air below the cloud base (Figure 2.4 a). This leads to destabilisation and enhanced mixing within the boundary layer (Feingold et al., 1996) that can maintain or even increase cloudiness (Jiang et al., 2002; Stevens and Feingold, 2009).

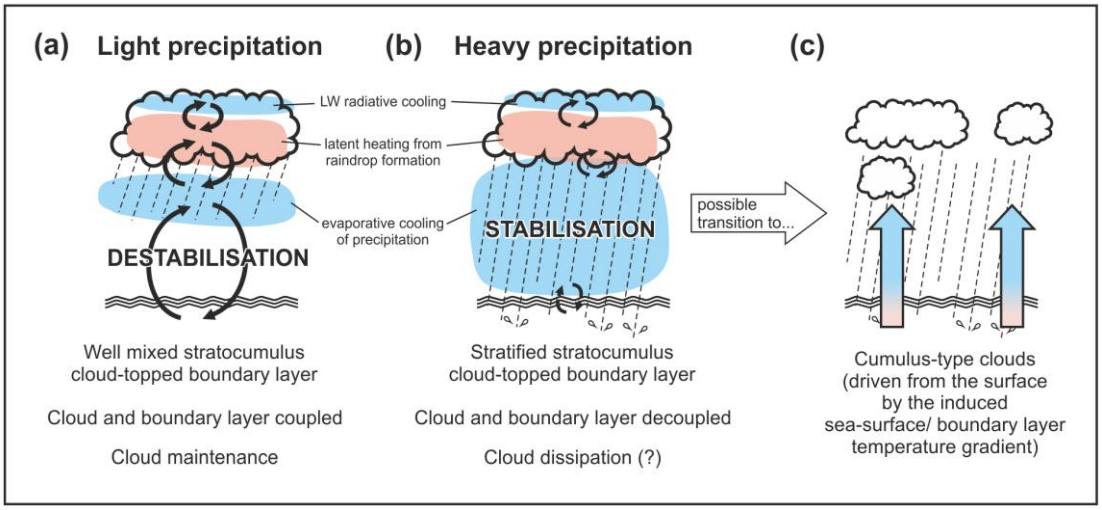

Figure 2.4 *– Possible MSc-topped boundary layer dynamical responses to precipitation for: (a) light precipitation; (b) heavy precipitation; (c) transition to cumulus-type cloud structure.*

For heavier precipitation, evaporation can continue through the depth of the sub-cloud boundary layer (Figure 2.4 b). This deeper cooling can act to stabilise the boundary layer, leading to decoupling of the cloud and sub-cloud boundary layers (Feingold et al., 1996; Caldwell et al., 2005; Savic-Jovcic and Stevens, 2008). This can lead to cloud dissipation, and the formation of pockets of open cells (Wang et al., 2010; Berner et al., 2011). The deep evaporative cooling in the boundary layer also increases the temperature gradient between the sea surface and the overlying boundary layer. As such, the MSc clouds can transition towards more surface-originating, cumulus-type convective behaviour (Figure 2.4 c) (Nicholls, 1984; Paluch and Lenschow, 1991; Stevens et al., 1998; Savic-Jovcic and Stevens, 2008). Such a transition can be considered analogous to the MSc to cumulus cloud transition that occurs over warmer waters (Section 2.3.1).

As these responses to precipitation are sensitive to the vertical distributions of cooling through the boundary layer, they will be highly dependent upon atmospheric and boundary layer conditions (Wang et al., 2010). These include sea-surface temperature and the strength of large-scale subsidence (Sandu and Stevens, 2011; Berner et al., 2013). Computer modelling of such phenomena must also be able to capture the extent of mixing within the boundary layer (Sandu et al., 2009).

As was the case for entrainment (and as indicated in Figure 2.3), N_d also has an effect on precipitation (P5 and P6). As this relationship is again relevant to the indirect aerosol effects and the MCB proposal, it is discussed separately in Section 2.4.2.1.

2.3.5 Open and Closed Cells

At the mesoscale, MSc clouds exhibit self-organised cellular cloud patterns that occur at scales of tens of kilometres (Agee, 1987; Bretherton et al., 2004). These cellular features can largely be classified as either open or closed cellular regimes. As exemplified in satellite imagery of such features (Figure 2.5), MSc cloud regions comprising an open cellular structure are characterised by lower cloud fractions and lower albedos than their closed cellular counterparts. Cloud fractions are typically less than 40% for open cell regions compared with up to almost 100% for closed cells (Rosenfeld et al., 2006), with albedos of ~0.35 for open cells, and up to ~0.75 for closed cells (Savic-Jovcic and Stevens, 2008).

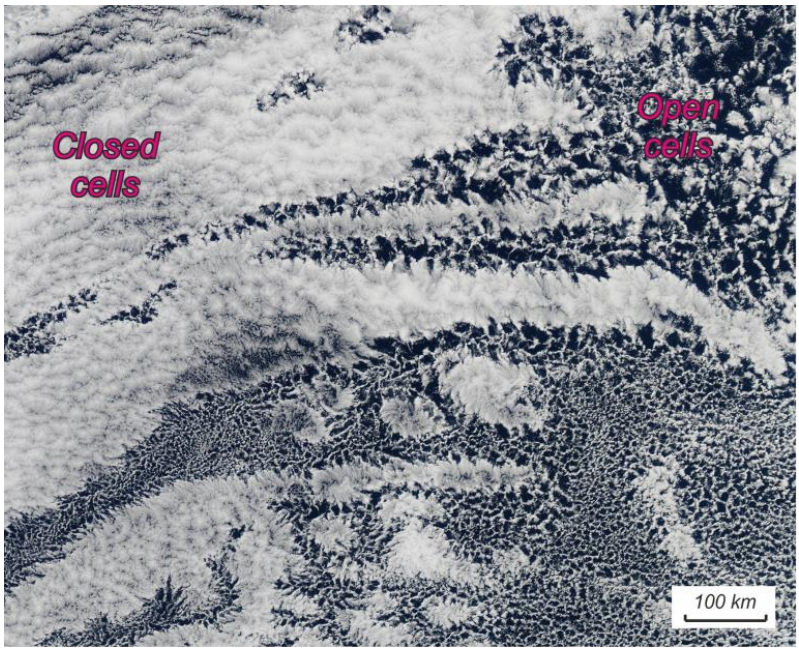

Annotations added to image obtained by the Moderate Resolution Imaging Spectroradiometer (MODIS) on NASA's Aqua satellite of clouds over the Pacific Ocean off the coast of Peru on April 17, 2010. Adapted from NASA image by NASA/GSFC/Jeff Schmaltz/MODIS Land Rapid Response Team. Obtained from http://earthobservatory.nasa.gov/IOTD/view.php?id=43795 on 22nd July 2013.

Figure 2.5 *– Example satellite image indicating open and closed cell formations.*

Dynamically, open cells are characterised by broad regions of downdrafts surrounded by narrow columns of updrafts that produce the slender cloud walls of the cells. Such spatial dominance of downdrafts is consistent with the subsidence and decent of air associated with the evaporative cooling of precipitation. Indeed, open cellular regions tend to be associated with strong precipitation (Stevens et al., 2005b; Comstock et al., 2005; Wood et al., 2008; Wood et al., 2011). Open cellular regions therefore tend to occur in areas of lower aerosol concentrations (Rosenfeld et al., 2006; Wang et al., 2010; Wood et al., 2011). Fields of such cellular structures can persist for tens of hours (Stevens et al., 2005b), although observations and computer modelling suggest that this apparent steady-state actually comprises of on-going cyclic transformations (Feingold et al., 2010). For open cells, it is suggested that the

cloudy cell walls deepen to the point of precipitation, at which they become the centre of a new cell (Wang and Feingold, 2009a).

In contrast to open cellular regimes, regions of closed cells are less likely to be precipitating and tend to occur in areas of higher aerosol concentrations (Wang and Feingold, 2009a). Closed cell regimes are dominated by strong downdrafts resulting from cloud-top radiative cooling. These strong downdrafts are compensated for by large regions of weaker updrafts, producing the large areas of clouds that characterise the centres of the closed cells (Wang and Feingold, 2009a).

2.4 Aerosols

Aerosols range in size, composition and spatial and temporal distribution and can have either natural or anthropogenic sources based in either marine or continental regions. As introduced in Chapter 1, marine-originating aerosol largely comprises of wind-driven sea spray. Biogenic processes (for example, planktonic emission of the dimethyl sulphide aerosol precursor gas) and shipping exhaust products also contribute (Andreae and Rosenfeld, 2008). Continental-originating aerosol, comprising soil dust; biogenic aerosols; products of biomass and fossil fuel burning; and the products of industrial processes can also be transported to marine regions (Andreae and Rosenfeld, 2008). Owing to lower emission rates, marine regions tend to be cleaner than continental regions. This is exemplified by CCN concentrations that are of the order of tens of aerosols per cm^3 for marine regions compared with hundreds or thousands per cm^3 for anthropogenic regions, assuming a 0.4% supersaturation in both cases (Andreae, 2009).

Atmospheric aerosol concentrations depend not only on the strength of aerosol sources, but also on the strength of aerosol sinks. These sinks can remove aerosols from the atmosphere in several ways. Aerosols can be lost from the atmosphere through dry deposition at a surface. Aerosols can also be lost from the atmosphere when they are activated to cloud droplets (although if the droplet evaporates, the aerosol would be reintroduced). If these cloud droplets grow to form rain droplets that reach the surface, the aerosols will be lost via the process known as wet deposition (or scavenging). Furthermore, within this wet deposition process, as these rain droplets fall through the atmosphere, they can collide with, incorporate, and ultimately remove additional aerosols. This wet deposition process can mean that precipitation events can locally deplete CCN concentrations to such an extent that clouds cannot form. However, computer simulations suggest that a modest replenishment rate of the order of 1 mg^{-1} h^{-1} may be sufficient to maintain an open cell regime (Wang et al., 2010).

Aerosols play an important role in influencing the top of atmosphere radiative fluxes that are central in controlling the Earth's climate (Boucher et al., 2013). They alter this balance of radiative fluxes in a number of ways. Firstly, aerosols can affect the balance of radiative fluxes through a direct effect that results from the ability of atmospheric aerosols to scatter and absorb SW and LW radiation. The nature of this response depends upon the optical properties of the aerosols. Primarily scattering aerosols (e.g. sulphate aerosols, sea spray) tend to produce a net negative downward radiative forcing and an associated global cooling effect. A positive downward radiative forcing may, however, result from aerosols that contain absorbing material (e.g. black carbon), particularly if they overlie areas with higher albedo (e.g. snow and clouds). Direct aerosol effects are particularly important in clear-sky conditions, or when the aerosols overlie the cloud layer. It has been estimated that the direct aerosol effect has resulted in a radiative forcing of -0.35 Wm^{-2} for the period between 1750 and 2011, or -0.85 to +0.15 Wm^{-2} for the 90% confidence range (Myhre et al., 2013). Secondly, aerosols can have a semi-direct effect, whereby absorbing aerosols heat the air, leading to a reduction in cloud cover (Johnson et al., 2004). Lastly, aerosols can have an indirect effect on the balance of radiative fluxes, resulting from their interaction with clouds. It has been estimated this cloud-aerosol interaction has resulted in an effective radiative forcing of -0.45 Wm^{-2} for the period between 1750 to 2011, or -1.2 to 0.00 Wm^{-2} for the 90% confidence range (Myhre et al., 2013).

The indirect aerosol effect can be split into first and second indirect aerosol effects. The first indirect aerosol effect describes mechanisms by which aerosols modify the microphysics of the cloud under a fixed LWP assumption. The second indirect aerosol effect considers the effects of aerosol-induced LWP changes (having previously been described as the cloud lifetime effect). In reality – and as will be discussed – numerous cloud mechanisms will alter the LWP in response to changes in the microphysics of the cloud. As such, the fixed LWP assumption of the first indirect aerosol effect could never occur, meaning that this partitioning of the indirect aerosol effects is a wholly artificial construct. Such a hypothetical division is, however, useful for examining the potential effects of individual cloud mechanisms, and will therefore be utilised here.

Indirect aerosol effects are central to the MCB proposal, and discussions on their potential nature in MSc clouds form the focus of the remainder of this chapter. However, understanding of indirect aerosol effects is incomplete. While the IPCC describes the level of confidence in understanding the mechanisms associated with the direct aerosol effect as high, this falls to a low confidence for the first indirect aerosol effect (Boucher et al., 2013). This falls further to very low for the equivalent of the second indirect aerosol effect.

2.4.1 The First Indirect Aerosol Effect

As described, the first indirect aerosol effect considers the effects of a change in aerosols on a cloud whose LWP is held fixed. Relevant to the MCB proposal are the cloud changes associated with an increase in the aerosol concentration caused by the addition of MCB aerosols. These MCB aerosols are intended to result from artificially produced sea water droplets, and as such would be hygroscopic (Lewis and Schwartz, 2004). The introduction of these MCB aerosols is intended to increase the number of available CCN, particularly in the clean (and hence CCN limited) marine regions that are the intended target of MCB. Under conditions of supersaturation, water vapour condenses on to these CCN, and owing to their increased number, results in the formation of a relatively increased N_d. Ignoring cloud feedbacks, and assuming that adding aerosols will not alter the levels of supersaturation (i.e. omitting any resulting dynamical changes), the reapportionment of this supersaturation to the higher N_d will result in a higher number of smaller cloud droplets. It is this resulting increase in cloud optical thickness and albedo (Twomey, 1977), with associated enhancement of SW radiation reflection, negative radiative forcing, and cooling that is fundamental to the MCB proposal.

The ability of the addition of MCB aerosols to achieve a cloud albedo enhancement via this first indirect aerosol effect is, however, contingent on characteristics of both the background aerosols and emitted aerosols, and on meteorological conditions. As found in mesoscale MCB computer simulations (Wang et al., 2011a) and observations (Sechrist et al., 2012), albedo enhancements tend to be greatest when modifying clouds in cleaner (CCN limited) background conditions. This response assumes, however, that the MCB aerosols emitted are of a suitable size compared to the background aerosols. The size distribution of these background aerosols can vary depending on the strength and nature of emission sources and sinks. While size distributions of atmospheric aerosols tend to be dominated – in terms of mass – by aerosols in the accumulation mode, with dry diameters of 50-500 nm (Seinfeld and Pandis, 2006), smaller nucleation mode aerosols can be formed from the nucleation of precursor gases (resulting in aerosols with dry diameters of less than ~10 nm). While the natural planktonic emission of DMS has already been listed as an example, such precursor gases can also result from anthropogenic activities including, for example, sulphuric gases emitted from industrial processes (Andreae and Rosenfeld, 2008). These aerosols can then grow through condensation and coagulation to intermediate 10-100 nm dry diameters (Aitken mode), with the survival probability of nucleated aerosols (3 nm) reaching 100 nm typically being below 10% (Kuang et al., 2009). Larger aerosols in the atmosphere, with dry diameters over ~2 μm (coarse mode), comprise only around 5-10% of the total aerosol number concentration in the marine environment (Seinfeld and Pandis, 2006). Such coarse mode

aerosols can consist of dust particles, pollen and sea spray spume drops (O'Dowd et al., 1997; Seinfeld and Pandis, 2006). Observations and cloud modelling have shown that giant CCN, with diameters of 10μm, can form larger cloud droplets (Lehahn et al., 2011; Ghate et al., 2007). Hence, they may initiate precipitation, particularly in previously non-precipitating clouds (Feingold et al., 1999; Lu and Seinfeld, 2005).

For the addition of aerosols to result in an increase in cloud droplet concentration (and hence albedo) the aerosols must be of a sufficient diameter to activate. However, as discussed in Chapter 1, the outputs of global MCB modelling suggest that if the emitted MCB aerosols are larger than background aerosols, they may activate preferentially. This may lower the supersaturation, preventing background aerosols from activating, and hence reducing the cloud droplet concentration (Korhonen et al., 2010b). This competition effect thus results in cloud changes that are contrary to those intended from the MCB proposal. An activation parameterisation has been used to suggest that such a competition effect may only occur if the majority of the following conditions are met (Pringle et al., 2012): a high background aerosol concentration ($\geq$150 cm^{-3}); a low in-cloud updraft velocity ($\leq$0.2 ms^{-1}); a low emitted aerosol number concentration ($\leq$150 cm^{-3}); and a large emitted aerosol diameter ($\geq$250-300 nm). As such, a competition effect could be prevented by limiting MCB aerosol diameters to the 200 nm suggested in the proposal (Salter et al., 2008) and by maintaining high MCB aerosol emission rates. While the most important characteristics of both the background and emitted MCB aerosols are the number concentration and size distribution (Feingold, 2003; Dusek et al., 2006), there is some smaller sensitivity to chemical composition. This may be altered by the fraction of organics for example (Rissman et al., 2004). Consideration of this second-order sensitivity to such chemical effects is not, however, investigated in this work.

Assuming that the added aerosols are of suitable size, number concentration and chemical composition to produce a first indirect aerosol effect, the anticipated increase in albedo for clouds of varying background aerosol concentration is illustrated schematically in Figure 2.6. This figure additionally shows the possible effects of wet scavenging, which could remove some or all of the aerosols before they reach the cloud layer, thus voiding any potential effect on cloud albedo (Wang et al., 2011a).

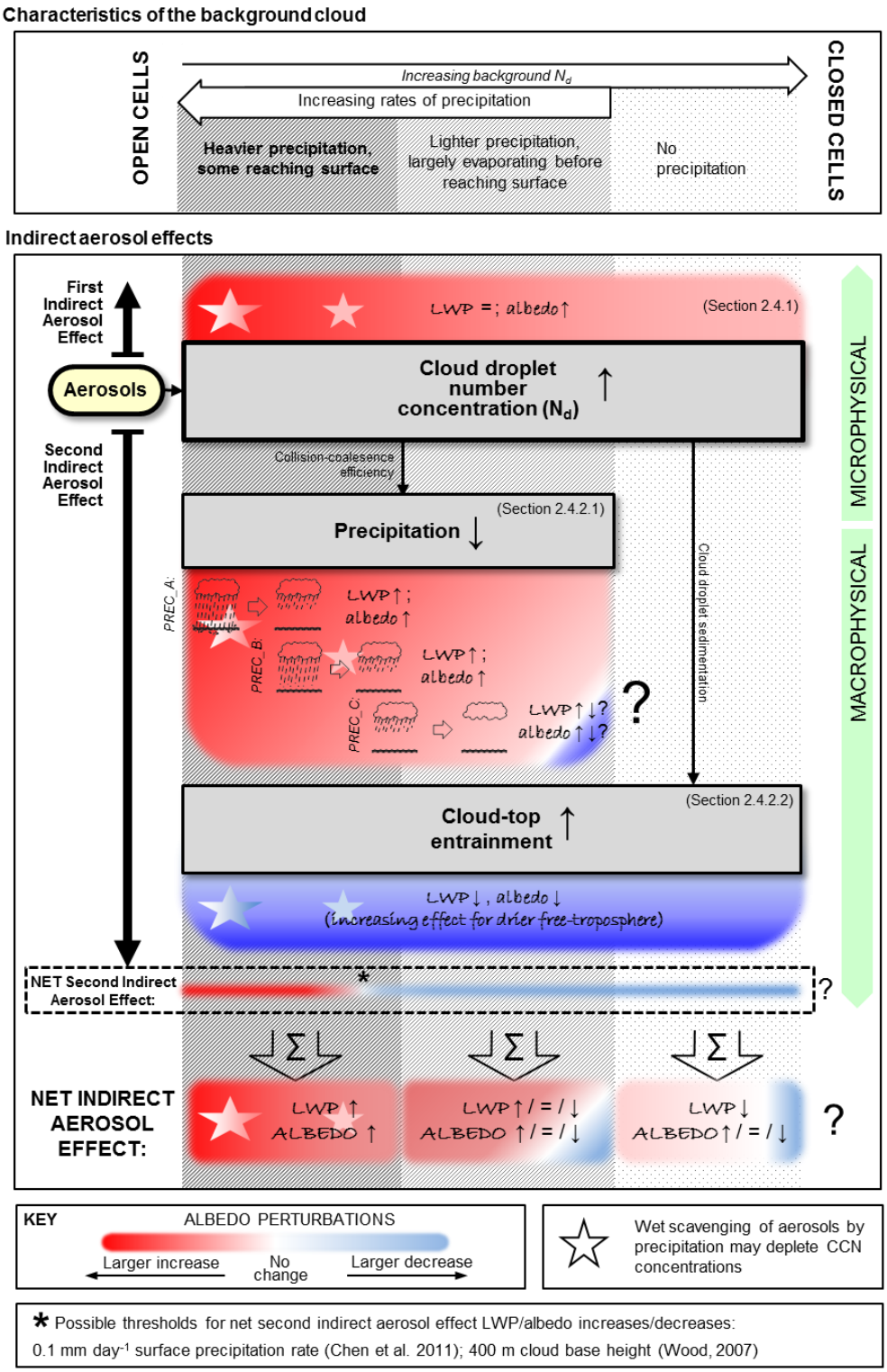

Figure 2.6 *– Schematic indicating possible first-order influences of the addition of aerosols on MSc-topped boundary layer LWP and cloud albedo across different cloud regimes, including both the first and second indirect aerosol effects. The added aerosols are assumed to be of similar size and composition to those existing in the background, and thus possible competition effects are omitted. PREC_A, PREC_B, and PREC_C are three different cases of precipitation, as referred to in the text. Red and blue shading is indicative of albedo increases and decreases (respectively), although owing to high levels of uncertainty in cloud response, they are intended to be suggestive of potential patterns only (with uncertainty indicated in the figure through the use of question marks).*

2.4.2 The Second Indirect Aerosol Effect

While the fixed LWP condition inherent to the first indirect aerosol effect produces conceptually straightforward cloud changes, it is typically not valid for MSc clouds (Twohy et al., 2005). As has been described in Sections 2.3.3 and 2.3.4, both cloud-top entrainment and precipitation readily alter the LWP. Owing to the importance of LWP in characterising cloud properties (e.g. Feingold, 2003), quantifying such LWP changes is crucial. This section will examine how rates of precipitation and cloud-top entrainment are affected by changes in N_d, which is in turn affected by the availability of aerosols that can act as CCN. As such, a discussion of the second indirect aerosol effect – comprising possible cloud albedo changes induced by aerosols via LWP perturbation – is presented.

The consideration of LWP changes in this second indirect aerosol effect necessitates the incorporation of complex feedbacks between processes and MSc-topped boundary layer properties. While understanding of individual processes is increasing, the interrelationships and sensitivity to various background conditions mean that the ultimate magnitude (and sign) of second indirect aerosol effects is not currently well understood. The aim of this section is therefore to summarise – within the constraints of current knowledge – possible second indirect aerosol effects that may result from the emission of MCB aerosols. This begins with a consideration of precipitation changes in response to the addition of aerosols.

2.4.2.1 The Contribution of Precipitation Effects

As introduced in Chapter 1 (Section 1.6.2), the second indirect aerosol effect is often presented in terms of LWP changes related to precipitation. As smaller cloud droplets tend to produce lower precipitation rates (Rosenfeld et al., 2012), it is frequently assumed that the addition of aerosols would lead to decreases in precipitation rates and a relative increase in LWP (e.g. Albrecht, 1989). The assumed resulting LWP increases would therefore be anticipated to increase both the albedo of the cloud, and the cloud lifetime. Such a cloud response would be advantageous for the MCB scheme, and would reinforce the first indirect aerosol effect. As intimated in Section 1.6.2, however, the cloud response is likely to be considerably more complex.

As for the first indirect aerosol effect, the initial change that would be expected to result from the introduction of additional aerosols is an increase in N_d with a concomitant reduction in droplet diameter. The reduced diameter would reduce the sedimentation rate of the cloud droplets which in turn would reduce the collision-coalescence efficiency of the droplets (P5; Figure 2.7), leading to reduced precipitation rates. In a further feedback, such a reduction in precipitation would lead to reduced turbulence within the boundary layer through stabilisation owing to changes in the dynamics (P3; Figure 2.7). This reduced turbulence would reduce drop recycling, further reducing the formation of precipitation (P4; Figure 2.7). Collision-coalescence is also dependent upon the size distribution of the droplets. Droplets of similar sizes will fall at similar speeds, reducing the rate of collision-coalescence. The presence of larger droplets will result in higher rates of collision-coalescence as these droplets fall faster than – and are able to collect -- smaller, slower moving droplets.

The changes to cloud properties resulting from these reduced droplet sedimentation rates are dependent upon the original precipitation rate.

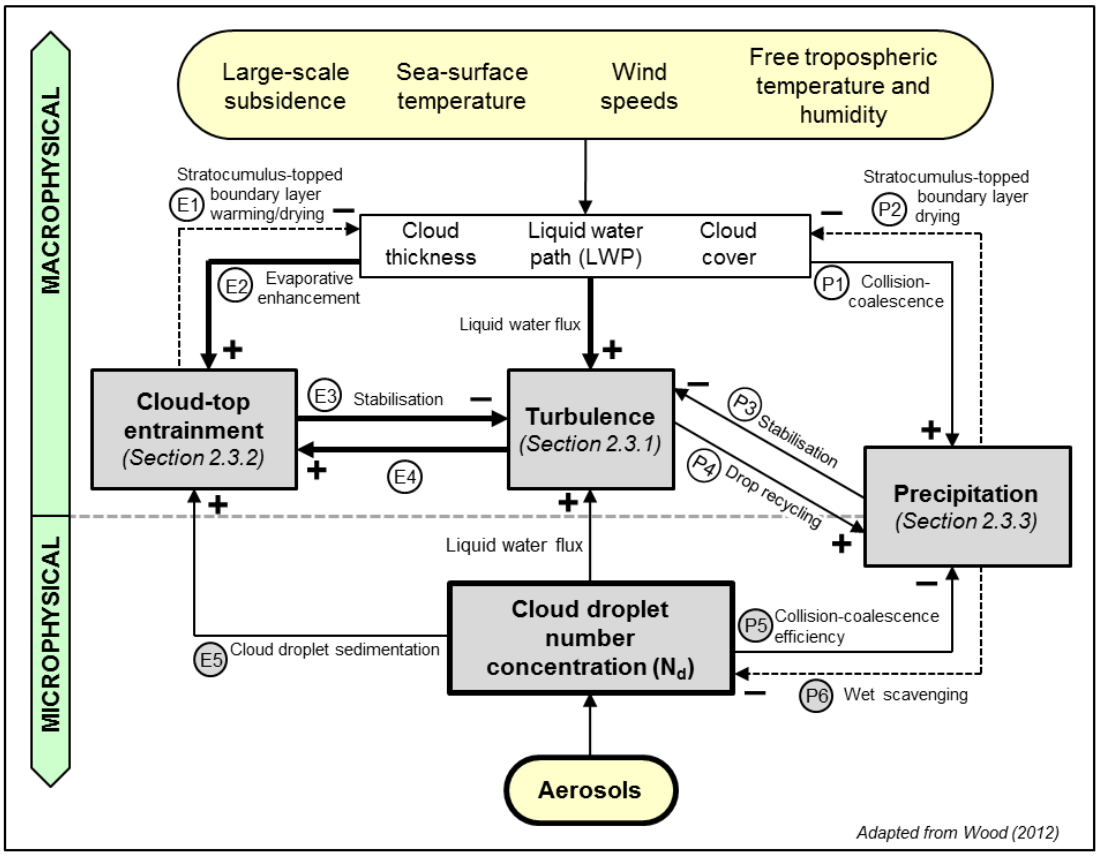

Figure 2.7 *– As Figure 2.3, but including changes relevant to changes in the N_d.*

Considering first more heavily precipitating background conditions, where liquid water reaches (and is lost at) the surface. The addition of aerosols in such cases may reduce the

precipitation rates sufficiently that precipitation no longer reaches the surface. Therefore, as the amount of liquid water lost at the surface could be reduced, a comparative LWP increase and accompanying albedo enhancement may result (Figure 2.6; PREC_A). In moving away from the heavily precipitating condition, the MSc-topped boundary layer may also become more destabilised and thus more self-sustaining, with possible associated lifetime enhancements (cf. Section 2.3.4).

For more lightly precipitating background conditions where little or no liquid water is lost at the surface (Figure 2.6; PREC_B), the effects on LWP are less obvious and less well understood. In these conditions, changes to the dynamics of the MSc-topped boundary layer are more important. For example, background conditions could occur where precipitation evaporates through much of the boundary layer, producing boundary layer stabilisation and potential cloud dissipation, while leaving little precipitation to reach (and be lost at) the surface (Wood, 2005). For such a background case, the addition of aerosols could reduce precipitation such that all precipitation evaporates in a thin sub-cloud layer – a case that may produce destabilisation and a self-sustaining precipitating condition (as discussed in Section 2.3.4). Such a transformation could possibly increase the LWP (and albedo) of the cloud system additionally enhancing the cloud lifetime.

Adding aerosols to a cloud exhibiting potentially self-sustaining light precipitation (that evaporates in a thin sub-cloud layer), could totally stop precipitation (Figure 2.6; PREC_C). In such an event, the cloud system may then transition from a precipitating to non-precipitating cloud regime (Rosenfeld et al., 2006). This may thus increase the albedo of the cloud. However, some computer simulations suggest that under particular conditions, the latent heat fluxes that drive the self-sustaining, lightly precipitating cloud may be more robust to diurnal radiative flux patterns than clouds driven largely by cloud-top LW radiative cooling (Sandu et al., 2008). Under such conditions, the lightly precipitating cloud may be better sustained during the day than a non-precipitating counterpart, and hence maintain a higher LWP and cloud albedo (Sandu et al., 2008). The frequency with which such conditions occur in real-life MSc cloud fields is not known.

Owing to such subtleties and the considerable parameter space of possible background conditions, the response of precipitating MSc clouds to aerosol increases remains poorly constrained. Such difficulties in understanding are compounded by the additional wet scavenging feedbacks (Figure 2.6 and P6 in Figure 2.7), whereby aerosol concentrations are reduced by precipitation. Depending on the strength of precipitation (and the resulting aerosol sink) it may not even be possible for added aerosols to reach the cloud layer. If enough aerosols were removed by this process, aerosols would not be able to reduce the cloud droplet diameters, stymying both the first and second indirect aerosol effects (Wang et al., 2011a).

2.4.2.2 The Contribution of Cloud-Top Entrainment Effects

As was demonstrated in Section 2.3.3, as well as precipitation, cloud-top entrainment can also affect the LWP of the MSc-topped boundary layer. This section therefore considers how adding additional aerosols may alter the rate of cloud-top entrainment, and hence the LWP and albedo of MSc clouds.

As already stated, the addition of aerosols can lead to a higher number of smaller cloud droplets being formed. This reduces their rate of sedimentation, allowing more of the cloud droplets to remain in the entrainment zone located at the cloud top. The presence, and evaporation, of additional droplets here increases turbulent production. This therefore increases rates of cloud-top entrainment of free tropospheric air (Ackerman et al., 2004; Bretherton et al., 2007; Hill et al., 2009) as indicated in Figure 2.7 (E5). This increased entrainment can be evident as a rise in the cloud-top height (Christensen and Stephens, 2011). Such increases in cloud-top entrainment with increasing N_d suggests that higher entrainment rates may contribute to the higher cloud-tops exhibited by closed cell clouds compared with open cell clouds in similar background conditions (Painemal et al., 2010). This turbulent enhancement could be further increased as the smaller cloud droplets evaporate more readily (Hill et al., 2009) as indicated in Figure 2.7 (E2). However, the increase in cloud top-entrainment also results in warming of the cloud-top. This offsets the LW radiative cooling, inducing stabilisation of the cloud and hence a reduction in turbulence and resulting reduction in entrainment (E3, E4; Figure 2.7).

The drying effect of enhanced cloud-top entrainment, and hence the magnitude of the LWP (and albedo) reductions will be intensified for drier overlying free-tropospheric air (Figure 2.6). While the cloud-top entrainment of drier overlying free-tropospheric air is known to enhance the evaporation of cloud droplets, the ultimate consequence of increasing the cloud-top entrainment is not fully understood. For example, the cloud-top entrainment instability hypothesis suggests that the turbulence and further enhanced entrainment generated from the enhanced evaporative cooling may result in a feedback loop that leads to cloud dissipation (Lilly, 1968; Deardorff, 1980). However, subsequent observations and modelling work finds that clouds are maintained even when the conditions for cloud-top entrainment instability are met (Stevens, 2010; Yamaguchi and Randall, 2008), suggesting that the hypothesis does not fully capture the effect that entrainment has on the clouds.

2.4.3 The Net Indirect Aerosol Effect for Marine Stratocumulus Clouds

In summary, increasing the number of aerosols suitable to act as CCN tends to produce a larger number of smaller cloud droplets. The first indirect aerosol effect (Section 2.4.1) leads to an increased cloud albedo of larger magnitude for background clouds with lower N_d. Such a cloud albedo increase, and associated planetary cooling effect is the basis for the MCB proposal. This first indirect aerosol effect assumes, however, that the LWP of the MSc-topped boundary layer remains constant. Examination of the second indirect aerosol effect (Section 2.4.2) suggests that this constant LWP assumption is unlikely to be the case in reality. While cloud-top entrainment tends to reduce the LWP of the cloud system (and hence act to reduce cloud albedo), the effects of precipitation changes in response to the addition of aerosols are more uncertain. Both increases and reductions in LWP (and cloud albedo) possible (Costantino and Bréon, 2013; Section 2.4.2.1). Thus, the second indirect aerosol effect could act to either enhance or counteract the cloud albedo increases associated with the first indirect aerosol effect. This effect could be either beneficial or detrimental for proposed MCB.

Uncertainties in the magnitudes and sign of cloud response to the addition of aerosols and the various timescales of response for different processes (Figures 2.3 and 2.7) along with considerable sensitivities to both existing conditions (Wood, 2007; Petters et al., 2013) and the attributes of the added aerosols, mean that a comprehensive explanation and quantification of the net response of MSc clouds to both first and second indirect aerosol effects is not currently possible. Instead, broad possible patterns of cloud response are presented for three general categories: heavier precipitation (some reaching the surface); lighter precipitation (largely evaporating before reaching the surface); and the non-precipitating condition (Figure 2.6). These categories span open to closed cell characteristics, and increasing N_d. Owing to the complexity of cloud response, there will be further sub-category variation relating to, for example, the moisture of over-lying free-tropospheric air.

These broad patterns of net indirect aerosol effect are illustrated schematically in the bottom row of Figure 2.6. In addition to being based on conceptual physical mechanisms relating to the constituent first and second indirect aerosol effects, these broad patterns of net indirect aerosol effect are also informed by observations. Owing to spatially and temporally variable background cloud conditions, the identification of the indirect aerosol effect in observations is challenging. One example where the indirect effect can be readily seen, however, is in ship tracks. Ship tracks (Figure 2.8) are localised regions of perturbed MSc cloud that occur in response to the aerosol emissions of ship engines (Hobbs et al., 2000) and hence evince the indirect aerosol effect.

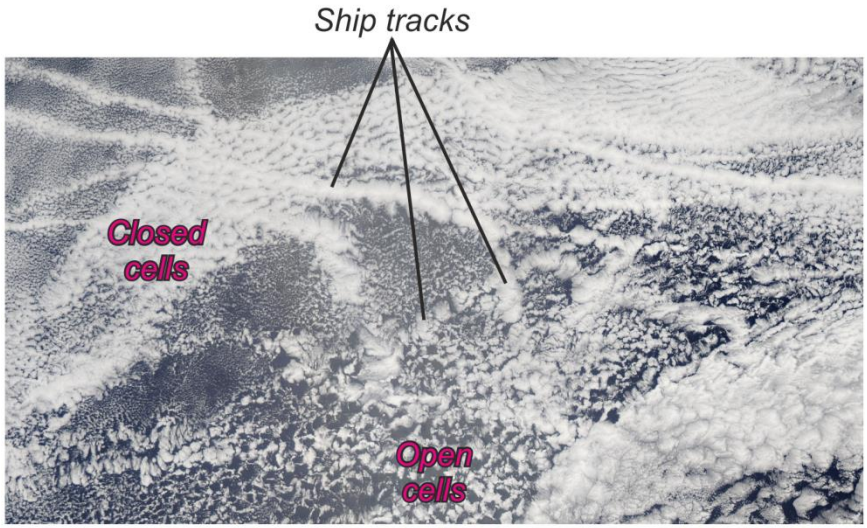

Annotations added to image obtained by MODIS on NASA's Aqua satellite of ship tracks in clouds over the northern Pacific Ocean on July 3, 2010. Modified from NASA image by NASA/ GSFC/Jeff Schmaltz/MODIS Land Rapid Response Team.
Obtained from http://www.flickr.com/photos/24662369@N07/4777967446 on 22nd July 2013.

Figure 2.8 *– Example satellite image indicating open and closed cell formations, along with ship tracks.*

Consider first the case of heavier precipitation with some reaching the surface (left column of Figure 2.6). Under these conditions, increases in albedo from both the first indirect aerosol effect and LWP increases from the suppression of precipitation (second indirect aerosol effect) are likely to be larger than the albedo decreases caused by the cloud-top entrainment induced drying. As such, there is likely to be a net increase in cloud albedo under such conditions (Ackerman et al., 2004; Lu and Seinfeld, 2005; George et al., 2013), which would be beneficial for MCB. This was found for the open cell, heavily precipitating case during the Eastern Pacific Emitted Aerosol Cloud Experiment (E-PEACE) campaign (Russell et al., 2013), whereby the intentionally introduced aerosol produced increases in LWP and albedo (Chen et al., 2012). This was also true for the satellite observation of open cells subject to ship tracks, which resulted in more liquid water (39%), but also higher cloud tops (Christensen and Stephens, 2011). This feature suggests that the clouds may be experiencing an increase in entrainment, but also that they may be moving towards the closed cell regime. However, as mentioned in Section 2.4.1, wet scavenging could remove some or all of the aerosols before they reach the cloud layer, as evidenced in the 'Evergreen Evergenius' ship track observed by airborne measurements (Ferek et al., 2000).

Next, conditions of lighter precipitation which largely evaporate before reaching the surface are considered (central column of Figure 2.6). Under such conditions, the first indirect effect is again likely to produce an increase in cloud albedo, while increased rates of cloud-top entrainment are likely to produce decreases in LWP and thus cloud albedo. Of much greater ambiguity is the sign of LWP (and cloud albedo) change associated with changes to the precipitation. Thus, for these conditions it is possible that cloud albedo could be either

increased or decreased, depending on existing conditions (Lu and Seinfeld, 2005). As understanding of the precipitation response is incomplete, the net cloud response in such lightly precipitating conditions remains highly uncertain. The variable response for lightly precipitating clouds was seen for the two lightly precipitating E-PEACE research flights reported by Chen et al. (2012). In one case, the cloud responded to the addition aerosol with an increased LWP, cloud thickness and cloud albedo. In the other case, the response was reversed, with decreased LWP and cloud albedo. This latter cloud was overlaid by a drier free-troposphere. This suggests that possible increases in LWP from the suppression of precipitation in both cases may have been overpowered by entrainment-induced drying. This drying may have been enhanced by absorption of heat by the 'dirty' particles in the case of the ship emissions (the semi-direct effect) (Coakley and Walsh, 2002). For a lightly precipitating cloud (with a cloud base height of ~200 m) airborne measurements found reduced drizzle and increased LWP, with some increase in cloud top height (Lu et al., 2007).

Finally, non-precipitating clouds are considered (right-hand column of Figure 2.6). For these conditions, the situation becomes somewhat simplified in the absence of precipitation. As such, the net albedo effect will be a combination of the albedo increases resulting from the first indirect aerosol effect, and LWP and albedo decreases resulting from increases in cloud-top entrainment drying as part of the second indirect aerosol effect. The magnitude of these opposing effects, and therefore the net effect on cloud albedo, is critically dependent upon background conditions and the number of added aerosols. Indeed, for drier free-troposphere air, the non-drizzling E-PEACE cloud case produced reduced LWP and cloud albedo, although such decreased albedos occurred in only 30% of the observed ship tracks (Chen et al., 2012). Similarly, of 132 satellite observations of ship tracks in closed cells, there was -6% change in LWP with no change in cloud height (Christensen and Stephens, 2011). Also possible, as found for satellite observations of crossing ship tracks (and as indicated in Figure 2.6), is that the LWP decreases, while the albedo increases (Sechrist et al., 2012). This could occur where the albedo increase resulting from the first indirect aerosol effect is larger than the albedo decrease resulting from the LWP losses associated with the second indirect aerosol effect.

Results of previous computer modelling of the second indirect aerosol effect, as collated by Chen et al. (2011), suggest that LWP increases may be expected for clouds that have surface precipitation rates of above 0.1 mm day^{-1}. Alternatively, modelling by Wood (2007) has suggested that at time scales of shorter than a few days, there may be a cloud base height threshold for LWP increases and decreases. While clouds with bases below 400 m were found to be characterised by LWP increases in response to aerosol increases (as sufficient

precipitation reached the surface), clouds with bases above 400 m were more prone to LWP losses as less precipitation reaches the surface and cloud-top entrainment drying dominated.

In this case of added aerosols, the potential decreases in LWP and albedo (second indirect aerosol effect) that act to offset the albedo increases associated with the first indirect aerosol effect are an example of buffering within the cloud system (Stevens and Feingold, 2009). More generally, the buffering concept suggests that changes to the cloud field in response to a forcing may be attenuated by cloud processes occurring over a range of spatial and time scales (Stevens and Feingold, 2009). The omission of such cloud processes from simulations may therefore lead to perturbations in the cloud fields being overestimated (Boucher et al., 2013). Another potential buffering mechanism has been identified in the mesoscale computer simulation of ship tracks (Wang and Feingold, 2009a; Wang and Feingold, 2009b). These simulations suggest that a ship track may increase the LWP sufficiently that precipitation may be formed, potentially leading to cloud dissipation (Wang and Feingold, 2009a; Wang and Feingold, 2009b). Such a response may explain why ship tracks in open cell regimes were more frequently observed to have increased rather than decreased precipitation rates in one satellite observation study (Christensen and Stephens, 2012). The time necessary for such a feedback to dissipate the ship track is, however, unclear, with observations suggesting that many ship tracks last longer than 12 hours (Durkee et al., 2000). Another satellite observation study suggests that, rather than dissipating the clouds, ship tracks can actually instigate a transition from an open cell to a closed cell regimes (Goren and Rosenfeld, 2012). Such a mechanism for transitioning from open to closed cells through the addition of aerosols has also been proposed theoretically (Rosenfeld et al., 2006). Thus, while both cloud behaviours are possible, accurate forecasting and comprehensive understanding of the responses are significantly hampered by the high sensitivities to a range of background conditions and added aerosols. This is further complicated by the effects of complex feedbacks and potential buffering mechanisms.

2.5 Conclusions

The processes that control the formation and development of MSc clouds are complex and diurnally varying. In order to examine the three case studies relating to MCB implementation details (introduced at the end of Chapter 1), computer simulated MSc base cases are needed that authentically reproduce these fundamental cloud system processes. Thus, in addition to reproducing characteristic cloud properties (such as thickness, fraction and cloud-top height), the fidelity of the simulations must also be judged on the presence and behaviour of key processes. These processes include: heating and cooling through the cloud layer; the spatial distribution of turbulence; the entrainment of overlying air; and the effects of precipitation.

Further to these characteristic MSc processes is the relationship between MSc clouds and aerosols, which is central to the MCB proposal. The inherent complexities of the system currently prevent a comprehensive quantification of this indirect aerosol effect. However, based on current evidence, a schematic of anticipated cloud changes to the addition of aerosols was developed in this chapter. This was based on how dominant cloud system mechanisms may respond to the addition of aerosols, under different background aerosol concentrations. In spite of intricate, and typically non-linear, feedback responses, clouds formed in conditions of low background aerosol concentrations are most likely to experience notable albedo enhancements through the addition of aerosols. The addition of aerosols to clouds formed in higher background aerosol conditions could lead to smaller cloud albedo enhancements, or even decreases in cloud albedo resulting largely from the second indirect aerosol effect. This sensitivity of the indirect aerosol effect (and hence MCB) to background aerosol concentrations means that a thorough examination of possible MCB effects requires a range of base case MSc simulations. This range of simulations must therefore be informed by a range of realistic background aerosol concentrations (Chapter 3).

The modelling work in this thesis is carried out at a cloud-resolving resolution. Therefore, the cloud simulations are able to explicitly capture the MSc cloud system processes and feedbacks – described in this chapter – that govern cloud behaviour, the indirect aerosol effects, and therefore MCB. This allows the details and assumptions regarding the MCB proposal that are encapsulated in the three case studies to be examined in detail. Such detailed considerations cannot be carried out in global-scale models owing to the relatively coarse resolution, and parameterised cloud behaviour. This detailed approach is therefore a powerful and innovative technique for the examination of MCB.

Chapter 3
Marine Stratocumulus Cloud Base Case Simulations

3.1 Introduction

To enable the three MCB implementation detail case studies – introduced at the end of Chapter 1 – to be examined, computer simulations of the background MSc conditions are needed.

To provide a suitable basis for the subsequent MCB effectiveness experiments, the simulated base cases must adequately capture the key MSc cloud processes and cloud properties that were described in Chapter 2, for a range of background conditions, over the diurnal cycle. Key to representing the MCB process is simulation of indirect aerosol effects (Chapter 2, Section 1.4). This necessitates the representation of the relationship between aerosols of various size and number concentrations and cloud droplets, and the relationship between cloud droplets and precipitation, both under varying dynamical conditions.

This chapter describes how a cloud-resolving model, capable of representing the indirect aerosol effect, is initialised with a range of three realistic background aerosol conditions in order to produce three MSc base cases. Of these three MSc base cases, one is precipitating while two are non-precipitating. The model, set-up and initialisations used to produce these base cases are described in Section 3.2. Key dynamical and physical properties of the precipitating and non-precipitating base cases are presented and discussed in relation to the understanding of MSc clouds presented in Chapter 2 in order to evaluate the performance of the model in simulating MSc clouds (Sections 3.3 and 3.4).

In establishing that these simulated base cases adequately represent key features of the MSc cloud system over a range of conditions and over the diurnal cycle, they are then used as the basis of MCB experiments examining the three MCB implementation detail case studies (presented in Chapters 4, 5 and 8).

3.2 Model Setup

The model used is the WRF/Chem V3.3.1 model (Skamarock et al., 2008) in the large-eddy simulation configuration. This non-hydrostatic model incorporates interactive chemistry through the Carbon Bond Mechanism–Z (CBMZ) gas phase chemical mechanism scheme (Zaveri and Peters, 1999; Fast et al., 2006) and aerosol processes through the 8-bin Model for

Simulating Aerosol Interactions and Chemistry (MOSAIC) scheme (Zaveri et al., 2008). The size range of each of these bins is stated in Table 3.1.

Aerosols interact with the cloud through the Morrison et al. (2005) two-moment microphysics scheme. Activation of aerosols to cloud droplets follows the Abdul-Razzak and Ghan (2000) method. This activation method calculates an activated fraction of aerosols for each size bin, basing this calculation on both atmospheric conditions, and on the properties of the aerosols. For the atmospheric conditions, the maximum supersaturation is calculated from the mean vertical velocity of a grid cell and an assumed Gaussian vertical velocity spectrum. The aerosols are considered to have a critical supersaturation, above which they will activate to form a cloud droplet. This critical supersaturation depends upon the aerosol size, number concentration and composition (with composition being internally mixed within each size bin). Thus, the fraction of aerosols activated to form cloud droplets is therefore calculated from the fraction of aerosols in a given size bin where the maximum supersaturation exceeds the critical supersaturation.

The Morrison two-moment microphysics scheme uses the cloud droplet number concentration and cloud water mixing ratio to determine a gamma distributed cloud droplet size spectrum. Raindrops follow an exponential distribution (Morrison et al., 2009). The number concentrations and mass mixing ratios of cloud water droplets are altered by sources (primarily the activation of aerosols as described above), and sinks (including autoconversion and accretion) (Yang et al., 2012). Autoconversion is included using an explicit autoconversion rate, based on (Khairoutdinov and Kogan, 2000), where q_r is the rain water mixing ratio, q_c is the cloud water mixing ratio, and N_d is the cloud droplet number concentration:

$$\frac{\partial q_r}{\partial time} = 1350 \times {q_c}^{2.47} \times {N_d}^{-1.79} \qquad \textbf{(3.1)}$$

Collection within the model does not depend upon turbulence. This microphysics scheme uses a wet deposition scheme that removes both aerosols that have been activated to form cloud droplets, and interstitial aerosols (i.e. those that have not been activated), thus removing aerosols from both within and below the cloud. These scavenged aerosols are instantly removed, and the scheme does not allow for re-suspension of aerosols during the evaporation of rain droplets (Saide et al., 2012). This behaviour is hence likely to lead to an overly strong aerosol sink. This scheme also includes cloud droplet sedimentation.

LW radiation calculations were performed by the Community Atmospheric Model (CAM) spectral-band LW scheme (Collins et al., 2004). SW radiation calculations were performed by the Rapid Radiative Transfer Model for Global Circulation Models (RRTMG) transfer scheme. This RRTMG SW radiation scheme uses cloud droplet effective radii from the

Morrison microphysics scheme, with these radii being defined as the ratio of the third to the second moment of the gamma droplet size distribution (Yu et al., 2013). Sensitivity tests using this combination of radiation schemes produced patterns of LW cloud-top radiative cooling, daytime SW radiative warming and resulting cloud properties that are characteristic of MSc cloud diurnal behaviour (discussed further in the Results section). The two-moment nature of the microphysics scheme – allowing cloud droplet effective radii to be estimated from information on both the number concentration and mass mixing ratio of cloud droplets – is important for capturing aerosol-cloud-radiation interactions and thus, the indirect aerosol effects. For example, in the event of the emission of an increased number of accumulation mode sized aerosols (as would occur in the proposed MCB scheme), an increased number of aerosols would become activated to form cloud droplets. Assuming, as in the first indirect aerosol effect, that the LWP is fixed, this would produce a higher number of cloud droplets. Under a maintained cloud water mixing ratio, this would alter the size distribution of cloud droplets assumed by the microphysics scheme, leading to an increased number of smaller droplets. Furthermore, changes to the LWP (and hence the second indirect aerosol effect) are captured in the model, largely by alterations in the dynamics in the boundary layer. This is contributed to by the explicit calculation of turbulent kinetic energy, along with parameterisation of sub-grid turbulence. The 1.5 order 3-D turbulent kinetic energy closure scheme (Skamarock et al., 2008) was utilised to simulate sub-grid turbulence. Advection was constrained by the monotonic flux limiter option (Wang et al., 2009). Surface layer physical processes were represented by the Monin-Obukov scheme. Horizontal boundary conditions were periodic, and a 250 m damping layer was included at the model top. The model time step was 2 seconds for dynamical processes, and 1 minute for the radiative processes. Subsidence was included through a large-scale divergence of 3.75×10^{-6} s^{-1}. Large-scale wind was initialised at zero, following Wang and Feingold (2009a) and Wang et al. (2011a). Input soundings follow Research Flight 02 (RF02) of the DYCOMS-II field campaign which observed drizzling stratocumulus (Ackerman et al., 2009). The inversion height was 795 m. Total water mixing ratio was initialised at 9.45 g kg^{-1} in the boundary layer, decreasing to 5.0 g kg^{-1} in the free troposphere. The potential temperature was initialised to 288.3 K in the boundary layer, increasing to 303.9 K by 1500 m height. These initialisation profiles are illustrated in Figure 3.1. The sea surface temperature was held fixed at 288.8 K.

Table 3.1 *– Aerosol dry diameter sizes for the 8-bin Model for Simulating Aerosol Interactions and Chemistry (MOSAIC) scheme.*

Bin Number	Lower Diameter (μm)	Upper Diameter (μm)
1	0.0390625	0.078125
2	0.078125	0.15625
3	0.15625	0.3125
4	0.3125	0.625
5	0.625	1.25
6	1.25	2.5
7	2.5	5.0
8	5.0	10.0

As these simulations are intended to produce a range of base cases for the forthcoming MCB simulations, they use a unique combination of initialisations (e.g. background aerosol concentrations) and as such are not intended to reproduce either the observed RF02 case, or previous simulations of it (Ackerman et al., 2009). The ability of this set-up to achieve patterns of dynamics and cloud properties characteristic of MSc clouds is discussed in Section 3.4.

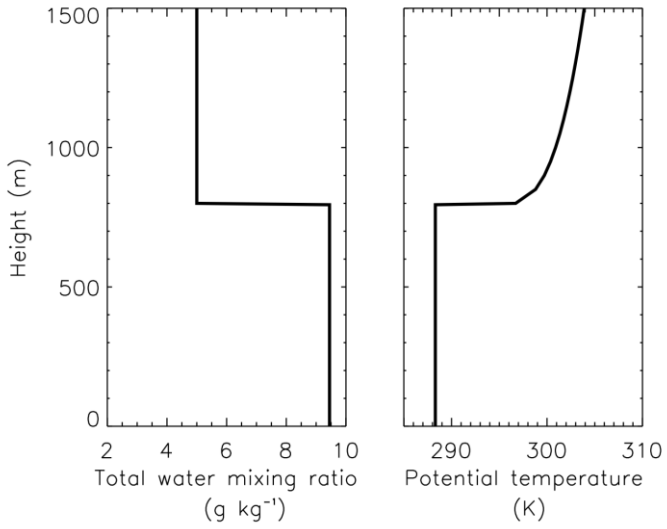

Figure 3.1 *– Total water mixing ratio and potential temperature initialisation profiles.*

To produce three control cases reproducing a range of stratocumulus cloud conditions, three background aerosol concentration initialisations for SO_4, NH_4, NO_3, Na, Cl, black carbon and organic carbon were selected from model output of the GLOMAP model (Mann et al., 2010). The three representative aerosol locations chosen were: the Southern Ocean (a pristine case); the North-East Pacific (the location of the DYCOMS-II mission (Stevens et al., 2003b) and

an area of persistent MSc cloud); and the East China Sea (an area of high atmospheric aerosol concentration resulting from mainly anthropogenic sources). These three locations were chosen to represent the wide range of aerosol conditions that occur in reality. The data was in the form of annual means associated with the early-2000s, with each location being represented by data from a single representative grid cell from the GLOMAP model. The 8-bin size distributions for these background aerosol initialisations are presented in Figure 3.2.

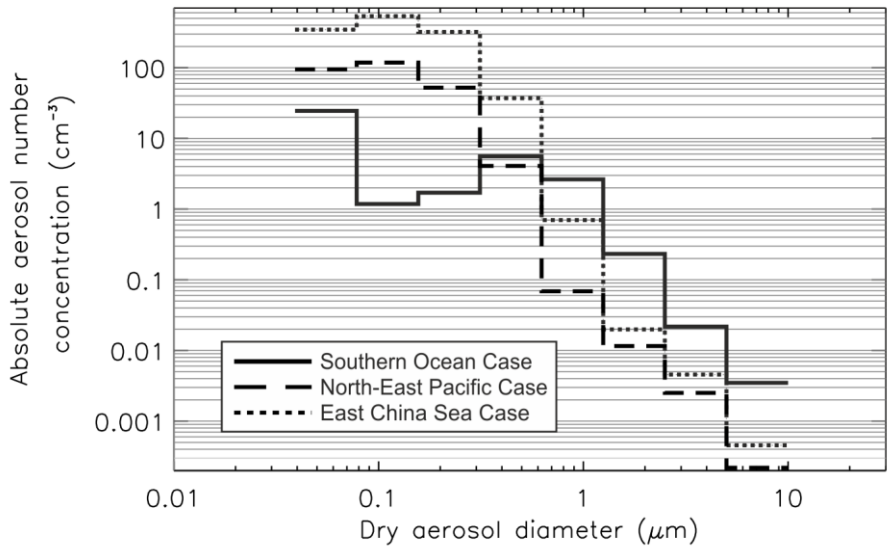

Figure 3.2 *– Background absolute aerosol initialisation for the three MSc base cases based on the increasingly polluted aerosol concentrations of: the Southern Ocean; the North-East Pacific and the East China Sea.*

The background aerosol budget comprised a natural wind-driven sea spray source (Fuentes et al., 2010); nucleation of emitted gases; and a wet deposition sink. The gases SO_2, H_2O_2, NH_3, CO and O_3 were initialised with values typical of the oceanic boundary layer atmosphere in regions of MSc (Georgii and Gravenhorst, 1977; Khalil and Rasmussen, 1994; Kazil et al., 2011). The concentration of SO_2 was increased by 1.0 pptv h^{-1} to represent the processes associated with dimethyl sulphide, in lieu of an explicit scheme, following the observations and modelling of Gray et al. (2011) and Yang et al. (2011a). The model time step for chemistry and aerosol processes was 2 minutes.

The horizontal domain size was 9 km x 9 km with grid cell resolution of 300 m. The model extends 1.5 km vertically, with 50 vertical layers (increasing in depth with height). Each control case was simulated for 35 hours, starting at 22:00:00 local time (LT) on 21 July 2001. The sun rose at 05:20:00 LT, and set at 19:00:00 LT. Control case results are presented from the beginning of the model run (and therefore include the model spin-up). The choice of relatively coarse horizontal resolution follows Wang and Feingold (2009a) and has been used

in subsequent modelling studies (Wang et al., 2011a). Selecting a relatively small horizontal domain allows us to perform detailed analysis of the aerosol emission, aerosol interaction with clouds, and rapid cloud response within the computational constraints present. It does however preclude the representation of mesoscale features associated with MSc cloud decks (e.g. Wood and Hartmann, 2006; Wood et al., 2008) and secondary circulations that can be triggered by aerosol concentration gradients (e.g. Wang and Feingold, 2009a; Wang and Feingold, 2009b; Feingold et al., 2010; Wang et al., 2011a). Despite these exclusions, the variations in simulated cloud properties are consistent with characteristic changes in radiative and dynamical features of the stratocumulus topped boundary layer over the diurnal cycle (discussed further in Sections 3.3 and 3.4), and follow the similar or smaller domain sizes that have previously been used to study the behaviour of MSc clouds (e.g. Stevens et al., 2005a; Ackerman et al., 2009) and their sensitivities to atmospheric variables over the diurnal cycle (Chen et al., 2011).

3.3 Base Case Simulations

Of the three background aerosol concentrations, the pristine marine conditions of the Southern Ocean produced a precipitating case (PR). The North-East Pacific location typical for MSc, and the most heavily polluted East China Sea background aerosol conditions both produced non-precipitating regimes (NP-Pa and NP-Ch respectively).

3.3.1 Precipitating Base Case

This PR control case demonstrated a clear diurnal cycle in both cloud properties (Figure 3.3) and dynamical and physical processes (Figure 3.4).

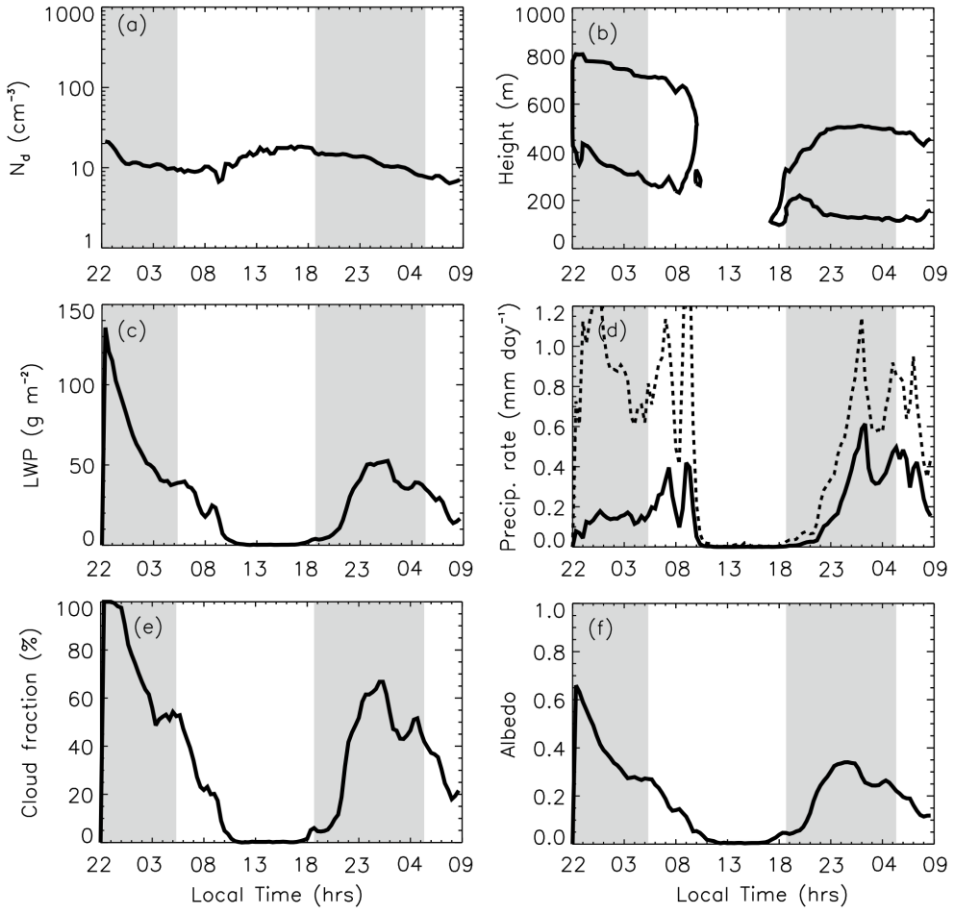

Figure 3.3 *– Time evolution of domain averaged cloud properties for the PR control case. (a) N_d, (cm^{-3}); (b) cloud top and cloud base height (contour at cloud water mixing ratio of 0.01 g kg$_{dry\ air}^{-1}$); (c) LWP (g m^{-2}); (d) surface rain rate (solid), and cloud base rain rate (dotted) (mm day^{-1}); (e) cloud fraction (%); and (f) domain averaged cloud albedo (calculated from cloud properties, as detailed in Chapter 4, Equation 4.1). Shading indicates the night.*

Cloud-top LW radiative cooling (Figure 3.4 c) produced a band of negative buoyancy atop positive cloud layer buoyancy (Figure 3.4 d). This negative buoyancy produced turbulent kinetic energy (TKE) (Figure 3.4 e and f) which led to boundary layer mixing.

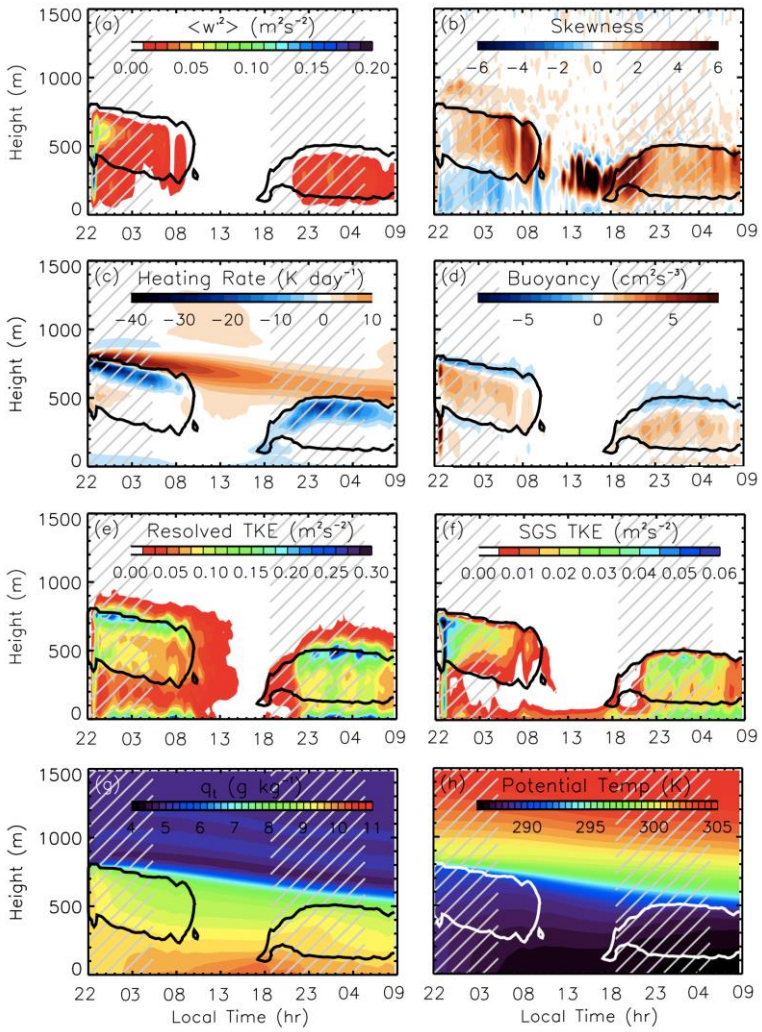

Figure 3.4 *– Time evolution of domain averaged dynamic and physical properties for the PR control case. (a) Vertical velocity variance (<w'²>, $m^2\ s^{-2}$); (b) vertical velocity skewness; (c) radiative heating rate (K day^{-1}); (d) buoyancy ($cm^2\ s^{-3}$); (e) resolved turbulent kinetic energy ($m^2\ s^{-2}$); (f) sub-grid scale turbulent kinetic energy ($m^2\ s^{-2}$); (g) total water mixing ratio (g $kg_{dry\ air}^{-1}$); and (h) potential temperature (K). Solid lines indicate the cloud top and cloud base height (a contour at cloud water mixing ratio of 0.01 g $kg_{dry\ air}^{-1}$). Hatch lines indicates the night.*

The dynamics within the MSc-topped boundary layer can also be considered by using the measures of vertical velocity variance (<w'²>; Figure 3.4 a) and the skewness of the vertical velocity field (Figure 3.4 b). The vertical distribution and strength of <w'²> can be considered to be analogous to turbulence produced mixing within the MSc-topped boundary layer. Where clouds are present in this PR simulation, the boundary layer distribution of <w'²> shows minima at the cloud top and surface, with a single maximum, as is typical of a well-coupled MSc-topped boundary layer, or coupled cloud and boundary layers (Wood, 2012; Nicholls, 1989; Stevens et al., 2005a). The skewness (or third moment) of vertical velocity is a measure of the ratio of the intensity of updrafts to downdrafts (e.g. Moeng and Rotunno, 1990). As there is precipitation in this case, the large-scale downward sedimentation of droplets induces wide-spread downdrafts, balanced by intense updrafts (also characteristic of

open-cell behaviour; Section 2.3.5), resulting in a positive skewness in the cloud (Figure 3.4 b; Stevens et al., 1999).

The SW radiation, present during the day, offset the cloud-top cooling, reducing the TKE and mixing through the boundary layer. The reduced vertical transport of moisture from the surface was evident in an accumulation of total water mixing ratio at the surface during the day leading to a stratified vertical profile (Figure 3.4 g). As the SW radiation dissipated into the second night, the TKE recovered, allowing improved mixing within the boundary layer. Simulated surface heat fluxes also demonstrated a diurnal cycle, with domain average surface latent heat flux varying between 6 Wm^{-2} during the day and a maximum of 10 Wm^{-2} during the night (not shown). Domain average sensible heat flux was approximately 1 Wm^{-2} during the day, reaching a maximum of 4 Wm^{-2} during the night. This periodicity in the strength of dynamical and physical processes was reflected in the pattern of cloud properties. During the more turbulent night (and outside of the initial ~3 to 4 hours where the model was spinning-up), cloud fraction reached 70% (Figure 3.3 e), LWP reached 50 g m^{-2} (Figure 3.3 c) and the cloud was approximately 400 m deep (Figure 3.3 b). In these conditions, the low N_d of around 10 cm^{-3} produced precipitation (Figure 3.3 a and d). The peak surface precipitation rate was 0.6 mm day^{-1}, whilst the cloud base rate at this time was nearly 1.2 mm day^{-1} (Figure 3.3 d). The domain average calculated cloud albedo reached 0.35 during the night (Figure 3.3 f). Even during the night, the cloud and boundary layers were not well coupled. Turbulence (and vertical velocity variance) was largely confined to the cloud layer, additionally indicating boundary layer stratification (Figure 3.4 g). During the daytime, the continuation of precipitation, augmented by the inhibition of moisture transport to the cloud region in the less turbulent conditions resulted in loss of supersaturation below the inversion. Therefore, for the combination of radiative and thermodynamic conditions established by this formation of atmospheric conditions, cloud formation abated and cloud fraction, LWP, precipitation and albedo fell to zero. For this PR case, there was a period of approximately 6 hours during the day between cloud dissipation and cloud recovery. Over the 35 hour long control simulation, cloud top and cloud base heights decreased (by approximately 350 m and 300 m respectively). This descending cloud top is indicative of smaller entrainment rates, which are also typical of open cell-like behaviour (Berner et al., 2013).

The diurnal pattern of cloud changes can also be considered from an aerosol activation viewpoint. During the day, the decrease in turbulence was concomitant with decreases in vertical velocity (with the peak vertical velocity falling from ~1.0 ms^{-1} in the night to ~0.4 ms^{-1} during the day). This reduction in vertical velocities thus reduced the maximum atmospheric supersaturation calculated by the Abdul-Razzak and Ghan parameterisation (described in Section 3.2). With the maximum atmospheric supersaturation decreasing into

the day, fewer aerosols had sufficiently large critical supersaturations to be activated. Hence, cloud fraction reduced significantly into the day. Similarly, as vertical velocities recovered into the second night (along with turbulence, and qualitatively characterised by the vertical velocity variance), maximum supersaturations also increased. Thus, as the critical supersaturation of the background aerosols would remain approximately constant throughout the simulation, more aerosols were activated to cloud droplets, and cloud fraction recovered.

3.3.2 Non-precipitating Base Cases

Similar to the PR case, the NP cases also showed clear diurnal patterns in cloud properties (Figure 3.5) and physical and dynamical processes (Figure 3.6).

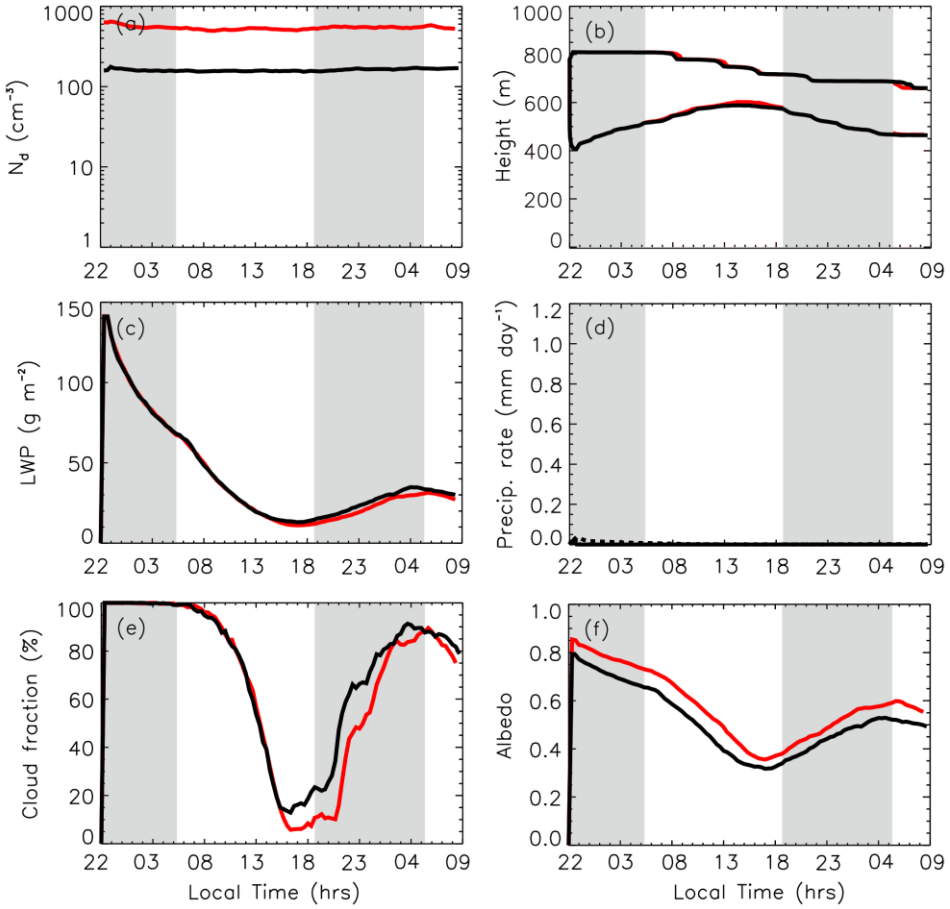

Figure 3.5 *– Time evolution of domain averaged cloud properties for the NP-Ch (red) and NP-Pa (black) cases. Descriptions as Figure 3.3.*

The background aerosol concentration initialisations led to cloud average N_d of almost 200 cm^{-3} for NP-Pa and around 500 cm^{-3} for NP-Ch case. In both cases, the N_d was sufficient to inhibit precipitation formation (Figure 3.5 d). As in the PR case, LW cloud-top radiative cooling (Figure 3.6 c) produced a band of negative buoyancy at the cloud top (Figure 3.6 d) that resulted in TKE (Figure 3.6 e and f). Cloud-top radiative cooling was stronger in the NP case than in the PR case, resulting in a stronger vertical velocity variance (Figure 3.6 a) and a

better mixed/less stratified boundary layer (Figure 3.6 g and h). The boundary layer can be seen to be particularly well mixed during the night (Figure 3.6 g and h) in agreement with MSc observations (Bretherton et al., 2004). Simulated surface heat fluxes again demonstrated a diurnal cycle, with domain average latent heat flux reaching approximately 10 Wm^{-2} during the night, from approximately 3 Wm^{-2} during the day. Domain average sensible heat fluxes remained at approximately 0 Wm^{-2} during the day and night.

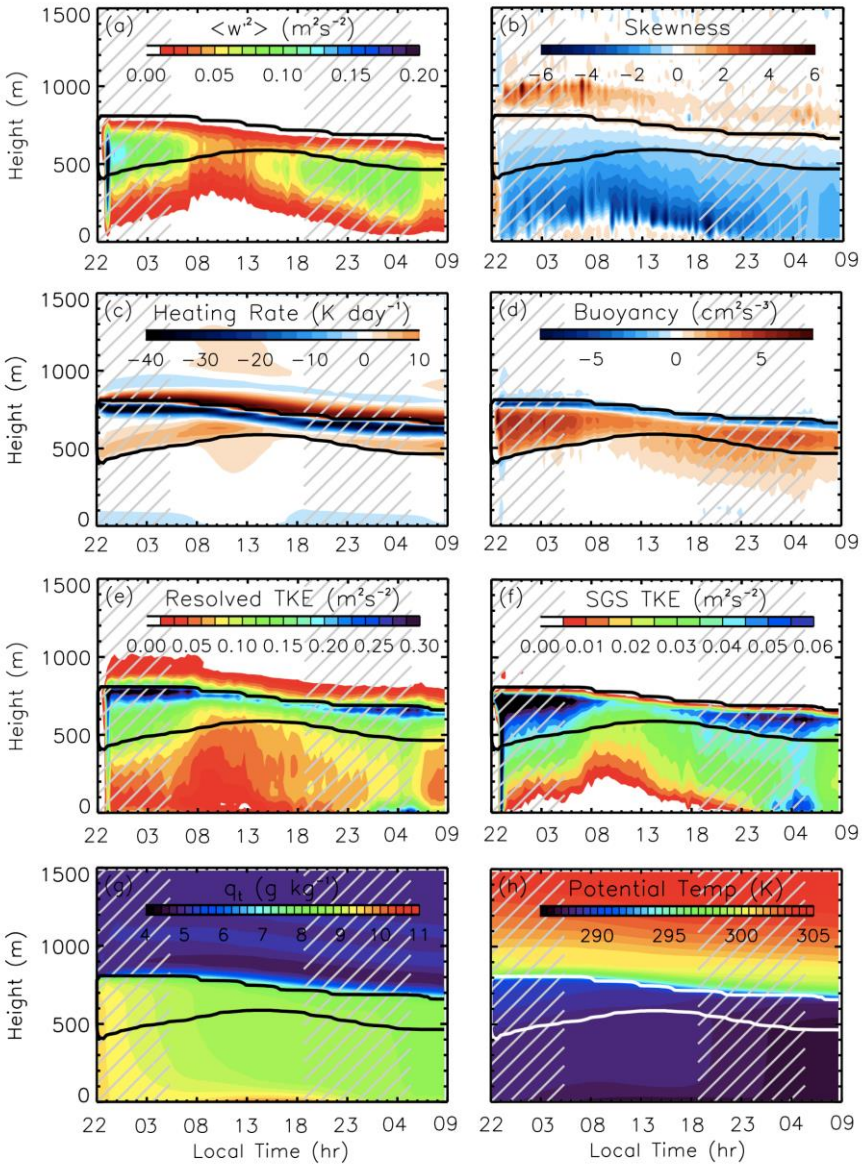

Figure 3.6 *– Time evolution of domain averaged dynamic and physical properties for NP-Pa control case. Descriptions as Figure 3.4.*

Whilst SW radiation during the day again heated the clouds (subduing cloud-top LW radiative cooling and negative buoyancy; Figure 3.6 c) they did not fully dissipate. Thus, although weakened during the day, these dynamical and physical processes were maintained over the diurnal cycle. The diurnal cycle was again seen in the cloud properties. Unlike the total loss of LWP during the day seen in the PR case, the minimum LWP for both of the NP

cases was approximately 10 g m^{-2}. This recovered to around 35 g m^{-2} (NP-Pa) and 30 g m^{-2} (NP-Ch) during the subsequent night (Figure 3.5 c). Similarly, whereas the daytime cloud fraction in the PR case fell to zero, in the NP cases this minimum was maintained at 15% for NP-Pa, and 5% for NP-Ch, recovering to 90% for both cases into the night (Figure 3.5 e). Cloud was also maintained at a higher fraction for longer, with slower dissipation into the day, and a shorter period of low cloud fraction. Owing to the inverse relationship between cloud droplet radius and optical thickness, the higher cloud average N_d for NP-Ch caused the domain average calculated cloud albedo to be consistently higher than the NP-Pa case, despite the lower cloud fraction and LWP values (Figure 3.5 f). This cloud albedo also showed a diurnal cycle, ranging from approximately 0.35 to 0.6 for the day and night-time values in NP-Ch and from approximately 0.3 to 0.5 for NP-Pa.

As for the PR case, these diurnal patterns of cloud changes can also be considered from an aerosol activation viewpoint. Firstly, during the night, the peak vertical velocity in the NP cases was slightly smaller than in the PR cases (~0.6 ms^{-1} and ~1.0 ms^{-1}, respectively). However, in the NP cases, high vertical velocities – and so higher maximum supersaturation – cover a larger area than in the PR case (as is demonstrated by the negative skewness in Figure 3.6 b). Secondly, the NP simulations are initiated using more polluted background aerosol concentrations than were used for the WP simulation (Figure 3.2). In these more polluted conditions, there are a greater number of aerosols with critical supersaturations low enough to be exceeded by the maximum atmospheric supersaturation. Hence, the number of activated aerosols is higher than was the case in the PR simulations. Therefore, with more activated aerosols, the N_d in the NP cases exceeds the N_d in the PR case. Similarly to the PR case, the maximum vertical velocity reduces into the day (again falling to ~0.4 ms^{-1}), concomitant with the pattern of turbulence. This again reduces the maximum atmospheric supersaturation, meaning that fewer aerosols had sufficiently large critical supersaturations to be activated. Cloud fraction again reduced significantly into the day (Figure 3.5 e).

Cloud-top height decreased by 150 m over the 35 hours simulation, with the decrease being more exaggerated during the day as turbulence levels decrease. This is again in agreement with MSc observations (Bretherton et al., 2004). There was additionally a diurnal cycle in cloud base height, with the base rising during the day, causing cloud thinning to around 100 m. The cloud doubled in thickness during the night. These cloud height properties were similar for both NP cases. Whilst there were some similarities between processes in the PR and NP clouds (albeit of differing strength), one area of disparity was the vertical velocity skewness (Figure 3.4 b and Figure 3.6 b). In these NP base cases, strong downdrafts driven by the cloud top LW radiative cooling descended towards the surface (a feature that is characteristic of closed-cell behaviour; Section 2.3.5). This produced a negative skewness

throughout the boundary layer. This was in contrast to the PR case, which showed positive skewness within the cloud layer.

3.4 Discussion

The ability to successfully simulate observed conditions is challenging as several areas of the modelling must be adequately realistic. These areas include: the atmospheric conditions (including moisture and temperature profiles, and aerosol concentrations and composition) and inputs and outputs to the modelled domain (including aerosol sources, changes to subsidence, and the advection of heat etc. associated with larger-scale meteorology). Importantly, to simulate observed conditions, the representation of processes within the model must also be captured realistically. These numerous processes were discussed in detail in Chapter 2 (see Figure 2.2), and include radiative heating and cooling within the cloud; moisture and heat fluxes at the surface; latent heat fluxes throughout the boundary layer, microphysical processes, and dynamical processes including the entrainment of free tropospheric air. Simulating the diurnal cycle of marine stratocumulus clouds is particularly challenging as the changing balance of processes, atmospheric conditions and cloud conditions must all be captured.

Several aspects of the modelling strategy used here mean that even with the use of detailed observed inputs of the atmospheric conditions, reproducing particular MSc observational cases would not be possible. These aspects include: periodic boundary conditions (i.e. preventing the accountability of large-scale meteorology); a fixed representation of subsidence (i.e. no diurnal variability as occurs in reality); and no initialised wind speeds. Thus, while the simulations presented in this chapter were based on observed input soundings of moisture and temperature, these simulations were not intended to reproduce such observations. Instead, the aim of these simulations was to develop MSc base cases that, firstly, exhibit a range of cloud conditions (namely, a range in N_d, to which it is known that the indirect aerosol effects are sensitive to). Secondly, these clouds were required to exhibit patterns of dynamics and cloud properties typical for MSc clouds over a diurnal cycle. Whilst these simulations therefore cannot be compared to a single observed case, they can be critically assessed against typically observed cloud behaviours.

The range in N_d was attained by applying aerosols conditions associated with three representative aerosol locations in simulations initialised with identical input soundings of moisture and temperature (described in Section 3.2). A similar approach was used by Wang et al. (2011a), who developed a range of cloud conditions by altering background CCN concentrations. The resulting N_d in the simulations presented here ranged from ~10 cm^{-3} in the PR case, to ~200 cm^{-3} in the NP-Pa case, reaching ~600 cm^{-3} in the most polluted NP-Ch

case. Low values of N_d (typically less than 50 cm^{-3}) tend to occur over the remote oceans, with N_d of less than 10 cm^{-3} being possible in extremely aerosol-rare conditions (Wood, 2012). However, satellite-based observations suggest that clouds demonstrating N_d as low as those in the PR case are relatively rare (Latham et al., 2012a). The N_d of ~200 cm-3 resulting in the NP-Pa simulation is more typical of MSc clouds. This is expected given that the background aerosol concentration used in this simulation was based on those typical of MSc cloud regions. Satellite-based observations again suggest that, whilst possible, the higher N_d value of ~600 cm^{-3} (in the NP-Ch simulation) represents a more extreme MSc cloud case. These simulations therefore successfully produce clouds that cover a broad range of feasible N_d values, as required. However, it is acknowledged that both the lowest and highest N_d captured by the simulations are close to the bounds of observed clouds. In view of this, interpretations and conclusions regarding the response of the clouds to MCB aerosol emission (presenting in forthcoming chapters) are constrained to broader patterns of change rather than focus on narrow quantitative measures. These patterns are taken to be characteristic of broader cloud regimes, with the patterns of change also being critically assessed against those expected from both theory and observations. It is acknowledged that while some broader conclusions can be drawn, the limited number of cloud samples precludes an comprehensive interpretation of all possible conditions. Thus, beyond the time and computational constraints of this current work, further population of the N_d parameter space would be informative in the future. Of particular interest would be conditions between the PR and NP-Pa cases where transition occurs between precipitating and non-precipitating conditions.

The LWP magnitudes of these simulations were somewhat lower than those observed during the DYCOMS-II (RF02) research flight (90 to 120 g m^{-2}) on which the input soundings of these simulations were based. Such underestimation of LWP was also experienced in the simulations of Wang and Feingold (2009a), Wang et al. (2011a) and Chen et al. (2011).

While the surface heat fluxes exhibit a diurnal cycle, they are relatively small (cf. measured nocturnal surface heat fluxes of 93 Wm^{-2} (latent) and 16 Wm^{-2} (sensible) from DYCOMS-II RF02 (Ackerman et al., 2009)). This is likely linked with the initialisation of wind speed to zero, which produces maximum base-layer wind speeds from the convergence of downdrafts that reach 2 ms^{-1}. These are lower than the 5 to 10 ms^{-1} wind speeds typical of MSc regions (Fan et al., 2012). In the large-eddy simulation MSc modelling of Chen et al. (2011), cloud properties were found to be less sensitive to changes in wind speed than to other environmental settings, including sea-surface temperature, free-tropospheric moisture, and the strength of large-scale subsidence. As demonstrated in the results, while the surface fluxes are relatively low, they are sufficient to maintain cloud during the PR night and NP night and day, and to allow a pattern of rebuilding into the second night in both regimes.

While cloud dissipation into the day is characteristic of MSc, satellite observations suggest that the total cloud dissipation of the PR case is atypical for MSc clouds (Rozendaal et al., 1995; Stubenrauch et al., 2006). Total daytime cloud dissipation has however been observed during aircraft/ground based field campaigns (Albrecht et al., 1988; Minnis et al., 1992), suggesting that its occurrence is more likely over small, localised areas rather than being evident as a mean cloud property over tens or hundreds of square kilometres. Whilst having no cloud to affect, forthcoming experiments whereby MCB aerosols are emitted into the PR simulation in the day, will still be of interest. As, during the day, the cloud fraction in reality is somewhat smaller than during the night, the direct aerosol effect will play a larger role. Again, while the three base cases described in this chapter demonstrate a range of conditions across increasing values of N_d, it is acknowledged that these represent only a small subset of the considerable parameter space of possible background conditions possible for MSc. This reinforces that further simulations in the future, capturing a greater number of possible conditions will be of value.

Other features of these base cases support the conclusion that these cloud simulations can capture representative MSc behaviour. Negative vertical velocity skewness in the NP cases, peaking in the lower third of the boundary layer, agrees with the observations of Hogan et al. (2009). The positive skewness within the cloud in the PR case being consistent with wide downward motions associated with droplet sedimentation within the cloud (Ackerman et al., 2009) and strong, narrow downdrafts, associated with precipitation below the cloud (Wang and Feingold, 2009a). Additionally, the stratification observed in the total water mixing ratio of the PR case suggests uncoupling of the cloud and boundary layers (Jones et al., 2011b) which is typical of precipitating MSc. While cloud conditions do not recover fully into the second night owing to imbalances in forcings, the clear diurnal patterns in cloud properties and – importantly – in underlying cloud system physics and dynamics allows the cloud response to aerosol emission to be related to the characteristic physical status of the cloud system at different times of the diurnal cycle.

Sensitivity testing of model resolution and domain size suggests that the enhancement of horizontal resolution from 300m to 100m (with the vertical resolution being maintained at ~30 m) improves recovery of LWP into the second night. However, computational restrictions would require such a resolution to be run over a smaller domain size than currently used, further limiting the aerosol emission analysis time. Conversely, increasing both the horizontal and vertical resolutions from 300 m and ~30m to 100m and ~15m resulted in a poorer recovery of LWP and cloud fraction, suggesting that this particular MSc cloud modelling set-up did not benefit from the increased resolution as would be expected. Similarly, increasing the vertical resolution from 20 m to 5 m did not induce significant

improvements in cloud response in the sensitivity study of Chen et al. (2011). In spite of the vertical model resolution being larger than the 5 to10 m typically suggested for resolved entrainment (e.g. Bretherton et al., 1999; Stevens and Bretherton, 1999), diurnal variations in entrainment (exhibited as cloud top height variations, given the constant large-scale divergence) behave as expected, with decreases in entrainment during the day in response to weakening cloud-top negative buoyancy, and increased entrainment rates following the aerosol emission-induced N_d increases in the PR case as will be presented in the next chapter. Beyond the time and computational constraints of this current work, larger domain size simulations, with higher resolution in both the horizontal and vertical directions would be a desirable feature of future work. Additional future work would benefit from extending the simulation durations to incorporate an additional diurnal cycle. This would better inform on the recovery of the modelled cloud system into the night, and would hence aid in the development of more robust cloud simulations.

It is important to recognise that these cloud modelling simulations use only one model, and one model set-up. These simulations use the Morrison double-moment microphysics scheme. While this scheme handles data on both the number and mixing ratio of cloud droplets, it assumes a fit to a gamma distribution. The use of a bin (or sectional) scheme may thus handle such data on the distribution of cloud droplets more accurately (although this would entail even greater computational implications). Similarly, the RRTMG SW radiation scheme utilises the assumed two-moment microphysics scheme cloud droplet distribution for its calculations. Thus, inaccuracies may persist through to calculations of the radiative impact of the clouds in these simulations. While representations of such real-life processes – as in all computer modelling – is imperfect, the impacts on the overall realism of the simulated behaviour will also depend upon the other factors. For example, the microphysics and SW radiation implications of the simulated clouds will also be dependent upon the simulated dynamics within the boundary (and thus dependent upon parameterisations of turbulent kinetic energy and model resolution etc.) along with initialised parameters and assumed physical processes (for example the constant large-scale divergence assumed here to simulate subsidence).

In spite of the limitations of this modelling work, these simulations produce patterns of radiative heating, cloud properties and dynamics over the diurnal cycle that are believed to be adequately representative of MSc clouds to form the basis of the forthcoming MCB simulations. The range of cloud conditions, incorporating moderately precipitating and non-precipitating conditions, is sufficient to examine the patterns of cloud response to the addition of MCB aerosols. However, owing to the constraints of this modelling investigation, and the wider uncertainties regarding the indirect aerosol effects (described in Chapter 2), moving

beyond the identification of these broader patterns of change would be imprudent at this stage. This investigation therefore represents an initial 'first order' consideration of the possible importance of capturing details of MCB implementation mechanisms. Confidence in making more detailed assertions would require a significant number of multi-model simulations, ideally integrated with observational data. The possibilities, and ramifications of such potential future work are discussed in Chapter 9.

3.5 Conclusions

This chapter describes the simulation of three MSc cloud cases using the WRF/Chem cloud-resolving model. The results show that the methodology adopted is capable of adequately producing the spatial and temporal patterns of many aspects characteristic to MSc clouds across the diurnal cycle. These key processes and properties include turbulence, skewness, cloud thickness, cloud fraction and cloud albedo.

The MSc clouds simulations were sensitive to background aerosol concentrations. Initialising the simulations with a range of three realistic background aerosol concentrations resulted in one precipitating case (under the cleanest background conditions), and two non-precipitating cases (for the more polluted background conditions). These precipitating and non-precipitating cloud cases additionally exhibit attributes – including precipitation rates, skewness and cloud fraction – associated with open cell and closed cell regimes, respectively. Thus, in spite of the limited number of cases, these simulations cover a broad range of cloud properties.

Sufficient confidence is engendered by the concordance between simulated and expected cloud characteristics that these three MSc cloud cases are used as the base case conditions for the MCB effectiveness experiments, presented in Chapters 4, 5 and 8.

The first experiment, presented in the next chapter, examines the first MCB implementation detail case study in determining how MCB effectiveness varies with the timing of MCB implementation through the diurnal cycle of MCB clouds.

Chapter 4
Aerosol Emissions During the Diurnal Cycle

4.1 Introduction

While continuing developments in global-scale climate modelling are producing improvements in the representation of clouds and precipitation, capturing realistic features (such as, for example, diurnal cycles) in these parameterised representations remains challenging (Flato et al., 2013). Hence, global-scale models are unable to realistically capture how MCB effectiveness varies with changes in MSc cloud and boundary layer properties over a diurnal cycle (described in Chapter 2).

As described in Chapter 2, proposals for the MCB scheme suggest a fleet of sea-going vessels. Each vessel would potentially emit aerosols continuously as they sailed. Thus, previously unaffected clouds could be targeted at different times throughout the diurnal cycle. This chapter uses the cloud-resolving modelled MSc clouds described in Chapter 3 – which adequately represent diurnally varying cloud behaviour over a range of conditions – as base cases in determining how MCB effectiveness varies with this timing of implementation through the diurnal cycle. This work therefore examines the first MCB implementation detail case study.

First, the methodology of the MCB experiments is described (Section 4.2), before cloud and cloud system changes, along with albedo perturbations are presented and discussed for both the precipitating and non-precipitating base cases (Section 4.3 and 4.4). These sections also incorporate an examination of how the rate of MCB aerosol emission affects MCB effectiveness. The chapter closes by describing possible implications of the detected variation in MCB effectiveness according to implementation timing, for both the MCB proposal and the production of future MCB effectiveness estimates (Section 4.5).

4.2 Methodology

For each of the three MSc base cases, four aerosol emission simulations were performed, corresponding to aerosol emission in the early morning (03:00:00 LT), mid-morning (08:00:00 LT), day (13:00:00 LT) and evening (18:00:00 LT). These times represent emissions into the various conditions of the diurnally varying MSc. Analysis of the post-aerosol emission simulations is limited to the five hour period subsequent to emission. After this time, the aerosols pervade the domain, and owing to the use of periodic boundary conditions would therefore result in unrealistic behaviour. Additional experiments

investigated the effects of varying the aerosol emission rate and were carried out for precipitating conditions only.

The spraying vessel was assumed to travel the length of the 9 km domain once, along the middle of the domain, at a speed of 5 ms^{-1}. This moving aerosol emission was simulated as an increase in Na and Cl aerosol in one base-layer grid cell at a time. This follows Wang et al. (2011a) in simulating the point source aerosol emission from individual spraying vessels (as opposed to uniform emission of the MCB aerosols over the domain as a whole). It is noted that whilst this 'point source' emission still comprises of a uniform aerosol emission over the 300 m x 300 m grid cell (and is therefore still two orders of magnitude larger than the 2.4 m diameter emission rotors proposed by Salter et al. (2008)), it is more realistic than a uniform aerosol emission over the whole domain. The mass and number fluxes were based on emission rates estimated by Salter et al. (2008) with an emission rate of 30 kg s^{-1} of sea water forming a wet spray of 800 nm diameter. As such, these aerosols were emitted into the third size bin, representing a dry diameter one quarter of the diameter of the wet droplets (Lewis and Schwartz, 2004), i.e. 200 nm. The number flux ($1.24x10^{12}$ m^{-2} s^{-1}) was calculated as the number of 800 nm diameter sea water droplets (assumed to be spherical) produced for the 30 kg s^{-1} sea water flux. The mass fluxes of Na and Cl (4436 μg m^{-2} s^{-1} and 6840 μg m^{-2} s^{-1} respectively) were calculated by assuming a 200 nm dry salt diameter, assuming that the fraction of Na and Cl follows the ratio of atomic weights (23.00 : 35.45). In preliminary testing, it was found that emission rates greater than half the mass and number fluxes of Salter's full emission rate resulted in failure of the SW radiation scheme, ultimately leading to overall simulation failure. Given that the Salter et al. (2008) emission rate is dependent on the wind speed and decreases at speeds below 6-8 ms^{-1} (Korhonen et al., 2010b), and that half of the maximum Salter emission rate (denoted here as 0.5xSA) produced clear perturbations in the cloud and cloud system, this will be the maximum emission rate used. Experiments to investigate the effects of varying the aerosol emission rate on the precipitating case consisted of emitting a quarter of the Salter emission rate (0.25xSA) and a tenth of the Salter emission rate (0.1xSA) at each of the four times through the diurnal cycle. The MCB aerosol emission experiments are summarised in Table 4.1.

Table 4.1 *– MCB aerosol emission experiments. PR indicates aerosol emission into the precipitating control case. NP-Pa and NP-Ch indicate aerosol emission into the non-precipitating cases initialised with aerosol concentrations associated with the North-East Pacific (intermediately polluted) and the East China Sea (heavily polluted) respectively. 0.5xSA, 0.25xSA and 0.1xSA describe the aerosol emission rate, as a fraction of the emission rate proposed by Salter et al. (2008).*

Time of aerosol emission (LT)	Aerosol emission rate		
	0.5xSA	0.25xSA	0.1xSA
03:00:00	PR	PR	PR
	NP-Pa	–	–
	NP-Ch	–	–
08:00:00	PR	PR	PR
	NP-Pa	–	–
	NP-Ch	–	–
13:00:00	PR	PR	PR
	NP-Pa	–	–
	NP-Ch	–	–
18:00:00	PR	PR	PR
	NP-Pa	–	–
	NP-Ch	–	–

4.3 Results

The effects of aerosol emissions on albedo were considered by three measures. Since the brightening of clouds is only effective at producing a negative radiative perturbation during daylight, all measures of albedo were calculated only when downward SW radiation is present. As such, the early morning and evening emission times have a reduced analysis period. Emission into the early morning captures the latter portion of cloud alterations, while the emission into the evening captures only 40 min after the beginning of emission. The three measures were:

1. A broad estimate of the change in domain average calculated cloud albedo for times of SW radiation in the 5 hours subsequent to emission compared to the control. This uses the simplified calculation of Twomey (1977) for optical cloud thickness (τ), described in Equation 4.1.

$$\tau = \sum 2\pi N \bar{r}^{\,2} h \qquad \textbf{(4.1)}$$

where:

N = drop concentration (m^{-3})

$\bar{r}$ = a representative mean radius calculated from the mass of liquid water and droplet concentration at each grid cell (m)

h = depth of the grid cell (m)

This was then converted into albedo (A) using the approximation described by Equation 4.2 (Lacis and Hansen, 1974; Zhang et al., 2012).

$$A = \frac{\tau}{6.8 + \tau} \qquad \textbf{(4.2)}$$

where:

τ = optical cloud thickness (from Equation 4.1)

An estimation of the aerosol effect on cloud albedo in the absence of LWP increase was also included (i.e. a fixed LWP assumption), whereby the calculation was repeated with control case LWP and change in N_d weighted for this control case LWP. This fixed LWP calculation is intended only as an approximate indication of the contribution of the first indirect aerosol effect.

These calculated cloud albedo estimates do not include the effects of solar zenith angle. As such there is likely a high bias in the calculated cloud albedo for times close to noon and a low bias for times of larger solar zenith angle.

2. The domain average change in all-sky planetary albedo for times of SW radiation in the 5 hours subsequent to emission compared to the control was calculated as the ratio of upward to downward SW radiation at the top of atmosphere. This incorporates the concurrent effects of cloud albedo and cloud fraction changes as well as direct aerosol effects, over a constantly low ocean surface albedo. This output is calculated using output from the SW radiation scheme.

3. The domain average change in clear-sky albedo for times of SW radiation in the 5 hours subsequent to emission compared to the control. This calculates the albedo for all columns in the domain, omitting cloud layer effects. Therefore, the masking effect of overlying clouds is removed, and the change in clear-sky albedo is a measure of the maximum direct aerosol effect. This output is calculated using output from the SW radiation scheme.

4.3.1 Marine Cloud Brightening Aerosol Emission into the Precipitating Cloud Case

The 0.5xSA emission of MCB aerosols into the PR base case resulted in cloud average N_d increases at all four emission times during the diurnal cycle. This increase ranged from a five-fold increase (to 117 cm^{-3}) for emission into the low cloud fraction during the day (13:00:00 LT), to an increase of almost 17 times the original concentration (to 234 cm^{-3}) for emission in the mid-morning (08:00:00 LT) (Table 4.2).

Table 4.2 *– Results for the 0.5xSA aerosol emission rate. Domain and time-period averaged liquid water path (LWP, g m^{-2}), cloud fraction (f_c, %), cloud droplet number concentration (N_d, cm^{-3}) and surface rain rate (R_r, mm day^{-1}). The time average is taken for the times of shortwave (SW) radiation present in the 5 hours subsequent to aerosol emission.*

Case	Time of aerosol emission (LT)	LWP, g m^{-2}		f_c, %		N_d, cm^{-3}		R_r, mm day^{-1}	
		Control	0.5xSA	Control	0.5xSA	Control	0.5xSA	Control	0.5xSA
PR	03:00:00	31.8	45.3	37.9	76.3	10.8	176.3	0.25	0.03
	08:00:00	7.0	15.2	6.8	19.8	13.5	234.3	0.09	0.05
	13:00:00	0.6	0.5	0.4	0.3	20.6	116.9	0.00	0.00
	18:00:00	3.6	3.6	5.6	5.6	19.5	171.1	0.00	0.00
NP-Pa	03:00:00	59.8	60.8	97.9	98.6	156.2	315.0	0.00	0.00
	08:00:00	31.7	31.6	79.7	79.3	156.2	180.7	0.00	0.00
	13:00:00	14.8	14.8	22.9	22.7	156.5	259.8	0.00	0.00
	18:00:00	14.3	14.3	22.4	22.5	156.3	178.8	0.00	0.00
NP-Ch	03:00:00	59.6	59.1	98.2	98.7	526.6	632.2	0.00	0.00
	08:00:00	31.6	31.4	80.8	80.3	513.2	517.0	0.00	0.00
	13:00:00	13.4	13.7	18.8	19.1	516.9	556.1	0.00	0.00
	18:00:00	11.8	11.8	9.1	9.1	528.1	528.3	0.00	0.00

These N_d increases were sufficient to reduce the domain mean precipitation rate by up to 88% averaged over the time where SW radiation was present in the 5 hours subsequent to emission. However, no change occurred for emission into the cloud-free early afternoon at which time background precipitation has already ceased, or for evening emission (18:00:00 LT) where precipitation rates had not yet recovered. The precipitation decreases produced an increase in LWP compared to the control case of 43% for early morning emission (03:00:00 LT), and 114% for mid-morning emission. In addition to LWP increases, emitting aerosols into cloudy conditions resulted in an increase in cloud fraction. Early morning emission doubled the cloud fraction while mid-morning emission tripled the cloud fraction. The cloud fraction, and associated perturbations were negligible for day and evening emissions. Aerosol emission also affected the cloud height, particularly when emitted into the dissipating cloud in the early and mid-mornings. Here, the cloud top descent seen in the control case was replaced by cloud top height maintenance (Figure 4.1).

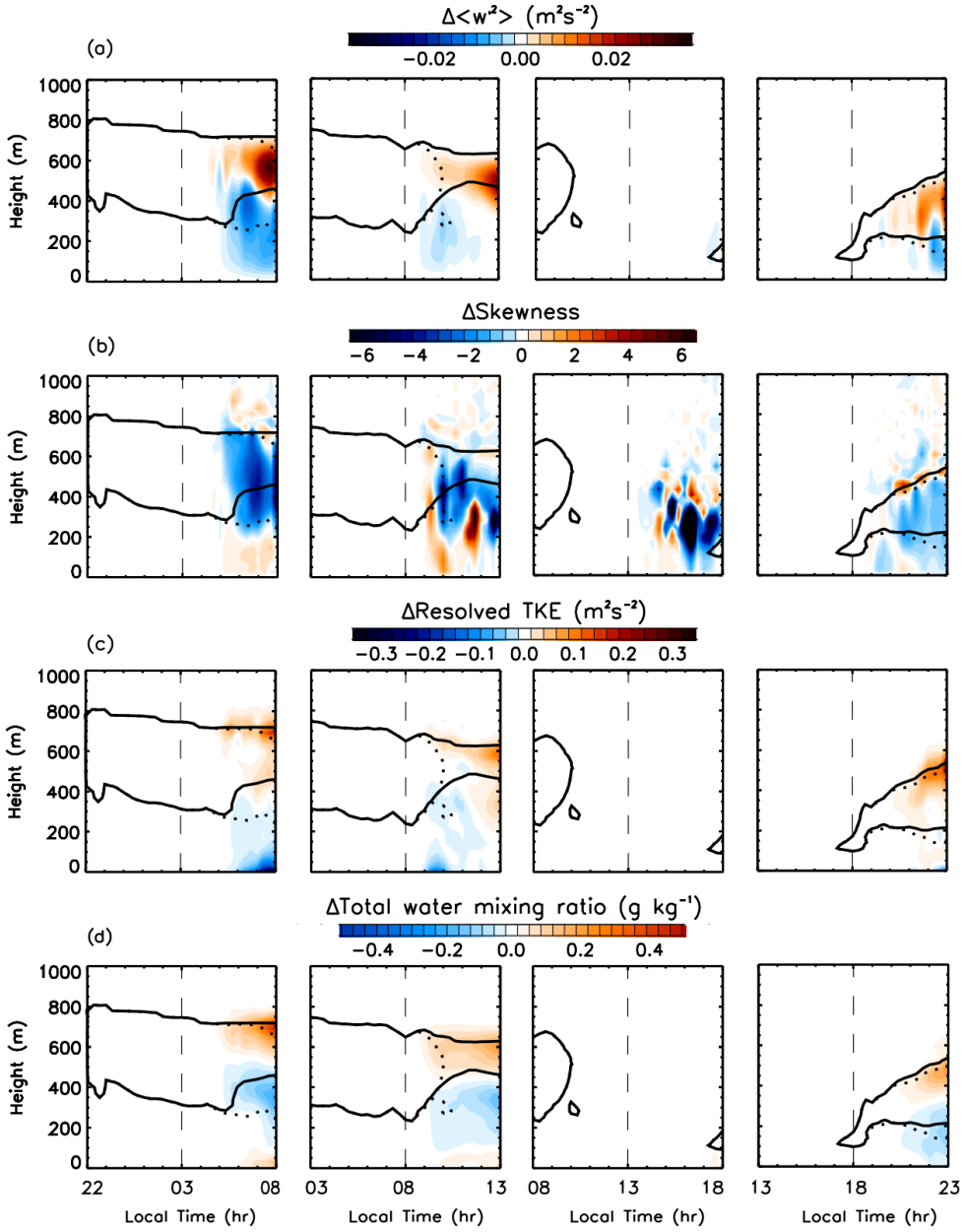

Figure 4.1 *– Time evolution for PR 0.5xSA emission-induced perturbations in domain averaged: (a) vertical velocity variance (<w'²>,m^2s^{-2}); (b) vertical velocity skewness; (c) resolved turbulent kinetic energy (m^2s^{-2}); and (d) total water mixing ratio (g $kg_{dry\ air}^{-1}$). Solid lines indicate the perturbed domain average cloud top and base (contour at cloud water mixing ratio of 0.01 g $kg_{dry\ air}^{-1}$). Control case domain average cloud top and base are indicated by the dotted lines. The dashed vertical lines indicate the time of aerosol emission.*

A slight cloud top increase was also seen for evening emission, although as this is into the post-SW radiation growth phase of the cloud, the perturbation is less marked. Again, no cloud changes occurred when emitting into the cloud-free early afternoon. Considering how these changes to cloud properties are related to albedo, Figure 4.2 shows the change in calculated cloud albedo, change in all-sky albedo and change in clear-sky albedo for an aerosol emission rate of 0.5xSA.

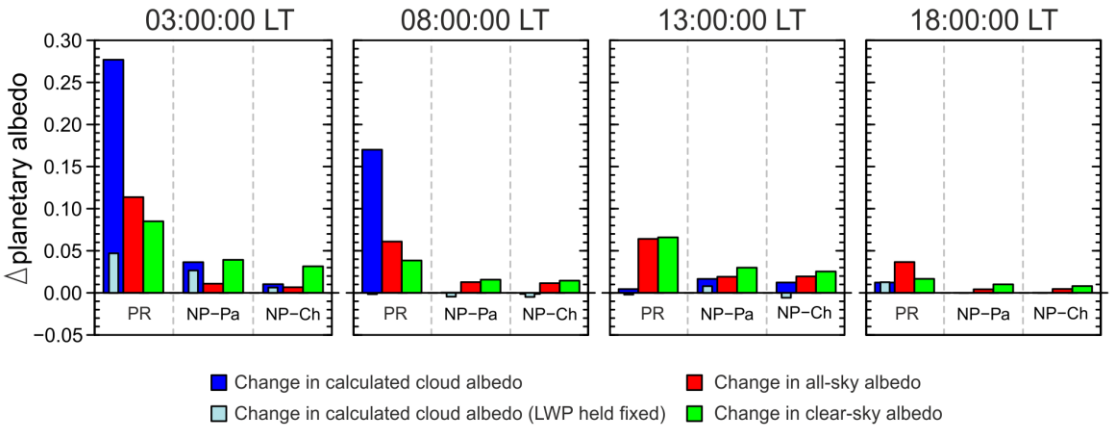

Figure 4.2 *– Domain and time averaged albedo perturbations associated with aerosol emission at the 0.5xSA rate, at 03:00:00 local time (LT), 08:00:00 LT, 13:00:00 LT and 18:00:00 LT into the PR, NP-Pa and NP-Ch cases. In each case, four measures of the effects of aerosol emission on albedo perturbations are shown: the change in calculated cloud albedo; the change in cloud albedo assuming a LWP fixed at the control magnitudes with weighted N_d increases; the change in all-sky planetary albedo; and the change in clear-sky albedo.*

For the PR base case, there is a clear variation in the change in calculated cloud albedo for aerosol emission at different times during the diurnal cycle. Early and mid-morning emissions produced the largest increase in calculated cloud albedo of 0.28 and 0.17 respectively. As the cloud recovered into the second night, evening emission produced a slight increase in calculated cloud albedo of 0.01. There was also a clear variation in both the all-sky albedo and clear-sky albedo responses for aerosol emission at different times during the diurnal cycle. These variations will be caused by differences in the distribution of the MCB aerosols in response to turbulent mixing throughout the boundary layer, and will, as such, depend upon the time of day. These patterns of all-sky and clear-sky albedo changes were different to those seen in cloud response only. The largest increase in all-sky albedo was seen for early morning emission at 0.11, reducing to an increase of 0.06 for mid-morning emission, and decreasing further for evening emission at 0.04. The clearest of the deviations from the pattern of change of calculated cloud albedo was during the cloud-free early afternoon, where the all-sky albedo increase was 0.06. As expected in these cloud-free conditions, the increase in all-sky albedo was matched by the increase in clear-sky albedo at this time, indicating that the all-sky albedo change was purely from the direct aerosol effect. The vertical distribution of the domain maximum unactivated aerosol concentration is shown for each emission time in Figure 4.3. The clear-sky albedo also increased the all-sky albedo more than the calculated cloud albedo for the evening emission where cloud fraction was low. The changes to clear-sky albedo again showed a different diurnal pattern. Early morning emission again produced the largest perturbation of 0.08, falling to 0.04 for emission in the mid-morning. This recovered into the day, producing a clear-sky albedo increase of 0.07. The response was again low for evening emission, producing a clear-sky albedo increase of 0.02.

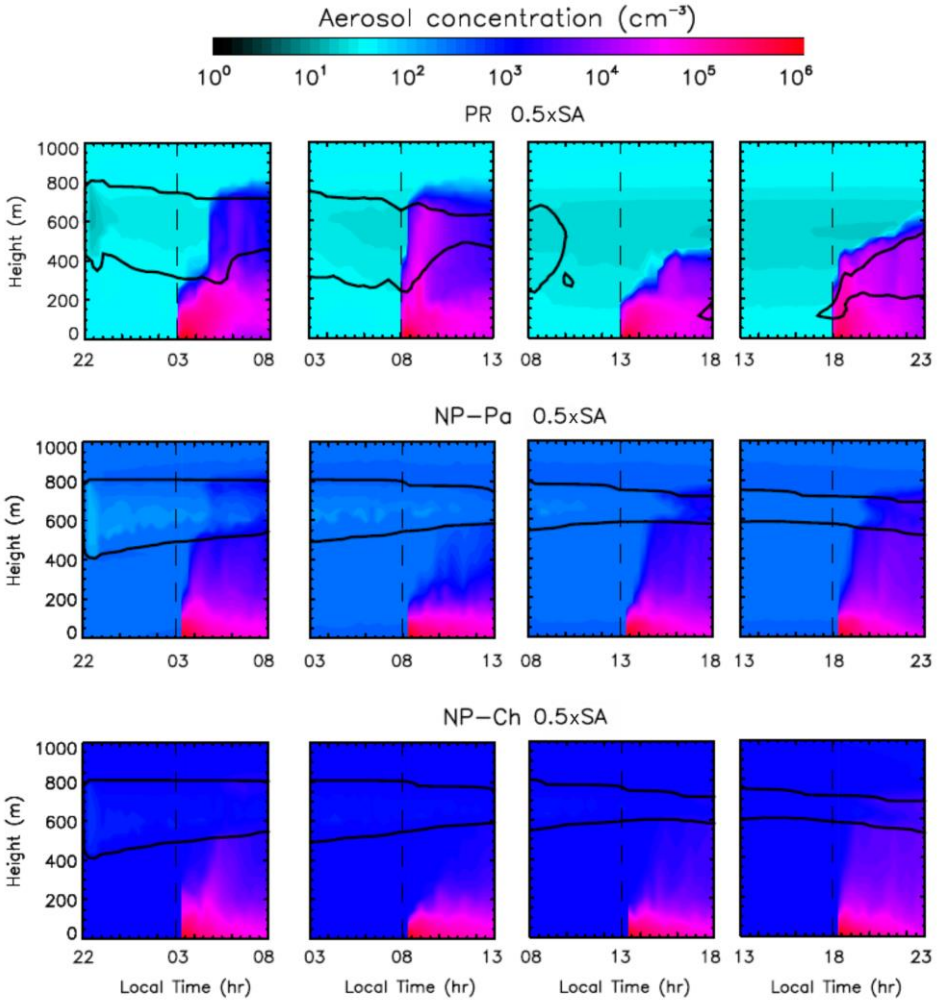

Figure 4.3 *– Time series of domain maximum aerosol concentrations (cm^{-3}) for the PR, NP-Pa and NP-Ch cases (all 0.5xSA aerosol emission rate). Plots include 5 hours prior to emission and 5 hours subsequent to emission, with aerosol emission start time being indicated by the vertical dashed line.*

4.3.2 Marine Cloud Brightening Aerosol Emission into the Non-Precipitating Cloud Cases

Emission into the NP cases resulted in larger absolute N_d increases than in the PR case (Table 4.2). Increases were also generally larger for the less polluted NP-Pa case than the more polluted NP-Ch case. The maximum resulting domain and time averaged N_d following emission ranged from 234 cm^{-3} (PR) to 315 cm^{-3} (NP-Pa) and 632 cm^{-3} (NP-Ch). These values decreased for emission at the least effective times of day to 117 cm^{-3}, 179 cm^{-3} and 517 cm^{-3} respectively. It is noted that these averages are for a small domain size, in the time immediately after emission and should therefore be larger than those obtained in longer time scale and larger domain size simulations. This is true when comparing to the finding of Wang et al. (2011), who report average resulting N_d of 65 mg^{-1} and 46 mg^{-1} for their precipitating cases (where 1 mg^{-1} is equal to 1 cm^{-3} for an air density of 1 kg m^{-3}). For these NP cases, as there was no precipitation to prevent, no precipitation change occurred (Table 4.2). The LWP

changes were small (up to 2%), with small losses during the NP-Ch morning. Cloud fraction, cloud top and cloud base heights all showed negligible perturbations. Whilst the magnitudes of calculated cloud albedo increase were generally significantly smaller for the NP cases compared to the PR cases, these were also sensitive to the timing of emission. For NP-Pa no perturbation was produced for mid-morning emission, although an increase in calculated cloud albedo of 0.04 resulted from early morning emission. This peak value was only 13% of the maximum increase in calculated cloud albedo, reached when emitting into the PR cloud. For the more heavily polluted NP-Ch case, the pattern was repeated, although where changes to the calculated cloud albedo occur, the magnitude was less than half that of the NP-Pa case. The change in all-sky albedo was similarly significantly lower than for the PR case. The maximum all-sky albedo increase obtained for the NP cases occurred for emission into the day (0.02) and was around a sixth of that achieved in the PR case. The values of the all-sky albedo changes were similar for both NP cases. The changes in all-sky albedo followed the same alternating pattern as that of the PR case, with higher perturbations in the early morning and day.

4.3.3 Rate of Marine Cloud Brightening Aerosol Emission into the Precipitating Cloud Case

For early and mid-morning emission into the PR case, N_d increased with emission rate. However, the relationship was non-linear and tended to flatten at higher aerosol emission rates (Table 4.3).

Table 4.3 *– Results for the PR case. Notes as Table 4.2.*

Time of aerosol emission (LT)	Case	LWP, g m^{-2}	f_c, %	$N_{d,}$ cm^{-3}	R_r, mm day^{-1}
03:00:00	Control	31.8	37.9	10.8	0.25
	0.5xSA	45.3	76.3	176.3	0.03
	0.25xSA	44.6	73.0	141.5	0.04
	0.1xSA	44.1	69.7	92.9	0.04
08:00:00	Control	7.0	6.8	13.5	0.09
	0.5xSA	15.2	19.8	234.3	0.05
	0.25xSA	14.4	17.5	200.3	0.05
	0.1xSA	13.1	14.6	124.4	0.06
13:00:00	Control	0.6	0.4	20.6	0.00
	0.5xSA	0.5	0.3	116.9	0.00
	0.25xSA	0.5	0.3	134.7	0.00
	0.1xSA	0.5	0.4	181.6	0.00
18:00:00	Control	3.6	5.6	19.5	0.00
	0.5xSA	3.6	5.6	171.1	0.00
	0.25xSA	3.6	5.6	180.6	0.00
	0.1xSA	3.6	5.6	139.9	0.00

The opposite relationship occurred for day and evening emissions, with decreasing N_d as aerosol emission rates increased. Future investigation of the reason of such a pattern would be of interest, although the low cloud fractions during the day reduce the impact that such cloud changes have on the overall albedo perturbations. Precipitation rates were uniformly reduced across all emission rates for the early and mid-morning. The LWP showed small increases with aerosol emission rates for the early and mid-morning emission times, as did the cloud fraction. The calculated cloud albedo also increased with increasing aerosol emission rates for both the early and mid-morning emissions (Figure 4.4). This relationship was non-linear, showing a flattening gradient at higher aerosols emission rates. For example, the rate of calculated cloud albedo increase with respect to increase in emission rate reduced to a third for the higher emission rates (0.25xSA to 0.5xSA) into the cloud in the mid-morning compared to the lower emission rates (0.1xSA to 0.25xSA). This reduction was just under a half for emission into the early morning cloud. Emitting into the cloud-free conditions of the PR early afternoon produced no change in calculated cloud albedo, regardless of aerosol concentration. Increasing the emission rate between 0.1xSA and 0.5xSA also had little effect on calculated cloud albedo when emitting into the recovering evening cloud. The effect of increasing the aerosol emission rates on the change in all-sky albedo also varied through the diurnal cycle. The change in all-sky albedo showed a positive correlation with increasing emission for early and mid-morning emission. Again, the rate of all-sky albedo increase with emission rate was non-linear, the gradient of the response typically halving for the higher emission rates. This relationship was again weaker for the evening, with little variation in the increase in all-sky albedo for different emission rates. The clear-sky albedo again showed a non-linearly increasing response.

It is noted that the phenomenon of the calculated cloud albedo being lower than the all-sky albedo in the 18:00:00 LT case is likely due to the omission of solar zenith angle from the cloud albedo calculation.

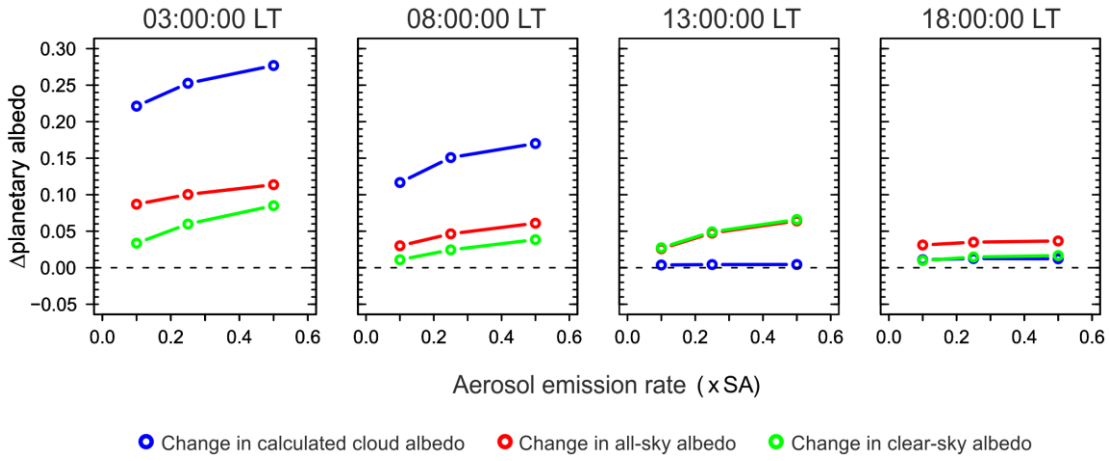

Figure 4.4 *– Domain and time average albedo perturbations associated with 0.1xSA, 0.25xSA and 0.5xSA aerosol emission rates at 03:00:00 LT, 08:00:00 LT, 13:00:00 LT and 18:00:00 LT into the PR regime. In each case, three measures of the effects of aerosol emission on albedo perturbations are shown: the change in calculated cloud albedo; the change in all-sky planetary albedo; and the change in clear-sky albedo.*

4.4 Discussion

The albedo response to aerosol emission for the PR regime is significantly larger than for the NP regime, in agreement with the MCB simulations of Wang et al. (2011a) and the behaviour expected based on current understanding of MSc (Figure 2.6 and discussions in Chapter 2). Whilst aerosol emission into both the NP and PR regimes demonstrate the first indirect aerosol effect (Twomey, 1977), only aerosol emission into precipitation in the PR regime (i.e. early and mid-morning) demonstrates a strong second indirect aerosol effect (Albrecht, 1989), as discussed in Section 2.4 (Chapter 2). For the PR case, the LWP increases associated with this second indirect aerosol effect and negative radiative forcing are more effective at increasing the calculated cloud albedo than the first indirect effect, again in agreement with Wang et al. (2011a). However, there is no significant second indirect aerosol effect when emitting into the PR regime cloud-free early afternoon or into the PR regime evening where the cloud is in a period of regrowth and has not recovered sufficiently for precipitation. The LWP increases in the PR regime, and small decreases in LWP in the NP regime illustrate the complexities and uncertainties surrounding the magnitude – and sign – of the second indirect aerosol effect (discussed in Chapter 2). The slight LWP losses for the early and mid-morning aerosol emissions in the NP-Ch case suggest a small positive second indirect aerosol effect. As discussed in Section 2.4.3 (Chapter 2), the LWP response to additional aerosols depends on comparative gains in water (from either dynamical changes or the suppression of precipitation caused by the reduced coalescence of smaller droplets), and increased entrainment drying resulting from the presence of smaller cloud droplets in the entrainment zone and increased TKE. That section also described two potential thresholds for characterising whether a cloud system would gain or lose LWP in response to the addition of

aerosols. From these, LWP increases would be expected for clouds with surface precipitation rates in excess of 0.1 mm day^{-1} (Ackerman et al., 2004; Chen et al., 2011) , or for clouds with bases below 400 m (Wood, 2007). Both of these thresholds hold for the disparity in LWP response between the PR and NP regimes (cf. Figures 3.3 and 3.5), suggesting that the LWP increases resulting from precipitation suppression in the PR case were sufficient to overcome the increased evaporation of cloud droplets that resulted in small LWP losses in the NP case.

It is noted that small negative fixed LWP calculated cloud albedo changes (evident in Figure 4.2) are likely artefacts of the approximate nature of the estimation method used rather than being symptomatic of a robust a physical feature.

While the simulations therefore produce an interesting range of responses to the emission of aerosol, they are a small subset of possible cloud conditions. Previous global-scale computer model simulations have found that the lifetime of the emitted aerosols is up to 4.8 days (Jones and Haywood, 2012). Whilst the focus here is on the rapid cloud responses to aerosol emission, particularly contrasting the cloud responses at different times in the diurnal cycle, we can infer insights into longer time-frame cloud changes from the simulations. Changes in cloud properties suggest that the PR cloud subject to MCB aerosol emission is undergoing a regime change to a more persistent, non-precipitating cloud type, as discussed in the last paragraph of Section 2.4.3 (Chapter 2). Consistent with changes in cloud-top entrainment associated with increases in aerosol concentrations as described in Section 2.4.2.2, aerosol emissions in the early and mid-mornings produce increased turbulent mixing at the cloud-top (evinced by the larger vertical velocity variance at the cloud top; Figure 4.1 a). The associated increases in entrainment rate are suggested by the relative increase in cloud top height, consistent with the cloud top height increases observed in ship tracks in the open cellular regime (Christensen and Stephens, 2011). Emission of aerosols in to the PR case during the early and mid-mornings also resulted in both an increase in LWP, and persistence of the cloud into the day where enhanced albedo is important for reflection of SW radiation. The indication of regime change from a precipitating to non-precipitating regime is also evident in changes to the vertical velocity skewness as the positive cloud-top skewness of the control case becomes more negative after emission (Figure 4.1 b). The effectiveness of this morning emission is consistent with the hypothesis proposed by Wang et al. (2011a), with the stronger night-time response also agreeing with the large-eddy simulations of Ackerman et al. (2003). Whilst the immediate impact of aerosol emission into the clouds in the evening is reduced owing to the lack of SW radiation, regime change may continue through the night, persisting into the subsequent day. Indicators of regime change do not occur for emission into the cloud-free early afternoon, regardless of aerosol emission rate. Indicators of regime change are also not evident for the NP regime at any emission time.

Whilst there was no indication of regime change in the cloud-free early afternoon of this particular PR simulation, the future investigation of further cloud conditions would be of interest. Of particular interest would be the case of a precipitating cloud that was better maintained into the daytime than was the case here. Furthermore, the behaviour of clouds with weaker precipitation (i.e. evaporating before reaching the surface) would also yield interesting results.

For the PR case, while aerosol emission did not increase cloudiness during the day, the all-sky albedo was still increased owing to a larger direct effect under the cloud-free conditions. This balance of direct and indirect aerosol effect is important, as the direct aerosol effect will somewhat compensate for the lack of indirect aerosol effect under lower cloud fractions (particularly during the day). This cloud fraction dependent direct aerosol effect therefore moderates the diurnal patterns of cloud response to some extent.

The lack of rapid cloud response for daytime emission may allow the aerosols to disperse horizontally within the boundary before being drawn into the cloud region by updrafts during the subsequent night. As the aerosols will then cover a larger horizontal extent, the local concentration of aerosols will be diminished, and the pattern of aerosol uptake will be altered. For example, Wang et al. (2011a) found that cloud albedo enhancement was larger for uniform compared to point source emission in their weakly precipitating case, however, the converse was true in a more heavily precipitating case. In addition to changes in cloud response, both the horizontal and vertical distribution of aerosols will be important for the direct aerosol effect. This, importantly, also depends upon cloud fraction which reinforces the benefits of exploring a greater range of cloud conditions in future work.

Considering the effect of aerosol emissions on planetary albedo changes in the PR case suggests that an asymptotic limit in increasing the all-sky albedo may lie above 0.5xSA (Figure 4.4).

As described in Chapter 1, the effects of the locally high aerosol concentrations resulting from a point source emission cannot be considered in the uniform aerosol application assumed in global-scale models. The disparities between changes in the calculated cloud albedo and all-sky albedo in the PR case for early and mid-morning emissions (Figure 4.2 and Figure 4.4) suggests that the large increases in calculated cloud albedo are not being fully achieved in the planetary albedo response. While differences in the calculation methods between the albedo responses will contribute towards this disparity, it is also suggested that the high concentration of aerosols emitted via the point source emission technique could also contribute towards this disparity through an offsetting/tempering effect. The high concentration of aerosols emitted from the point source produced large increases in N_d, particularly in the early/mid-morning and evening PR cases (Table 4.3). These increases

cause cloud-top radiative cooling to strengthen, leading to intensification of cloud-top turbulence and the entrainment of dry air from the free troposphere above (evidenced by the increase in cloud top height). This entrainment of warm, dry air increases the evaporation of cloud droplets, leading to the accumulation of interstitial aerosols overlying the cloud top (Figure 4.3).

The sea salt aerosols modelled here are highly scattering, but non-absorbing in the ultra-violet/visible wavelengths. Whilst a layer of pure NaCl would therefore typically not be associated with a reduction in planetary albedo when overlying clouds, several factors could cause these overlying aerosols to reduce the upward SW radiation at the top of the atmosphere. Radiative transfer modelling of atmospheric concentrations of non-absorbing sea salt aerosol overlying a low surface albedo (0.1) have produced a positive SW forcing of up to +5 Wm^{-2} for solar zenith angles of up to 30° (Li et al., 2008) (equivalent to between 10:00:00 LT and 14:00:00 LT in these simulations). Here, the predominantly forward scattering of the sea salt aerosols causes the majority of the SW radiation to pass through the aerosol layer, with the magnitude of SW radiation being reflected back to space being reduced by near-infrared absorption, at which wavelengths sea salt aerosols are more absorbing than in the ultraviolet/visible wavelengths (Hatzianastassiou et al., 2007). The presence of absorbing material in the sea salt aerosol would exacerbate the effect, with previous modelling and observational studies showing that partially absorbing aerosols overlying clouds reduce the measured upward irradiance and hence produce low biases in satellite retrievals of cloud optical depth (Haywood et al., 2004; Coddington et al., 2010). A radiatively positive effect was also shown in the modelling of mildly absorbing organic aerosols internally mixed in sea salt aerosols at mass fractions as low as 10% (Randles et al., 2004). Attenuation of upward radiation may also result from increases in total water mixing ratio above the cloud top (Figure 4.1 d), resulting from the emission of the MCB aerosols. The apparent offsetting/tempering role of the direct effect increases with increasing emission rate, demonstrated by the increasing disparity between changes in calculated cloud albedo and all-sky albedo in the early and mid-morning cases (Figure 4.4). However, this is not sufficient to overcome the increasing calculated cloud albedo and all-sky albedo with aerosol emission rate (Figure 4.4). Without the parameterisation of the effects of the locally high (point source originating) aerosol concentration, global-scale models are unable to simulate this effect. The possible presence and magnitude of such an offsetting effect could be of interest in future observational studies or possible future experimental work.

4.5 Conclusions

The results of this first MCB experiment (examining the first MCB implementation detail case study), show that the effectiveness of MCB depends on the timing of MCB implementation during the diurnal cycle. The results additionally reaffirm that MCB effectiveness is sensitive to the base case cloud regime, with the albedo increases associated with the precipitating regime being distinctly larger than those associated with the non-precipitating regime. For the more efficacious precipitating regime, the optimal timing for MCB aerosol emission was the early morning. At this time, the emission of MCB aerosols led to a large second indirect aerosol effect and coincident cloud regime change to the more persistent non-precipitating state. Such cloud regime changes did not occur when the MCB aerosols were instead emitted into the cloud-free early afternoon. In the absence of cloud albedo enhancements, and in spite of compensating direct aerosol effect albedo increases, MCB was hence less effective when implemented at this time.

One benefit of identifying this optimal timing of MCB implementation will be in the design of efficient MCB operational strategies. In addition to this practical benefit, these results also demonstrate that incorporating this diurnally varying MCB efficacy will be essential for improving the realism of model-derived MCB effectiveness estimates. For example, MCB effectiveness may be overestimated in studies where this feature is omitted. Likewise, owing to the challenges of realistically parameterising the MSc diurnal cycle in global-scale models, increasingly realistic MCB effectiveness estimates may be informed by accounting for the model's veracity in representing such temporal sensitivities. Further simulations in the future, covering a broader range of cloud and atmospheric conditions would be useful in exploring this phenomenon.

Chapter 5
The Inclusion of Water with Emitted Aerosols

5.1 Introduction

As described in Chapter 1, MCB aerosols could be produced by evaporating sea water droplets generated by specifically designed sea-going vessels (Salter et al., 2008). With the design of the production mechanism yet to be finalised (Salter et al., 2008; Latham et al., 2012a; Neukermans et al., 2014), it is possible that such evaporation would not occur until the sea water droplets had left the generating mechanism and entered the marine boundary layer. This evaporation of sea water droplets could lead to latent heat fluxes large enough to change the buoyancy and dynamics of the boundary layer, thus affecting the transport of the MCB aerosols to the cloud layer. However, all previous MCB simulations neglect this potential real-world formation mechanism, and assume that the MCB aerosols are in equilibrium with the background relative humidity upon emission.

This chapter, in examining the second MCB implementation detail case study, utilises the cloud-resolving model described and used in Chapters 3 and 4 to examine how representing the emitted MCB aerosols as sea water droplets ultimately affects estimates of MCB effectiveness. This chapter begins by explaining the methodology used (Section 5.2) before pertinent features of the simulations are presented (Section 5.3). Section 5.4 then discusses these outputs, and conceptualises how the diurnally-varying significance of the sea water droplet MCB assumption can be related to changing patterns of boundary layer dynamics. This chapter concludes by describing the implications that these findings have both for future implementation mechanism design considerations and for MCB modelling.

5.2 Methodology

To examine the effects of representing the emission of MCB aerosols as water droplets, the WRF/Chem model was again used, as for Chapters 3 and 4 (and as described in Section 3.2). Two of the MSc base cases described in Chapter 3 (and utilised in Chapter 4) were considered here: the non-precipitating NP-Pa case and the precipitating PR case.

As in Chapter 4, model aerosol emissions simulated the sea-going emission vessel, travelling the length of the domain once, at a speed of $5 ms^{-1}$, starting and ending at the centre of the domain. Owing to the unnaturally high local aerosol emission causing failure of the SW radiation scheme, and ultimately model failure (see Section 4.2), a reduced sea water

emission rate of 7.5 kg s^{-1} was used (i.e. 0.25xSA). Aerosols within the model are either unactivated interstitial aerosols, or activated in the cloud phase. The simulated emission of dry aerosol particles (hereinafter denoted as DRY) used Na and Cl mass fluxes of 1109 and 1710 µg $m^{-2}s^{-1}$, respectively (corresponding to the 7.5 kg s^{-1} sea water emission rate with assumed salinity of 35 g of sea salt per litre of sea water), with a number flux of $0.31x10^{12}$ m^{-2} s^{-1}. These aerosols, simulating a dry diameter of 200 nm, were emitted into the interstitial aerosol bin size 3 (dry diameter range of 156–313 nm). It is noted that this DRY emission technique is that used for the MCB simulations in Chapter 4.

The simulation of the emission of sea water droplets (hereinafter denoted as WET), utilized the model cloud phase, and thus included microphysical processes (for example, evaporation and coalescence). Aerosols were introduced into the cloud phase with mass and number fluxes as in the DRY case. Water was introduced into the cloud phase with a mass flux of 7.5 kg s^{-1} and number concentration equal to that of the aerosols, simulating sea water droplets of 800 nm diameter (as suggested by Salter et al. (2008)).

As in Chapter 4, post-emission analysis was again restricted to 5 hours subsequent to emission in order to avoid the effects of aerosol interference at the periodic boundaries.

On the basis of the hypothesis that the evaporative cooling of the sea water droplets (and resulting negative buoyancy) affects the aerosol plume height achieved, an additional set of experiments was carried out. DRY aerosols were emitted for 1 minute into the centre lowermost grid cell of the NP-Pa regime at 03:00:00 LT coincident with an applied temperature perturbation ranging from -0.1 to -2K. Thus the effects of a temperature perturbation were isolated from the effects of increases in specific humidity. The subsequent plume heights were then analysed. These temperature perturbations are approximately equivalent to the cooling associated with sea water emission rates of 2 to 45 kg s^{-1} assuming evaporation within one grid cell (between 0.07 and 1.5 times the emission rate proposed by Salter et al. (2008)). Descriptions of these three simulation sets are summarised in Table 5.1.

Table 5.1 *– Summary descriptions of the three simulation sets used in Chapter 5.*

Experiment	Description
DRY	MCB simulated as the emission of aerosol particles (as in Chapter 4)
WET	MCB simulated as the emission of sea water droplets
DRY with applied temperature perturbation	DRY aerosol particles emitted in the presence of an applied negative temperature perturbation (representing the effects on temperature of the evaporative cooling of droplets, in isolation from any changes in specific humidity)

5.3 Results

The WET simulations did not produce any additional precipitation or wet deposition of aerosols, with emitted water droplets evaporating within one 2 second model time step in all cases. This water droplet evaporation resulted in a cooling and moistening of the lowest model layer, in grid cells local to the emissions. Potential temperatures decreased by roughly 0.3 K in all WET simulations. A maximum moisture increase of 0.1 g $kg_{dry\ air}^{-1}$ occurred for the emission of aerosols at 03:00:00 LT into the PR and NP-Pa regimes (increasing background levels by ~1%). As a result, cold pools – regions of negative buoyancy in excess of -0.005 ms^{-2} (Tompkins, 2001; Devine, 2007) – and associated flow patterns were formed along the emission path (Figure 5.1). These cold pools were short-lived, dissipating within 1.5 hours of the WET aerosol emission (Figure 5.1, left-hand column). In contrast, the DRY aerosol emissions produced no temperature, moisture or buoyancy changes and as such, the WET simulation aerosols remained lower in the boundary layer (Figure 5.2).

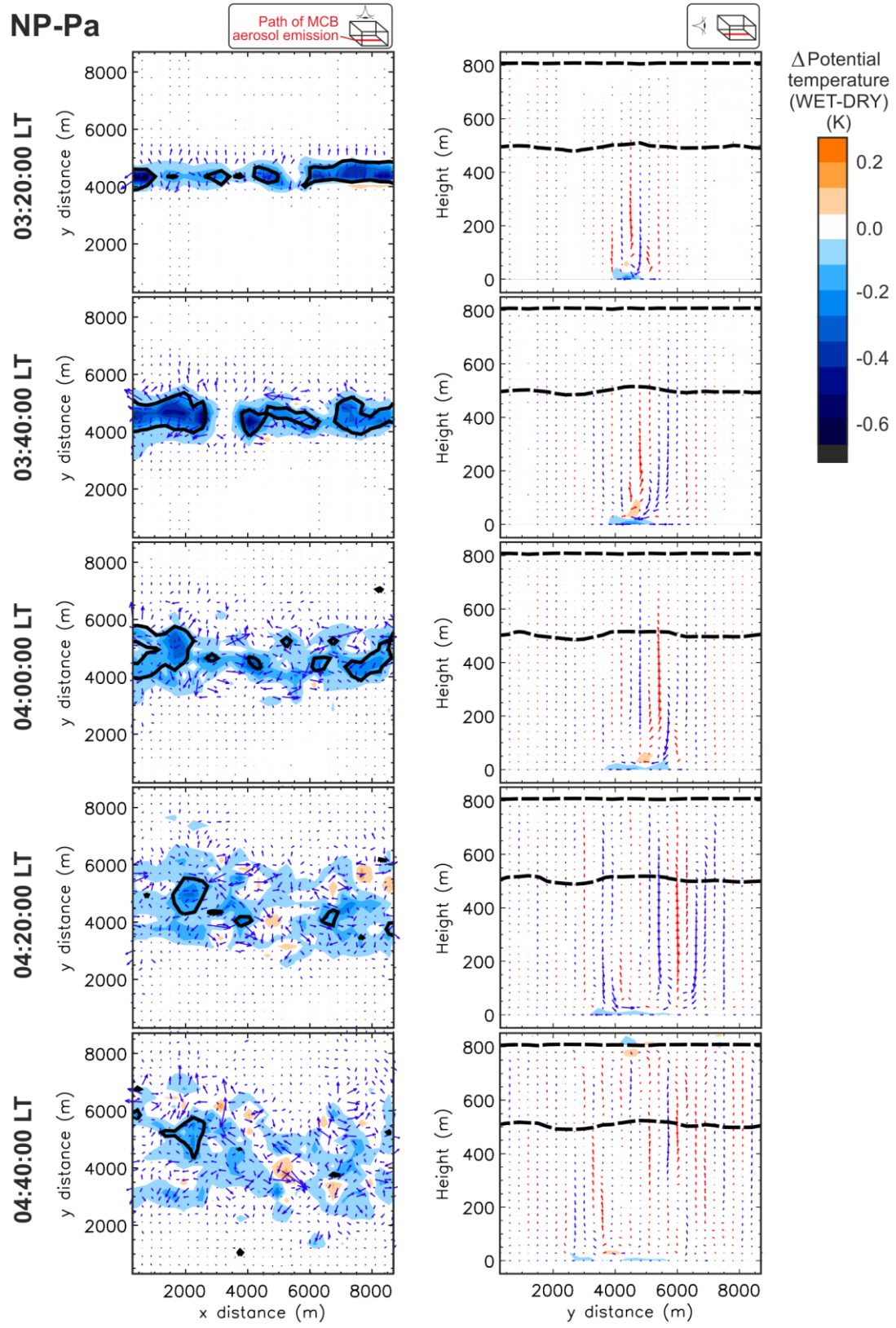

Figure 5.1 *– Left column: Colour-filled contours show the difference in surface potential temperature (WET minus DRY) for aerosol emission into the NP-Pa regime at 03:00:00 LT. Arrows show differences in surface flow patterns. Thick black contours outline cold pools (buoyancies in excess of -0.005 ms^{-2}); Right column: Mean (averaged over the x-direction) of difference in potential temperature (WET minus DRY) for aerosol emissions into NP-Pa regime at 03:00:00 LT. Arrows show differences in mean flow patterns (red=updrafts, blue=downdrafts). Black dashed lines show mean cloud outline. Continued overpage.*

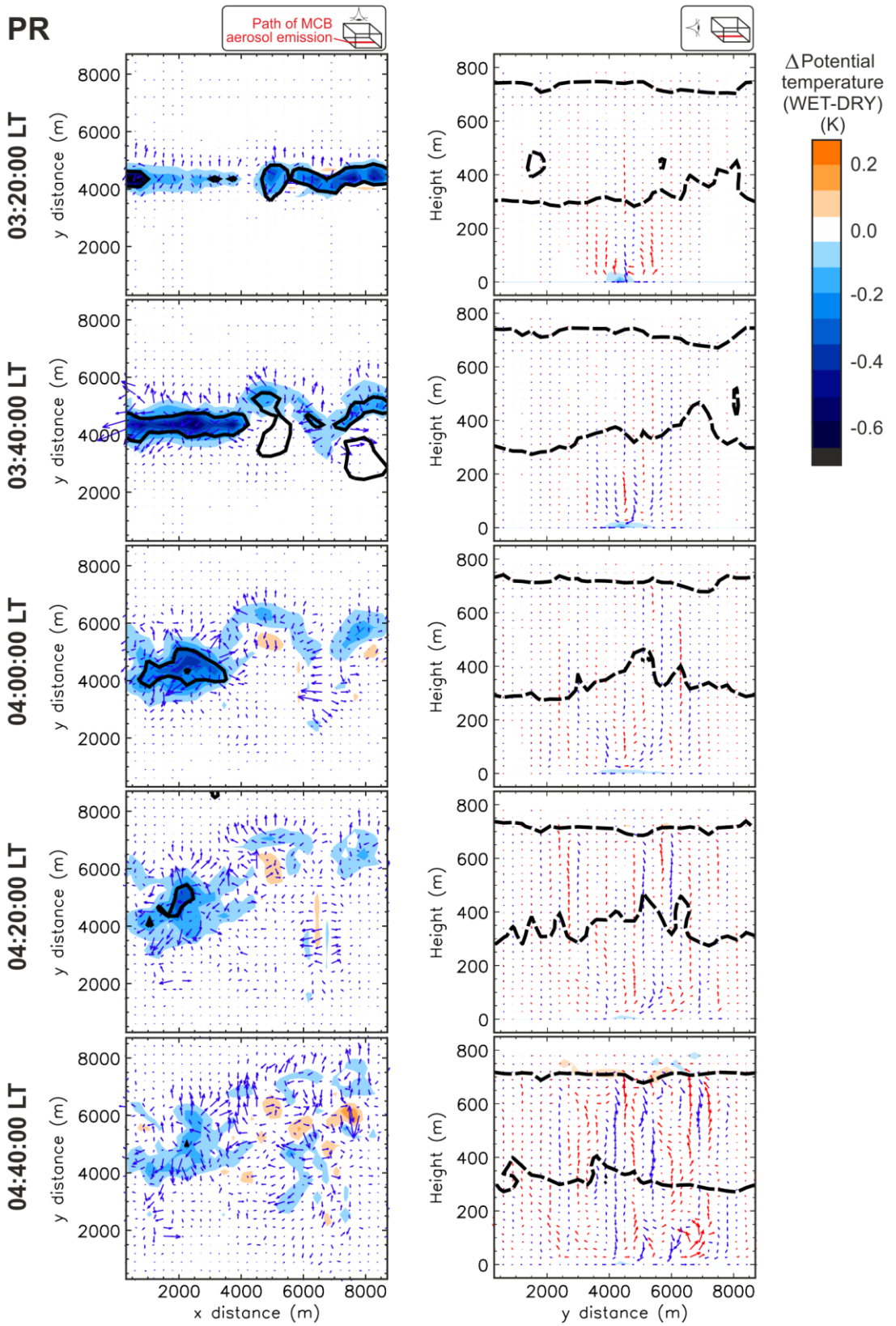

Figure 5.1 continued *– Left column: As previous left column, but for PR regime for emissions at 03:00:00 LT; Right column: As previous right column but for PR regime for emissions at 03:00:00 LT.*

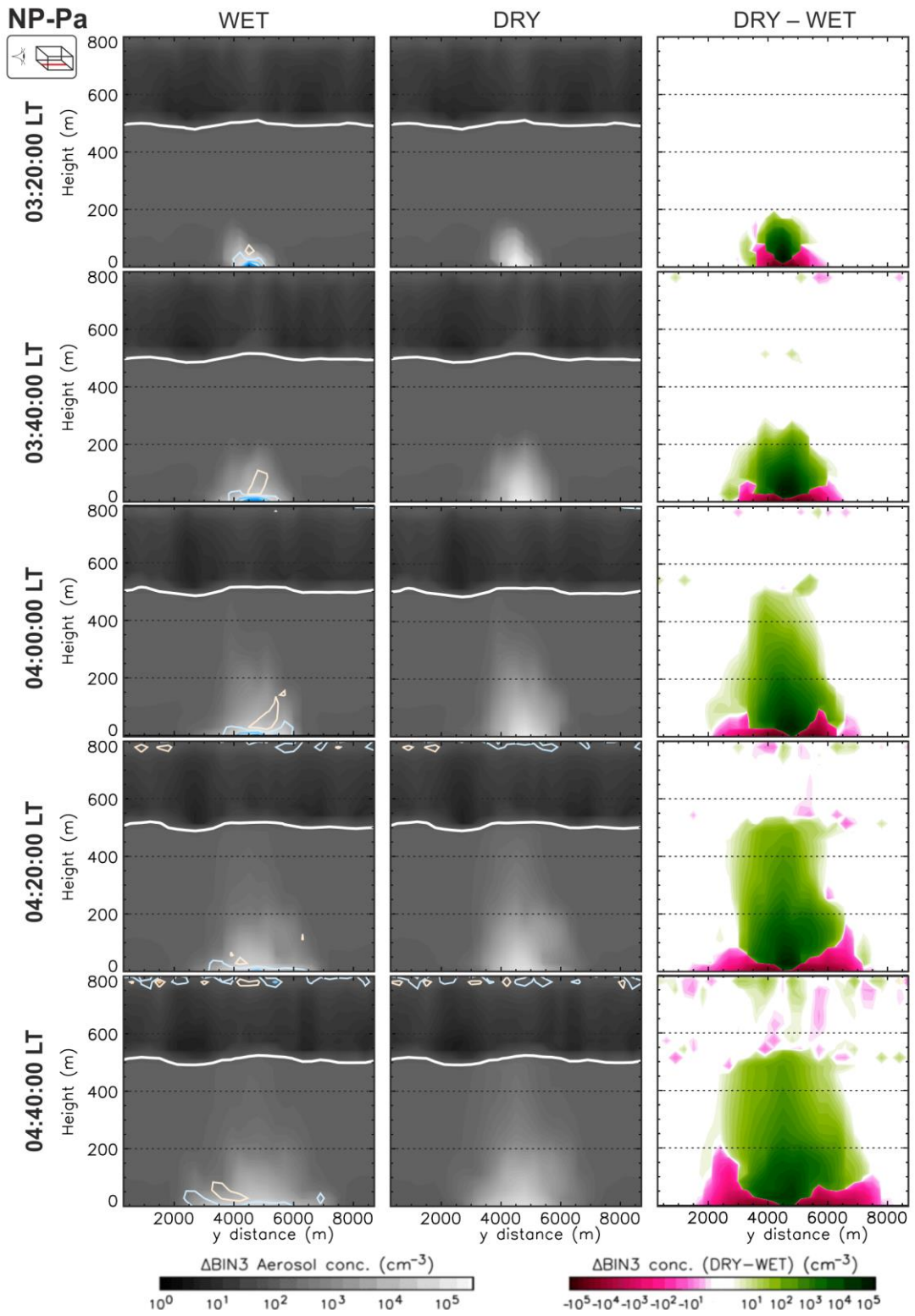

Figure 5.2 *– For NP-Pa base case. Progression through time for emissions at 03:00:00 LT. Left column (WET case): emitted aerosol (bin 3) concentration (grey scale filled contours), difference in potential temperature (WET minus NO EMISSION control case) (coloured contour lines with scale as in Figure 5.1), and cloud top and base (thick white outline). All outputs are averaged over the x-direction; Middle column (DRY case): as left column but for the DRY case; Right column (DRY minus WET): Difference in emitted aerosol (bin 3) concentrations (DRY minus WET). Continued overpage.*

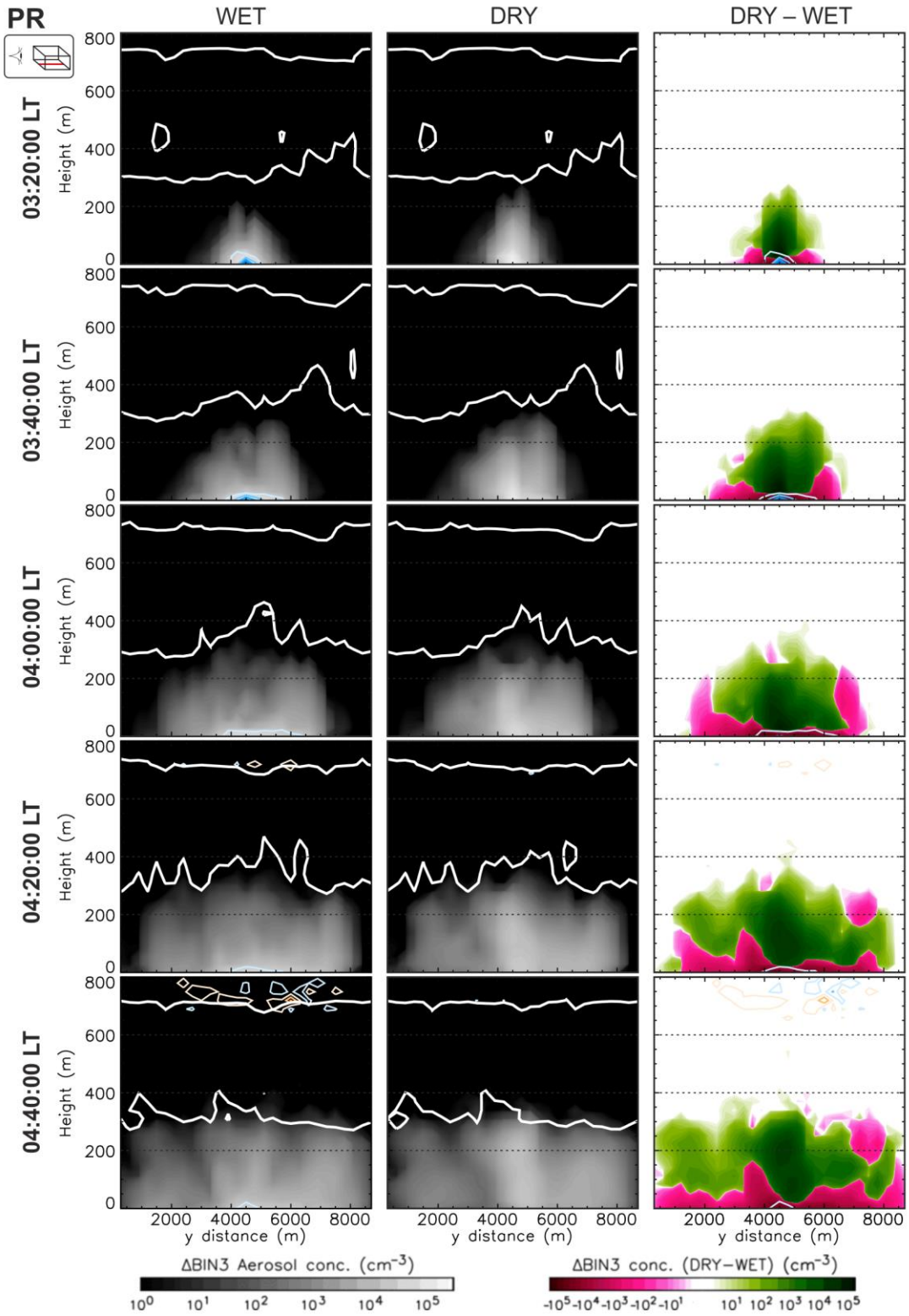

Figure 5.2 continued *– As previously, but for the PR regime.*

The aerosol plumes in the WET simulations were suppressed to between 70 and 78% of the heights reached by the DRY aerosol plumes in the first hour after emission (height reductions of between 33.2 and 46.0 m; Figure 5.3 a). The set of DRY experiments initialized with the applied temperature perturbations similarly show suppression of the aerosol plume height (Figure 5.3 b).

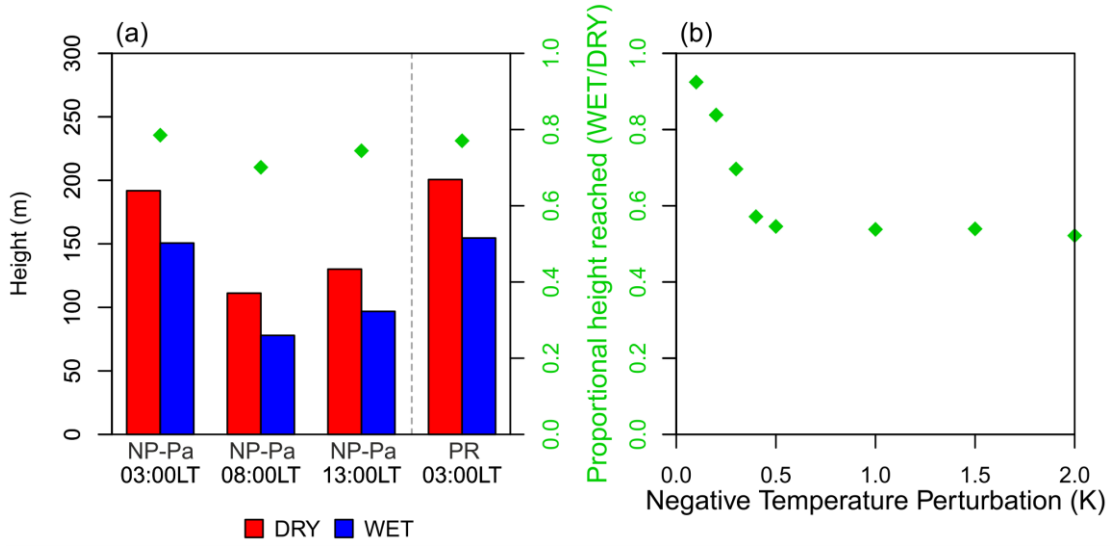

Figure 5.3 *– Initial aerosol plume heights: (a) height achieved by DRY and WET aerosol plumes averaged over the first hour after emission (bars). Also shown as a proportional height, i.e. WET plume height/DRY plume height (green diamonds). Heights are taken as the 100 cm^{-3} isoline of the emitted aerosol size bin (bin 3); (b) proportional heights reached by DRY aerosol emissions under applied initial negative temperature perturbations (20 minutes after emission with heights taken as the 50 cm^{-3} isoline of bin 3 aerosols).*

The proportional plume height associated with a temperature perturbation similar to those in the WET simulations (i.e. about 0.3 K) was 72%, fitting well with the plume height suppressions seen in the WET simulations themselves. This supports the idea that it is the temperature decreases resulting from evaporative cooling of the sea water droplets that affects the aerosol plume height achieved, rather than changes to the moisture profile resulting from the addition of water. It is noted that the plateauing of the proportional heights reached in the applied temperature perturbation simulations (Figure 5.3 b) may result from physical limits of the horizontal spreading of the plume. Future work could also examine the sensitivity of the magnitude of this asymptote to the vertical grid cell resolution, although such extension is unlikely to yield significant further insight.

Although the cold pools were short-lived, the height suppression of the WET simulation aerosols continued for the duration of the simulations (Figure 5.2, right-hand columns). As such, the number of emitted aerosols reaching the cloud base was smaller in all WET cases compared with DRY. This difference was dependent on regime and emission time (Figure 5.4 a to d).

Considering first the NP-Pa regime. For emission at 03:00:00 LT, the number of aerosols reaching the cloud base was consistently halved for the WET compared with DRY emissions (reaching domain averages of 62 and 125 cm^{-3} respectively by the end of the simulations; Figure 5.4 a). For emissions at 08:00:00 LT into the increasingly uncoupled boundary layer, the number of aerosols reaching cloud base was small for both WET and DRY emissions (fewer than 10 cm^{-3} averaged over the domain; Figure 5.4 b). While aerosols emitted at 03:00:00 LT began to reach the cloud base after 1 hour (Figure 5.4 a), DRY aerosols emitted at 13:00:00 LT took around 2 hours to begin to reach the cloud base (Figure 5.4 c). WET aerosols emitted at 13:00:00 LT, took approximately 3 hours to begin to reach the cloud base (Figure 5.4 c). By the end of the 13:00:00 LT simulations, the increase in aerosol number concentration of bin 3 aerosols (the emitted aerosol size) just below the cloud base was ~170 cm^{-3} for the DRY and ~50 cm^{-3} for WET emissions. In terms of calculated cloud albedo increases (Figure 5.4 e to h), emissions at 13:00:00 LT into the NP-Pa cloud showed most sensitivity to the WET/DRY aerosol assumption. Here, the average calculated cloud albedo over the 5 hour simulation increased by 0.014 (4.3%) for the DRY emission but by only 0.005 (1.4%) in response to the WET emission (Figure 5.4 g). Including water in the simulated aerosol emission therefore lessened the calculated cloud albedo increase by 67%. For emission at 03:00:00 LT, the calculated cloud albedo increased by 0.018 (2.9%) for the DRY emission and by 0.012 (1.9%) for the WET emission (Figure 5.4 e). For emission at 08:00:00 LT into the increasingly uncoupled boundary layer, the calculated cloud albedo increases were 0.002 (0.6%) for the DRY emission and 0.001 (0.3%) for the WET (Figure 5.4 f). For emission at 03:00:00 LT into the PR regime, the average increase in calculated cloud albedo was 0.160 (94.1%) for the DRY emission and 0.148 (88.5%) for the WET (Figure 5.4 h). So, whilst including water in the simulated aerosol emission lessens the calculated cloud albedo increase by only 7.5%, this equates to an absolute difference in calculated cloud albedo increase of 0.012. This is larger than the 0.009 difference in calculated cloud albedo increase for NP-Pa 13:00:00 LT emissions.

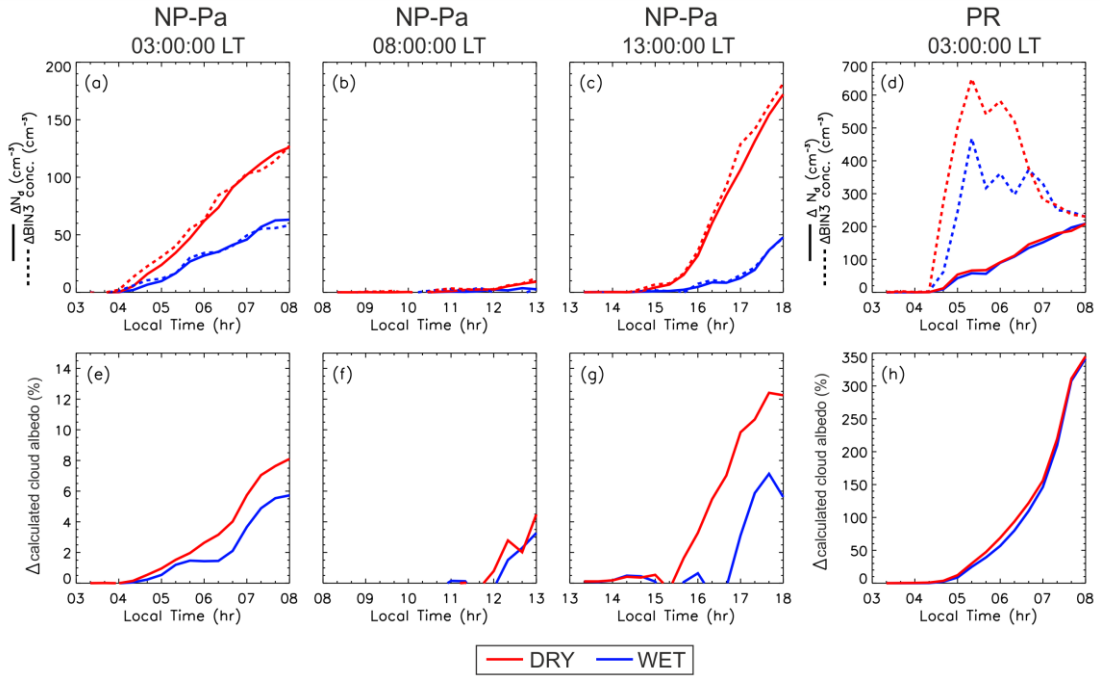

Figure 5.4 *– (a) Time series of the increase in domain average emitted aerosol concentration in the layer below cloud base (ΔBIN3 conc; cm^{-3}; dotted line) and the increase in domain average N_d (ΔN_d; cm^{-3}; solid line) for the NP-Pa regime with aerosol emission at 03:00:00 LT; (b) as '(a)' but for aerosol emission at 08:00:00 LT; (c) as '(a)' but for aerosol emission at 13:00:00 LT; (d) as '(a)' but for the PR regime with aerosol emission at 03:00:00 LT; (e) time series of the domain average calculated cloud albedo increase for the NP-Pa regime with aerosol emission at 03:00:00 LT; (f) as '(e)' but for aerosol emission at 08:00:00 LT; (g) as '(e)' but for aerosol emission at 13:00:00 LT; (h) as '(e)' but for the PR regime with aerosol emission at 03:00:00 LT.*

5.4 Discussion

The speed at which droplets evaporate within these simulations is consistent with calculations for similarly sized droplets (Lewis and Schwartz, 2004). The absence of sufficient water droplet coalescence to cause the loss of aerosols through wet deposition may however be a consequence of the initial dispersal of the emitted droplets within the grid cell; lack of sensitivity of the microphysics scheme to turbulence; and the way in which the emission is represented in this simulation (i.e. no upward velocity). Whilst model grid cell spacings of hundreds of metres are able to resolve cloud processes (Wang and Feingold, 2009a), they are too coarse to capture the detailed emission processes occurring from a proposed rotor diameter of 2.4 m (Salter et al., 2008). Further investigation of these processes are carried out in Chapters 6 and 7. The initial suppression of WET aerosol plume heights was fairly uniform across all regimes and emission times (Figure 5.3 a). The analysis suggests that subsequent differences in the plume heights, N_d and cloud albedo response for the NP-Pa regime are related to the turbulent structure of the boundary layer through the diurnal cycle, and are hence dependent on time of emissions. This is represented schematically in Figure 5.5.

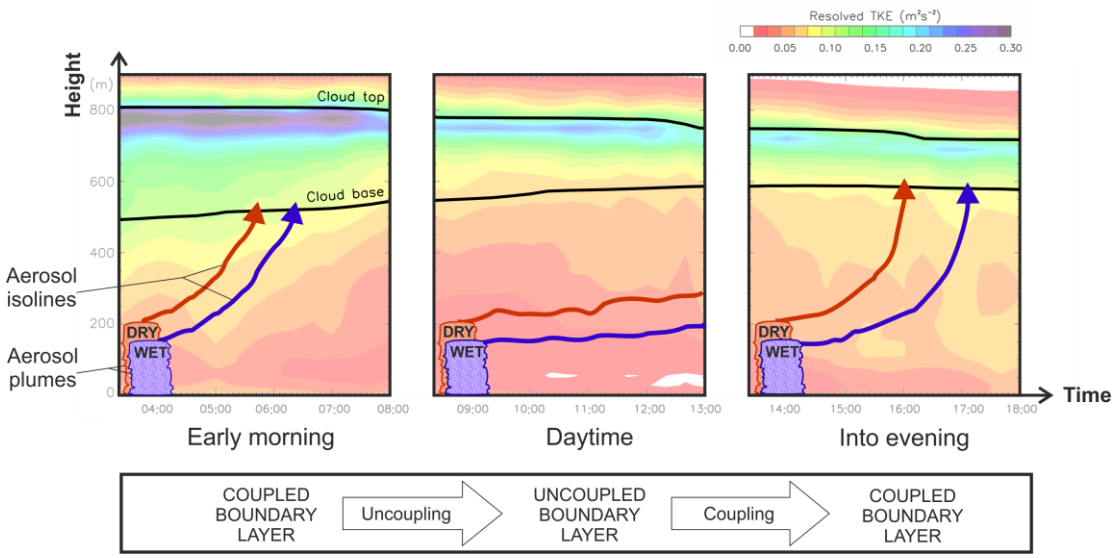

Figure 5.5 *– Schematic showing proposed relationship between initial WET and DRY aerosol plumes, subsequent transport of aerosols (represented by aerosol isolines) and turbulence within the MSc topped boundary layer over time (coloured contour transparencies showing the domain average resolved TKE for the NP-Pa case).*

The turbulent structure of the system is illustrated by the TKE (Figure 5.5). Whilst turbulence is maintained throughout the boundary layer, its distribution varies over the diurnal cycle (as discussed in Chapter 2). Early in the morning, turbulence that originates from cloud-top LW radiative cooling penetrates deep into the boundary layer, meeting turbulent mixing in the layer near the surface that results from surface fluxes and wind shear. In this coupled state, aerosols are able to be drawn up to the cloud. It is proposed that as the WET aerosol plume height is suppressed compared with the DRY case, more aerosols stay closer to the surface, and thus fewer are drawn to the cloud base, resulting in smaller cloud albedo increases (cf. Figure 5.4 a and e). Into the day, as solar heating offsets the cloud-top originating production of turbulence, the depth of cloud-originating TKE penetration decreases, and the boundary layer becomes uncoupled. Thus, for MCB emissions at 08:00:00 LT, whilst mixing of the aerosol plumes still occurs close to the surface, the lack of coupling inhibits transport of the aerosols up to the cloud region, and hence little cloud albedo change occurs (cf. Figure 5.4 b and f). Into the evening, solar heating of the cloud diminishes and the strength of turbulent production at the cloud top increases. Whilst the cloud and boundary layers remain poorly coupled at the time of 13:00:00 LT aerosol emission, after approximately 2 hours, the cloud-top originating turbulence has penetrated deep enough into the boundary layer to coincide with the mixed region of DRY aerosols, thus transporting them up to the cloud layer. Owing to the suppression in plume height characteristic to the WET aerosol assumption, aerosols are not drawn up into the cloud layer until TKE has deepened into the boundary layer and recoupling of the cloud and boundary layers has occurred. This occurs approximately 1 hour later than for the DRY assumption (cf. Figure 5.4 c and g). Previous large-eddy simulation

modelling has similarly suggested that transport of ship effluents to the cloud layer may be inhibited by boundary layer decoupling (Liu et al., 2000).

As the magnitude of cloud albedo perturbation is dependent on aerosol height, it is also sensitive to the aerosol emission height assumption. For emission into the second model layer from bottom for the NP-Pa regime, the maximum difference in mean cloud albedo perturbation between the WET and DRY simulations increases to 0.011 (from 0.009 for emission into the bottom layer).

Whilst these simulations provide estimates of the sensitivity to the WET/DRY assumption for both NP-Pa and PR cloud regimes, it is again acknowledged that these simulations represent only a small subset of potential conditions encountered in MSc cloud regions. For example, the low cloud base in the PR regime allowed a sufficient number of aerosols to reach the cloud base to instigate a strong second indirect aerosol effect in both WET and DRY cases. This resulted in a relatively small percentage difference in cloud albedo increase. The sensitivity to the WET/DRY assumption may increase for PR clouds with higher cloud bases as the vertical gradient of emitted aerosols becomes more important. Future experiments, exploring the sensitivity of aerosol transport to the cloud under a range of atmospheric conditions including moisture and temperature profiles, large-scale divergence rates, wind speeds and inversion heights would be of interest. The relative humidity of the boundary layer will also affect the rate of evaporation of emitted droplets, affecting temperature perturbations and resulting plume suppression. Furthermore, conditions may exist where the near-surface boundary layer relative humidity is close to saturation, while the emitted droplets contain a lower fraction of water. Under such conditions, it may be possible that the boundary layer could then condense onto the emitted MCB droplets, instead causing them to grow. While such high relative humidity near-surface conditions are not considered to be widespread in regions of potentially target marine stratocumulus clouds, future work could investigate the ramifications of such conditions.

Finally, these simulations use emission rates equivalent to one quarter of those suggested by Salter et al. (2008). The DRY experiments initialized with forced temperature perturbations suggest that the greater evaporative cooling associated with increased sea water emission rates may lead to the aerosol plume heights being suppressed by up to 46% (Figure 5.3 b). This larger disparity between initial aerosol emission plume heights may lead to more significant sensitivities across many of the cases (although the daytime emissions would likely remain relatively insensitive).

5.5 Conclusions

The results of this second MCB experiment (in examining the second MCB implementation detail case study), expose an important mechanism that affects the efficiency of aerosol transport to the cloud layer, associated with emitting MCB aerosols as sea water droplets.

This mechanism results from the rapid evaporation of the emitted MCB sea water droplets, producing a cooling local to the emission path. The resulting negative buoyancy alters the dynamics of the marine boundary layer, reducing the initial height of the MCB aerosol plume by nearly a third. This impedes the subsequent transport of MCB aerosols to the cloud layer, and produces smaller cloud albedo increases.

The magnitude of this effect depended both on background cloud conditions and timing through the diurnal cycle, with the largest percentage reductions in cloud brightening occurring in the simulations when the MCB sea water droplets were emitted into the non-precipitating cloud regime in the afternoon. The time dependency was a consequence of the dependence of MCB aerosol transport on the vertical extent of turbulent mixing through the marine boundary layer. The effect was exacerbated in the afternoon because the descending turbulence originating from the cloud-top reached the stunted aerosol plume – associated with ('WET') MCB sea water droplet emission – later than it reached the taller aerosol plume associated with ('DRY') MCB aerosol emission. The lower sensitivity of the precipitating cloud regime is suggested to result from the CCN-limited conditions allowing even lower numbers of MCB aerosols to substantially increase the cloud albedo. Additionally, with the base of the precipitating clouds being over 100 m lower than in the non-precipitating case, delays in the transport of aerosols to the cloud layer over these shorter distance became less critical.

The identification of this mechanism is of practical interest, and could inform the design of both future physical experiments, and eventual implementation strategies. However, because the impact on cloud albedo perturbations is modest, taking account of this mechanism would likely not vastly improve the realism of global-scale MCB effectiveness estimates.

Chapter 6
Processes within the Emission Rotor

6.1 Introduction

The final MCB implementation detail case study considers the effect that processes within the emission rotor and emission plume have on the number concentration and size distribution of emitted MCB aerosols, and the effect that these changes have on the resulting albedo perturbations.

Consideration of the coagulation process – where aerosols (or coalescing droplets) join together to produce fewer, but larger aerosols (or droplets) – is critical for the rotor and plume regions. This is because these regions have high aerosol concentrations and because coagulation rates increase with the square of particle concentration (Smoluchowski, 1916). The effect of the coagulation process on the emitted MCB aerosols is important for the overall effectiveness of MCB as the coagulation process results in both larger aerosols, and a reduced number concentration. Results in Chapters 4 and 5 showed that reducing the number of MCB aerosols reaching the cloud layer reduced the achievable cloud brightening. Additionally, previous MCB research has similarly shown that lower MCB aerosol number concentrations are associated with smaller cloud albedo increases (Chapter 4; Bower et al., 2006; Latham et al., 2008; Korhonen et al., 2010b; Latham et al., 2012a; Partanen et al., 2012; Pringle et al., 2012; Alterskjær and Kristjánsson, 2013), while larger MCB aerosols have been shown to be a possible mechanism for reducing cloud albedo via the competition effect (Bower et al., 2006; Korhonen et al., 2010b; Latham et al., 2012a; Pringle et al., 2012; Alterskjær and Kristjánsson, 2013). By uniformly distributing the MCB aerosols across the coarse grid cells, previous global-scale modelling omit these areas of locally high aerosol concentrations, and hence cannot capture the realistic effects of coagulation.

The research performed to examine this final MCB implementation detail case study is presented in three chapters (Figure 6.1). This chapter uses a simple numerical integration to estimate the effects of droplet coalescence within the rotor. Chapter 7, for the first time, uses a large-eddy simulation to capture details of the plume structure and dynamics, quantifying the effects of aerosol coagulation within the MCB aerosol emission plume. Chapter 7 includes several sensitivity experiments, one of which utilises the in-rotor estimates of aerosol change in size and number concentration derived in this chapter. Chapter 8 then utilises the findings of the plume simulations to evaluate how the changes to the MCB aerosols ultimately affect the effectiveness of MCB.

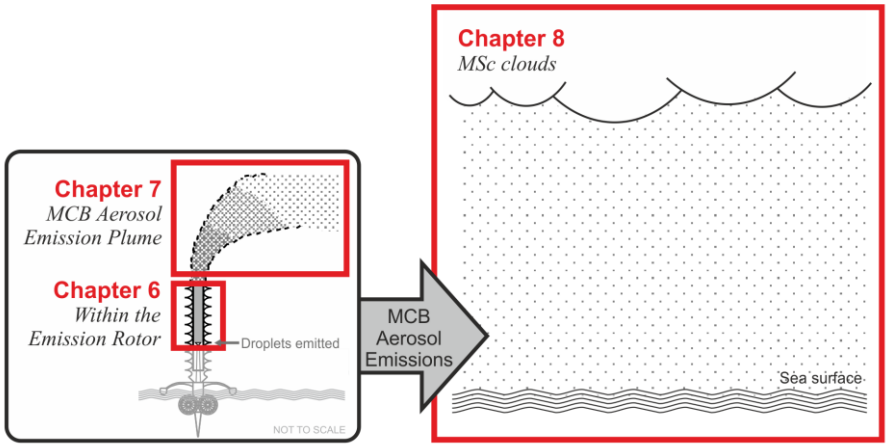

Figure 6.1 *– Schematic showing regions considered in investigating the effects of aerosol coagulation on MCB effectiveness (MCB emission vessel cross-section modified from Salter et al. (2008)).*

This chapter focuses on the rotor section, with the proposed technology designs (Salter et al., 2008) suggesting that the MCB aerosols would be formed as sea water droplets near to the base of the rotor, which is approximately 20 m in length and 2.4 m in diameter (Figure 6.2). These droplets would be blown through the rotor by a 12 ms^{-1} air flow, whereby evaporation of the droplets may also occur. The processes that occur for droplets in turbulent pipe flow include complex fluid flow, droplet dynamics and droplet-wall interactions (Friedlander, 2000). The coalescence of these droplets potentially reduces the droplet number concentration, increases the size of droplets, but conserves the mass if losses to the wall are neglected (discussed below) (Figure 6.2). In this chapter, a first order estimate of the effects of these processes on monodisperse water droplets as they travel through the rotor (Figure 6.2) is calculated. This estimate is obtained by using a simple numerical integration turbulent coagulation scheme, with the outputs being used to inform one of the sensitivity experiments for the MCB aerosol emission plume, presented in Chapter 7.

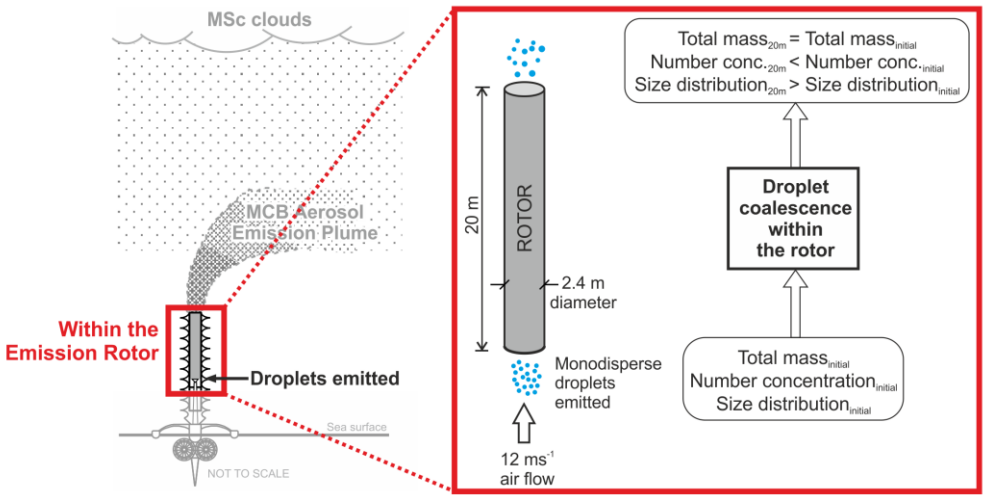

Figure 6.2 *– Schematic overview of the region of interest for the estimation of coalescence within the rotor.*

6.2 Methodology

The numerical integration scheme used is based on the work of Saffman and Turner (1956) which describes the fundamental principles of turbulent coagulation (e.g. Friedlander, 2000). The simplicity of the selected scheme allows estimates of the changes in number concentration and droplet size to be made efficiently without the use of complex computational modelling. This coagulation scheme estimates the collision rate (N) of droplets to be dependent upon characteristics of the droplets (radii (r_1, r_2) and number concentration (n_1, n_2)), and flow characteristics (rate of turbulent energy dissipation (ε) and kinematic viscosity (υ)) according to Equation 6.1.

$$N = 1.30(r_1 + r_2)^3 \, n_1 n_2 \, (\varepsilon/\upsilon)^{0.5} \qquad \textbf{(6.1)}$$

The collision of droplets during coalescence leads to the growth of droplets, and the depletion of droplet number concentrations. This process can be approximated by Equations 6.2, where n_i is the droplet number concentration with the subscript *i* representing multiples of the initial droplet mass, and time denoted as t. All droplets are input into n_1 at initialisation. Thus, a droplet in n_2 could be formed from the coalescence of two droplets from n_1, and likewise, a droplet in n_3 could be formed from the coalescence of either three droplets from n_1, or from the coalescence of one droplet from n_1 and one droplet from n_2.

$$\left.\begin{aligned}
\frac{dn_1}{dt} &= 1.30(\varepsilon/\upsilon)^{0.5}\left[-(2r_1)^3 n_1^{\,2} - (r_1+r_2)^3 n_1 n_2 - (r_1+r_3)^3 n_1 n_3 - \ldots\right] \\
\frac{dn_2}{dt} &= 1.30(\varepsilon/\upsilon)^{0.5}\left[0.5(2r_1)^3 n_1^{\,2} - (r_1+r_2)^3 n_1 n_2 - (2r_2)^3 n_2^{\,2} - (r_2+r_3)^3 n_2 n_3 - \ldots\right] \\
\frac{dn_3}{dt} &= 1.30(\varepsilon/\upsilon)^{0.5}\left[(r_1+r_2)^3 n_1 n_2 - (r_1+r_3)^3 n_1 n_3 - (r_2+r_3)^3 n_2 n_3 - (2r_3)^3 n_3^{\,2} - \ldots\right] \\
\frac{dn_4}{dt} &= 1.30(\varepsilon/\upsilon)^{0.5}\left[(r_1+r_3)^3 n_1 n_3 + 0.5(2r_2)^3 n_2^{\,2} - (r_1+r_4)^3 n_1 n_4 - (r_2+r_4)^3 n_2 n_4 - \ldots\right]
\end{aligned}\right\} \textbf{(6.2)}$$

To estimate the changes in number concentration and size distribution of the droplets along the length of the rotor resulting from coalescence, Equations 6.2 were extended to n_{32} and integrated numerically with respect to time, using a time step of $1\text{x}10^{-3}$ seconds. The base droplet number concentration (n_1) was initialised with a number concentration of $2.061\text{x}10^{15}$ droplets per m^3, equivalent to a 30 kg s^{-1} flux of water comprising 800 nm diameter water droplets (equivalent to a dry diameter of 200 nm), travelling through a 2.4 m diameter rotor at a velocity of 12 ms^{-1}. The length of the rotor is assumed to be 20 m (Salter et al., 2008).

The use of this scheme is suitable for this situation because of the high (~$1.9\text{x}10^6$) Reynolds Number associated with the flow through the rotor (described by the standard Equation A.1,

included for completeness in Appendix A, for a flow velocity of 12 ms^{-2}, through a rotor of diameter 2.4 m with kinematic viscosity of air of ~$1.5x10^{-5}$ m^2 s^{-1}). This exceeds the 4000 threshold needed for turbulent flow behaviour.

This situation also fulfils the requirement for the droplet number concentration to be sufficiently high that the distance between the particles (λ_p = $7.9x10^{-6}$ m as defined by Equation 6.3; Friedlander (2000)) is less than the characteristic Kolmogorov microscale (λ_k = $2.1x10^{-4}$ m as defined by Equation 6.4; Friedlander (2000)).

$$\lambda_p = n^{-1/3} \qquad \textbf{(6.3)}$$

where:

λ_p = distance between particles (m)

n = particle concentration = $2.061x10^{15}$ droplets per m^3

$$\lambda_k = \left(\frac{\upsilon^3}{\varepsilon} \right)^{0.25} \qquad \textbf{(6.4)}$$

where:

υ = kinematic viscosity of air ~ $1.5x10^{-5}$ m^2s^{-1} at 20 °C

ε = rate of turbulent energy dissipation per unit mass (m^2s^{-3}) ~ $0.0025U^3/L$

U = velocity through the rotor = 12 ms^{-1}

L = length scale = diameter of the rotor = 2.4 m

The use of this simple numerical integration scheme also necessitates several assumptions.

Assumption 1: The first assumption is that no evaporation occurs through the rotor. Thus, the initially monodisperse droplets remain as droplets. If the droplets were to evaporate in the rotor, the size reduction may reduce the likelihood of collisions, thus reducing coalescence rates. Thus, the omission of evaporation may overestimate these coalescence rates.

Assumption 2: The second assumption omits interaction of droplets with the interior walls of the rotor. If droplets collides with the rotor wall, they may be deposited. However, as the non-slip condition at the wall causes the flow speed to fall to zero, for a droplet to reach the wall, it would require sufficient inertia to overcome this quiescence. This tends to occur for droplets diameters larger than 1 μm (Friedlander, 2000), and may be less significant for the smaller droplets considered in this case. Also, the 2.4 m diameter of the rotor provides a larger volume to surface area ratio than occurs for the millimetre or centimetre diameter pipes typically considered (Friedlander, 2000), again reducing the significance of rotor wall effects.

Assumption 3: Finally, this scheme does not include treatment of enhanced coalescence rates resulting from differences in relative droplet motion caused by the widening of the size distribution. Thus, this approach leads to an underestimation of the coalescence rates.

The potential implications of these assumptions are discussed in Section 6.4.

6.3 Results

Initial testing of the numerical integration scheme (against previously published results) showed that the method of execution formulated for this work performed successfully. As such, the numerical integration scheme was then applied as described in Section 6.2. Figure 6.3 shows how coalescence increases the number concentrations of larger droplets as they move through the rotor. At initialisation (at the base of the rotor), all droplets were in n_1.

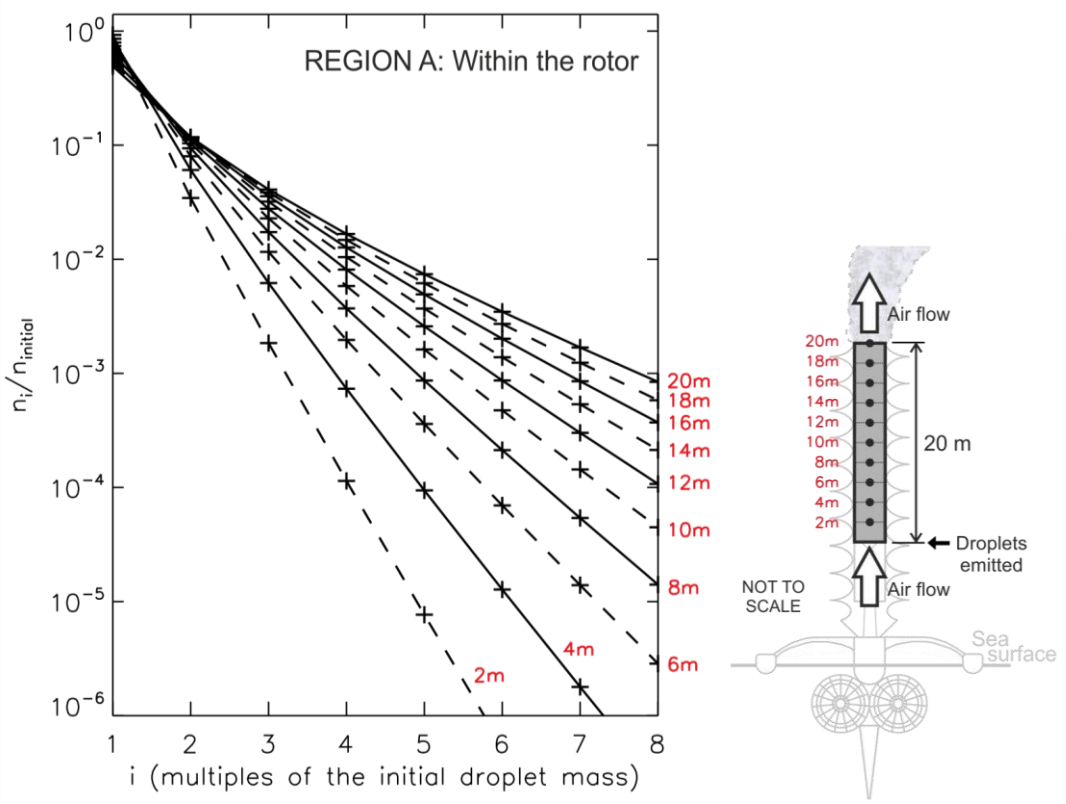

Figure 6.3 *– Calculated ratios of the number concentration (n_i) to the initial number concentration ($n_{initial}$) for droplets up to 8 times the mass of the initial droplets. Ratios are shown for various distances travelled through the rotor.*

These droplets were then sorted into the equivalent WRF/Chem dry aerosol size bins, with n_1, n_2 and n_3 remaining in the initial bin size 3 (equivalent dry diameters up to 312 nm), with n_4 to n_{30} entering bin size 4 (equivalent dry diameters up to 625 nm), with the remaining n_{31} and

n_{32} entering bin size 5 (dry diameters above 625 nm). The transition of droplets from the initial bin size 3 into the larger bin sizes is shown in Figure 6.4.

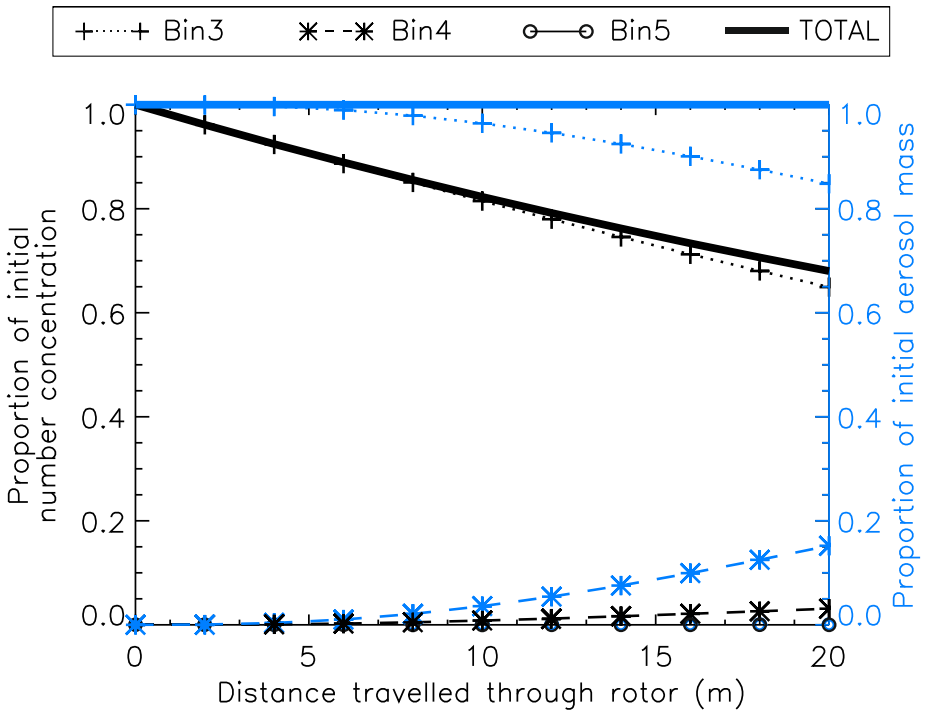

Figure 6.4 *– The transition of droplets from the initial bin size 3 into the larger bins 4 and 5 with distance travelled through the rotor. This transition is represented as a proportion of the initial number concentration and a proportion of the initial aerosol mass for each of the three bin sizes. Also shown is the evolution of the total number concentration and mass through the rotor.*

Thus, on leaving the rotor (after travelling 20 m), the total mass of aerosols is conserved, while the number concentration reduces by approximately 32%. The mass of aerosols in bin 3 has reduced to around 85% of the initial value, with around 15% of the initial mass now being in bin 4. A negligible number of droplets grew to enter bin 5 through the rotor (less than $1x10^{-7}$% of the initial mass). The number concentration of aerosols in bin 3 reduced to around 65% of the initial value. The number concentration of aerosols in the larger bin 4 was around 3% of the initial aerosol number concentration on leaving the rotor. Again, a negligible number of aerosols were present in bin 5.

6.4 Discussion and Conclusions

This chapter has described the novel use of a simple numerical integration scheme in estimating the amount of droplet coalescence that could occur through the MCB rotor. In so doing this contributes towards the examination of the final MCB implementation detail case study. The use of the turbulent coagulation assumption produced estimates of aerosol number concentration losses of approximately one third, while aerosol growth was largely restricted to the equivalent of the next model aerosol size bin.

The coalescence of droplets caused by turbulence is not fully understood, with estimates suggesting that the rate of coalescence estimated via this mechanism be considered approximate to a factor of 10, and likely overestimated (Friedlander, 2000). This could cause the resulting estimates of MCB aerosol number concentration reductions within the rotor to be overestimated. In addition to the fundamental uncertainties regarding turbulence in coalescence, the assumptions made here omit the increases in coalescence that occurs owing to the relative motion of droplets. This has been estimated to become important when the ratio of droplet radii becomes larger than 2. Considering Figure 6.3, approximately one in 1000 of the original aerosol number would be sufficiently large to meet this criteria by the end of the rotor. This suggests that the coalescence rates would be underestimated, particularly near the end of the rotor. Finally, the assumption that no evaporation occurs through the rotor may, as discussed in Section 6.2, lead to an overestimation of the coalescence rates. However, such phase changes may also induce temperature and dynamical changes through the rotor, the effects of which cannot be anticipated here owing to the complexity of such flow of aerosols.

Refinements to these coalescence estimates could be achieved through more complex, computationally expensive, computational fluid dynamics modelling for example. However, there are sufficient unknowns in the engineering design of the rotor and aerosol formation mechanism to suggest that more intricate rotor flow modelling at this stage would be imprudent.

These estimates of the effects of droplet coalescence through the rotor are used to inform one of the plume region sensitivity experiments (Section 7.4.1.4) in the latter part of next chapter.

Chapter 7
Detailed Representation of the MCB Aerosol Emission Plume

7.1 Introduction

Chapter 6 examined the effect that aerosol processes within the emission rotor could have on the number concentration and size distribution of MCB aerosols that would then be emitted as the plume.

This chapter examines the second part of this final case study, and examines the effects that aerosol processes (primarily coagulation) within the aerosol plume have on the number concentration and size distribution of MCB aerosols (Figure 7.1). The ultimate impact that these changes have on the potential effectiveness of MCB are considered in Chapter 8.

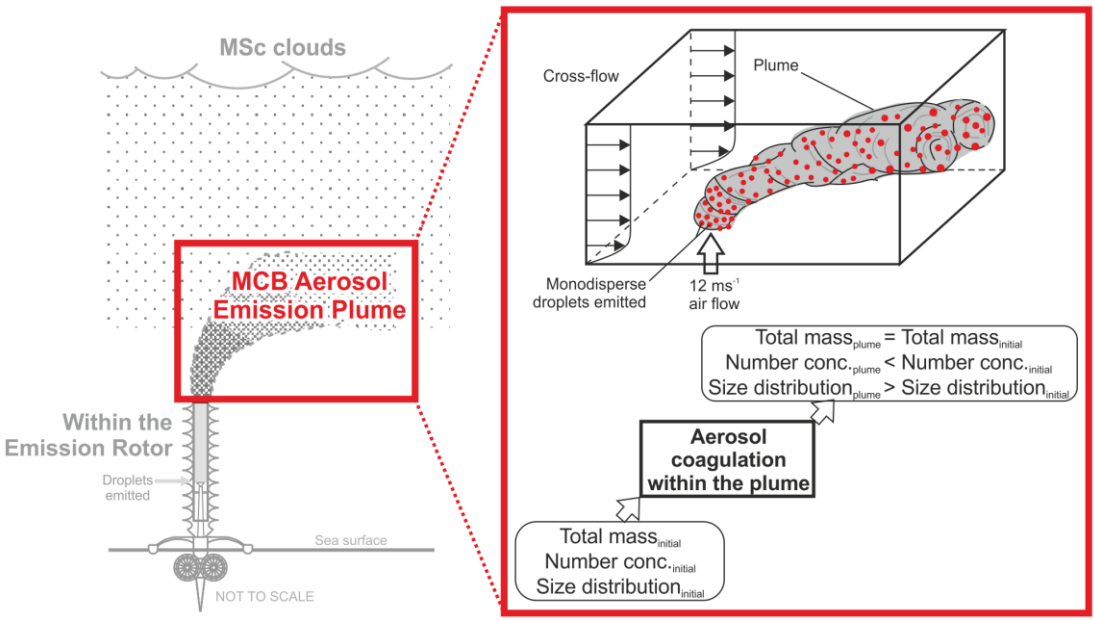

Figure 7.1 *– Schematic overview of the region of interest for the estimation of aerosol coagulation within the plume.*

As explained in Section 6.1, coagulation becomes increasingly important for higher aerosol concentrations. To produce realistic estimates of the effect of coagulation, it is therefore necessary to capture details of the highly concentrated aerosol plume upon emission from the rotor of a Salter et al. (2008) designed vessel. These highly concentrated aerosol plumes – and hence the effects of coagulation – are not captured by the uniform distribution of aerosols across coarse grid cells of previous global-scale modelling. According to the Salter et al. (2008) design, the aerosol plume would be formed by a jet of air carrying the MCB aerosols upwards out of the rotor, into the boundary layer cross-winds (inset, Figure 7.1), a situation

called a ‘jet in a cross-flow’ (Figure 7.2). Jets in cross-flows are common in several engineering scenarios, with comprehensive overviews of the field being presented by Margason (1993), Mahesh (2013) and Balachandar and Eaton (2010).

Fundamentally, as the jet and the cross-flow interact, the jet deflects, with the trajectory depending on the ratio of jet momentum to cross-flow momentum. This interaction of flows additionally produces characteristic vortical structures (Figure 7.2), with a pair of counter-rotating vortices being a dominant structure (Cortelezzi and Karagozian, 2001; Kelso et al., 1996). This counter-rotating vortex pair can lead to a split plume, a phenomenon that has been observed in chimney stack emissions (Fanaki, 1975), wildfires (Cunningham et al., 2005; Haines and Smith, 1987), and volcanic eruptions (Ernst et al., 1994). As these characteristic vortices govern the jet dispersal (Campolo et al., 2005), they also influence the aerosol concentrations within the plume, and ultimately, the rates of coagulation.

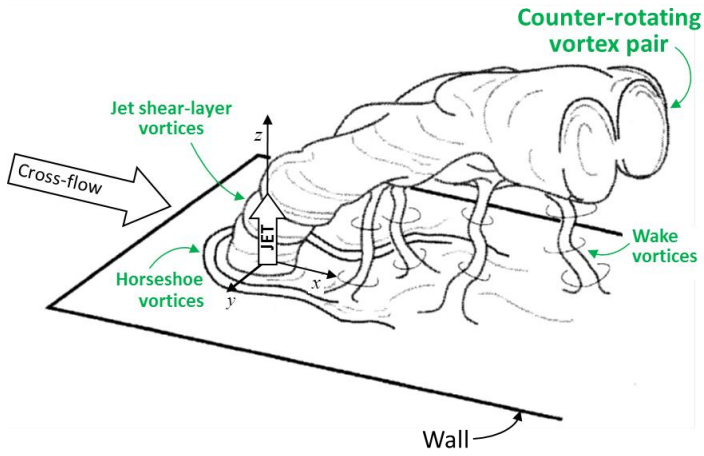

Figure 7.2 *– Schematic showing the four types of vertical structure in the near-field of a jet in a crossflow, emitted flush from a surface. Modified from Fric and Roshko (1994), reproduced by permission of Cambridge University Press, from ‘Vortical structure in the wake of a transverse jet’, Fric and Roshko, Journal of Fluid Mechanics, 279, 1994.*

The structure of the plume can, however, be altered by other conditions. For example, the presence of the solid rotor, in acting as non-aerodynamic (bluff) body, could induce the weaving vortex shedding distinctive of Kármán vortex streets.

While Gaussian distributions of plumes (modified by dispersal parameters) are capable of producing estimates of aerosols concentrations, and hence coagulation rates (e.g. Turner, 1970; Stuart et al., 2013), they do not simulate details of the plume dynamics and vortical structures.

This chapter describes how, for the first time, the MCB aerosol plume was modelled using a large-eddy simulation to capture details of the plume structure. For this, the WRF/Chem model was again utilised, at the higher resolution of 0.5 m (horizontal), with limited domain

size of 120 m x 40 m x ~60 m (height). The set-up of the model and experimental methodology are detailed in Section 7.2.

Section 7.3 goes on to describe the simulation of the control plume. This control plume is interrogated to evaluate the ability of the model to capture key critical characteristics of the MCB aerosol plume.

After this initial validation, the model is then used to determine how coagulation rates – and the resulting changes in MCB aerosol concentration and size distribution – vary under a range of different assumptions as may occur in reality (Section 7.4). These sensitivity experiments cover a range of: aerosol emission rates (Section 7.4.1.1); cross-wind speeds (Section 7.4.1.2); and background temperatures (Section 7.4.1.3). Additionally considered are: the effects of emitting the number concentration and size distribution of aerosols associated with those expected to result from coagulation within the rotor (as found in Chapter 6) compared to the monodisperse bin 3 emission (Section 7.4.1.4); changes to the plume dynamics resulting from the simulation of a solid rotor as an obstacle to the cross-wind (Section 7.4.1.5); the inclusion of water vapour in the emission of aerosols (Section 7.4.1.6); and the inclusion of water droplets in the emission of aerosols (Section 7.4.1.7).

7.2 Methodology

As for previous experiments, the WRF/Chem model was used in large-eddy simulation configuration, with the 8-bin MOSAIC aerosol scheme and CBMZ gas phase chemical mechanism scheme. The coagulation rate varies with the square of particle concentrations and the Brownian coagulation kernel (Jacobson et al., 1994). This form of coagulation is typically dominant for nanoparticles (Miller and Garrick, 2004; Yu et al., 2006; Jacobson et al., 1994) and is therefore suitable for the simulation of the proposed 200 nm dry diameter MCB aerosols of the Salter et al. (2008) design. Aerosol dry deposition was included in the simulations. Aerosol interaction with droplets was carried out by the Morrison two-moment microphysics scheme and included droplet sedimentation. The coalescence of droplets uses a parameterisation based on an assumed distribution of sub-grid vertical velocities. The CAM spectral-band LW, and RRTMG SW radiation schemes were again used, although as simulations were carried out during the night (22:00:00 LT) SW radiation was not an important factor. The 1.5 order 3-D turbulent kinetic energy closure scheme was again used to simulate sub-grid turbulence. Advection was again constrained by the monotonic flux limiter option. Surface layer physical processes were represented by the Monin-Obukov scheme. In a preliminary sensitivity test, a numerical timestep of 0.006 s was found to induce spurious dynamical rippling above the outlet. This phenomenon was removed by halving the timestep to 0.003 s, which is the timestep that was used subsequently. The aerosol and

chemistry timestep was 0.36 s. Whilst a chemistry timestep of 0.06 s produced smoother time series in preliminary testing, the difference in performance was not deemed significant enough to warrant the significantly increased computational expense. Owing to computational limitations, most simulations were run for a 44 second model time, with analysis using the last 20 seconds. An extended run up to 88 seconds was carried out for the control run to assess the implications of the development of the plume before, during and after the standard analysis period.

The large-scale cross-wind (which would result from a combination of both wind speed and vessel motion; Figure 7.3 a) was initialised with a 10 m wind speed of 6 ms^{-1} and the profile shown in Figure 7.3 b. The boundary layer total water mixing ratio was initialised at 10 g $kg_{dry\ air}^{-1}$, with potential temperature initialised at 288.3 K. The background aerosol profile used was that of the previously described PR case, although, as the simulated aerosol emissions are so high, the simulations are unlikely to be very sensitive to this selection.

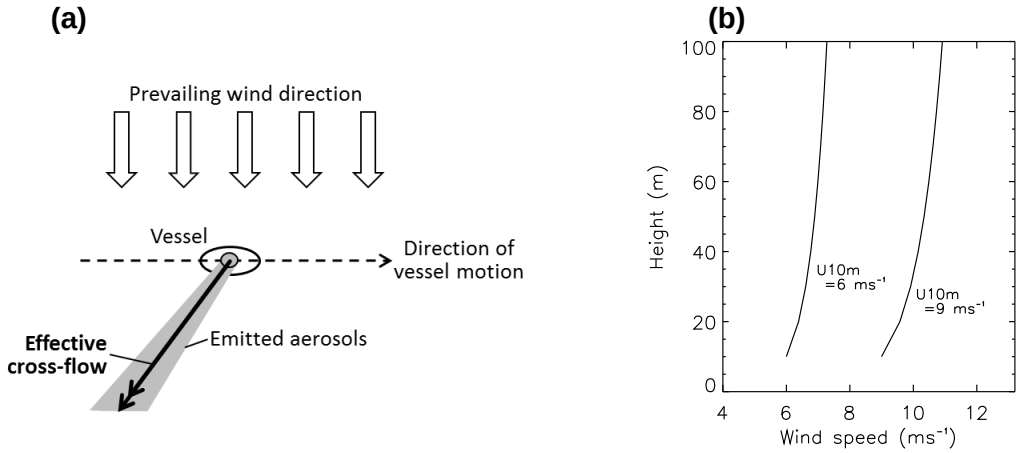

Figure 7.3 *– (a) Schematic showing the direction and composition of the effective crosswind; (b) Vertical profiles of the initialisation wind profile.*

The domain was 120 m long, 40 m wide and approximately 60 m high, and is shown schematically in Figure 7.4 a. There was a 3 m damping layer at the model top and the horizontal boundaries were open, allowing the emitted MCB aerosol plume to leave the domain. The horizontal resolution was 0.5 m, with the vertical resolution being approximately 1 m. To represent the rotor outlet height, the jet was located 20 m from the longitudinal 'input' boundary at a height of ~20 m. The geometry and assumptions used in simulating the rotor are shown in Figure 7.4 b. Two variations of the rotor geometry are assumed. For the first variation, the presence of a long solid rotor is omitted and the rotor emission is assumed to occur in one model layer only. To simulate the rotor dynamics, the 13 central cells are assigned an upward velocity of 12 ms^{-1} (based on the updraft velocity suggested by Salter et al. (2008)). This uniform velocity assignment essentially produces a 'top-hat' velocity profile which is akin to turbulent flow in the pipe. The upward and

horizontal velocities of the surrounding cells are held at 0 ms^{-1} to simulate the solid rotor walls. In the second variation, where a long solid rotor is assumed, these dynamic conditions are extended down in the model to ~2 m above the surface.

Aerosol emissions again followed the Salter et al. (2008) assumptions of a 30 kg s^{-1} sea spray emission rate (1.0xSA). While the aerosols were assumed to be water droplets while travelling through the rotor (Chapter 6), here, as in Chapter 4, the aerosols are emitted as interstitial aerosols with a dry diameter of 200 nm. Water associated with the aerosol emission is only included as part of the sensitivity experiments, as discussed below. While the aerosols are now emitted over the more confined rotor area (Figure 7.4 b) compared to the 300 m x 300 m grid used previously, the emission number flux is maintained at $1.1x10^{17}$ s^{-1} for the 1.0xSA emission rate. This is equivalent to a mass emission fluxes of 123 g m^{-2} s^{-1} for Na and 189 g m^{-2} s^{-1} for Cl. The aerosol (and later the water) emission height coincides with the top of the rotor (20 m).

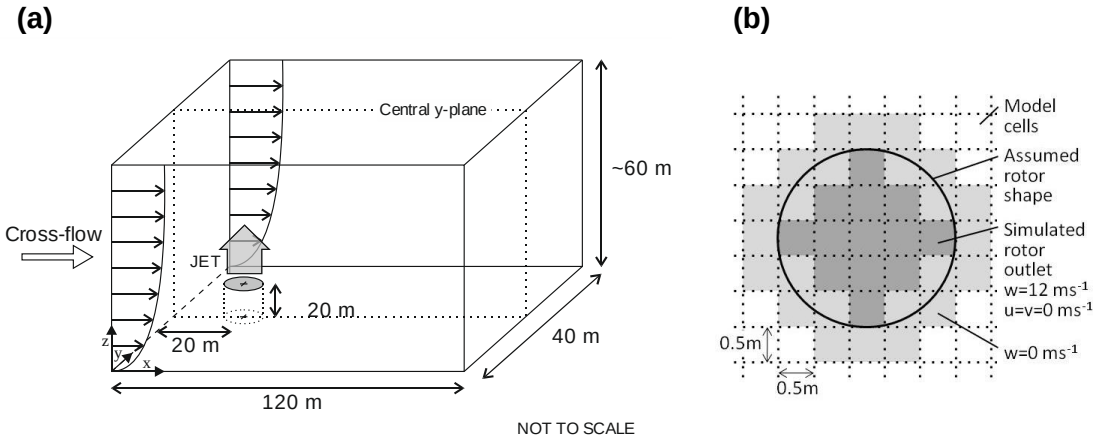

Figure 7.4 *– (a) Schematic of the computational domain;(b) Plan view of the simulated rotor, indicating velocity distributions in relation to model cells.*

The simulations undertaken are tabulated in Table 7.1. The initial control simulation, of a 1.0xSA emission rate of aerosols into bin 3 (simulating assumed monodisperse aerosols of 200 nm dry diameter) is initially considered over an extended time period (88 seconds). This simulation is then used as the baseline for later comparisons in this section.

In addition to this initial baseline simulation, additional simulations are undertaken over a time period of 44 seconds (with the choice of this duration discussed in Section 7.3.1.1). These attempt to capture sensitivities owing to uncertainties and variability in the design of the MCB emission technology (aerosol emission rates, Section 7.4.1.1), and to natural variability in the atmospheric conditions (cross-wind speed and background temperature, Sections 7.4.1.2 and 7.4.1.3). These sensitivity experiments were chosen to represent a range of feasibly encountered conditions. While the number of conditions simulated for cross-wind

speed and background temperature are small, they allow trends in behaviour to be identified, and allow verification that the model simulates physically plausible output.

Further simulations aim to quantify the sensitivity of aerosol coagulation within the plume to alterations that may increase the realism of the simulated output. Therefore, one case includes the simulation of the MCB aerosol emission number concentration and size distribution resulting from the coalescence processes within the rotor as found in Chapter 6 (Section 7.4.1.4). Another case includes the representation of a solid rotor acting as a bluff body (Section 7.4.1.5).

For each case, two simulations are carried out: one including aerosol and chemical processes (denoted as 'CHEM') and another where the aerosol and chemical processes are suppressed (denoted as 'NO_CHEM'). The differences between these CHEM and NO_CHEM simulations are assumed to result primarily from aerosol coagulation. The NO_CHEM simulations are intended to provide a baseline scenario, approximating the substantially reduced rates of coagulation that would occur for the more broadly dispersed MCB aerosol emissions over the tens-of-kilometre scale grid cells in global-scale models.

The last two simulations (summarised in Table 7.1) include water with the aerosol emissions, either as water vapour (Section 7.4.1.6), or as water droplets (Section 7.4.1.7). Both water emission assumptions add water with a mass flux of ~30 kg s^{-1}. As these simulations may incorporate droplet coalescence as well as aerosol coagulation, they are compared against the control case NO_CHEM simulation which omits both emitted water and aerosol coagulation. It is noted that the water vapour sensitivity experiment is unlikely to be realistic. Fundamentally, the mechanism that would be needed to produce water vapour from sea water would be highly energy intensive, and so undesirable from a practical design standpoint. This largely hypothetical simulation is therefore presented here in order to offer some possible points of interest, likely relevant more for future design decisions.

Table 7.1 *– List of plume simulations, describing the emission rate (xSA), the 10 m cross-flow velocity (ms^{-1}), the background temperature (K), the characteristics of the marine cloud brightening (MCB) aerosols emitted into the plume (where 'Mono' denotes the monodisperse bin 3 emission), the simulation of a solid rotor, the emission of water with the aerosols, and the section reference. Each experiment comprised of two simulations: one simulation being run under the CHEM configuration (i.e. simulating the effects of aerosol coagulation), and the other simulation being run under the NO_CHEM configuration (i.e. suppressing aerosol coagulation).*

	Emission rate (xSA)	Cross-flow velocity (ms^{-1})	B/g Temp. (K)	MCB aerosols emitted	Solid rotor?	Emission of water	Section ref.
CONTROL Plume	1.0	6.0	288.3	Mono	No	None	7.3
Sensitivity experiments							
Aerosol emission rates	**5.0**	6.0	288.3	Mono	No	None	7.4.1.1
	3.0	6.0	288.3	Mono	No	None	
	0.5	6.0	288.3	Mono	No	None	
	0.25	6.0	288.3	Mono	No	None	
	0.1	6.0	288.3	Mono	No	None	
Cross-wind speed	1.0	**9.0**	288.3	Mono	No	None	7.4.1.2
Background temperature	1.0	6.0	**300.0**	Mono	No	None	7.4.1.3
No. concentration and size distribution of emitted aerosols	1.0	6.0	288.3	**From rotor**	No	None	7.4.1.4
Inclusion of a solid rotor (acting as a bluff body)	1.0	6.0	288.3	Mono	**Yes**	None	7.4.15
Inclusion of water vapour in the emission of aerosols	1.0	6.0	288.3	Mono	No	**As water vapour**	7.4.1.6
Inclusion of water droplets in the emission of aerosols	1.0	6.0	288.3	Mono	No	**As water droplets**	7.4.1.7

7.3 Control Plume

7.3.1 Control Plume: Results

To aid orientation, Figure 7.5 illustrates the shape of a typical jet in cross-flow simulated output (for the case where a solid rotor is omitted). To demonstrate the model behaviour, this section first presents, and then discusses key characteristics of the control plume.

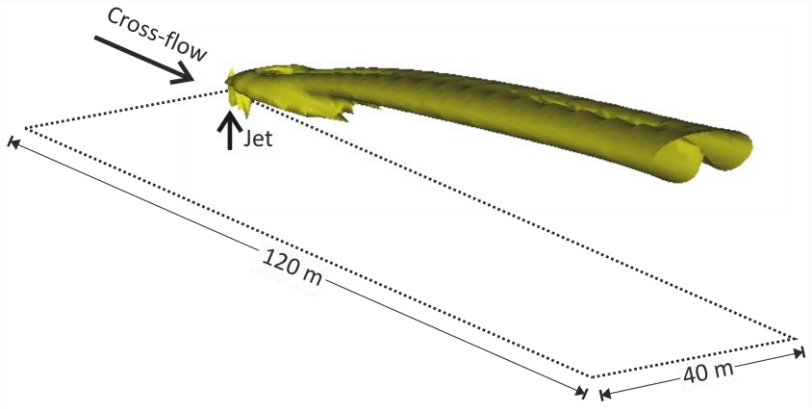

Figure 7.5 *– Instantaneous isosurface for a given aerosol concentration, illustrating the typical structure of a simulated jet in cross-flow in the absence of a solid (bluff) rotor during the approximately steady-state phase. (The case shown is a simulation used during trials of the methodology).*

7.3.1.1 Plume Development

The development of the plume through time is shown in Figure 7.6, showing the displacement of the emitted aerosols caused by the 12 ms^{-1} vertical air jet and crossflow.

In the first 24 seconds of the simulation, formations similar to shear-layer vortices were observed on the windward edge of the plume. These stayed near to the head of the plume, leaving the domain after around 28 seconds. From this time on, the distribution of plume aerosols remained fairly uniform. The upper and lower boundaries maintained approximately constant paths, with the upper boundary rising by approximately 0.048 m per second between 28 and 88 seconds. Aerosols descended into the jet wake rapidly upon emission, creating a lower aerosol boundary up to 10 m below the 20 m aerosol emission height. Bifurcation of the plume in the y-plane was also evident (as illustrated at t=88 seconds in Figure 7.6). In this bifurcation, high concentrations of aerosols followed both the upper boundary, and a trajectory around mid-way between the upper and lower plume boundaries.

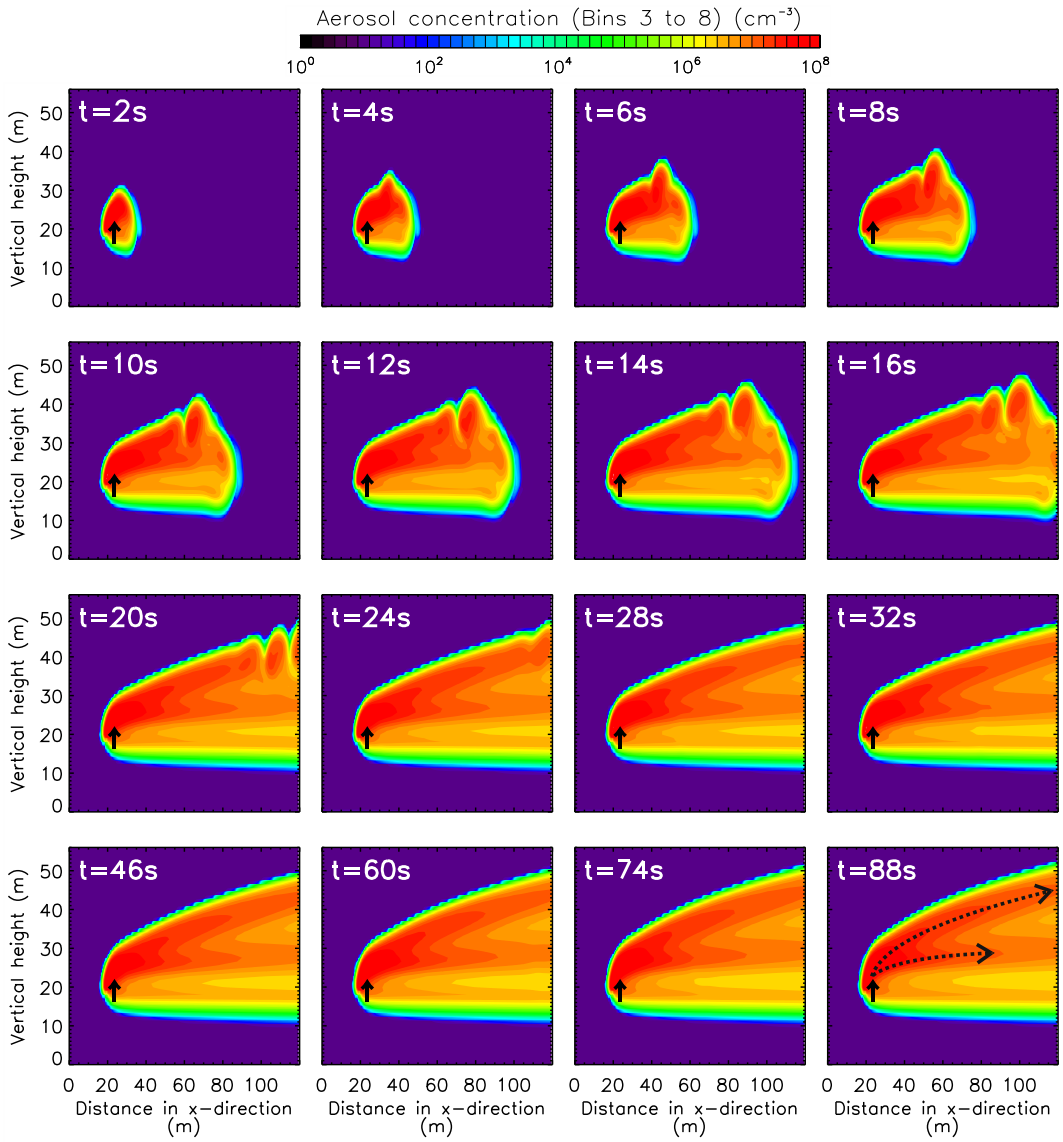

Figure 7.6 *– Interstitial aerosol concentrations (total of bin sizes 3 to 8, averaged over the y-direction) through time. Crosswind flows from left to right. Black solid arrows indicate the location of the aerosol emission. Black dotted arrows at t=88s illustrate the apparent vertical bifurcation of the flow which begins at ~14 seconds.*

Figure 7.7 (panels a and b) shows the time series of the domain averaged aerosol mass and aerosol number concentration for simulations including and omitting aerosol coagulation (CHEM and NO_CHEM respectively). During the initial 18 seconds of the simulation, both the aerosol mass and aerosol number concentration increased as the plume extended to fill the domain. After this time, aerosols were able to exit at the open boundary and the mass and number concentrations reached an approximate steady-state. A true steady-state in domain average aerosol mass was not reached, with a continuing increase in mass suggesting that the mass of aerosols being emitted into the domain exceeded the mass of aerosols exiting the domain. This increase in mass over the latter 70 seconds of the simulation was equivalent to around 25% of the mass needed to initially fill the domain.

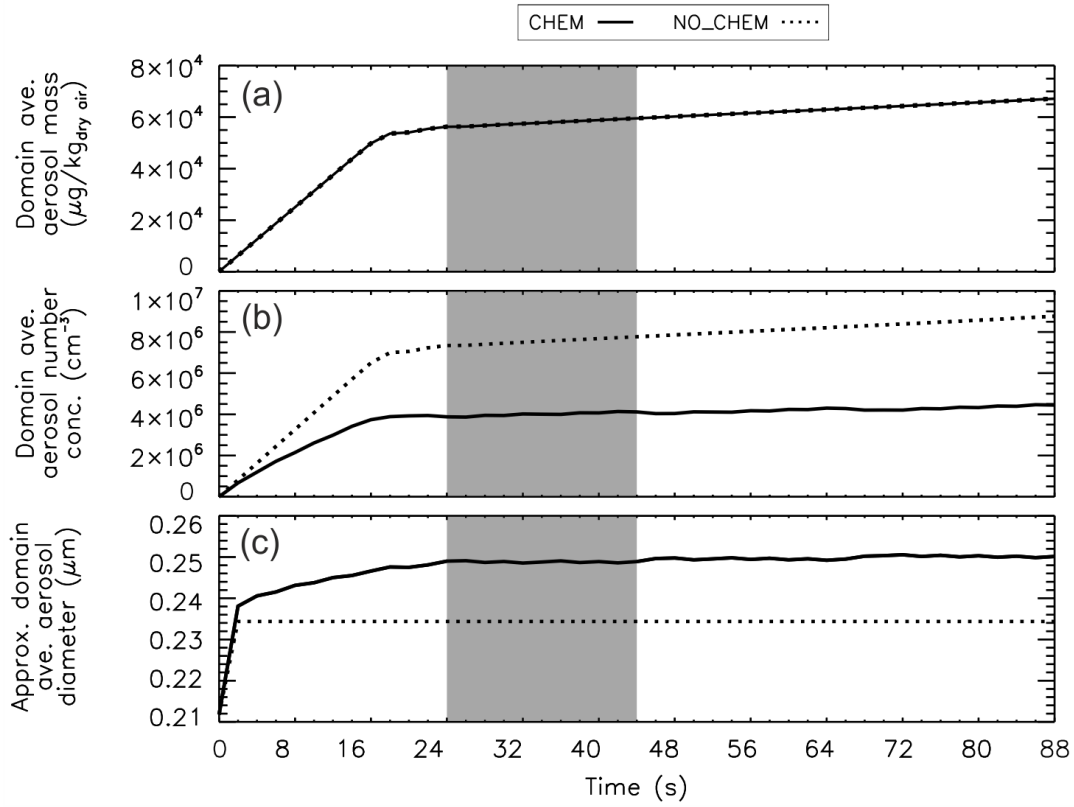

Figure 7.7 *– Time series for: (a) domain average aerosol mass (μg $kg_{dry\ air}^{-1}$); (b) domain average aerosol number concentration (cm^{-3}); and (c) an approximate domain average aerosol diameter (μm). Grey shading indicates the time period used for later analysis.*

The time series for mass concentrations for the CHEM and NO_CHEM simulations were the same (coagulation does not alter the total mass of aerosols; Figure 7.7 a). However, the domain average number concentration was reduced by approximately half for the CHEM simulation compared to the NO_CHEM simulation (Figure 7.7 b). The maintenance of mass, but reduction in aerosol number concentration caused by aerosol coagulation, produced an increase in the approximate particle diameter for the CHEM simulation compared to the NO_CHEM simulations (Figure 7.7 c). It is noted that this particle diameter is presented as an approximate indication of aerosol size changes only.

These results also show that there is little difference between the coagulation-induced aerosol number concentration reductions over a 24 to 44 second time interval (shaded grey in Figure 7.7), and a longer 24-88 second time interval, with the number concentration reductions averaging 48.1% and 46.9% respectively. Therefore, to enhance computationally efficiency, subsequent simulations were run for only 44 seconds, with analysis being carried out over the 24 to 44 second time interval.

To evaluate the ability of the model in adequately representing key features of the jet in cross-flow, simulation outputs will now be presented from the end of the analysis period (44 seconds after the start of the simulation).

7.3.1.2 Plume Trajectory

The plume trajectory was found using the height of the maximum aerosol concentrations located on the central y-plane (refer to Figure 7.4 panel a, for illustration). The location of the maximum aerosol concentration for bin size 7 is shown in Figure 7.8 (red data points)[1]. Figure 7.8 also shows the fit of these data points to the standard trajectory equation (solid black line) described in Equation 7.1 (Margason, 1993; Muppidi and Mahesh, 2005). This fit to the trajectory equation used the coefficients A=1.19 and B=0.48. Finally, Figure 7.8 also shows upper and lower bounds for a fit to Equation 7.1 using the empirically derived coefficient limits of A=2.6 with B=0.34, and A=1.2 with B=0.28 which are typical for jets in cross-flows (blue shading; Margason, 1993; Muppidi and Mahesh, 2005).

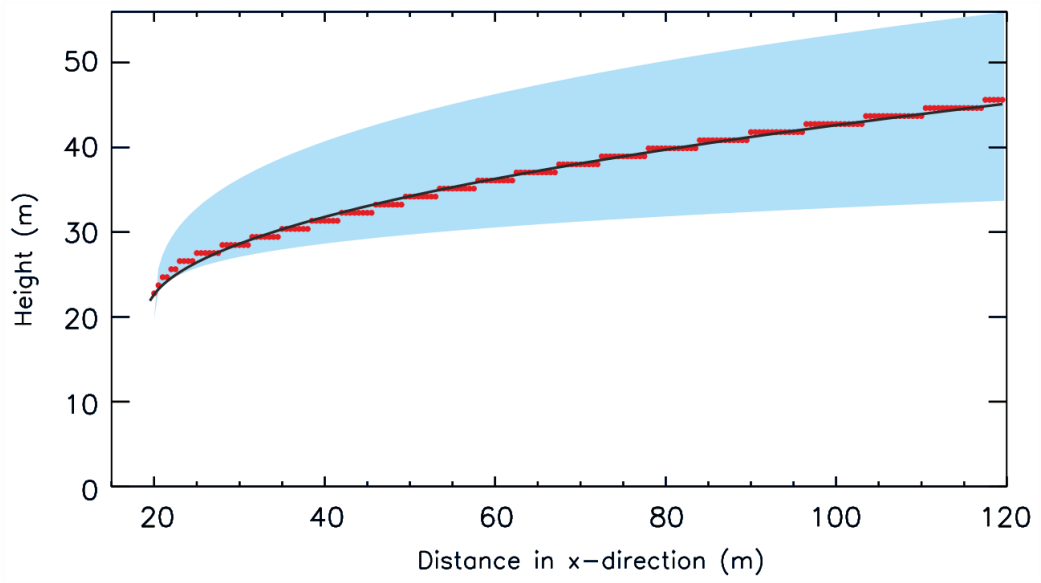

Figure 7.8 *– Trajectory fitted to Equation 7.1 (solid black line) associated with points of maximum aerosol concentration for bin 7 (red data points) along the central y-plane. Blue shading indicates empirically derived bounds for the trajectory, having coefficients A=2.6 with B=0.34 and A=1.2 with B=0.28 which are typical for jets in cross-flows (Margason, 1993; Muppidi and Mahesh, 2005).*

[1] Owing to the effects of the coagulation of emitted bin size 3 aerosols (presented in Section 7.3.1.4 and discussed in Section 7.3.2), the counter-rotating vortex pair structure was most consistently traced over the length of the domain by aerosols in bin sizes 5 to 7. These aerosols followed similar trajectories, with only bin size 7 being shown here for clarity.

$$\frac{z}{rd} = A\left(\frac{x}{rd}\right)^{B} \qquad \textbf{(7.1)}$$

where:

z = distance vertically upwards

x = distance in the direction of the cross-flow

r = the ratio of jet to cross-flow velocities (assuming approximately equal jet and cross-flow densities)

d = jet diameter at emission

A = coefficient

B = coefficient

7.3.1.3 Flow Patterns and Pressure Distributions

Figure 7.9 (panel a) shows that the cross-flow speed decreased over the height of the jet, with the jet acting as an obstacle. This cross-flow speed decrease was larger in three regions: upwind of the initially bending vertical jet emission (labelled 'F1'); in the lee of the initial jet emission (labelled 'F2'); and in the lee of the upper portion of jet flow (labelled as 'F3'). The jet obstacle also led to an increase in pressure of up to 20 Pa on the upwind side of the jet, shown in Figure 7.9 b. While the flow speed reduced, momentum would be conserved owing to the subsequent rotation of the flow in forming the counter-rotating vortex pair. This counter-rotating vortex pair can be seen in both the flow structures and regions of opposing vorticity (Figure 7.9 c). The development of these counter-rotating vortices with distance from jet emission led to a weakening in vorticity, with a growth in vortex diameter. For this 6 ms^{-1} cross-flow case, the distance between the vortex pair centres increased from approximately 3 m to 5 m between distances along the trajectory of 5 and 40 times the diameter of the rotor (denoted as '5d' and '40d' respectively).

Preliminary sensitivity experiments found that these dynamical features of the jet in cross-flow resulted from the fluid flows and were not affected by the presence of aerosols.

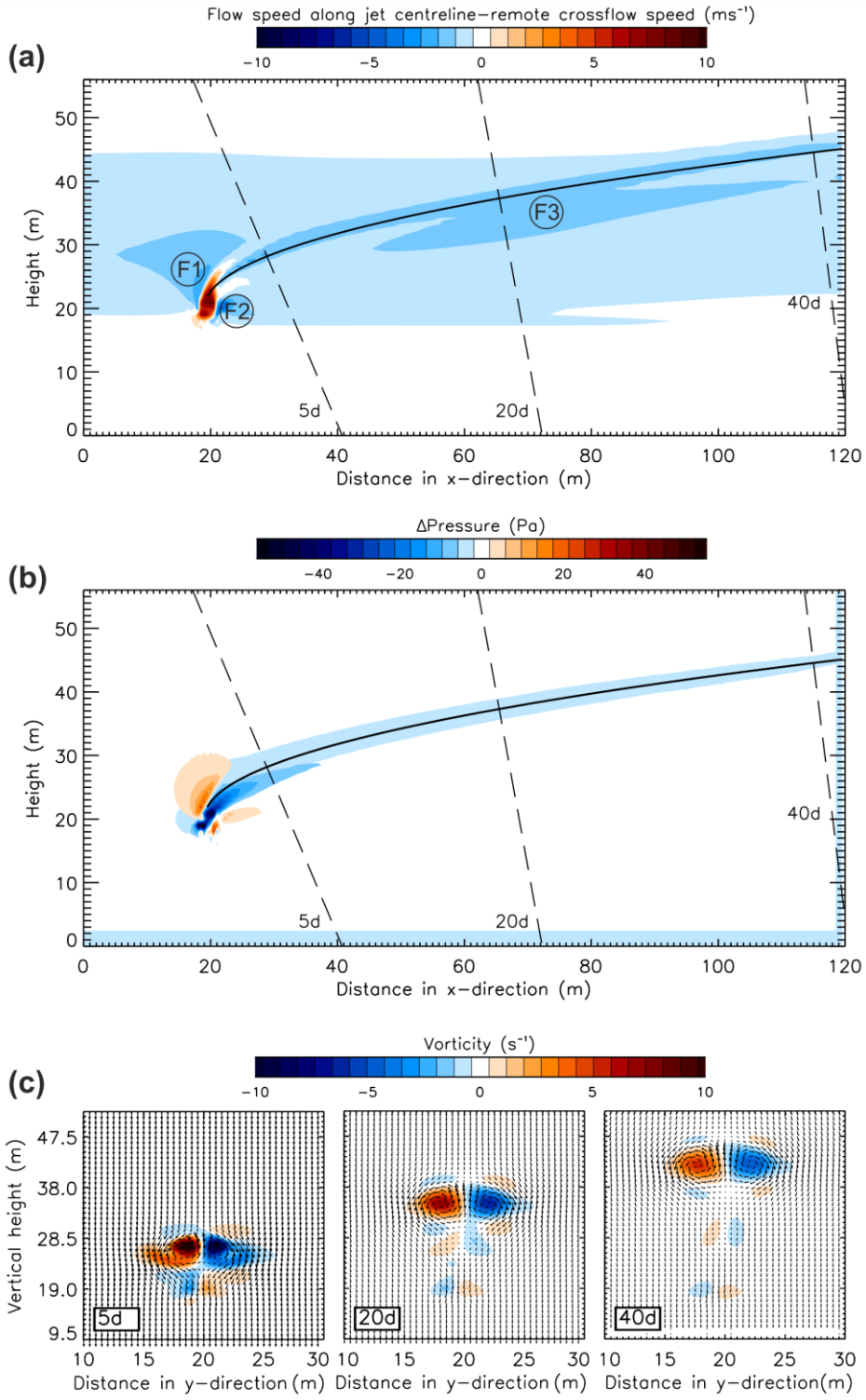

Figure 7.9 *– (a) Contours showing the difference between the flow speed along the central y-plane and the cross-flow speed remote from the emission source. Black solid line indicates the trajectory fit to the highest concentration of bin 7 aerosols. Black dashed lines indicate the planes perpendicular to the trajectory at distances along the trajectory of 5, 20 and 40 times the diameter of the rotor (5d, 20d and 40d); (b) Contours showing the difference in pressure along the central y-plane and the pressure remote from the emission source. Black solid and dashed lines as for panel 'a'; (c) Sections of planes perpendicular to the trajectory at 5d, 20d and 40d, showing the vorticity of flow, overlaid by arrows indicating flow velocity. All panels show 44 seconds from the simulation start.*

7.3.1.4 Distribution of Aerosols Across the Plume Cross-section

The distribution of aerosols within these dynamical flow patterns is demonstrated in Figure 7.10. To readily observe these aerosol distributions in the absence of complicating aerosol processes, the NO_CHEM case is shown for bin 3 aerosols (into which the MCB aerosols were emitted). In the absence of aerosol processes including coagulation, the emitted aerosols remained in bin 3 during the simulation. Over the whole trajectory, the aerosols were preferentially concentration within the counter-rotating vortex pair. However, the maximum aerosol concentration decreases further from the emission source as the cross-sectional area of the plume increased. This increased area resulted largely from a vertical spreading that was also seen in Figure 7.6, and was related to the increasing upper boundary height of the plume, but maintenance of the lower plume boundary just below the emission height. The bifurcation of higher aerosol concentration that was also evident in Figure 7.6 is manifest in the cross-sections of Figure 7.10. This secondary peak in aerosol concentrations became more distinct further from the source, resulting the chevron formation at a height of 30 m in the '40d' section (circled in Figure 7.10).

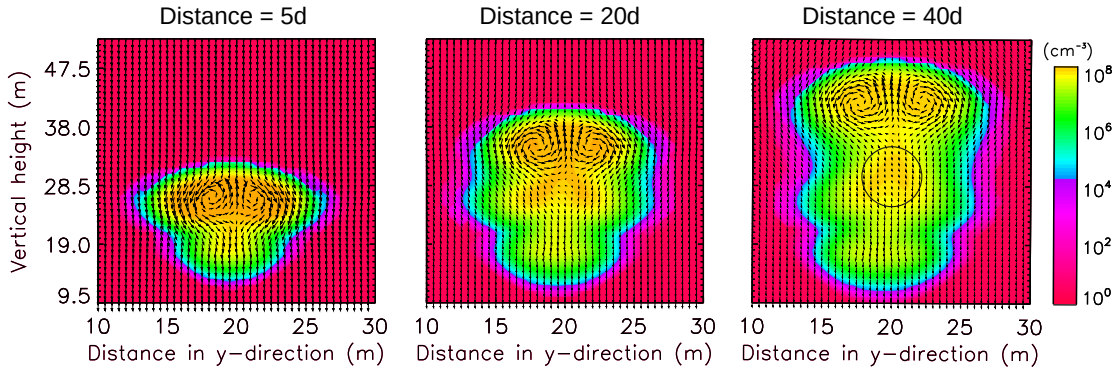

Figure 7.10 *– Sections of planes perpendicular to the trajectory at 5, 20 and 40 times the diameter of the rotor (5d, 20d and 40d; refer to Figure 7.9 for locations), showing the distribution of bin 3 interstitial aerosol concentrations (cm^{-3}) for the NO_CHEM simulation overlaid by arrows showing velocities of the flow. The black circle at 40d indicates the chevron aerosol formation referred to in the text. All show 44 seconds from the simulation start.*

Now considering the effect of coagulation on these aerosol distributions, Figure 7.11 shows bin sizes 3 to 8 for the CHEM case. Again, planes perpendicular to the trajectory at distances of 5, 20 and 40 times the rotor diameter are shown.

The highest concentrations were again for bin 3 aerosols close to the emission source, however, their coagulation resulted in a decrease in their concentration further from the emission source (Figure 7.11) as the aerosols move into the larger size bins. This pattern was reversed for the higher bin sizes, with bins 6 and 7 particularly clearly illustrating higher

aerosol concentrations further from the emission source (Figure 7.11). The aerosol concentrations for each size bin diminished with increasing size (with peak concentrations of bin 7 aerosols being around eight orders of magnitude smaller than those for the emission bin 3), with no aerosols growing sufficiently to enter size bin 8.

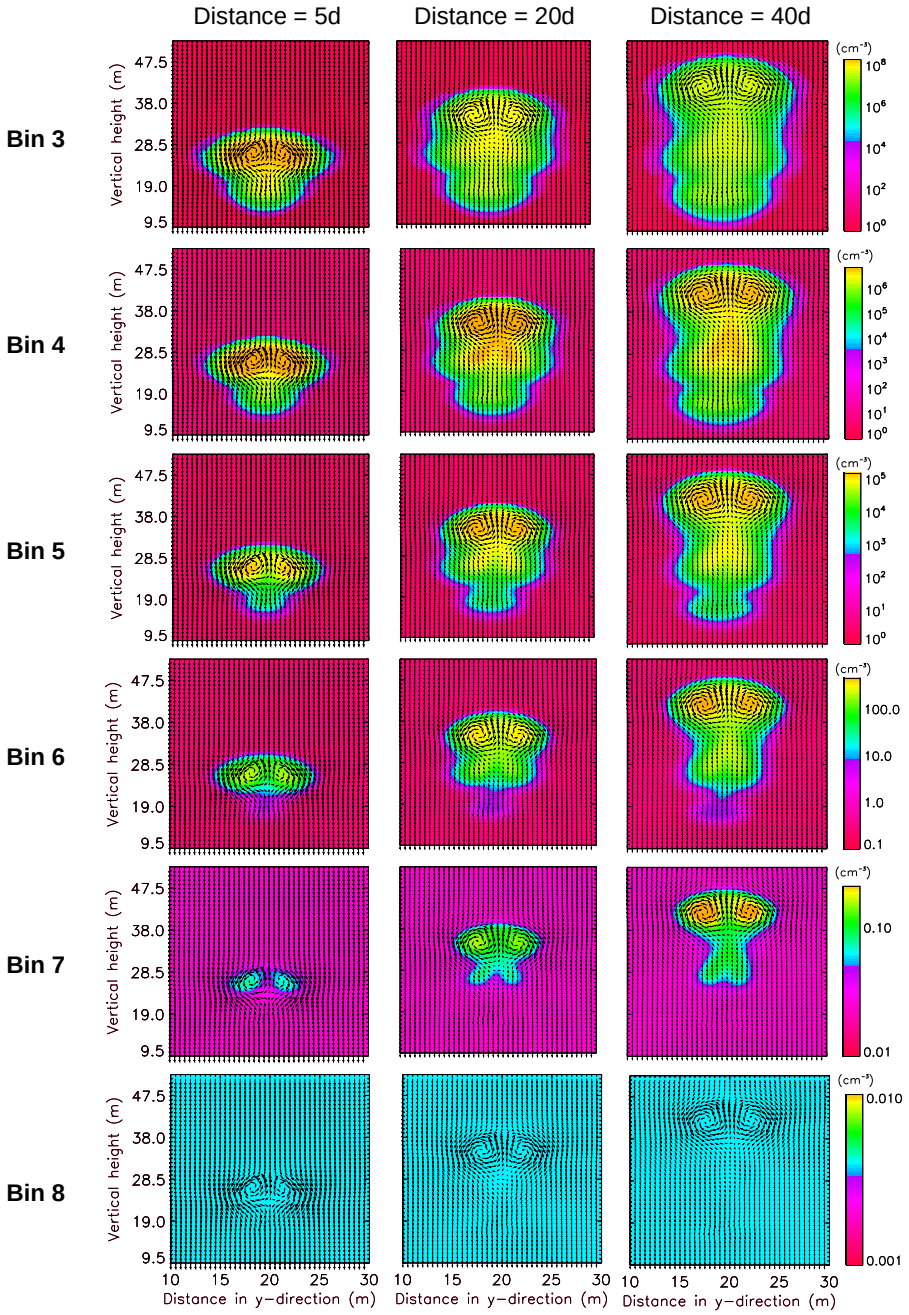

Figure 7.11 *– Sections of planes perpendicular to the trajectory at 5, 20 and 40 times the diameter of the rotor, showing the distribution of bin 3 to bin 8 interstitial aerosol concentrations (cm^{-3}) for the CHEM simulation overlaid by arrows showing velocities of the flow. All show 44 seconds from simulation start. Note the different contour colour ranges.*

7.3.1.5 Distribution of Aerosols Along the Plume Path

These changes in aerosol size distributions along the length of the domain are shown in Figure 7.12. The greatest aerosol transfer rate from bin 3 to bin 4 occurred close to the emission source (indicated by the steepest gradients in aerosol number fraction) and approached a steady state by the end of the domain. As this steady state would approach conditions typical to the wider plume (outside of the modelled domain), in addition to domain average changes, a section close to the domain end will also be used for analysis. This 5 m end section, indicated in Figure 7.12, will be referred to as the END section.

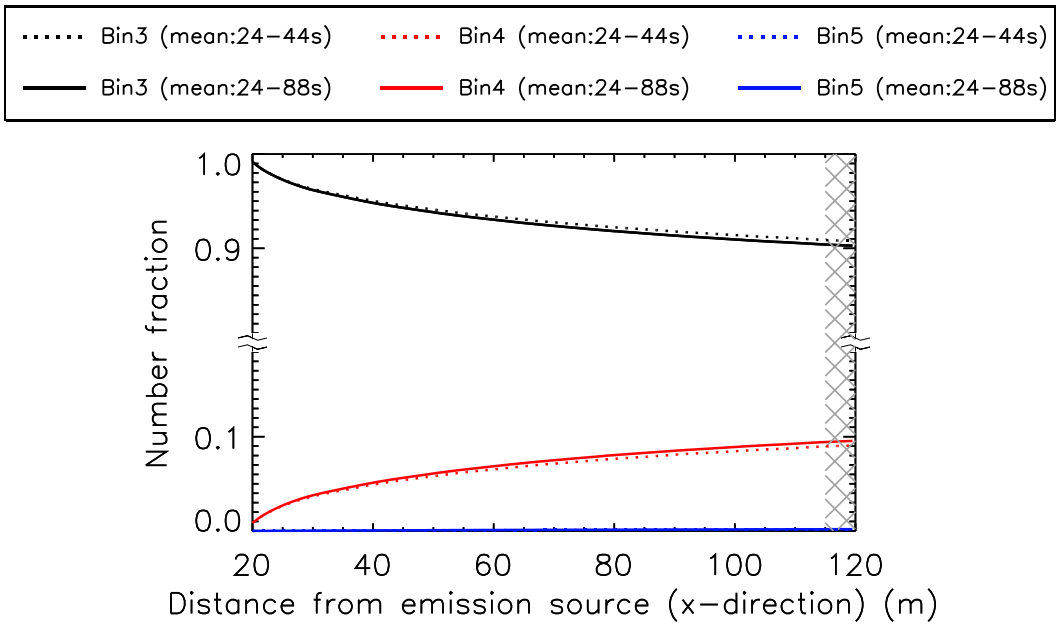

Figure 7.12 *– The fraction of the total aerosol number concentration comprising bin 3, bin 4 and bin 5 aerosols along the domain length averaged over the 24 to 44 second and 24 to 88 second time periods. Grey hatching indicates the last 5 metres of the domain which is a secondary analysis region known as END.*

In this END section, the majority of aerosols (around 90%) were still in bin 3, while the remaining 10% largely comprised of bin 4 aerosols. Only a small percentage (0.17%) of the aerosols were in bin 5, with less than 0.001% in bins 6 and above.

Increasing the analysis time period from between 24 and 44 seconds to between 24 and 88 seconds resulted in a slightly larger number fraction of aerosols in the larger size bins. For bin 4, this number fraction increased from 9.04% to 9.54%, while for bin 5, the increase was from 0.17% to 0.19%. There was a correspondingly reduced number fraction of aerosols in the original bin 3 (90.27% compared 90.79%).

The similarities demonstrated in Figure 7.12 again suggest that the shorter analysis time period (24 to 44 second) adequately captures the aerosol processes that are apparent over longer time periods (24 to 88 second), as discussed in Section 7.3.1.1.

As coagulation leads to the formation of larger aerosols, there is an accompanying decrease in total aerosol number (as demonstrated in Figure 7.7). The spatial distribution of this total aerosol number concentration decrease is shown in Figure 7.13 (as the percentage reduction between the CHEM and NO_CHEM simulations). The percentage losses in total number concentrations increase with distance from the emission source. In the END section, the total number concentration has reduced by up to ~85%, with this highest value corresponding to the counter-rotating vortex pair region.

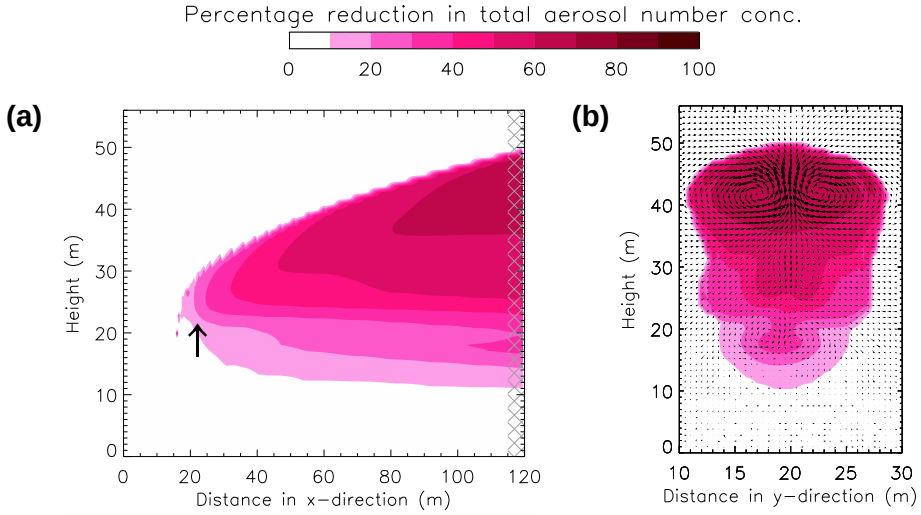

Figure 7.13 *– The percentage loss in total aerosol number concentration in the CHEM simulation compared to the NO_CHEM simulation for (a) the domain average along the length of the domain, with grey hatching indicating the END region as in Figure 7.12 and the solid black arrow indicating the location of the emission point; and (b) the average percentage loss in total aerosol number concentration in the END region. Both averaged between 24 and 44 seconds.*

Considering the domain and END section averages, Table 7.2 details the perturbations in aerosol number concentration and mass from the background concentrations for the proposed Salter et al. (2008) emission rate (denoted as 1.0xSA) over the 24 to 44 second analysis period. Bins 1 and 2 are omitted from the table as the effects of the comparatively small maximum aerosol perturbations (e.g. -2 cm^{-3} for bin 1 CHEM simulation) on cloud droplet activation would be negligible.

In the NO_CHEM simulation (where coagulation was not included), the aerosol number concentration increased by a domain average of $7.5x10^{6}$ cm^{-3}, almost entirely in the emission bin 3. The domain average aerosol mass increased by $5.8x10^{4}$ µg $kg_{dry\ air}^{-1}$. These values were larger in the END section, being increases of $7.9x10^{6}$ cm^{-3} and $6.1x10^{4}$ µg $kg_{dry\ air}^{-1}$ for the number concentration and mass respectively. In the CHEM simulation (where coagulation was included), the aerosol number concentration increased by a domain average of $4.0x10^{6}$ cm^{-3} and an END section average of $3.3x10^{6}$ cm^{-3}. Thus, including coagulation

caused number concentration increases to be reduced by 46.9% for the domain, and 58.1% for the END section. Masses were conserved however.

Table 7.2 *– Domain average perturbation in aerosol number concentrations (cm^{-3}) and aerosol mass concentrations ($\mu g\ kg_{dry\ air}^{-1}$) from background aerosol concentrations in NO_CHEM and CHEM conditions for the control case. Averages for the END section are given in brackets. Values are averaged over the 24 to 44 second analysis period. Bins 1 and 2 are omitted for clarity. To aid readability, small increases (i.e. below 1 cm^{-3}) are indicated by italics.*

	ΔAerosol number conc. (cm^{-3})		ΔAerosol mass ($\mu g\ kg_{dry\ air}^{-1}$)	
	NO_CHEM	CHEM	NO_CHEM	CHEM
Bin 3	$7.5x10^6$ ($7.9x10^6$)	$3.8x10^6$ ($3.0x10^6$)	$5.8x10^4$ ($6.1x10^4$)	$2.9x10^4$ ($2.3x10^4$)
Bin 4	*$7.8x10^{-3}$* (*$7.7x10^{-3}$*)	$2.4x10^5$ ($3.0x10^5$)	*$1.6x10^{-1}$* (*$1.6x10^{-1}$*)	$2.6x10^4$ ($3.3x10^4$)
Bin 5	*$1.9x10^{-3}$* (*$1.8x10^{-3}$*)	$3.4x10^3$ ($5.5x10^3$)	*$6.0x10^{-1}$* (*$6.0x10^{-1}$*)	$3.0x10^3$ ($4.8x10^3$)
Bin 6	*$1.3x10^{-3}$* (*$1.3x10^{-3}$*)	$7.5x10^0$ ($1.5x10^1$)	*$4.5x10^{-1}$* (*$4.5x10^{-1}$*)	$5.4x10^1$ ($1.0x10^2$)
Bin 7	*$4.7x10^{-4}$* (*$4.8x10^{-4}$*)	*$3.2x10^{-3}$* (*$6.4x10^{-3}$*)	*$3.8x10^{-1}$* (*$3.8x10^{-1}$*)	*$5.4x10^{-1}$* (*$7.3x10^{-1}$*)
Bin 8	*$6.8x10^{-5}$* (*$6.8x10^{-5}$*)	*$6.8x10^{-5}$* (*$6.8x10^{-5}$*)	*$4.9x10^{-1}$* (*$4.9x10^{-1}$*)	*$4.9x10^{-1}$* (*$4.9x10^{-1}$*)
TOTAL (all bins)	$7.5x10^6$ ($7.9x10^6$)	$4.0x10^6$ ($3.3x10^6$)	$5.8x10^4$ ($6.1x10^4$)	$5.8x10^4$ ($6.1x10^4$)

The number concentrations in each size bin also changed for the CHEM case compared to the NO_CHEM case. The domain average number concentration increase in bin 3 in the CHEM simulation was $3.8x10^6$ cm^{-3}, or 49.9% of that in the NO_CHEM case. In the CHEM simulation, coagulation allowed aerosols to grow. This coagulational growth resulted in there being an increased aerosol number concentration in bin 4 of $2.4x10^5$ cm^{-3}. This number of aerosols equates to 3.1% of the total aerosol number concentration increase that occurred in the NO_CHEM case (when coagulation was prohibited). For bin 5, these values were $3.4x10^3$ cm^{-3} (0.04% of the NO_CHEM case), falling to 7.5 cm^{-3} (0.0001%) for bin 6, and falling further to increases below thousandths per cm^3 for bins 7 and 8. The bin 3 aerosol number concentrations are smaller still for the CHEM simulation averaged over the END section, whilst in this region the larger aerosols (bins 4, 5 and 6) increase in number by more than the domain average.

7.3.2 Control Plume: Discussion

The ability of the model to simulate structures characteristic of a jet in a cross-flow is now discussed. These structures are important as they govern the flow, and hence control aerosol distributions and coagulation rates (Soldati and Marchioli, 2009).

The model successfully simulated the interaction of the jet and cross-flow. These interactions can be seen in the changes in flow speed and pressure resulting from the presence of the jet of air and aerosols that acts as a physical obstacle. This produces, for example, the region of high pressure on the upwind side of the jet, illustrated in Figure 7.9 (Keffer and Baines, 1963; Muppidi and Mahesh, 2005). This interaction additionally caused the jet to deflect, with the trajectory of the plume generally falling within a range expected from previous empirically derived bounds, illustrated by the blue shading in Figure 7.8 (Margason, 1993; Muppidi and Mahesh, 2005). However, the coefficients associated with fitting the plume data to the standard trajectory (Equation 7.1) were outside of the empirically derived ranges of 1.2 to 2.6 and 0.28 to 0.34 (for coefficients A and B respectively) for both the 6 ms^{-1} and 9 ms^{-1} cross-flow velocities. The shape of the simulated flow particularly differed from that expected from the empirical limits close to the emission point. The discrepancy may arise from several factors. Firstly, in forming the counter-rotating vortex pair, the jet flow rotated (Mahesh, 2013) and caused the planar jet speed along the centreline of the jet to diminish within 5 rotor diameters of the source (Figure 7.9 a). To facilitate analysis, rather than fitting the trajectories to the peak flow speeds (which are commonly used for the empirical derivation of the equation coefficients), the trajectories were instead fitted to the more easily identifiable peak aerosol concentrations. These peak aerosol concentrations have previously been shown to follow shallower trajectories than the peak flow speeds (Campolo et al., 2005). Secondly, the profile of the jet velocity across the jet exit has been observed to be important in dictating resulting flow patterns (Su and Mungal, 2004). In this model, the fairly coarse resolution compared with the rotor diameter may have exaggerated the slowing of the flow near the jet edges, leading to an overly shallow exit angle.

In addition to deflecting the jet, the model also successfully captured the formation of a counter-rotating vortex pair, a dominant feature in the cross-sectional behaviour of the jet in cross-flow (Cortelezzi and Karagozian, 2001). As the ratio of particle response time to air flow response time was significantly smaller than one (~$1x10^{-6}$ for bin 3 aerosols, as captured by the Stokes Number – described for completeness by Equation A.2 in Appendix A), the MCB aerosols behaved as tracers, following the fluid flow (Crowe et al., 1985; Eaton and Fessler, 1994; Diez et al., 2011). Thus, aerosols congregated towards the vortex cores, as demonstrated in Figures 7.12 and 7.13 and in agreement with the numerical modelling of Tu and Liu (2012) and the observations of Wen et al. (1992). Analogously, higher concentrations

of gas tend to co-locate with regions of high vorticity (Fairweather et al., 1988; Crabb et al.; Smith and Mungal, 1998; Huq and Dhanak, 1996). The structure of the counter-rotating vortex pair changed with distance from the emission point (Figure 7.9 c). The increase in diameter of the vortices, weakening of the vorticity and spreading of the vortex pair centres demonstrate the entrainment of cross-flow air that acts to dilute the jet flow (Miller and Garrick, 2004).

In terms of other vortical structures in the simulation, shear layer vortices were apparent as the plume filled the domain (up to t=24 s, Figure 7.6). They were, however, absent in the later, approximately steady-state, flow. This suggests that despite having a scaling of horizontal grid to rotor which is similar to the previous large-eddy simulation experiments of Rudman (1996), the vertical grid spacing may have been insufficient to represent these structures here. As the Brownian coagulation kernel (which depends on aerosol concentration rather than turbulence) was used, these secondary shear layer vortices were less critical than the counter-rotating vortex pair that governs the flow, and hence the distribution of aerosols. These small-scale features would, however, become more critical if a turbulent coagulation kernel were to be used instead (Fu et al., 2013). Simulations investigating the sensitivity of the plume representation to such a turbulent coagulation kernel may be of interest for future work.

While horseshoe and filament-like wake vortices (Figure 7.2) are associated with jets emitted flush from a surface, and were therefore neither expected, nor seen in these elevated jet simulations, other wake phenomenon were present. Aerosols were drawn into the wake of the jet wake, with some vertical bifurcation (Figure 7.6). These phenomena may be the result of physically realistic behaviour, artefacts of the model set-up, or a combination of both.

Wind-tunnel observations have shown that when the jet velocity is less than twice that of the cross-flow velocity – as was the case in these simulations – downwash of the jet fluid into the wake of a jet can occur (Huang and Hsieh, 2002; Huang and Hsieh, 2003). The ensuing horizontal path of the aerosols in these simulations (Figure 7.6) could be a result of their subsequent transport through the domain by the cross-wind. A similar splitting of the plume has been additionally been observed in horizontally-emitted buoyant jets (Arakeri et al., 2000; Deri et al., 2011).

However, the model set-up, particularly the grid spacing, may also contribute towards the vertical bifurcation of the plume. Again, the fairly coarse resolution compared with the rotor diameter may have exaggerated the slowing of the flow near the jet edges. Thus, the faster-moving jet core could have produced the primary trajectory (and counter-rotating vortex pair), while the overly slowed edge flow could have produced the shallower, secondary flow path. Overly coarse model resolution has previously been suggested as a possible cause for

the over-intensification of similar flow patterns in large-eddy simulation modelling of a jet emitted flush to the surface (Majander and Siikonen, 2006).

Aside from the initial cause of the vertical spread of aerosols, it is likely that flow dynamics reinforced the bifurcation apparent in the flow further from the jet emission point (Figure 7.6 and Figure 7.10). As the rotation of the counter-rotating vortex pair entrained surrounding air into the leeside of the jet (Figure 7.14), it created wedges of relatively low aerosol concentration, forcing the more heavily aerosol loaded air into a chevron pattern located below the counter-rotating vortex pair (circled; Figure 7.14).

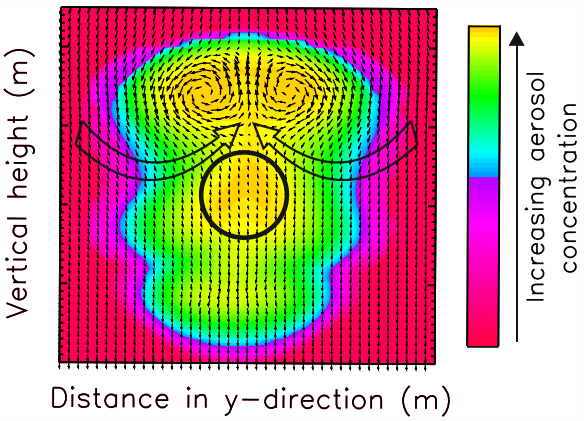

Figure 7.14 *– Reproduction of Figure 7.10 c (Distance = 40d) with black arrow outlines schematically indicating entrained flow, with chevron pattern of jet wake high aerosol concentration circled.*

As the coagulation rate varies with the square of the number concentration (Smoluchowski, 1916), the areas of high aerosol concentration in the counter-rotating vortices exhibited the greatest reductions in aerosol number concentration caused by coagulation (Figure 7.13 b). Further from the emission source, aerosols had more opportunity to coagulate owing to the longer residence times (Yu et al., 2006; Tu and Liu, 2012). This led to the greatest reductions in aerosol number concentration occurring further from the emission source (Figure 7.13 a). It also meant that more larger bin size aerosols were similarly located further from the emission source (Figure 7.11).

These discussions show that the model in this configuration is capable of adequately capturing several key features of the jet in cross-flow behaviour. The validity of these simulations is also supported by the similar coagulation rates achieved using a Gaussian plume model (Stuart et al., 2013). This large-eddy simulation plume model was therefore further utilised to determine how coagulation rates – and the resulting changes in MCB aerosol concentration and size distribution – vary under a range of different assumptions. These sensitivity experiments are presented and discussed in the next section.

7.4 Sensitivity Experiments

This section presents and discusses a range of sensitivity experiments, as detailed in Table 7.1.

7.4.1 Sensitivity Experiments: Results

7.4.1.1 Sensitivity Experiments: Aerosol Emission Rates

The changes in number concentration and mass distribution for the control case are shown in Figure 7.15, along with data for a range of aerosol emission rates from 5.0xSA to 0.1xSA. Owing to the small percentage contribution of the larger bin sizes to the total aerosol number concentration, only bins 3 to 5 are shown. These values are represented as percentages of number concentration or mass in bins 3, 4 and 5 of the CHEM simulation, compared with the sum of number concentration or mass over all bin sizes in the NO_CHEM equivalent simulation. For the domain averages of the lowest emission rate considered (0.1xSA), 90.1% of the aerosol number concentration present in the NO_CHEM case remained in bin 3 in the CHEM simulation. Coagulation led to a number concentration in bin 4 of 0.7% of the total NO_CHEM aerosol number concentration, with 0.001% being present in bin 5. The total aerosol number loss associated with coagulation in the 0.1xSA case was therefore less than 10%. For the domain averages of the highest emission rate considered (5.0xSA) however, only 18.0% of the aerosol number concentration present in the NO_CHEM case remained in bin 3 in the CHEM simulation, with 3.8% in bin 4 and 0.2% in bin 5. Thus, the total aerosol number loss associated with coagulation in the 5.0xSA case was almost 80%.

The relationship between the numbers of aerosols lost and the emission rate is shown in Figure 7.16 (panel a). Increasing emission rates led to increasing percentages of aerosol number concentration loss, although this relationship was not linear with losses increasing rapidly between 0.1xSA and 1.0xSA, but increasing more slowing between 1.0xSA and 5.0xSA. This relationship produced a non-linear increase in total aerosol number with aerosol emission rate (Figure 7.16 b). Thus, the bulk coagulation rates causing this pattern of behaviour appear to not follow the simple proportionality with the square of aerosol concentration relationship (for example, Section 7.2). This phenomenon may be related to the non-uniform distribution of the aerosol concentration through the plume (Section 7.3.1.4) associated with the higher concentrations of aerosols in the counter-rotating vortex pair region. The relative distributions of aerosol concentrations will likely alter under the different aerosol emission rates, leading to the divergence from the bulk ‘proportionality with the square’ relationship.

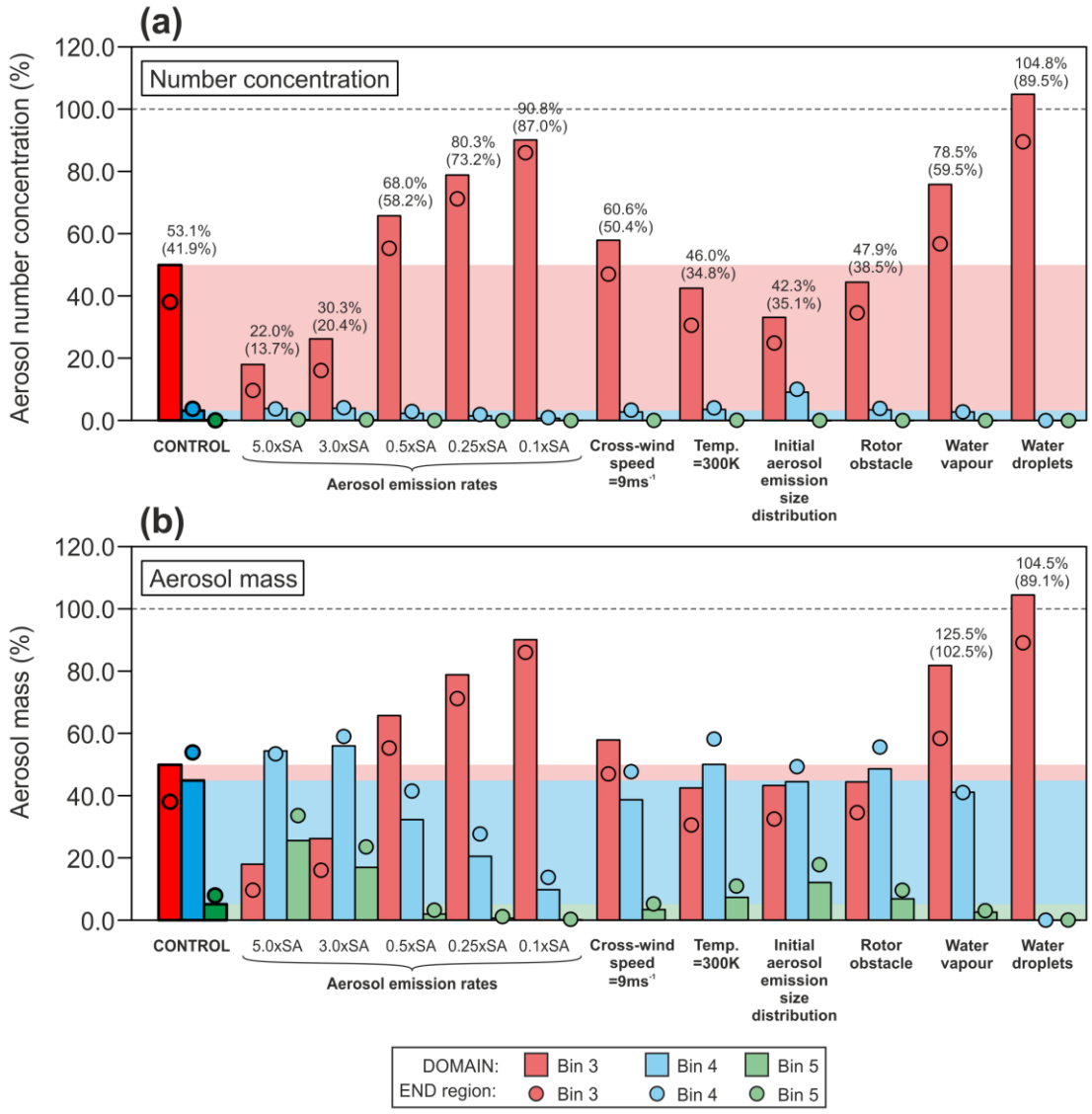

Figure 7.15 *– (a) Percentage of the aerosol number concentration in bins 3, 4 and 5 for the CHEM simulation compared to the NO_CHEM simulation for the domain average (bars) and for the END region average (circles). For the water vapour and water droplets results, this percentage is compared to the control NO_CHEM simulation (therefore omitting both water and aerosol coagulation). Aerosol emission rates given as multiples of that proposed by Salter et al. (2008) (denoted as xSA). Percentages for the sum of all aerosol size bins (1 to 8) are stated numerically for the domain average, and for the END section in brackets; (b) Percentage of the total mass of bin 3, 4 and 5 aerosols as for 'a'.*

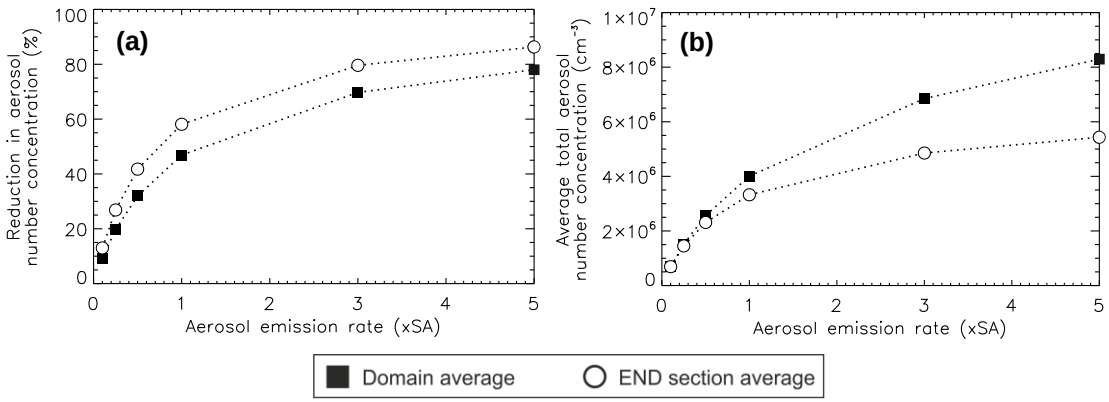

Figure 7.16 *– (a) Percentage reduction in total aerosol number concentration for the CHEM simulations compared to the NO_CHEM simulations for various emission rates; (b) Aerosol number concentrations against aerosol emission rates for the CHEM simulations. Emission rates given as multiples of that proposed by Salter et al. (2008) (denoted as xSA).*

7.4.1.2 Sensitivity Experiments: Cross-wind Speeds

Increasing the cross-wind speed from 6 ms^{-1} to 9 ms^{-1} resulted in a shallower trajectory (Figure 7.17).

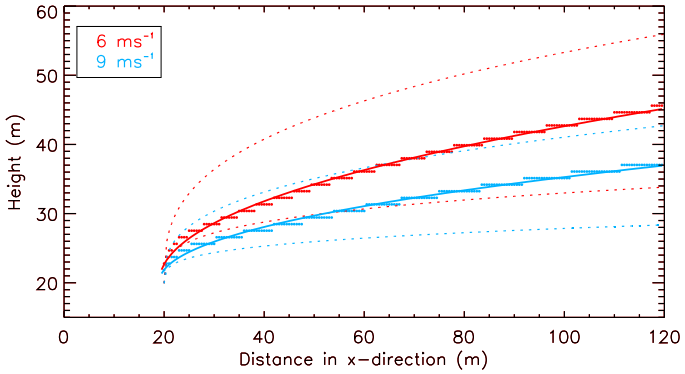

Coefficients to fit Equation 7.1

	A	B
6 ms^{-1} (Bin 6)	1.19	0.48
9 ms^{-1} (Bin 6)	1.03	0.47

Figure 7.17 *– Trajectories for cross-wind speeds of 6 ms^{-1} and 9 ms^{-1}, fitted to Equation 7.1 (solid lines) associated with points of maximum aerosol concentration for bin 6 along the central y-plane. Coefficients for each trajectory fit are stated. Dotted lines indicate expected bounds for the trajectory from previous literature (A=2.6, B=0.36; A=1.2, B=0.28). Data shown 44 seconds from simulation start.*

Owing to the increased cross-flow, the aerosols emitted in the jet travelled through the domain faster for the 9 ms^{-1} flow compared to the 6 ms^{-1} flow. This produced both a lower domain average number concentration (Figure 7.18 a) and lower concentrations of aerosols in each grid cell (Figure 7.18 b) for the 9 ms^{-1} flow compared to the 6 ms^{-1} flow.

The resulting changes in aerosol number concentration and mass distribution are shown in Figure 7.15. The increased wind speed reduced the growth of aerosols to the larger size bins. The inclusion of coagulation therefore reduced domain average aerosol number concentration increases by 39.6% in the 9 ms^{-1} case, compared to a reduction of 46.9% for the 6 ms^{-1} case.

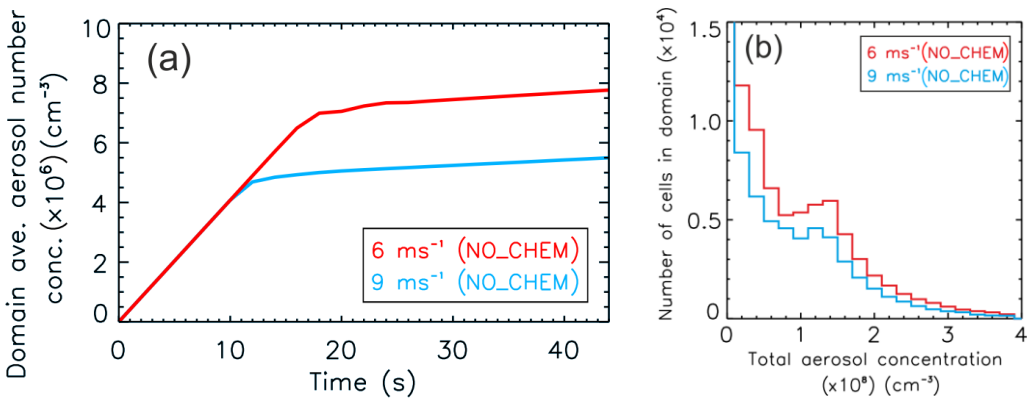

Figure 7.18 *– Cross-wind speed: (a) time series of the domain average aerosol number concentration (cm^{-3}) for the NO_CHEM cases; and (b) the number of cells in the domain containing various aerosol number concentrations (cm^{-3}) in the 6 ms^{-1} and 9 ms^{-1} NO_CHEM simulations, averaged over the 24 to 44 second time period.*

7.4.1.3 Sensitivity Experiments: Background Temperatures

Increasing the background temperature from 288.3 K to 300.0 K increased the rate of coagulation. This increased the transfer of aerosols from bin 3 to the larger bin sizes (Figure 7.15). In doing so, the domain average aerosol losses increased from 46.9% to 54.0%.

7.4.1.4 Sensitivity Experiments: Initial Aerosol Emission Size Distributions

The effect of emitting aerosols into the jet in cross-flow with a size distribution resulting from coagulation within the rotor, as estimated in Chapter 6, is now compared to the case of emitting a monodisperse bin 3 aerosol. Figure 7.15 shows the remaining number concentration and mass when compared to the NO_CHEM monodisperse bin 3 aerosol emission. Thus, the rotor output emission values incorporate both changes that occurred within the rotor, and those that occurred within the plume.

Including the estimated coagulation that occurred within the rotor led to a larger transfer of aerosols from bin 3 to larger bin sizes. This led to an overall decrease in domain averaged total number concentration of 57.7% compared to the monodisperse bin 3 emission case (which led to a total number decrease of 46.9%). For the END section, these coagulation-induced number concentration decreases were 64.9% and 58.1% respectively. Table 7.3 states the number concentrations of aerosols compared to the background case for the monodisperse (bin 3) emission case and the rotor output emission case. The increased losses in bin 3 number concentration for the rotor output emission case compared to the monodisperse emission case, and resulting increases in number concentrations in larger bins (notably bins 4 and 5) can be seen.

Table 7.3 *– Domain average perturbation in aerosol number concentrations (cm^{-3}) from background concentrations for monodisperse (bin 3) emission and rotor output emission. Values are averaged over 24 to 44 seconds. END section averages are given in brackets.*

Bin size	ΔAerosol number conc. (cm^{-3})	
	Monodisperse (bin 3) emission	Rotor output emission
Bin 3	$3.8x10^{6}$ ($3.0x10^{6}$)	$2.5x10^{6}$ ($2.0x10^{6}$)
Bin 4	$2.4x10^{5}$ ($3.0x10^{5}$)	$6.8x10^{5}$ ($8.0x10^{5}$)
Bin 5	$3.4x10^{3}$ ($5.5x10^{3}$)	$8.0x10^{3}$ ($1.2x10^{4}$)
Bin 6	$7.5x10^{0}$ ($1.5x10^{1}$)	$1.8x10^{1}$ ($3.4x10^{1}$)
Bin 7	$3.2x10^{-3}$ ($6.4x10^{-3}$)	$6.9x10^{-3}$ ($1.4x10^{-2}$)
Bin 8	$6.8x10^{-5}$ ($6.8x10^{-5}$)	$6.8x10^{-5}$ ($6.9x10^{-5}$)

In an additional test, the rotor output emission was scaled up such that the total number concentration was equal to the monodisperse (bin 3) emission. This experiment resulted in coagulational total number concentration losses of 46.2% for the domain (and 57.4% for the section average). These were similar to the monodisperse (bin 3) emission number concentration reductions of 46.9% and 58.1% respectively, suggesting that coagulation rates are more sensitive to changes in aerosol number concentrations than they are to the presence of larger aerosols that could potentially be formed within the rotor.

7.4.1.5 Sensitivity Experiments: Inclusion of a Rotor Obstacle

Emitting the jet in to the cross-flow in the absence of the rotor produced a straight plume and obvious counter-rotating vortex pair (Figure 7.5). The Kármán vortex street flow pattern induced by the inclusion of a rotor is shown in Figure 7.19 (panel a). Figure 7.19 b is a schematic of the cross-section of this rotor case, defining terminology used in presenting and discussing this case.

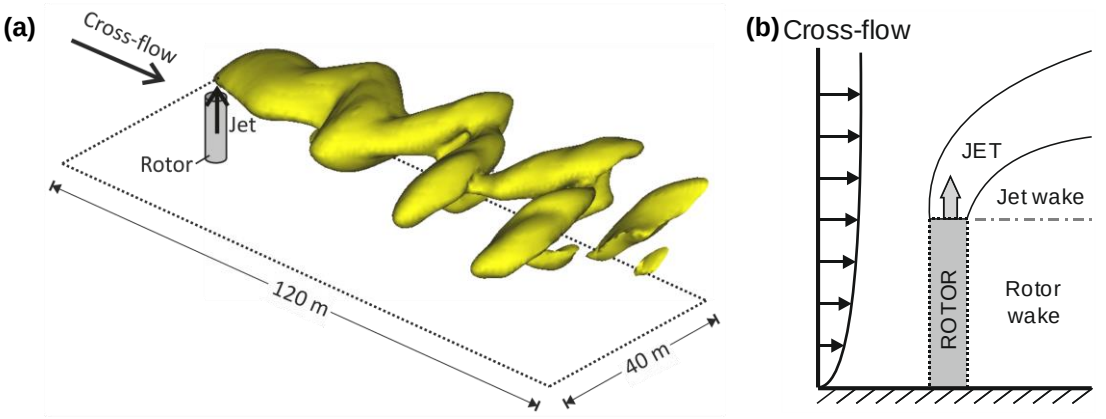

Figure 7.19 *– (a) Instantaneous isosurface for a given aerosol concentration, showing the typical structure of a simulated jet in cross-flow in the presence of a rotor. (b) A schematic depicting the jet and rotor wake regions, following Adaramola et al. (2012).*

Figure 7.20 shows horizontal sections through the rotor and jet wakes, with flow vorticities, indicating a weaving flow pattern. Vortices shed from either side of the rotor can be identified by the opposing signs of vorticity. The oscillations observed in the rotor wake (Figure 7.20 a) exhibit a more regular structure than those in the jet wake (Figure 7.20 b) which appear to be elongated. This is illustrated by the labelled points (W1, W2 and W3) in the figure. Over the final 20 seconds of the simulation, approximately four cycles were shed, leading to a vortex shedding frequency of approximately 0.2 Hz.

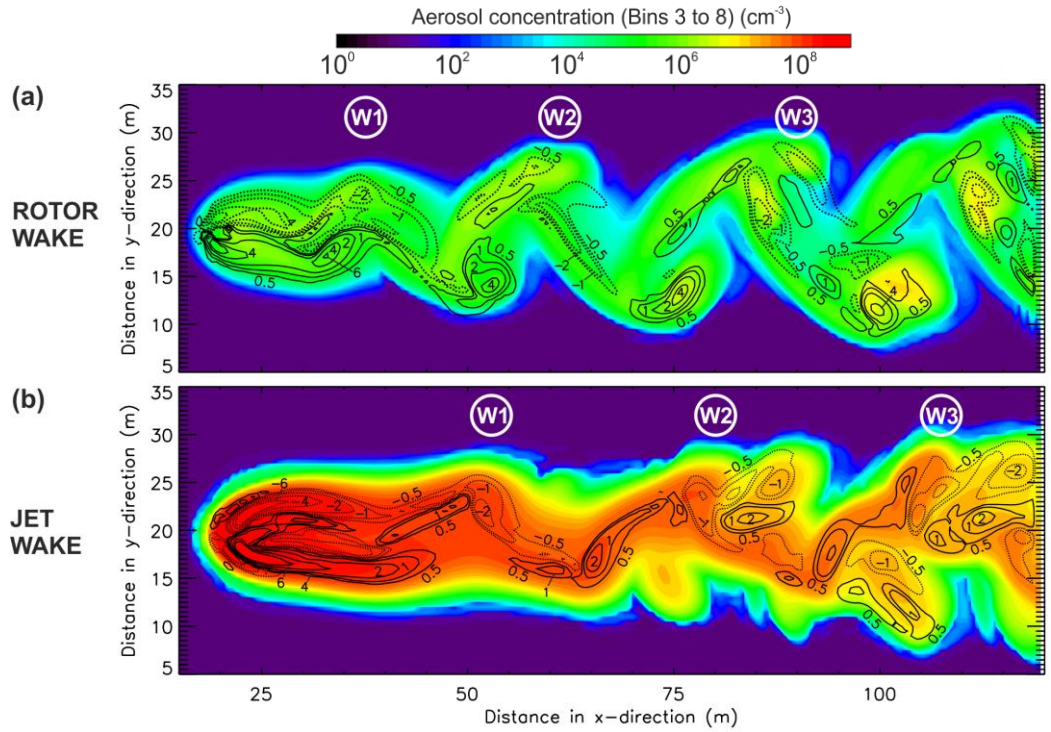

Figure 7.20 *– Horizontal sections for the inclusion of rotor case. Rotor located at x=20m, flow from left to right. Filled coloured contours show the interstitial aerosol number concentration totalled over bins 3 to 8 (cm^{-3}); with black line overlay contours indicating vorticity (solid = positive, dotted = negative) for the: (a) Rotor wake (~10 m above the surface); and (b) Jet wake (~24 m above the surface). Both at 44 seconds from simulation start. Labels W1, W2 and W3 indicate vortex tips for discussion in the text.*

The vertical distribution of aerosols in response to the inclusion of the rotor is shown in Figure 7.21. The aerosols were rapidly drawn lower than was the case when the rotor was omitted (cf. Figure 7.6). Further differences include a shallower trajectory of the upper bound of the plume compared to the rotor omitted case, and the previously smooth flow path becoming disordered (although some periodicity in the flow pattern is evident).

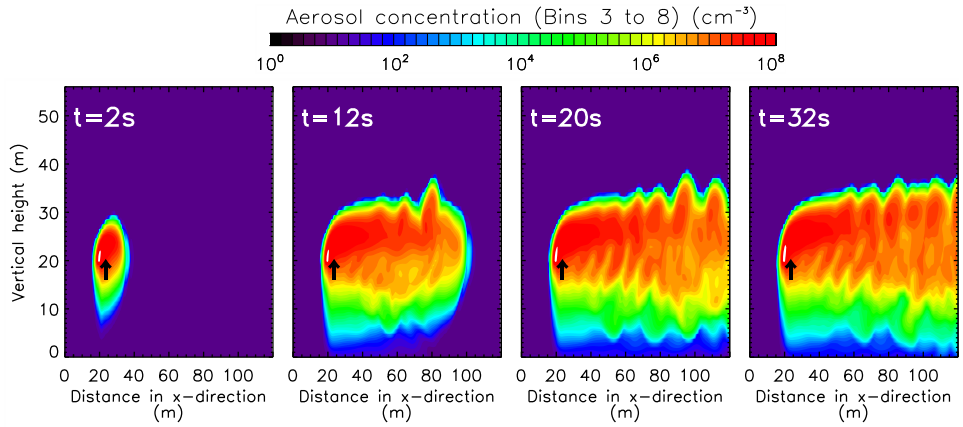

Figure 7.21 *– Domain average aerosol concentrations (total of bin sizes 3 to 8, averaged over the y-direction) through time with inclusion of the solid rotor. The crosswind flows from left to right. Black solid arrows indicate the location of the emission point.*

The inclusion of the rotor increased the domain average total number concentration compared to when the rotor is omitted by around 13% by the end of the simulation (Figure 7.22 a), suggesting that the rotor influenced plume was slower to leave the domain. Figure 7.22 b indicates that the presence of the rotor results in a narrower distribution of aerosol concentrations, with a larger number of grid cells having a lower aerosol concentration, and fewer grid cells containing a high aerosol concentration.

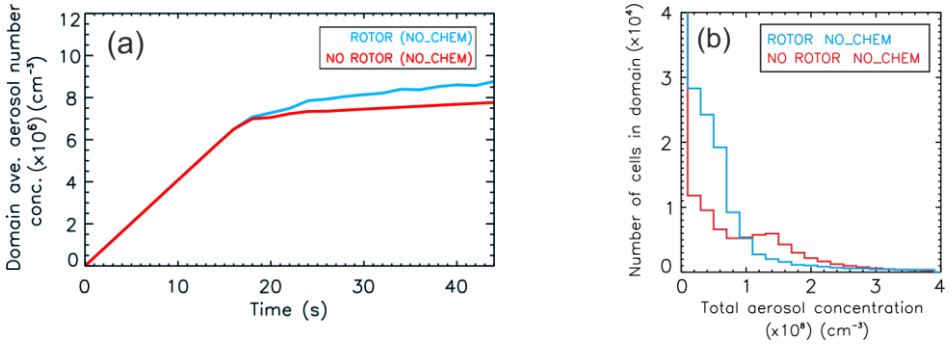

Figure 7.22 *– Inclusion of rotor: (a) time series of the domain average aerosol number concentration (cm^{-3}) for the NO_CHEM cases; and (b) the number of cells in the domain containing various aerosol number concentrations (cm^{-3}) in the rotor and no rotor NO_CHEM simulations, averaged over the 24 to 44 second time period.*

Figure 7.15 shows that there was an increase in coagulation when the rotor was included, with a reduction in aerosol number concentration of 52.1% (compared to 46.9% for omission of the rotor). This increase in coagulation may be caused by the higher domain average

aerosol number concentration when the rotor is included, in spite of there being fewer cells with higher aerosol concentrations.

7.4.1.6 Sensitivity Experiments: Including Water Vapour With the Emission

Including water vapour with the jet and MCB aerosol emission into the cross-wind resulted in a more disordered plume (Figure 7.23) compared with the case where water vapour was omitted (cf. Figure 7.6). The lower edge of the plume generally rose higher than the water vapour omitted case, while in some locations, the upper edge of the plume was also several meters higher. The plume also reached the end of the domain more rapidly. Unlike the plume resulting from the inclusion of the rotor, there was no apparent periodicity in the plume structure (cf. Figure 7.21).

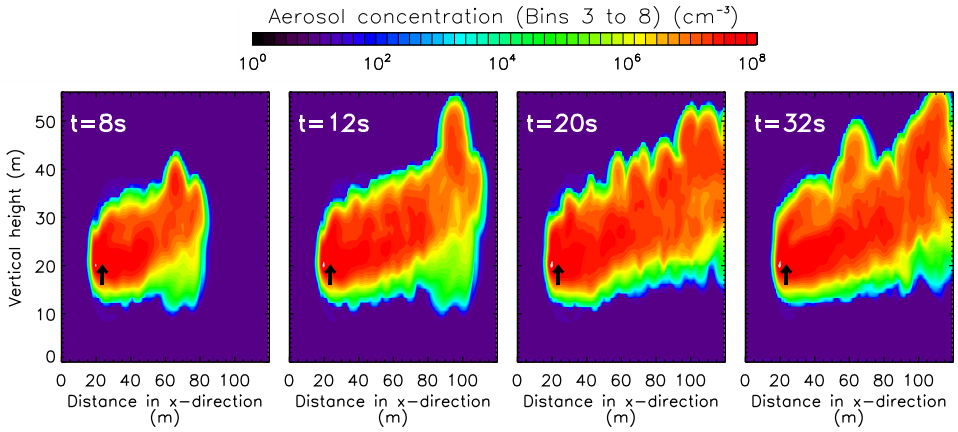

Figure 7.23 *– Domain average interstitial aerosol concentrations (total of bin sizes 3 to 8, averaged over the y-direction) through time, for the case where water vapour emission is included. The crosswind flows from left to right. Black solid arrows indicate the location of the emission point.*

In the plume cross-section (Figure 7.24), a counter-rotating vortex pair was still present with similarly spaced centres and rotational directions as for the non-water vapour simulation (labelled ‘A’). However, including water vapour in the jet emission did alter portions of the plume cross-sections. Close to the emission source (at a distance of approximately 5 rotor diameters, ‘5d’) and at a height approximately equal to it, arose an area of updrafts (labelled ‘B’, Figure 7.24). This region of updrafts was coupled to the overlying counter-rotating vortex pair via a series of eddies which extended to around double the width of the counter-rotating vortex pair. Further from the emission source (at approximately 20 rotor diameters, ‘20d’; Figure 7.24), these updrafts diverged (labelled ‘C’; Figure 7.24) resulting in a broadening of the plume. Here, the symmetry of the counter-rotating vortex pair was lost. No indication of the counter-rotating vortex pair remained further from the emission source (at approximately 35 rotor diameters, ‘35d’). Here, the outward flow of the deflected updrafts continued to widen the plume, which now filled the domain, and several eddy structures were present throughout the plume.

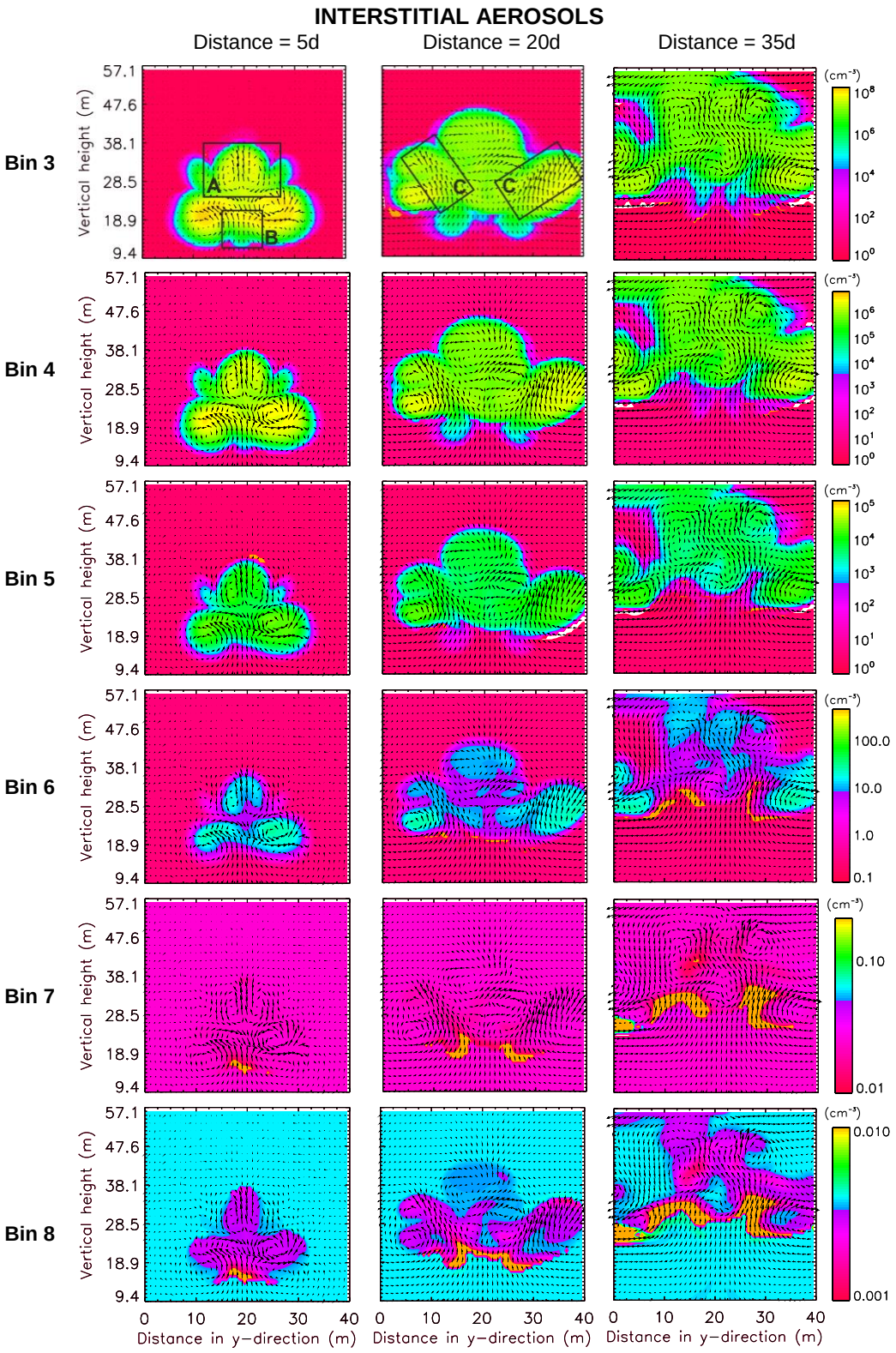

Figure 7.24 *– Sections of vertical planes at 5, 20 and 35 times the diameter of the rotor (following the control simulation trajectory), showing the distribution of bin 3 to bin 8 interstitial aerosol concentrations (cm^{-3}) for the CHEM simulation including water vapour emission overlaid by arrows showing velocities of the flow. Data shown 44 seconds from simulation start. Boxes labelled A, B and C denote areas of dynamical interest for discussion in the text.*

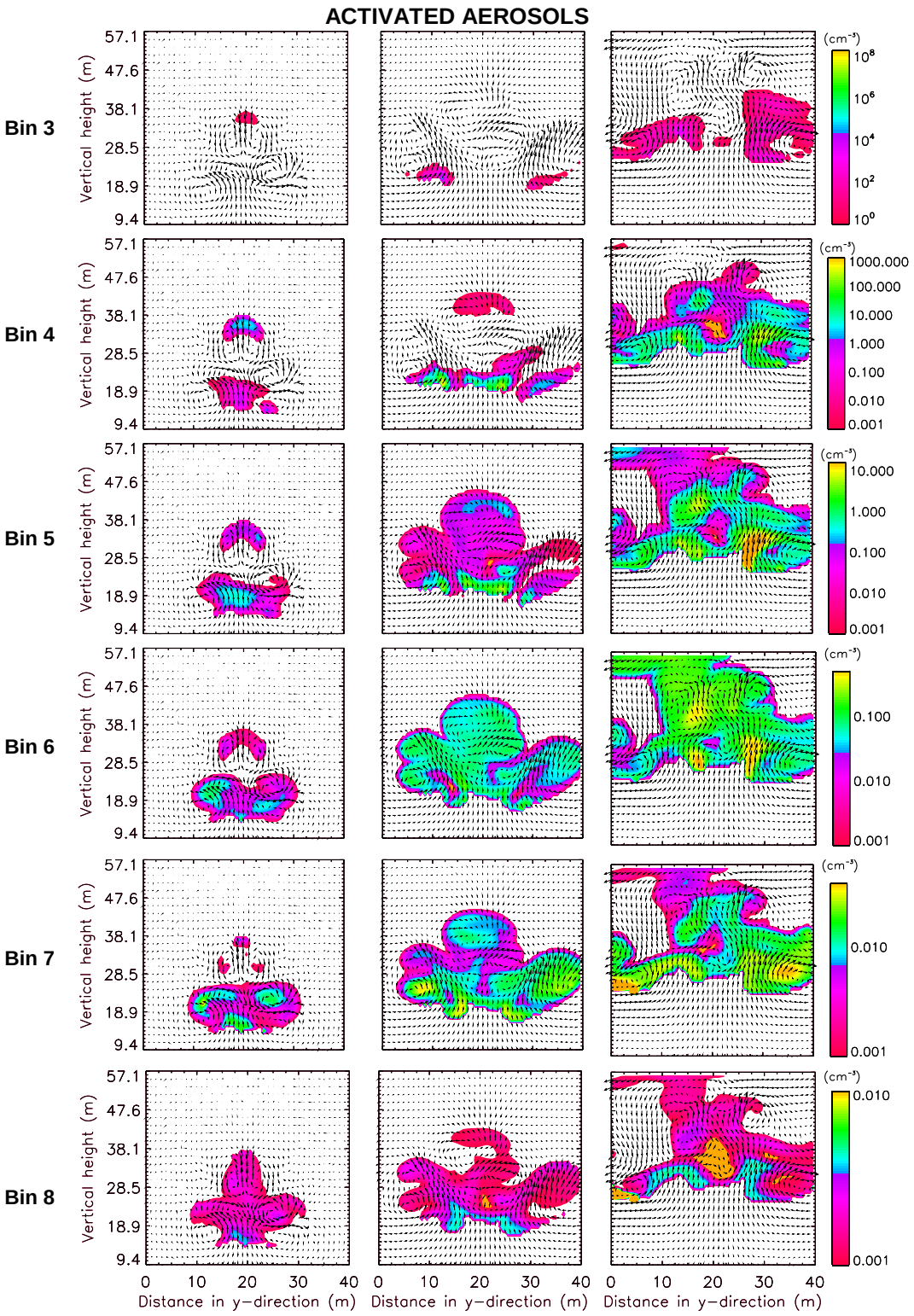

Figure 7.25 *– Sections of vertical planes at 5, 20 and 35 times the diameter of the rotor (following the control simulation trajectory), showing the distribution of bin 3 to bin 8 activated aerosol concentrations (cm^{-3}) for the CHEM simulation including water vapour emission overlaid by arrows showing velocities of the flow. Data shown 44 seconds from simulation start.*

The distribution of interstitial aerosols within these flow structures (Figure 7.24) again showed preferential concentration in areas of high vorticity, similar to the simulations that omitted water vapour emission. Thus peaks in interstitial aerosol concentration were again formed in vortical regions. Also as occurred for the water vapour omitted simulation, the interstitial aerosols grew in these regions of aerosol. However, the aerosol concentrations in bin sizes 4, 5 and 6 were consistently an order of magnitude smaller than the water vapour omitted case (Figure 7.24, cf. Figure 7.11).

The increase in supersaturation associated with this emission of water vapour was sufficient for some aerosols to become activated (Figure 7.25). The distribution of activated aerosols shows bin 8 interstitial aerosols were being activated at a concentration of up to ~0.01 cm^{-3}, resulting in an apparent depletion of bin 8 interstitial aerosols in these areas. The number concentration of activated bin 3 aerosols was, however, approximately four orders of magnitude larger (~100 cm^{-3}). The concentration of activated aerosols increases with distance from the source.

Figure 7.26 shows that the inclusion of water vapour in the emission led a maximum temperature increase of 78 K resulting from the condensation of water onto the aerosol particles. Close to the emission source, the water vapour mixing ratio rose by 500 g $kg_{dry\ air}^{-1}$, while the cloud water mixing ratio rose by 25 g $kg_{dry\ air}^{-1}$. Further from the source, where the plume has dispersed, temperature increases along the centreline were below 10 K and cloud water and water vapour mixing ratio increases were 1 g $kg_{dry\ air}^{-1}$. While the sign of these changes are as expected (i.e. with warming associated with condensational heating), the magnitudes of the perturbations are unlikely to be realistic, particularly close to the emission source. From an energy conservation viewpoint, temperature increases of this magnitude reinforce that significant energy inputs would be needed in order to produce this water vapour emission scenario. Such an energy intensive process would likely prevent this scenario from being practically viable. Owing to lack of comparable observed cases, the performance of the model under these extreme conditions cannot be verified.

Finally, Figure 7.15 shows the aerosol number and mass changes associated with the inclusion of both water vapour and coagulation. Aerosols include both interstitial and activated aerosols. The inclusion of water vapour increased the total aerosol mass over the domain to 125.5% of the case where both water vapour and coagulation were omitted. This total aerosol mass was, however, only 102.5% for the END region, indicating similar aerosol amounts in this location. Both the number concentration and aerosol mass plots indicated that more aerosols remained in bin size 3 than grew sufficiently to enter bin 4 compared to the non-water vapour emitting case, both for the domain as a whole, and for the END region.

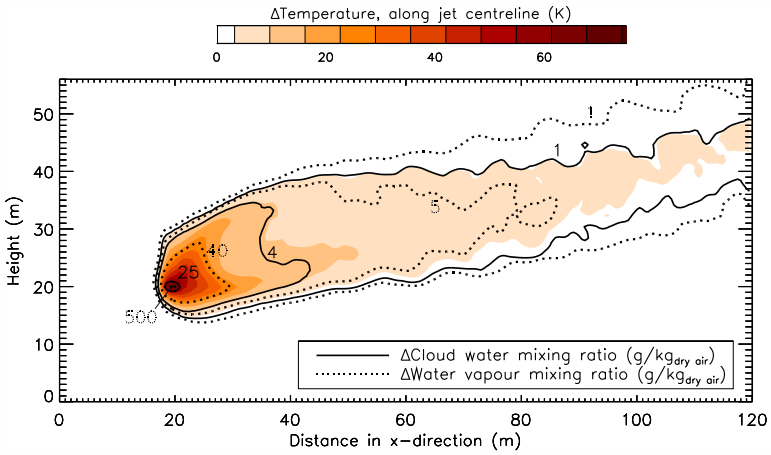

Figure 7.26 *– Temperature perturbation (K) (coloured contours); cloud water mixing ratio (g $kg_{dry\ air}^{-1}$) (solid black contours) and water vapour mixing ratio (g $kg_{dry\ air}^{-1}$) (dotted black contours) along the centreline of the jet for the case where water vapour emission is included.*

7.4.1.7 Sensitivity Experiments: Including Water Droplets With the Emission

Including water droplets with the jet and MCB aerosol emission into the cross-wind produced a plume with the shear-layer vortex type structures (Figure 7.27), and latterly smooth configuration as was associated with the dry aerosol emission simulation (cf. Figure 7.6). However, for this water droplet emission, the plume descended, with the lower edge reaching the surface approximately 16 seconds after the simulation start. The depth of the plume was also reduced compared to the non-droplet simulation.

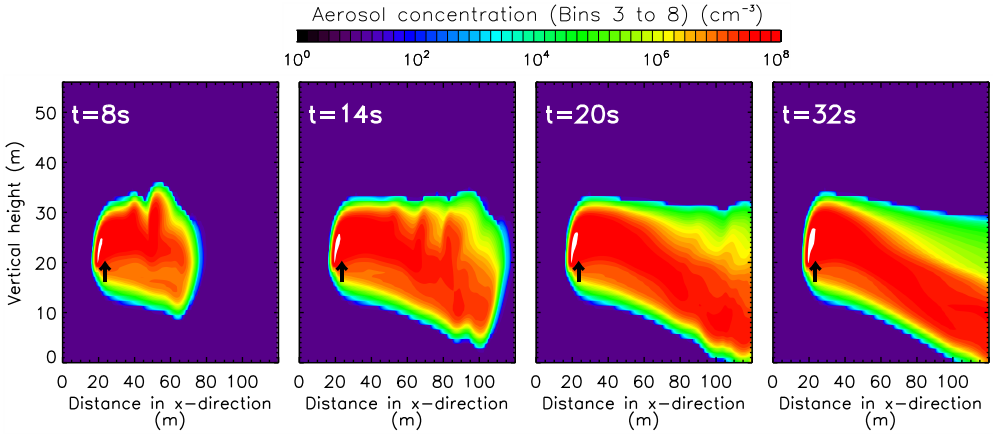

Figure 7.27 *– Domain average interstitial aerosol concentrations (total of bin sizes 3 to 8, averaged over the y-direction) through time, for the case where water droplet emission is included. The crosswind flows from left to right. Black solid arrows indicate the location of the emission point.*

A counter-rotating vortex pair was again present in the plume cross-section close to the emission point (labelled 'A' in Figure 7.28). While the directions of rotation were the same as for the non-droplet simulation, these counter-rotating vortices were smaller and had closer centres. The simulation of the emission as droplets again altered portions of the plume cross-section. Here, close to the emission source (at a distance of approximately 5 rotor

diameters, ‘5d’), an additional weaker counter-rotating vortex pair is formed below the main vortex pair feature. The rotations of this peripheral counter-rotating vortex pair are contrary to the main vortex pair, with flow being directed downwards at the centreline.

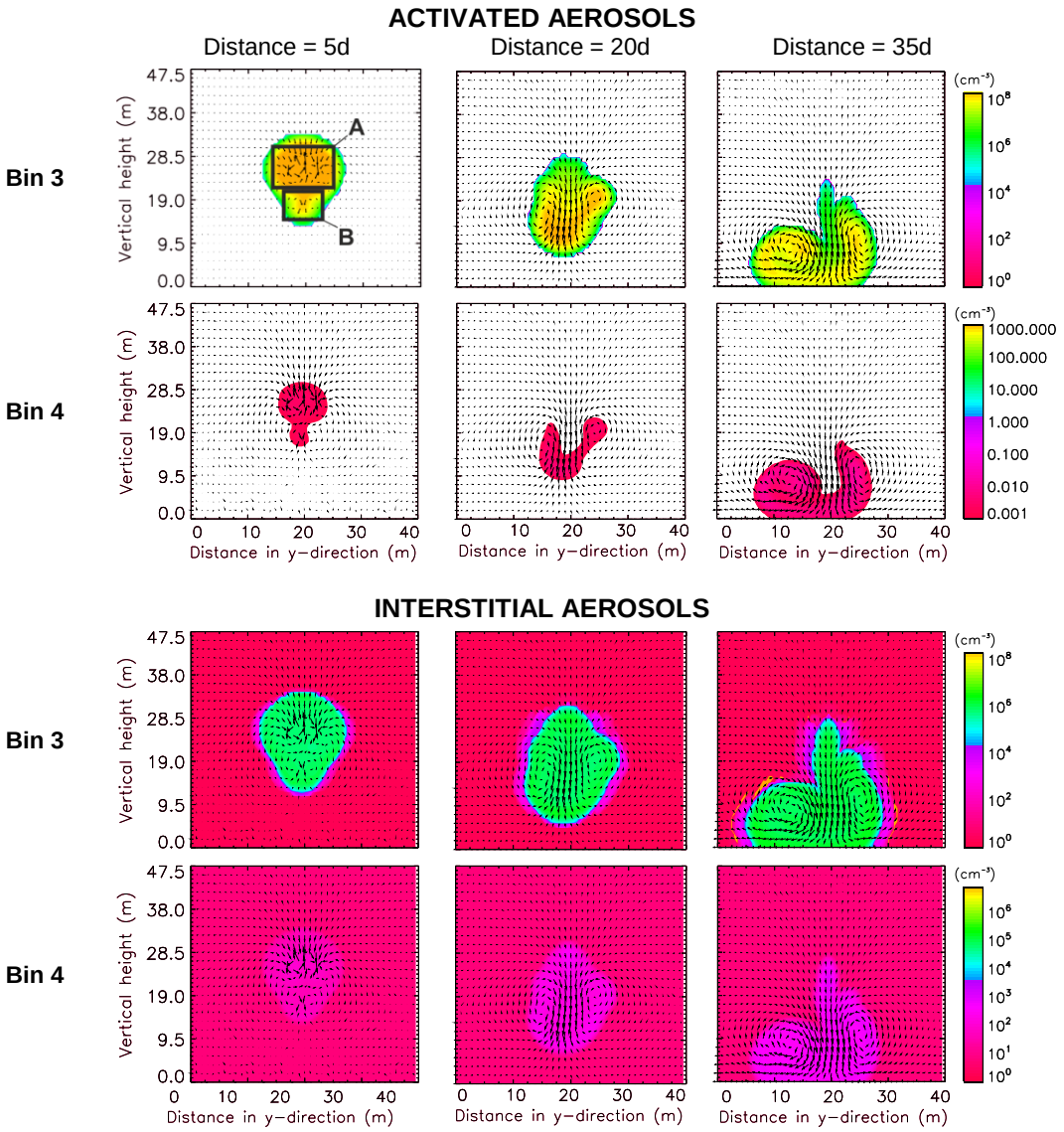

Figure 7.28 *– Sections of vertical planes at 5, 20 and 35 times the diameter of the rotor (following the control simulation trajectory), showing the distribution of bins 3 and 4 activated and interstitial aerosol concentrations (cm^{-3}) for the CHEM simulation including water droplet emission overlaid by arrows showing velocities of the flow. Data shown 44 seconds from simulation start. Boxes labelled A and B denote areas of dynamical interest for discussion in the text.*

Further from the emission source (at approximately 20 rotor diameters, ‘20d’), the double pairing of counter-rotating vortices is lost and only one counter-rotating vortex pair structure remains. This remaining counter-rotating vortex pair has the rotation of the lower vortices, characterised by the now more strongly descending central region. By approximately 35 rotor diameters (‘35d’), this vortex structure remains, although the downward motion has forced it to the sea surface.

While all aerosols were emitted into the activated bin size 3, evaporation of the droplets led to aerosols entering the interstitial phase (Figure 7.28). In this simulation set-up, around ten times the number of aerosols remained as activated droplets than evaporated to interstitial aerosols. Evaporation caused a small amount of cloud water mixing ratio to move to the water vapour phase (0.1 g $kg_{dry\ air}^{-1}$; Figure 7.29). This evaporation additionally resulted in a temperature decrease of just under 1 K in the region of the plume (Figure 7.29).

Very few of the activated droplets grew sufficiently to enter the activated bin size 4. Thus, no droplets grew to form raindrops, and no wet scavenging occurred. Aerosols that evaporated to the interstitial phase grew to bin 4 size, although the resulting number concentrations were around four orders of magnitude smaller than occurred in the dry aerosol emission case.

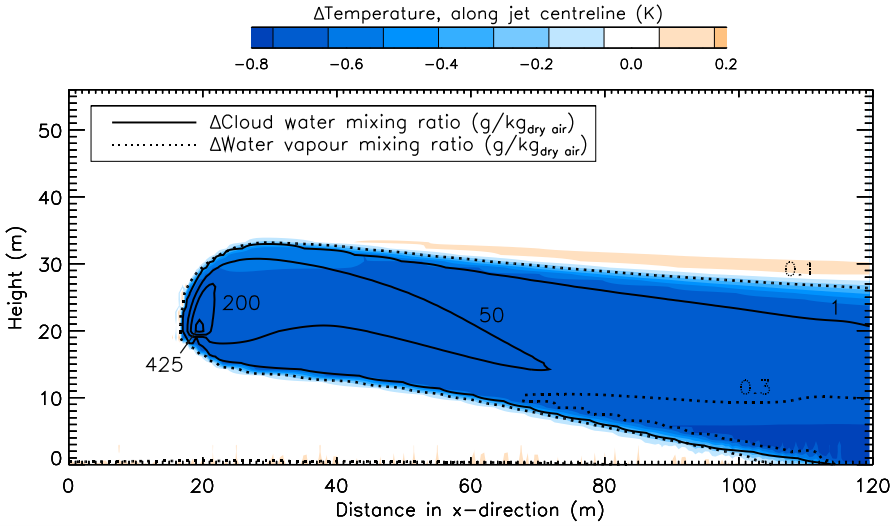

Figure 7.29 *– Temperature perturbation (K) (coloured contours); cloud water mixing ratio (g* $kg_{dry\ air}^{-1}$*) (solid black contours) and water vapour mixing ratio (g* $kg_{dry\ air}^{-1}$*) (dotted black contours) along the centreline of the jet for the case where water droplet emission is included.*

The aerosol number concentration and mass changes for the emission of droplets is compared to the simulation of dry aerosol, with no coagulation in Figure 7.15. Aerosols again include both interstitial and activated aerosols.

Emitting the aerosols as droplets did not largely affect the total domain mass (104.5% of the dry aerosol simulation), suggesting that – despite the different dynamics – similar amounts of aerosols were present in the domain. The number of aerosols growing to larger size bins in this droplet emission case was smaller than for all previous conditions considered, with the majority of aerosols remaining in bin size 3.

7.4.2 Sensitivity Experiments: Discussion

The counter-rotating vortex pair arose for sensitivity experiments covering the aerosol emission rates, cross-wind speeds, background temperatures and aerosol emission size distributions. The counter-rotating vortex pair was no longer apparent when the solid rotor was included in the simulated. Instead, the jet formed a Kármán vortex street. Unlike the distinct and sustained vortices that would be formed for a non-turbulent flow around a solid rotor (exemplified in Figure 7.30; Williamson, 1996), the Kármán vortex street formed here exhibited faster dissipation and correspondingly less uniform properties associated with turbulent flow (Roshko, 1954).

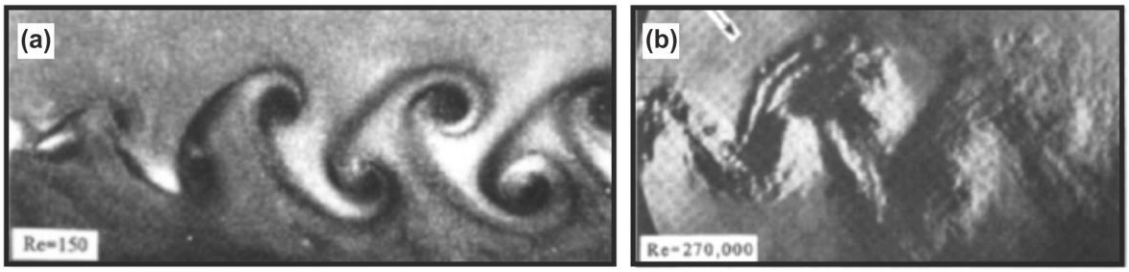

Figure 7.30 *– Visualisation of experimentally obtained Kármán vortex streets, as viewed from above, for (a) Non-turbulent flow and (b) Turbulent flow. Images from Williamson (1996). Flow is from left to right with the obstacle located near to the left edge of each panel.*

This turbulent nature is consistent with the high $1x10^6$ Reynolds Number associated with the flow (described by the standard Equation A.4 included for completeness in Appendix A, for an assumed fluid velocity of ~6 ms^{-1}, past a rotor of diameter 2.5 m with kinematic viscosity of air of ~$1.5x10^{-5}$ m^2 s^{-1}), which exceeds the $5x10^5$ threshold needed for turbulence. Figure 7.20 indicates that there was dynamical 'lock-in' between the flows in the rotor wake and in the jet wake (Moussa et al., 1977; Eiff et al., 1995). The apparent offsetting and elongation of the jet wake likely resulted from the faster cross-flow above the rotor obstacle, although details of the linkages between the two wakes are complex and currently not well-understood (Adaramola et al., 2012). To further validate the authenticity of these wake formations, Equation 7.2 can be used:

$$\text{Vortex shedding frequency} = \frac{StU}{D} \qquad (7.2)$$

where:

St = Strouhal Number

U = fluid flow velocity (ms^{-1})

D = obstacle diameter (m)

The simulated frequency of vortex shedding observed in the simulations (~0.2 Hz), cross-flow velocity (~4 ms^{-1}; reduced from the free-flow velocity of 6 ms^{-1} in the wake of the rotor obstacle) and rotor diameter (~2.5m) suggests a Strouhal Number of 0.125. While this value is lower than the 0.2 typical for a rough cylinder (Lienhard, 1966; Achenbach and Heinecke, 1981), the fit can be improved to 0.175 by increasing the rotor diameter to account for the crudity of the simulated rotor (Figure 7.4 b).

The resolution of the model necessitates the representation of the rotor as an essentially rough cylinder. However, in practice, the rotor would likely be smooth. Smooth cylinders have Strouhal Numbers of approximately 0.5 (Lienhard, 1966; Achenbach and Heinecke, 1981), which would increase the frequency of vortex shedding by more than two. The possible presence and nature of Kármán vortex streets has been explored by Latham et al. (2012a) using computational fluid dynamics. While Kármán vortex streets were simulated for a non-rotating rotor in turbulent flow (as here), rotating the rotor led to the organised wake structures breaking-down forming "unsteady three-dimensional structures". Adding the Thom discs (which are beneficial for the vessel's propulsion efficiency) eliminated Kármán vortex streets for the non-rotating rotor case, and decreased the amplitude of wake disturbances greatly compared to the bare rotor when rotating. Latham et al. (2012a) concede that further investigation would be needed to determine whether wake oscillations would be present. The slightly higher, more homogeneous, aerosol concentrations resulting from the rotor induced Kármán vortex street only slightly increased coagulation in the simulations presented here. This coagulation increase was less than increasing the background temperature from 288.3 K to 300.0 K, as so may not have a significant effect in reality.

The effect of the rotation of the rotor on the aerosol plume has not been considered here. Possible changes that may result to the turbulent profile of the plume, and therefore to the coagulation rates of aerosols within the plume would be an interesting feature to consider in future work.

As discussed in Chapter 5, while it is anticipated that the MCB aerosols would be formed from sea water (Salter et al., 2008), the formation mechanism has yet to be finalised. It is therefore possible that either water vapour or water droplets could be emitted as a result of this process. In these plume simulations, the inclusion of water affected both the structure of the counter-rotating vortex pair, and the trajectory of the plume.

When water vapour was added to the emission of interstitial aerosols, condensation onto the aerosols led to temperature increases, peaking close to the emission source. While the resulting temperature increases were likely larger than realistically feasible (particularly close to the emission point), the simulations can yield qualitative information on possible ensuing patterns of behaviour. For example, the resulting buoyancy increases caused by these

temperature increases led to updrafts in the plume (box labelled B; Figure 7.24). These updrafts disrupted the counter-rotating vortex structure and caused the plume cross-sectional area to expand, resulting in lower aerosol concentrations and, in spite of the temperature increases, consequently lower rates of coagulation. This plume expansion is likely underestimated, particularly further from the emission source, as the buoyant plume now impinges on the upper domain boundary. The lower coagulation rates, and increased plume height would likely be beneficial for both cloud perturbations and for the delivery of the aerosols to the cloud.

While the concentrations of activated aerosols are several orders of magnitude smaller than the interstitial aerosols, coalescence may still be sufficient to induce precipitation, which could deplete the total aerosol concentration via wet scavenging. Owing to current model limitations, it is unclear whether the potential benefits for MCB of the buoyancy-induced plume rise and expansion would outweigh the potentially detrimental effects of condensing the emitted water vapour to form droplets. For modelling of this scenario to produce such information, it would have to be further developed, particularly to address the currently unrealistic droplet coalescence behaviour and magnitudes of temperature perturbations. It is again noted that producing sea salt aerosol from the evaporation of sea water – as is assumed in this particular scenario – would be a highly energy intensive production method (Neukermans et al., 2014). As such, it is unlikely that this particular scenario would occur in reality.

When the aerosol emission was simulated as sea water droplets, evaporation of these droplets led to temperature decreases throughout the plume. This finding reinforces the coarser resolution simulations performed in Chapter 5 and supports the idea that cold pools will hold the aerosol plume closer to the surface. The resulting negative buoyancy again disrupted the counter-rotating vortices, and caused the plume to descend to the surface. The small aerosol growth rates that occurred in this simulation are likely the result of two effects. Firstly, evaporation led to concentrations of interstitial aerosols that were at least two orders of magnitude smaller than previously simulated. Hence, along with the lower temperatures, the rates of interstitial aerosols coagulation were significantly reduced. Secondly, the rates of droplet coalescence were likely to be severely underestimated owing to the inadequacies of the representation of droplet coalescence within the two-moment microphysics parameterisation, as discussed for the water vapour simulation. Importantly, with the plume now being forced to the sea-surface, surface aerosol losses would be expected. Model inadequacies in simulating this case (just discussed) prevent realistically founded estimates of such losses from being produced from these simulations. This finding will likely be of significant interest in future work however.

The use of large-eddy simulations in modelling of MCB aerosol plume details is novel. The introduction of further details such as the rotor and water upon emission increasingly challenged the model's ability to represent the plume behaviour. Yet, the model was successful in simulating feasible responses, such as plume trajectories, counter-rotating vortex pairs, aerosol distributions, Kármán vortex streets, and responses to buoyancy changes resulting from the inclusion of water. The development of these findings could be extended along several routes. Firstly, the simulations presented here form only a small subset of possible conditions. These could be extended to provide a more comprehensive understanding of the sensitivities within the plume. Secondly, limitations of this model set-up have been demonstrated, particularly in the crudity of the rotor representations and in the likely underestimations of droplet coalescence in the droplet emission scenario. To advance these simulations, higher resolutions would be necessary, as well as refinements to the microphysical scheme suited to this application. Other modelling techniques, including computational fluid dynamics, may also improve the representation, with variable resolutions allowing detailed grid-cell spacing near to the emission source. However, the usefulness of extensive further simulations at this time may be limited owing to the uncertainties arising from both lack of observational data for verification, and design details. For example, validation of the flow behaviour here has largely been qualitative, owing to the paucity of appropriate experimental data. The data gained from scaled experiments with appropriate flow attributes and rotor dimensions would therefore be beneficial.

7.5 Conclusions

This chapter – the second to examine the final MCB implementation detail case study – presents simulations of the highly concentrated MCB aerosol plumes produced upon emission into the marine boundary layer.

The initial control plume, presented in the first part of this chapter, shows that the WRF/Chem model (used at increased resolution compared to previous cloud-resolving modelling) is capable of reproducing a number of features expected for a jet in a cross-flow scenario. These features include feasible plume trajectories, patterns of pressures and aerosol distributions within the plume, and the formation of a counter-rotating vortex pair. The ability to capture these details attests to the validity of these simulations. Coagulation within this highly concentrated MCB aerosol plume simulation approximately halved the total emitted aerosol number concentration, causing the diameter of some aerosols to increase by ~8 times.

Following on from the confidence gained in the performance of the model during this initial detailed examination of the control plume, the latter part of the chapter presented results of sensitivity experiments using the same model. Rates of coagulation were found to be

sensitive to a number of factors. However, the magnitude of these sensitivities varied. For example, increasing the MCB aerosol emission rate to five times the control rate increased aerosol number concentration reductions to nearly 80%, while reducing the emission rate to a tenth of the control rate decreased the reductions to less than 10%. However, increasing the wind speed from 6 ms^{-1} to 9 ms^{-1} only decreased number concentration reductions from 47% to 41%, while increasing the temperature from 288.3 K to 300.0 K only increased number concentration reductions from 47% to 54%. This limited number of experiments additionally reinforced the validity of the model by confirming that the simulated change in behaviour matched those expected based on physical principles. Covering the wider parameter space associated with all possible MSc conditions would require further simulations, and is outside of the scope of this current work.

A further sensitivity experiment included the additional coagulation that may occur within the rotor (resulting from the simple numerical integration scheme presented in Chapter 6). Along with increased number concentration reductions (from 47% to 58%), this deviation in the initial aerosol emission size distribution from the monodisperse assumption more than doubled the number concentrations of larger aerosols, with this change in size distribution being possibly important for how effectively the MCB aerosols alter cloud albedo.

By introducing a solid rotor into the simulations, the expected Kármán vortex streets in both the rotor and jet wakes were successfully reproduced. While the change in simulated dynamics was sufficient to disrupt the formation of the counter-rotating vortex pair, coagulation rates were not significantly altered, with number concentration losses increasing only from 47% to 52%.

Finally, while the inclusion of water in the plume led to some feasible features being represented (for example, latent heat fluxes and buoyancy perturbations), the inability of the model to adequately relate turbulence to droplet coalescence for this plume modelling, likely led to underestimated droplet growth. The inclusion of water did lead to evaporative cooling and plume descent (in support of the coarser model simulations of Chapter 5). Importantly, with the plume descending to the surface, aerosol losses to the surface in such circumstances could be significant.

That the number concentration and size of emitted MCB aerosols can be altered by processes that could realistically occur in the course of MCB implementation – thus potentially altering the effectiveness of MCB – is an important finding that has several implications.

Firstly, these results show that the MCB emission plume would be a complex and interesting region, apt for further modelling or observational investigation. This work suggests that measurements of plume trajectories and dispersion, along with distributions of aerosol

number concentrations and size through the plume would be of particular value for furthering understanding and validating and informing simulations. Secondly, the plume characteristics identified in this work could additionally be useful for informing the development of MCB implementation mechanism designs. The next chapter uses the findings presented here to determine how these aerosol number concentration and size changes alter MCB effectiveness.

Chapter 8
The Effect of Processes within the Emission Rotor and Plume on Marine Cloud Brightening Effectiveness

8.1 Introduction

Chapter 7 showed that aerosol coagulation within the plume can approximately halve the MCB aerosol number concentration, and increase the initial diameter of some aerosols by approximately 8 times. Previous research has found that lower MCB aerosol number concentrations, and larger MCB aerosols, can reduce the effectiveness of MCB (discussed in Section 6.1).

This chapter determines the effect that aerosol processes within the emission rotor and plume have on the resulting MCB albedo perturbations (Figure 8.1), and concludes the final MCB implementation detail case study.

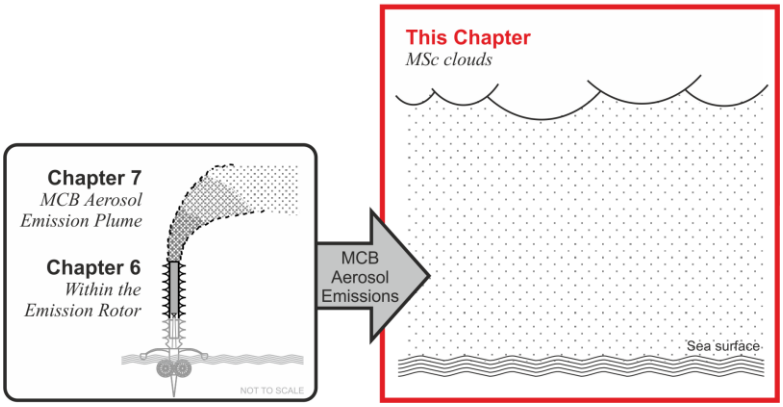

Figure 8.1 *– Schematic overview of the region of interest for estimating the effect of in-plume aerosol changes on clouds.*

To achieve this, aerosol number concentrations and sizes from Chapter 7 are used to inform cloud-resolving modelling. The methodology of these simulations is described in Section 8.2 before the results of the simulations are presented and discussed (Sections 8.3 and 8.4, respectively). In closing this chapter, the implications of these findings for the MCB proposal and the production of future MCB effectiveness estimates are advanced (Section 8.5).

8.2 Methodology

For these simulations, the WRF/Chem model was used at the 300 m horizontal and ~30 m vertical grid spacing and 9 km x 9 km x ~1.5 km domain size used in Chapters 3, 4 and 5.

For these final cloud-resolving simulations, the monodisperse (bin 3) aerosol emission assumption used previously is compared with three selected size distributions and number

concentrations. These three selected outputs are based on: the inclusion of aerosol coagulation within the plume only (as for the 'CONTROL' plume experiments described in Chapter 7, Section 7.3); the inclusion of coagulation within both the rotor and plume (based on the case described in Chapter 7, Section 7.4.1.4); and an experiment where all aerosols are emitted into the bin 8 aerosol size bin. For the bin 8 emission, all aerosols were assumed to have a dry diameter of 10 μm. As the mass is conserved, the aerosol number flux is therefore equivalent to reducing the number flux of the monodisperse (bin 3) control case (assuming a 200 nm dry diameter) by a factor of 125,000. The 10 μm dry diameter aerosols of the bin 8 case are larger than the aerosols found to result from in-plume coagulation (Chapter 7). This bin 8 case is therefore intended to serve as an extreme, rather than realistic, case of coagulation. The aerosol number and size compositions for these four cases are described in Table 8.1 and are based on the END section values of the plume simulations for a 1.0xSA aerosol emission flux. These END values are assumed to simulate the wider plume values more realistically than the domain averaged plume values that include the highly concentration conditions near to the emission source. The mass and number fractions described in Table 8.1 were applied to both a full 1.0xSA emission rate, and to a 0.5xSA emission rate. As the 0.5xSA emissions flux would have less coagulation and hence smaller reductions in aerosol number concentrations than the 1.0xSA flux (e.g. number concentrations reducing by 32.0% for 0.5xSA compared with 46.9% for the 1.0xSA aerosol emission cases; Chapter 7, Figure 7.16), the application of the 1.0xSA fractional reductions will lead to overestimated number losses. The aerosol emission configurations were input into the cloud model for the background PR, NP-Pa and NP-Ch cases, with the methodology described in Chapter 4.

In addition to the changes in cloud albedo perturbation, the effect of aerosol changes on the direct aerosol effect were considered. This case is important in the clear-sky conditions more frequently encountered for lower cloud fraction conditions during the day and for the open-cellular structure typically associated with precipitating clouds.

Table 8.1 *– Number and mass fractions of emitted aerosols (as a fraction of the monodisperse (bin 3) aerosol emission).*

		Number and mass fractions					
		Bin 3	Bin 4	Bin 5	Bin 6	Bin 8	Total
No coagulation (monodisperse, bin 3)	Number	1.0	–	–	–	–	1.0
	Mass	1.0	–	–	–	–	1.0
Coagulation (in plume only) *(based on case described in Section 7.3)*	Number	0.3803	0.0377	0.0007	$2x10^{-6}$	–	0.419
	Mass	0.3803	0.5390	0.0790	0.0017	–	1.0
Coagulation (in rotor and plume) *(based on case described in Section 7.4.1.4)*	Number	0.2488	0.1006	0.0016	$4x10^{-6}$	–	0.351
	Mass	0.3250	0.4932	0.1778	0.0039	–	1.0
Aerosols emitted into bin 8	Number	–	–	–	–	$8x10^{-6}$	$8x10^{-6}$
	Mass	–	–	–	–	1.0	1.0

8.3 Results

Time series of the domain averaged calculated cloud albedo and N_d for the base cases and simulations including MCB aerosols emitted at 03:00:00 LT are presented in Figure 8.2. Values of the domain and time averaged calculated cloud albedo, N_d and LWP are summarised in Table 8.2.

As occurred in previous PR simulations (Chapter 4), emission of the full spray rate (1.0xSA) led to simulation failure upon sunrise at 05:20 LT. Reducing the emission rate to 0.5xSA allowed the control emission to run successfully through the day, increasing the calculated cloud albedo (in the 5 hours after MCB aerosol emission where SW radiation was present) from 0.203 to 0.503. Simulations into the PR regime that included coagulation (both in the plume only, and in the rotor and plume cases) also failed at sunrise for both the 1.0xSA and 0.5xSA concentrations. Up to the point of simulation failure, including the effects of aerosol coagulation within the rotor and plume led to increases in the calculated cloud albedo that were around 13% smaller for the 1.0xSA emission rate, and over 20% smaller for the 0.5xSA emission rate.

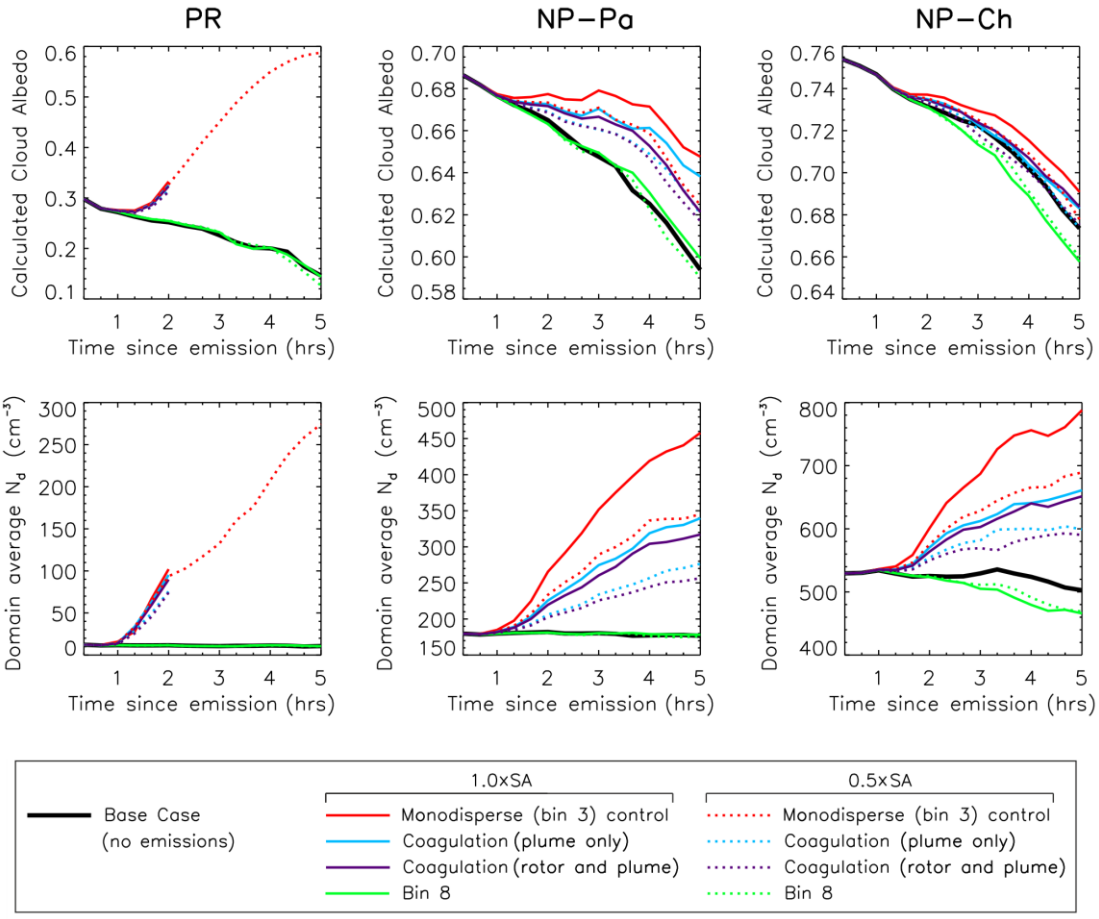

Figure 8.2 *– (top row) Time series of the domain average calculated cloud albedo over time for the PR, NP-Pa, and NP-Ch cases, and (bottom row) time series of the domain average N_d for the PR, NP-Pa, and NP-Ch cases. Aerosol emissions at 03:00:00 LT.*

Table 8.2 *– Absolute calculated cloud albedo for the PR, NP-Pa and NP-Ch cloud cases. Values are for the base case (with no MCB emissions) and for emission fluxes of 1.0xSA and 0.5xSA of four different MCB aerosol emission assumptions. Values are averaged over the domain and over the time during the five hours after MCB aerosol emission where SW radiation is present (or averaged over the night for values in bold, with grey shading indicating incomplete simulations that failed at sunrise). Perturbations in the calculated cloud albedo from the (no emissions) base case are shown (Δcalc. cloud albedo), with the percentage values shown in italics being the difference in calculated cloud perturbation compared with the monodisperse (bin 3) control emission assumption. Also shown are the domain averaged N_d and LWP for time periods described above.*

			1.0xSA				0.5xSA			
		Base Case (no emissions)	Monodis. (bin 3) control	Coag. (plume only)	Coag. (rotor and plume)	Bin 8	Monodis. (bin 3) control	Coag. (plume only)	Coag. (rotor and plume)	Bin 8
PR	Calc. cloud albedo	0.203 **0.270**	**0.292**	**0.290**	**0.289**	0.203	0.503 **0.290**	**0.287**	**0.286**	0.200
	Δcalc. cloud albedo	–	**+0.022**	**+0.020** ***-10.0%***	**+0.019** ***-13.3%***	+0.000 -100.0%	+0.300 **+0.020**	**+0.017** ***-17.4%***	**+0.016** ***-21.5%***	-0.003 *-101.0%*
	N_d, cm^{-3}	10.9 **11.7**	**39.5**	**38.4**	**36.4**	11.0	185.1 **38.2**	**31.9**	**30.4**	10.8
	LWP, $g\ m^{-2}$	32.2 **42.9**	**43.4**	**43.3**	**43.4**	32.9	49.1 **43.3**	**43.3**	**43.3**	32.8
NP-Pa	Calc. cloud albedo	0.630	0.668	0.659	0.652	0.633	0.656	0.649	0.647	0.629
	Δcalc. cloud albedo	–	+0.038	+0.029 *-24.1%*	+0.022 *-40.9%*	+0.003 *-91.9%*	+0.025	+0.019 *-25.4%*	+0.017 *-33.8%*	-0.002 *-107.0%*
	N_d, cm^{-3}	178.4	387.2	296.4	282.1	179.3	308.8	247.5	235.8	177.6
	LWP, $g\ m^{-2}$	60.7	59.9	60.7	59.9	61.0	59.5	60.4	60.3	60.2
NP-Ch	Calc. cloud albedo	0.706	0.718	0.710	0.711	0.695	0.711	0.707	0.705	0.697
	Δcalc. cloud albedo	–	+0.012	+0.004 *-67.6%*	+0.005 *-57.4%*	*-0.011* *-192.0%*	+0.005	+0.001 *-81.1%*	-0.001 *-122.8%*	*-0.009* *-271.1%*
	N_d, cm^{-3}	521.4	724.4	630.4	622.0	491.0	650.4	591.7	577.9	497.2
	LWP, $g\ m^{-2}$	59.1	57.6	57.1	57.8	57.4	57.3	57.4	57.1	57.8

For the PR regime, the bin 8 aerosol emissions cases ran successfully for both 1.0xSA and 0.5xSA fluxes. The 1.0xSA bin 8 emission produced no change in the baseline cloud albedo, while the 0.5xSA bin 8 emission resulted in a small reduction in mean calculated cloud albedo of 0.003 (equating to a 1% decrease in calculated cloud albedo over this time). This reduction in absolute cloud albedo was concomitant with a slight decrease in N_d from 10.9 cm^{-3} to 10.8 cm^{-3}.

For the intermediately polluted case (NP-Pa) all simulations ran successfully. For both the 1.0xSA and 0.5xSA emission rates, inclusion of the effects of coagulation within the plume reduced the increases in calculated cloud albedo by approximately 25% (over times where SW radiation was present). Inclusion of the effects of coagulation within both the rotor and the plume reduced the increases in calculated cloud albedo by 41% for 1.0xSA emission flux, and by 34% for 0.5xSA emission flux. Emitting bin 8 aerosols at the 1.0xSA flux produced a small increase in calculated cloud albedo of 0.003. This cloud albedo increase was 92% smaller than the monodisperse bin 3 control case emission. However, emitting bin 8 aerosols at the 0.5xSA flux resulted in an absolute cloud albedo decrease of 0.002 (or 0.3% of the background cloud albedo). As for the absolute cloud albedo decrease for the PR regime, this was accompanied by a small decrease in N_d (from 178.4 cm^3 to 177.6 cm^{-3}).

For the most polluted background conditions considered (NP-Ch), all simulations again ran successfully. In spite of lower overall albedo perturbations compared to the NP-Pa case, the comparative reductions caused by the effects of coalescence within the plume were larger. For the 1.0xSA emission rate, inclusion of the effects of coagulation within the plume reduced the increases in calculated cloud albedo by 68%. For the 0.5xSA emission rate, inclusion of the effects of coagulation within the plume reduced the increases in calculated cloud albedo by 81%. The reduction in calculated cloud albedo increase caused by coagulation within both the rotor and plume was 57% for the 1.0xSA emission rate, while the 0.5xSA emission rate led to small decrease in the absolute cloud albedo of 0.001 (or 0.1% of the background cloud albedo). Unlike for the PR and NP-Pa cases, this decrease in absolute cloud albedo was accompanied by an increase in N_d (from 521.4 cm^{-3} to 577.9 cm^{-3}). Finally for the NP-Ch background condition, emitting bin 8 aerosols at both the 1.0xSA and 0.5xSA emission rates led to decreases in the absolute cloud albedo (of 1.5% and 1.2% of the background cloud albedo respectively). As for the PR and NP-Pa background cases, these decreases in cloud albedo were concomitant with decreases in N_d (from 521 cm^{-3} to 491 cm^{-3} for the 1.0xSA emission rate, and to 497 cm^{-3} for the 0.5xSA emission rate).

The relationship between the emitted aerosol size, emitted aerosol number and calculated cloud increase for the three increasingly polluted background cases are depicted in Figure 8.3, which shows several key patterns (following Figure 2 of Pringle et al. (2012)).

Figure 8.3 illustrates that as the background aerosol concentration is increased, the increase in albedo for a given emitted aerosol size and number flux decreases. For a given background aerosol concentration, decreasing the number of emitted aerosol decreases the resulting albedo increase. Thus, the smallest increases in albedo were for lower aerosol emission numbers into the more polluted background. As has been described, decreases in the absolute calculated cloud albedo occurred in five of the 17 cases simulated here, typically occurring

for low concentrations of large emitted aerosols. The largest absolute decreases in calculated cloud albedo occurred for the most polluted NP-Ch case.

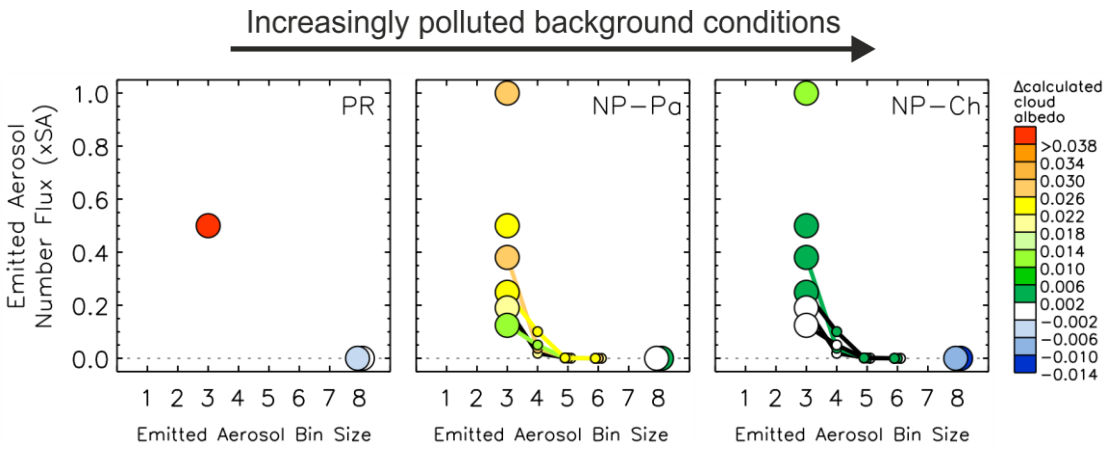

Figure 8.3 *– The perturbation in calculated cloud albedo (colour of data points) that occurs upon the emission of aerosols of bin size indicated on the x-axis, at a number flux relative to that suggested by Salter et al. (2008) (y-axis), for the increasingly polluted background cases: PR, NP-Pa, and NP-Ch. Data points connected with lines indicate the size distribution of emitted aerosols.*

In addition to altering the magnitude of the calculated cloud albedo increases, the changing aerosol profiles that resulted from the coagulation process also affected the direct aerosol effect. The 1.0xSA monodisperse (bin 3) aerosol emission resulted in a mean clear-sky ratio of upward to downward SW radiation at the top of atmosphere of 0.222 (averaged over the time during the five hours after 03:00:00 LT MCB aerosol emission where SW radiation is present) for the NP-Pa case. The 1.0xSA in-plume coagulation simulation reduced this to 0.212, while the 1.0xSA coagulation within both the rotor and plume produced an increase to 0.224. For the less realistic 1.0xSA bin 8 emission, this ratio decreased to 0.168 (which is only slightly larger than the 0.164 found for the case when no aerosol was emitted). The implications of these changes in the direct aerosol effect will largely be dependent on the extent of the clear sky fraction in the region of emissions. While it would be of interest to investigate these direct aerosol effects further in the future, these results suggest that in spite of the lower aerosol number concentrations, the larger aerosols present in the ‘rotor and plume’ simulations are effective at scattering the light, and so result in the larger fraction of SW reflected upwards than occurs in the monodisperse or ‘in-plume only’ cases. Conversely, in spite of the large aerosol size of the ‘bin 8’ emission simulations, the low numbers of aerosols result in only small increases in reflected SW radiation compared to the ‘no aerosol emission’ case.

8.4 Discussion

The simulations described in this chapter show that in addition to the coagulation of MCB aerosols that occurs within the plume and rotor (Chapters 6 and 7), further coagulation would occur as the aerosols are transported through the boundary layer to the cloud layer. This is suggested in these simulations by the increased concentrations in bin 4 aerosols activated to cloud droplets (and to a lesser extent, bin 5 aerosols) in response to the emission of monodisperse bin 3 aerosols in both the PR and NP-Ch cases (Figure 8.4 a).

When coagulation associated with aerosol processes within both the rotor and plume is included, MCB calculated cloud albedo increases are reduced. These reductions range from 13% for the cleanest background conditions (based on limited-duration simulations), to 41% for the intermediately polluted background conditions, to 57% for the most polluted background condition (all for a 1.0xSA emission flux). The inclusion of a Gaussian plume model-derived parameterisation of in-plume coagulation in a global-scale aerosol-climate model showed that the radiative flux perturbations produced over the emission regions would be reduced by around 25% (Stuart et al., 2013). That this value falls within the range of reductions in cloud albedo increases determined from this experiment suggests some agreement between findings, in spite of notably different methodologies. It is noted that the global-scale aerosol-climate model also found that the global reduction in radiative flux perturbation was greater than the reductions local to the aerosol emissions (Stuart et al., 2013). This 47% global reduction in radiative flux perturbation resulted, in part, from lower cloud fractions when coagulation was included (Stuart et al., 2013) and suggests that the inclusion of global-scale feedbacks would similarly inflate the reductions in cloud albedo enhancement found here.

As has been discussed in Chapter 1 and Section 2.4 of Chapter 2, previous studies have suggested that a competition effect may occur, whereby preferentially activated larger aerosols may reduce the supersaturation sufficiently to result in a decrease in the N_d. Such reductions in N_d, and calculated cloud albedo, were found in four of the cases simulated here (Table 8.2). The background condition most susceptible to decreases in both N_d and absolute cloud albedo in response to the emission of aerosols is the most heavily polluted (NP-Ch) case. This increased sensitivity of more polluted clouds to albedo reductions via the competition effect agrees with previous modelling of the effect (Pringle et al., 2012; Chapter 2). Absolute calculated cloud albedo losses for this NP-Ch case are simulated for both 1.0xSA and 0.5xSA bin 8 emissions. It is reiterated, however, that these bin 8 aerosol emissions are intended as an extreme (rather than realistic) case, as it would be anticipated that such large aerosols would neither be emitted intentionally (e.g. Salter et al., 2008) nor created via coagulation upon emission (Chapters 6 and 7). In these cases, there is also a

reduction in LWP compared to the base case (where no MCB aerosols were emitted). This decrease in LWP may be caused by reduced turbulence leading to less mixing within the cloud layer (Chapter 2). Such decreases in LWP (associated with the second indirect aerosol effect) would add to decreases in absolute cloud albedo caused by decreases in N_d (associated with the first indirect aerosol effect).

The effect of competition on aerosol activation to cloud droplets is illustrated in Figure 8.4. While the number concentration of activated bin 3 size aerosols (dark blue line, Figure 8.4 a) increases in favour of bin 2 background aerosols (purple line, Figure 8.4 a) for the emission of bin 3 aerosols, sufficient bin 3 aerosols are activated to cloud droplets for the total N_d (dotted black line in figure) to increase over time. A similar process occurs for the emission of aerosols that includes the effect of coagulation in the rotor and plume (Figure 8.4 b). In this case, there is an increase in activation of the aerosols emitted into bins 3, 4, 5 and 6. Concurrently there is a reduction in the number of smaller bin 2 aerosols. Again, the increase in activated emitted aerosols is sufficient to overcome the decrease in activated background aerosols, again resulting in an overall increase in N_d over time. However, when bin 8 aerosols are emitted (Figure 8.4 c), the increase in the number of these larger aerosols activated to cloud droplets is smaller than the decrease in the number of smaller aerosols (particularly bin 2 aerosols) that are activated to cloud droplets, producing a reduction in the total N_d compared to the background condition.

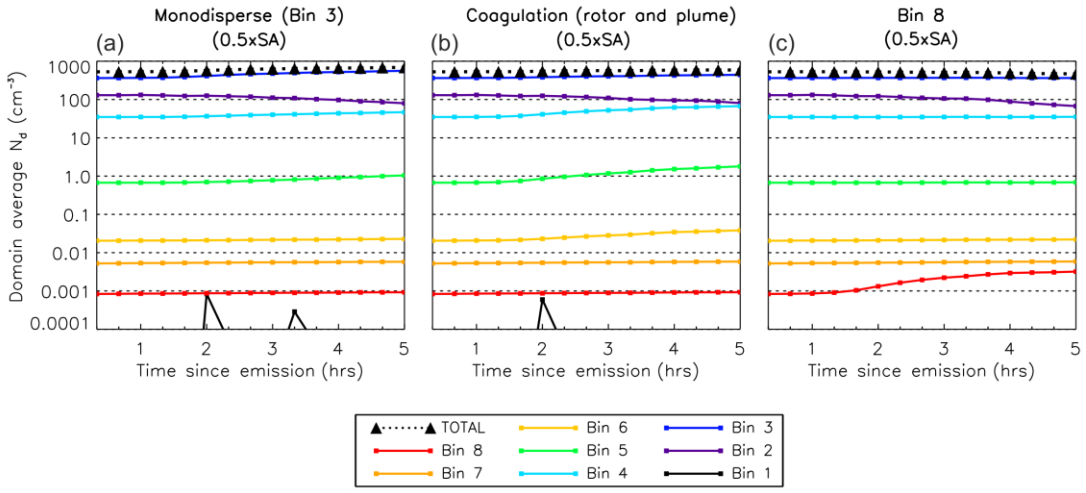

Figure 8.4 *– Time series for the total N_d and N_d associated with each aerosol size bin for the NP-Ch background case, for: (a) monodisperse (bin 3) emissions; (b) coagulation with rotor emissions; and (c) bin 8 emissions (all at 0.5xSA emission rate).*

The intermediately polluted NP-Pa case is also subject to small N_d losses and absolute albedo decreases upon 0.5xSA emission of the bin 8 aerosols. However, in agreement with previous modelling of the competition effect (Pringle et al., 2012; Chapter 2), increasing the emission rate to 1.0xSA is sufficient to overcome these losses.

The final case that resulted in a slight reduction in N_d and reduction in cloud albedo is for the 0.5xSA emission of bin 8 aerosols into the PR background. For this case, the precipitation rate increases by approximately 8%. This can be surmised to be related to the behaviour of the two-moment microphysics scheme, which uses an explicit autoconversion rate (described in Chapter 3). Thus, in the model, autoconversion increases with cloud water mixing ratio and the inverse of N_d. In this 0.5xSA emission of bin 8 aerosols into the PR background, the slightly lower number of cloud droplets formed, whilst maintaining a similar cloud water mixing ratio, may therefore result in higher autoconversion rates and so more precipitation. In spite of this increase in precipitation, there is an increase in LWP of around 2% (from 32.2 g m^{-2} to 32.8 g m^{-2}). This suggests that while more water may be lost through precipitation, water is gained through reduced evaporation of the larger cloud droplets (Chapter 2, Section 2.4.2). In spite of the increase in LWP, the small decrease in N_d is sufficient to produce a net decrease in calculated cloud albedo.

While, in the aforementioned cases, reductions in absolute cloud albedo are concomitant with competition effects linked to decreases in N_d, there is one additional case where a reduction in absolute cloud albedo occurs with an increase in N_d. This case is for 0.5xSA aerosol emission including coagulation within both the plume and rotor into the most polluted (NP−Ch) background. In this case, the LWP (averaged over the period of SW radiation present during the 5 hours subsequent to MCB aerosol emission) decreases, from 59.1 g m^{-2} to 57.1 g m^{-2} (a 3% decrease). This LWP reduction is likely the result of increased droplet evaporation owing to the increased surface area of the smaller droplets. Thus, the increase in cloud albedo inferred from the increase in N_d (first indirect aerosol effect) is exceeded by the decrease in cloud albedo related to LWP losses (second indirect aerosol effect). While this decrease in albedo was small (less than 0.2% of the mean calculated cloud albedo), the pattern of change is in agreement with the possible net indirect aerosol effects proposed in Figure 2.5 (Chapter 2) for background conditions with higher N_d.

8.5 Conclusions

The cloud-resolved modelling of coagulation-affected MCB aerosol emissions presented in this chapter forms the closing part of the final MCB implementation detail case study.

The results show that accounting for the MCB aerosol number concentration reductions and size increases produced by coagulation within the emission rotor and plume (modelled in Chapters 6 and 7) reduces MCB effectiveness. As for the previous two MCB experiments (Chapters 4 and 5), the magnitude of the impacts was dependent upon the base case cloud conditions. Here, the coagulation effects resulted in the cloud albedo enhancement being reduced by 13% for limited-duration simulations undertaken into the precipitating cloud

regime, but by up to 57% for the non-precipitating cloud regime. The larger absolute values of cloud brightening associated with the precipitating regime mean, however, that the effects of these aerosol changes on cloud brightening in both cloud regimes could be climatically important.

No competition effect (or absolute decrease in N_d or cloud albedo) resulted from the emission of the coagulation-altered MCB aerosols. Contrived simulations involving the emission of the largest possible aerosols within the model (up to 10 μm dry diameter) did produce such a competition effect, with the most polluted background case being the most susceptible. As these aerosols were considerably larger than those likely to result from coagulation within the rotor and plume, this finding is of limited value for MCB research. However, this simulation is of conceptual interest, and bolsters confidence in the ability of the model to capture cloud-aerosol behaviour.

The conditions included in this chapter represent only a select number of possible conditions. For example, simulations in Chapter 7 of the effects of representing the aerosol emission with wet droplets reinforced the findings of Chapter 5 in showing that the plume may descend. Thus, in addition to the implications on transport of aerosols to the cloud layer (described in Chapter 5), significant aerosol losses at the surface may also occur. Owing to inadequacies in the higher resolution simulations of this effect, this possible condition was not included in the analysis of this chapter. However, it is recommended that future consideration of this case may be beneficial in the future.

The finding that MCB effectiveness is reduced by the effects of rotor and plume region coagulation has important implications for MCB research. As the resolution of global-scale models prevents the representation of these detailed features, these models will have overlooked this effect. As such, MCB effectiveness estimates previously produced by global-scale models will likely be overestimations. It will therefore be critical that future global-scale modelling of MCB takes these effects into account.

Chapter 9
Conclusions and Recommendations

9.1 Summary of Major Findings

This study set out to determine whether accounting for details of geoengineering implementation mechanisms (currently not captured by global-scale computer models) could enhance the realism of modelled estimates of geoengineering effectiveness. In doing so, this work focussed on the MCB proposal, using three implementation details as case studies. These case studies were interrogated over a range of three base case MSc cloud conditions, the salient features of which were successfully simulated over a diurnal cycle using a limited domain-size, cloud-resolving WRF/Chem model (Chapter 3).

This work found that accounting for the effects of MCB implementation details markedly altered the magnitude of achievable MCB in two of the three case studies considered.

The first implementation detail that was found to be consequential for the modelled effectiveness of MCB was the timing of the MCB aerosol emission (Chapter 4). The importance of this MCB aerosol emission timing was found to be related to the characteristic diurnal cycle of cloud processes and cloud properties (introduced in Chapter 2). Conducting these experiments against the range of three base case MSc cloud conditions also facilitated the additional finding that the MCB effectiveness varied non-linearly with background conditions. As expected from theoretical understanding (presented in Chapter 2), MCB effectiveness was markedly higher for the precipitating cloud conditions (that showed characteristics of open cell behaviour) compared to the non-precipitating clouds (that showed characteristics of closed cell behaviour). For the more susceptible precipitating cloud condition, the optimal MCB aerosol emission time for maximum MCB effectiveness was into the early morning. Aerosol emission at this time caused a suppression of precipitation, with the newly non-precipitating cloud being more persistent through the radiatively-important daytime. This change in behaviour was predominantly manifest as an increase in LWP, associated with the second indirect aerosol effect. This change in precipitation was additionally concomitant with changes in cloud behaviour that were indicative of a change in regime from open to closed cell characteristics. No such response was evident when the MCB aerosols were emitted into these clouds during the daytime, when they are characteristically thinner and more dissipated. In spite of a compensating direct aerosol effect at this time, all-sky albedo increases were only half as large as they were for the early-morning emissions.

The second implementation detail that was found to be consequential for the modelled effectiveness of MCB regarded the coagulation of aerosols during the emission process and resulting plume of MCB aerosols (Chapters 6, 7 and 8). Using a simple numerical integration scheme for coagulation within the rotor, and the WRF/Chem model at resolutions sufficient to simulate key features of the aerosol emission plume, it was found that accounting for aerosol coagulation within these regions of high aerosol concentration typically led to the aerosol number concentration decreasing by approximately half, with the diameter of some aerosols also increasing by approximately 8 times. Simulations exploring the sensitivity of the model outputs to changes in aerosol emission rate, wind speed and temperature showed that changes in the coagulation rate were in agreement with theoretical expectations. The greatest coagulation-induced loss in MCB aerosol number concentration occurred when the emission rate was increased by five times, resulting in number concentration losses of nearly 80%. However, while including a simulated solid rotor altered the shape of the plume – successfully producing the expected Kármán vortex streets – its incorporation did not significantly alter rates of coagulation. Ultimately, the reductions in the number concentration of emitted MCB aerosols resulting from the coagulation of aerosols during the emission process led to MCB-induced calculated cloud albedo increases being approximately halved for the non-precipitating cloud cases.

Finally, while the impacts of representing the emitted MCB aerosols as sea water droplets rather than ‘dry’ aerosols produced only small changes in the effectiveness of MCB (Chapter 5), the identified processes associated with the assumption are of practical interest. Notably, the evaporation of the emitted sea water droplets resulted in a negative buoyancy that suppressed the initial height of the emitted aerosol plume by almost one third (40 m). Transport of these MCB aerosols to the cloud-layer is dependent upon mixing within the boundary layer. This is, in turn, controlled by the diurnally-varying vertical distribution of turbulence in the boundary layer. Therefore, the implications of this plume height suppression depends on both the cloud conditions (i.e. cloud base height) and on the phase of turbulent mixing through the marine boundary layer (dictated by the diurnal cycle). The largest impact in these simulations was for the emission of MCB aerosols into the non-precipitating cloud regime in the early afternoon. At this time, the descending turbulence, originating from the cloud-top, took longer to reach (and mix) the suppressed MCB aerosol plume associated with the emission of wet droplets than it did the taller plume associated with the emission of ‘dry’ aerosols. The effect was important for the non-precipitating cloud conditions owing to the higher cloud bases, and hence greater delays in the transport of the MCB aerosols from near the surface. However, the wet droplet versus ‘dry’ aerosol emission assumption merely resulted in delays to the transport of the MCB aerosols to the cloud-layer, with the ultimate impact therefore having little consequence to MCB effectiveness overall.

9.2 Conclusions and Recommendations

The direct conclusion of this work is that accounting for the effects of details of the MCB implementation scheme can markedly alter the magnitude of the resulting simulated effectiveness of the scheme. This major finding leads to several corollaries:

Corollary 1 – Values of MCB effectiveness, produced by global-scale computer models that do not account for the effects of MCB implementation details, may be overestimated. Such overestimations of geoengineering effectiveness may lead to the urgency of anthropogenic climate change mitigation and adaptation measures being downplayed.

It is therefore suggested that the findings presented here be used to qualitatively reframe existing global-model derived estimates of MCB effectiveness. However, it is considered that extending this reframing beyond broad patterns of behaviour and indications of strength would be imprudent at this stage. For, while the conspicuous patterns of behaviour found in response to the inclusion of implementation details match well with the those expected based on the theoretical understanding of processes (discussed throughout this thesis) and have additionally been supported by the contemporary studies of colleagues (Stuart et al., 2013), there are limitations to this work. For example, these values result from single model runs carried out using a single model. Additionally, the number of base case cloud conditions was constrained, as was the model domain size and length of the simulations. Furthermore, extrapolating explicit values for the effects of implementation details from this work would overlook the uncertainties still associated with the incompletely understood behaviour of cloud feedback behaviours in response to aerosol concentration changes under different cloud conditions (described in Chapter 2).

More broadly, these findings emphasise that an understanding and acknowledgement of the scale of the uncertainties surrounding computer model-derived geoengineering effectiveness estimates will be crucial at the policy-making level (Patt, 2009).

Corollary 2 – The process of identifying implementation details that are potentially pertinent for realistic computer simulations should be extended for the MCB scheme and undertaken for other geoengineering schemes.

This work focussed on three possible details of the MCB implementation scheme. While these details were considered by the author to be most likely to have a significantly impact on MCB effectiveness, further relevant details may remain unidentified.

While relating solely to MCB, the findings presented here also suggest that the effect of implementation details could be important for other geoengineering schemes. For example, the realism of global-scale modelling of sulphate injection into the stratosphere may be

improved by detailed consideration of the aerosol coagulation processes that may occur as the aerosols are emitted from the aircraft-based mechanisms (Rasch et al., 2008).

Identifying such pertinent details would benefit from open and active communication between climate modellers and the designers of the proposed geoengineering technologies. It is noted, however, that while private sector-led research may expedite design developments, matters of copyright may impinge upon the transparency necessary for such cooperation.

Corollary 3 – Further detailed modelling of the three case studies considered here, and other implementation details identified as being potentially pertinent to MCB and other geoengineering schemes, could be valuable.

While this work has identified that implementation details are important in the computer modelling of MCB, continuing detailed modelling of the MCB implementation processes themselves will also yield further insights. For example, it would be valuable to expand the work presented here beyond the current limitations to include a larger number of MSc base cases covering a larger parameter space of cloud and atmospheric conditions. Particularly interesting would be in the aforementioned transition between precipitating and non-precipitating conditions, which is currently poorly characterised. This region of transition could, for example, exhibit a discrete step-change (as suggested by Rosenfeld et al. (2006)). Such a step-change transition could relate to: the open or closed cell regime of the background cloud (as considered for the observation analysis of ship tracks, as discussed in Chapter 2); threshold precipitation rates (Figure 2.5; cf. Chen et al., 2011); or specific cloud structure characteristics, such as cloud base height (cf. Wood, 2007). Further valuable developments in the cloud-resolving modelling of MCB implementation detail effects would be to expand the domain size to incorporate mesoscale effects (Feingold et al., 2010; Wang et al., 2011a) and extend the timescale to incorporate the full aerosol life-span. Such enlarged simulations would additionally facilitate a more extensive detailed examination of the role of the direct aerosol effect under differing cloud conditions. The MCB implementation details could alternatively be explored using different modelling approaches. For example, the dynamics and coagulation of aerosols within the rotor and in the aerosol plume could be explored in more depth using a computational fluid dynamics model. The conspicuousness and theoretical rationality of the findings of this work suggest that while extended modelling may be able to produce some refinements, the broad patterns of behaviour will remain robust.

Detailed computer modelling processes could also help to assess the importance of implementation details identified for other geoengineering schemes.

Unlike the recommendations of reframing previous MCB effectiveness estimates, and working with geoengineering scheme designers to identify potentially pertinent

implementation details, such further resolved computer modelling would involve the dedication of considerably more resources.

Corollary 4 – The effects of pertinent implementation details should be taken into account in the future estimates for MCB and other geoengineering schemes derived from global-scale computer modelling.

In addition to affecting how previous estimates are interpreted, these findings should also be used to inform the future production of MCB effectiveness estimates. Without significant developments in global-scale models – such as sufficient increases in resolution, or the incorporation of multi-scale modelling frameworks (also known as 'super-parameterisations') (e.g. Khairoutdinov and Randall, 2001; Wang et al., 2011b) – these models will be inherently unable to explicitly capture the implementation details. As such, the inclusion of the effects of the implementation details would likely be through the development and refinement of specific parameterisations (e.g. Stuart et al., 2013). This would be more easily achievable for the effects of coagulation within the plume, where the effect could be represented by proxy size and number concentrations of MCB aerosols emitted into the global-scale model. The effect of timing of MCB emissions would be more challenging to capture owing to fundamental difficulties in the representation of MSc diurnal cycle within the global-scale computer models.

Corollary 5 – Geoengineering research would benefit from a multi-disciplinary approach.

As already stated, enhanced communication between climate modellers and the designers of the proposed geoengineering technologies could lead to the more efficient identification of implementation details pertinent to computer modelling. Such benefits could, however, be reciprocal, with the findings of these modelling case studies being of use in the development of the aerosol production technology design; the development of an MCB implementation strategy; and the design of prospective limited-area MCB testing. For example, the finding that the emission of MCB aerosols as wet droplets inhibits their transport to the cloud layer suggests the encouragement of developments in technologies able to produce 'dry' aerosols. However, the detrimental effects of aerosol coagulation within the plume on MCB effectiveness could not be reduced without a significant redesign of the proposed Salter et al. (2008) sea-going vessel implementation mechanism. For the implementation strategy, the knowledge that optimised MCB effectiveness may be achieved by targeting precipitating clouds early in the morning suggests the development of a sophisticated time and condition-dependent emission scheme. Future testing of MCB could also be informed by these findings. For example, this work identifies that the influence of the time-varying boundary layer dynamics on MCB aerosol transport would be of particular interest. This would require concurrent and collocated measurements of flow patterns and aerosol concentrations through

time. Observations could link aerosol dispersal patterns with characteristic MSc turbulent phases through the day, further elucidating the importance of daytime decoupling of the boundary and cloud layers on MCB effectiveness. These findings also indicate that observations of the dynamics and changes in aerosol size and number concentration within the MCB aerosol emission plume would also be of particular value. Hence, the design, observed testing, and computer modelling of geoengineering proposals will need to draw on the expertise and knowledge of engineers, observational scientists, computer modellers and climate scientists covering a range of specialisms (for example, from detailed cloud microphysics, to global patterns of dynamics and teleconnections). Of course, intertwined with these scientific and practical factors will be the crucial social, governance and moral considerations.

Further to these conclusions and recommendations based specifically on the findings presented in this thesis, there will be ongoing developments that will also contribute towards the future advancement of MCB research. A summary of these possible areas of future advancement, focussing specifically on MCB, is presented in Figure 9.1. The ongoing developments will include enhancements in the understanding of the complex and incompletely understood behaviour of MSc clouds and their interaction with aerosols. This development will be contributed to through the use of observational data and computer modelling. Furthermore, ongoing developments will improve the representation of clouds and their interaction with aerosols in models. An area in which this current study could have been developed is the more detailed examination of underlying microphysical process rates. Such information could have additionally informed interpretation of the causes of changes to the clouds in response to the addition of aerosols, as well as changes across the diurnal cycle. It is recommended that provision for such detailed analysis is incorporated into future studies of this kind.

While the cloud-resolved modelling presented here successfully captured key properties and processes associated with the base case MSc cloud over the diurnal cycle (Chapter 3), further work could refine the representation of heat fluxes, the effects of wind shear, and temporal patterns of large-scale subsidence for example. Additionally, increasing the resolution of the model may be possible in the future. In particular, high vertical resolutions have long been considered desirable in the detailed representation of entrainment at the interface between the cloud-top and free-troposphere (e.g. Bretherton et al., 1999; Stevens and Bretherton, 1999). Ongoing model developments could also include progress in cloud representation in global-scale climate modelling. This could occur through improved parameterisations or, as described in Corollary 4, increased model resolution or the use of multi-scale modelling

frameworks. Aside from these ongoing enhancements in the fundamental understanding and modelling of clouds, there will also be ongoing developments in the design of the MCB aerosol production technique (Neukermans et al., 2014) and subsequent field testing (Wood and Ackerman, 2013).

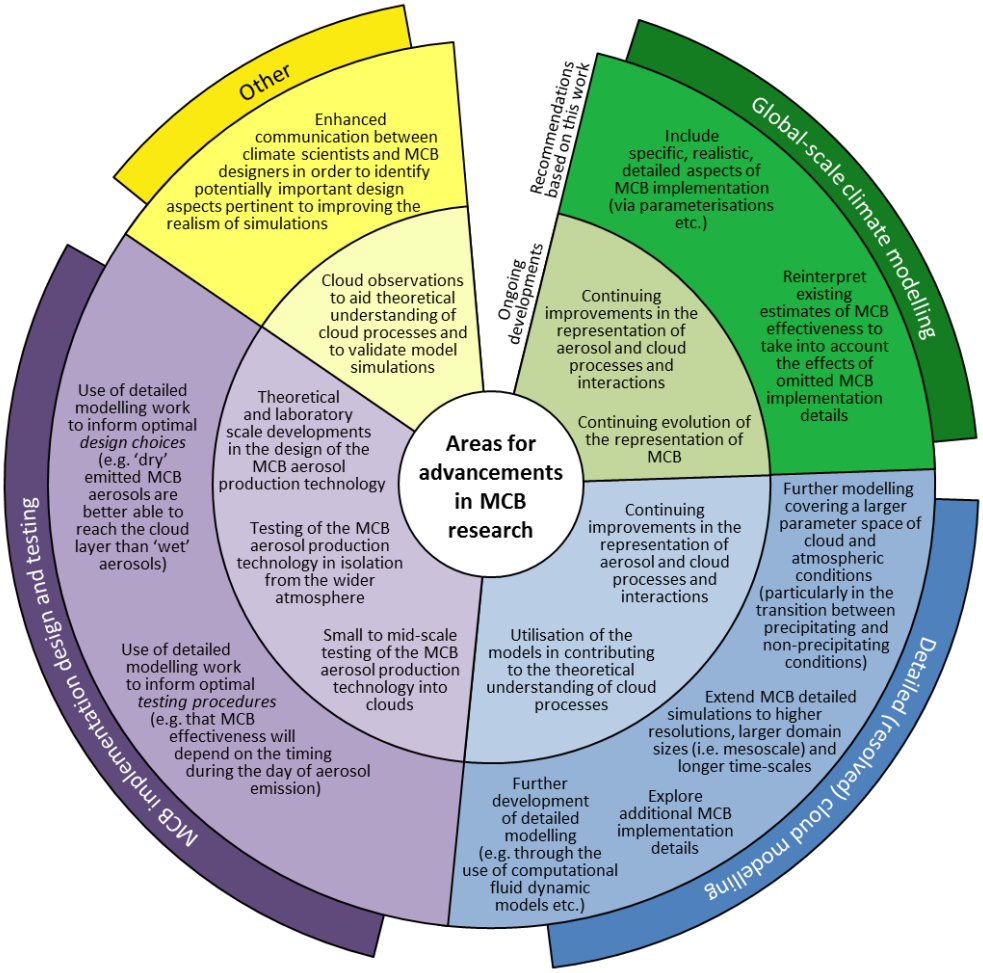

Figure 9.1 *– Areas for advancements in MCB research, showing both ongoing developments and recommendations based on this work.*

The recommendations for future work based on the conclusions presented here can be ranked in terms of priorities. The most immediate pathways for advancing geoengineering research will be through the reframing of previous MCB effectiveness estimates, and through the identification of potentially pertinent details omitted from the modelling of other geoengineering schemes. Following this, the utilisation of these findings in future global-scale MCB modelling and MCB implementation design and testing should naturally ensue. However, as there remains significant unknowns regarding the design of the MCB aerosol production technique (Neukermans et al., 2014) – unless it can be of mutual benefit to the wider understanding of cloud processes – the significantly more research-intensive continuation of detailed MCB modelling may be premature. Waiting for the development of a tangible MCB aerosol production technique would both reduce the need for assumptions in

such detailed modelling, and could also yield highly useful experimental data. Even isolated from the wider atmosphere and clouds, experiments would be invaluable in identifying unanticipated phenomena in the production and emission processes, while data would allow the evaluation of computer model simulations.

9.3 Closing Comments

The discovery here, that details of the MCB implementation process must be accounted for in producing realistic computer modelled estimates of MCB effectiveness, is timely. Geoengineering is increasingly part of the mainstream climate change debate, as illustrated by its inclusion in the Summary for Policymakers of the Fifth Assessment Report of the IPCC (IPCC, 2013). While policy relevant assessments of geoengineering (e.g. The Royal Society, 2009; Center for Science, 2011; Bracmort and Lattanzio, 2013) at present continue to be limited to broader qualitative assessments, future debate surrounding geoengineering will inevitably demand more realistic, quantified predictions of its effects. While such quantitative global-scale computer modelling of MCB has already begun (see Chapter 1), this work shows that by omitting the effects of implementation details, the resulting estimates of MCB effectiveness may be currently overestimated. As future geoengineering research will continue to rely on such computer modelling (because of necessary constraints on in-situ testing), the findings of this work offer an opportunity to materially enhance the realism of future MCB effectiveness estimates. More broadly, this work also indicates the potential benefits that could be achieved by expanding this approach – of identifying potentially pertinent implementation details currently omitted from the global-scale modelling – to other geoengineering proposals.

Ultimately, the benefits of improving the realism of geoengineering effectiveness estimates will extend beyond the field of geoengineering, contributing valuably towards informed decision-making on our response to anthropogenic climate change as a whole.

Appendix A

Supplementary Information Relevant to the Coagulation of MCB Aerosols within the Emission Rotor, and the Detailed Representation of the MCB Aerosol Emission Plume (Chapters 6 and 7)

I. Reynolds Number (for flow through a pipe):

$$\mathrm{Re} = \frac{U D}{\upsilon} \qquad \textbf{(A.1)}$$

where:

U = velocity of the flow through the pipe

D = hydraulic diameter of the pipe

υ = kinematic viscosity of air

II. Stokes Number:

$$\text{Stokes Number} = \frac{\text{response time of particles in the flow}}{\text{response time of the fluid flow}} = \frac{\tau U_0}{D} \qquad \textbf{(A.2)}$$

where:

τ = particle response time (s) and,

$$\tau = \frac{d_p{}^2 \rho_p}{18\mu} \qquad \textbf{(A.3)}$$

d_p = particle diameter

ρ_p = particle density

μ = kinematic viscosity of air

U_0 = fluid free velocity

D = characteristic dimension of the flow

III. Reynolds Number (for flow relative to a surface):

$$\text{Reynolds Number} = U_{flow} D / \upsilon \qquad \textbf{(A.4)}$$

where:

U_{flow} = velocity of the fluid

D = dimension of the rotor

υ = kinematic viscosity of air

References

Abdul-Razzak, H. & Ghan, S. J. (2000) A parameterization of aerosol activation 2. Multiple aerosol types. *Journal of Geophysical Research,* 105**,** 6837-6844.

Achenbach, E. & Heinecke, E. (1981) On vortex shedding from smooth and rough cylinders in the range of Reynolds numbers 6×10^3 to 5×10^6. *Journal of Fluid Mechanics,* 109**,** 239-251.

Ackerman, A. S., Kirkpatrick, M. P., Stevens, D. E. & Toon, O. B. (2004) The impact of humidity above stratiform clouds on indirect aerosol climate forcing. *Nature,* 432**,** 1014-1017.

Ackerman, A. S., Toon, O. B., Stevens, D. E. & Coakley, J. A., Jr. (2003) Enhancement of cloud cover and suppression of nocturnal drizzle in stratocumulus polluted by haze. *Geophysical Research Letters,* 30**,** 1381.

Ackerman, A. S., vanZanten, M. C., Stevens, B., Savic-Jovcic, V., Bretherton, C. S., Chlond, A., Golaz, J.-C., Jiang, H., Khairoutdinov, M., Krueger, S. K., Lewellen, D. C., Lock, A., Moeng, C.-H., Nakamura, K., Petters, M. D., Snider, J. R., Weinbrecht, S. & Zulauf, M. (2009) Large-eddy simulations of a drizzling, stratocumulus-topped marine boundary layer. *Monthly Weather Review,* 137**,** 1083-1110.

Adaramola, M. S., Bergstrom, D. J. & Sumner, D. (2012) Characteristics of turbulent flow in the near wake of a stack. *Experimental Thermal and Fluid Science,* 40**,** 64-73.

Adger, W. N., Dessai, S., Goulden, M., Hulme, M., Lorenzoni, I., Nelson, D., Naess, L., Wolf, J. & Wreford, A. (2009) Are there social limits to adaptation to climate change? *Climatic Change,* 93**,** 335-354.

Agee, E. M. (1987) Mesoscale cellular convection over the oceans. *Dynamics of Atmospheres and Oceans,* 10**,** 317-341.

Albrecht, B. A. (1989) Aerosols, cloud microphysics, and fractional cloudiness. *Science,* 245**,** 1227-1230.

Albrecht, B. A., Randall, D. A. & Nicholls, S. (1988) Observations of marine stratocumulus clouds during FIRE. *Bulletin of the American Meteorological Society,* 69**,** 618-626.

Alterskjær, K. & Kristjánsson, J. E. (2013) The sign of the radiative forcing from marine cloud brightening depends on both particle size and injection amount. *Geophysical Research Letters,* 40**,** 210-215.

Alterskjær, K., Kristjánsson, J. E. & Seland, Ø. (2012) Sensitivity to deliberate sea salt seeding of marine clouds – observations and model simulations. *Atmospheric Chemistry and Physics,* 12**,** 2795-2807.

American Meteorological Society (2012) *Glossary of Meteorology* [Online]. Available: http://glossary.ametsoc.org/ [Accessed 21st August 2013].

Andreae, M. O. (2009) Correlation between cloud condensation nuclei concentration and aerosol optical thickness in remote and polluted regions. *Atmospheric Chemistry and Physics,* 9**,** 543-556.

Andreae, M. O. & Rosenfeld, D. (2008) Aerosol-cloud-precipitation interactions. Part 1. The nature and sources of cloud-active aerosols. *Earth-Science Reviews,* 89**,** 13-41.

Andrews, T. & Forster, P. M. (2008) CO_2 forcing induces semi-direct effects with consequences for climate feedback interpretations. *Geophysical Research Letters,* 35**,** L04802.

Andrews, T., Gregory, J., Forster, P. & Webb, M. (2012) Cloud adjustment and its role in CO_2 radiative forcing and climate sensitivity: A review. *Surveys in Geophysics,* 33**,** 619-635.

Angel, R. (2006) Feasibility of cooling the Earth with a cloud of small spacecraft near the inner Lagrange point (L1). *Proceedings of the National Academy of Sciences,* 103**,** 17184-17189.

Arakeri, J. H., Das, D. & Srinivasan, J. (2000) Bifurcation in a buoyant horizontal laminar jet. *Journal of Fluid Mechanics,* 412**,** 61-73.

Archer, D., Eby, M., Brovkin, V., Ridgwell, A., Cao, L., Mikolajewicz, U., Caldeira, K., Matsumoto, K., Munhoven, G., Montenegro, A. & Tokos, K. (2009) Atmospheric lifetime of fossil fuel carbon dioxide. *Annual Review of Earth and Planetary Sciences,* 37**,** 117-134.

Arnell, N. W., Van Vuuren, D. P. & Isaac, M. (2011) The implications of climate policy for the impacts of climate change on global water resources. *Global Environmental Change,* 21**,** 592-603.

Bala, G., Duffy, P. B. & Taylor, K. E. (2008) Impact of geoengineering schemes on the global hydrological cycle. *Proceedings of the National Academy of Sciences,* 105**,** 7664-7669.

Balachandar, S. & Eaton, J. K. (2010) Turbulent dispersed multiphase flow. *Annual Review of Fluid Mechanics,* 42**,** 111-133.

Baughman, E., Gnanadesikan, A., Degaetano, A. & Adcroft, A. (2012) Investigation of the surface and circulation impacts of cloud-brightening geoengineering. *Journal of Climate,* 25**,** 7527-7543.

Bennartz, R. (2007) Global assessment of marine boundary layer cloud droplet number concentration from satellite. *Journal of Geophysical Research: Atmospheres,* 112**,** D02201.

Berner, A. H., Bretherton, C. S. & Wood, R. (2011) Large-eddy simulation of mesoscale dynamics and entrainment around a pocket of open cells observed in VOCALS-REx RF06. *Atmospheric Chemistry and Physics,* 11**,** 10525-10540.

Berner, A. H., Bretherton, C. S., Wood, R. & Muhlbauer, A. (2013) Marine boundary layer cloud regimes and POC formation in a CRM coupled to a bulk aerosol scheme. *Atmospheric Chemistry and Physics,* 13**,** 12549-12572.

Blackstock, J. J., Battisti, D. S., Caldeira, K., Eardley, D. M., Katz, J. I., Keith, D. W., Patrinos, A. A., Schrag, D. P., Socolow, R. H. & Koonin, S. E. (2009) Climate engineering responses to climate emergencies. arXiv:0907.5140v2. Available: http://arxiv.org/abs/0907.5140 [Accessed 14th January 2014].

Blaskovic, M., Davies, R. & Snider, J. (1991) Diurnal variation of marine stratocumulus over San Nicolas Island during July 1987. *Monthly Weather Review,* 119**,** 1469-1478.

Bony, S. & Dufresne, J.-L. (2005) Marine boundary layer clouds at the heart of tropical cloud feedback uncertainties in climate models. *Geophysical Research Letters,* 32**,** L20806.

Boucher, O., Forster, P. M., Gruber, N., Ha-Duong, M., Lawrence, M., Lenton, T. M., Maas, A. & Vaughan, N. E. (2014) Rethinking climate engineering categorization in the context of climate change mitigation and adaptation. *WIREs Climate Change,* 5**,** 23-35.

Boucher, O., Randall, D., Artaxo, P., Bretherton, C., Feingold, G., Forster, P., Kerminen, V.-M., Kondo, Y., Liao, H., Lohmann, U., Rasch, P., Satheesh, S. K., Sherwood, S., Stevens, B. & Zhang, X.-Y. (2013) Clouds and Aerosols. In: Climate Change 2013: The Physical Science Basis. Contribution of Working Group I to the Fifth Assessment Report of the Intergovernmental Panel on Climate Change. Available: http://www.ipcc.ch/report/ar5/wg1/#.UnOrnBBzo4I [Accessed 1st November 2013].

Bower, K., Choularton, T., Latham, J., Sahraei, J. & Salter, S. (2006) Computational assessment of a proposed technique for global warming mitigation via albedo-enhancement of marine stratocumulus clouds. *Atmospheric Research,* 82**,** 328-336.

Bracmort, K. & Lattanzio, R. K. (2013) Geoengineering: Governance and Technology Policy (R41371). *Congressional Research Service*.

Bretherton, C. S., Blossey, P. N. & Uchida, J. (2007) Cloud droplet sedimentation, entrainment efficiency, and subtropical stratocumulus albedo. *Geophysical Research Letters,* 34**,** L03813.

Bretherton, C. S., Macvean, M. K., Bechtold, P., Chlond, A., Cotton, W. R., Cuxart, J., Cuijpers, H., Mhairoutdinov, M., Kosovic, B., Lewellen, D., Moeng, C. H., Siebesma, P., Stevens, B., Stevens, D. E., Sykes, I. & Wyant, M. C. (1999) An intercomparison of radiatively driven entrainment and turbulence in a smoke cloud, as simulated by different numerical models. *Quarterly Journal of the Royal Meteorological Society,* 125**,** 391-423.

Bretherton, C. S., Uttal, T., Fairall, C. W., Yuter, S. E., Weller, R. A., Baumgardner, D., Comstock, K., Wood, R. & Raga, G. B. (2004) The EPIC 2001 stratocumulus study. *Bulletin of the American Meteorological Society,* 85**,** 967-977.

Bretherton, C. S., Wood, R., George, R. C., Leon, D., Allen, G. & Zheng, X. (2010) Southeast Pacific stratocumulus clouds, precipitation and boundary layer structure sampled along 20° S during VOCALS-REx. *Atmospheric Chemistry and Physics,* 10**,** 10639-10654.

Bretherton, C. S. & Wyant, M. C. (1997) Moisture transport, lower-tropospheric stability, and decoupling of cloud-topped boundary layers. *Journal of the Atmospheric Sciences,* 54**,** 148-167.

Caldeira, K., Bala, G. & Cao, L. (2013) The Science of Geoengineering. *Annual Review of Earth and Planetary Sciences,* 41**,** 231-256.

Caldwell, P. & Bretherton, C. S. (2009) Large eddy simulation of the diurnal cycle in southeast Pacific stratocumulus. *Journal of the Atmospheric Sciences,* 66**,** 432-449.

Caldwell, P., Bretherton, C. S. & Wood, R. (2005) Mixed-layer budget analysis of the diurnal cycle of entrainment in southeast Pacific stratocumulus. *Journal of the Atmospheric Sciences,* 62**,** 3775-3791.

Campolo, M., Salvetti, M. V. & Soldati, A. (2005) Mechanisms for microparticle dispersion in a jet in crossflow. *AIChE Journal,* 51**,** 28-43.

Carbon Engineering Ltd. (2013). Available: http://www.carbonengineering.com [Accessed 2nd August].

Center for Science, Technology, and Engineering (2011) Technology Assessment. Climate Engineering: Technical Status, Future Directions, and Potential Responses. *United States Government Accountability Office.* Available: http://www.gao.gov/products/GAO-11-71 [Accessed 1st August 2013].

Charlson, R. J., Lovelock, J. E., Andreae, M. O. & Warren, S. G. (1987) Oceanic phytoplankton, atmospheric sulphur, cloud albedo and climate. *Nature,* 326**,** 655-661.

Chen, T., Rossow, W. B. & Zhang, Y. (2000) Radiative effects of cloud-type variations. *Journal of Climate,* 13**,** 264-286.

Chen, Y. C., Christensen, M. W., Xue, L., Sorooshian, A., Stephens, G. L., Rasmussen, R. M. & Seinfeld, J. H. (2012) Occurrence of lower cloud albedo in ship tracks. *Atmospheric Chemistry and Physics,* 12**,** 8223-8235.

Chen, Y. C., Xue, L., Lebo, Z. J., Wang, H., Rasmussen, R. M. & Seinfeld, J. H. (2011) A comprehensive numerical study of aerosol-cloud-precipitation interactions in marine stratocumulus. *Atmospheric Chemistry and Physics,* 11**,** 9749-9769.

Christensen, M. W. & Stephens, G. L. (2011) Microphysical and macrophysical responses of marine stratocumulus polluted by underlying ships: Evidence of cloud deepening. *Journal of Geophysical Research,* 116**,** D03201.

Christensen, M. W. & Stephens, G. L. (2012) Microphysical and macrophysical responses of marine stratocumulus polluted by underlying ships: 2. Impacts of haze on precipitating clouds. *Journal of Geophysical Research,* 117**,** D11203.

Church, J. A. & White, N. J. (2006) A 20th century acceleration in global sea-level rise. *Geophysical Research Letters,* 33**,** L01602.

Coakley, J. A. (2002) Reflectance and albedo, surface. *In:* J.R. Holton & Curry, J. A. (eds.) *Encyclopedia of the Atmosphere.* Academic Press.

Coakley, J. A. & Walsh, C. D. (2002) Limits to the aerosol indirect radiative effect derived from observations of ship tracks. *Journal of the Atmospheric Sciences,* 59**,** 668-680.

Coddington, O. M., Pilewskie, P., Redemann, J., Platnick, S., Russell, P. B., Schmidt, K. S., Gore, W. J., Livingston, J., Wind, G. & Vukicevic, T. (2010) Examining the impact of overlying aerosols on the retrieval of cloud optical properties from passive remote sensing. *Journal of Geophysical Research,* 115**,** D10211.

Collins, W. D., Rasch, P. J., Boville, B. A., Hack, J. J., Mccaa, J. R., Williamson, D. L., Kiehl, J. T., Briegleb, B., Bitz, C., Lin, S.-J., Zhang, M. & Dai, Y. (2004) Description of the NCAR Community Atmosphere Model (CAM 3.0). *NCAR Technical Note,* NCAR/TN-464+STR.

Comstock, K. K., Bretherton, C. S. & Yuter, S. E. (2005) Mesoscale variability and drizzle in southeast Pacific stratocumulus. *Journal of the Atmospheric Sciences,* 62**,** 3792-3807.

Convention on Biological Diversity (2010) *Climate-related Geoengineering and Biodiversity* [Online]. Available: http://www.cbd.int/climate/geoengineering/ [Accessed 24th April].

Cortelezzi, L. & Karagozian, A. R. (2001) On the formation of the counter-rotating vortex pair in transverse jets. *Journal of Fluid Mechanics,* 446**,** 347-373.

Costantino, L. & Bréon, F. M. (2013) Aerosol indirect effect on warm clouds over South-East Atlantic, from co-located MODIS and CALIPSO observations. *Atmospheric Chemistry and Physics,* 13**,** 69-88.

Coumou, D. & Rahmstorf, S. (2012) A decade of weather extremes. *Nature Climate Change,* 2**,** 491-496.

Crabb, D., Durao, D. & Whitelaw, J. (1980) A round jet normal to a cross-flow. *American Society of Mechanical Engineers, Winter Annual Meeting, Chicago, Illinois.*

Crowe, C., Gore, R. & Troutt, T. (1985) Particle dispersion by coherent structures in free shear flows. *Particulate Science and Technology,* 3**,** 149-158.

Crutzen, P. (2006) Albedo enhancement by stratospheric sulfur injections: A contribution to resolve a policy dilemma? *Climatic Change,* 77**,** 211-220.

Cunningham, P., Goodrick, S. L., Hussaini, M. Y. & Linn, R. R. (2005) Coherent vortical structures in numerical simulations of buoyant plumes from wildland fires. *International Journal of Wildland Fire,* 14**,** 61-75.

Deardorff, J. W. (1980) Cloud top entrainment instability. *Journal of the Atmospheric Sciences,* 37**,** 131-147.

Deri, E., Monavon, A., Studer, E., Abdo, D. & Tkatschenko, I. (2011) Early development of the veil-shaped secondary flow in horizontal buoyant jets. *Physics of Fluids,* 23**,** 073604.

Devine, G. (2007) The behaviour of trace gases and aerosol particles in a cumulonimbus environment. *Doctor of Philosophy, University of Leeds.*

Diez, F., Torregrosa, M. & Pothos, S. (2011) A comparison between round turbulent jets and particle-laden jets in crossflow by using time-resolved stereoscopic particle image velocimetry. *Journal of Fluids Engineering,* 133**,** 091301.

Dlugokencky, E. & Tans, P. (2014) *NOAA/ESRL* [Online]. Available: http://www.esrl.noaa.gov/gmd/ccgg/trends/global.html [Accessed 14th January 2014].

Dow, K., Berkhout, F., Preston, B. L., Klein, R. J. T., Midgley, G. & Shaw, M. R. (2013) Limits to adaptation. *Nature Climate Change,* 3**,** 305-307.

Durkee, P. A., Chartier, R. E., Brown, A., Trehubenko, E. J., Rogerson, S. D., Skupniewicz, C., Nielsen, K. E., Platnick, S. & King, M. D. (2000) Composite ship track characteristics. *Journal of the Atmospheric Sciences,* 57**,** 2542-2553.

Dusek, U., Frank, G. P., Hildebrandt, L., Curtius, J., Schneider, J., Walter, S., Chand, D., Drewnick, F., Hings, S., Jung, D., Borrmann, S. & Andreae, M. O. (2006) Size matters more than chemistry for cloud-nucleating ability of aerosol particles. *Science,* 312**,** 1375-1378.

Duynkerke, P. G., De Roode, S. R., Van Zanten, M. C., Calvo, J., Cuxart, J., Cheinet, S., Chlond, A., Grenier, H., Jonker, P. J., Köhler, M., Lenderink, G., Lewellen, D., Lappen, C.-L., Lock, A. P., Moeng, C.-H., Müller, F., Olmeda, D., Piriou, J.-M., Sánchez, E. & Sednev, I. (2004) Observations and numerical simulations of the diurnal cycle of the EUROCS stratocumulus case. *Quarterly Journal of the Royal Meteorological Society,* 130**,** 3269-3296.

Eastman, R., Warren, S. G. & Hahn, C. J. (2011) Variations in cloud cover and cloud types over the ocean from surface observations, 1954-2008. *Journal of Climate,* 24**,** 5914-5934.

Eaton, J. K. & Fessler, J. (1994) Preferential concentration of particles by turbulence. *International Journal of Multiphase Flow,* 20**,** 169-209.

Eiff, O., Kawall, J. & Keffer, J. (1995) Lock-in of vortices in the wake of an elevated round turbulent jet in a crossflow. *Experiments in Fluids,* 19**,** 203-213.

Ernst, G. G., Davis, J. P. & Sparks, R. S. J. (1994) Bifurcation of volcanic plumes in a crosswind. *Bulletin of Volcanology,* 56**,** 159-169.

Fairweather, M., Jones, W. & Marquis, A. (1988) Predictions of the concentration field of a turbulent jet in a cross-flow. *Combustion Science and Technology,* 62**,** 61-76.

Fan, Y., Lin, S.-J., Held, I. M., Yu, Z. & Tolman, H. L. (2012) Global ocean surface wave simulation using a coupled atmosphere-wave model. *Journal of Climate,* 25**,** 6233-6252.

Fanaki, F. (1975) Experimental observations of a bifurcated buoyant plume. *Boundary-Layer Meteorology,* 9**,** 479-495.

Fast, J. D., Gustafson, W. I., Jr., Easter, R. C., Zaveri, R. A., Barnard, J. C., Chapman, E. G., Grell, G. A. & Peckham, S. E. (2006) Evolution of ozone, particulates, and aerosol direct radiative forcing in the vicinity of Houston using a fully coupled meteorology-chemistry-aerosol model. *Journal of Geophysical Research,* 111**,** D21305.

Feingold, G. (2003) Modeling of the first indirect effect: Analysis of measurement requirements. *Geophysical Research Letters,* 30**,** 1997.

Feingold, G., Cotton, W. R., Kreidenweis, S. M. & Davis, J. T. (1999) The impact of giant cloud condensation nuclei on drizzle formation in stratocumulus: Implications for cloud radiative properties. *Journal of the Atmospheric Sciences,* 56**,** 4100-4117.

Feingold, G., Cotton, W. R. & Stevens, B. (1996) The relationship between drop in-cloud residence time and drizzle production in numerically simulated stratocumulus clouds. *Journal of the Atmospheric Sciences,* 53**,** 1108-1122.

Feingold, G., Koren, I., Wang, H., Xue, H. & Brewer, W. A. (2010) Precipitation-generated oscillations in open cellular cloud fields. *Nature,* 466**,** 849-852.

Ferek, R. J., Garrett, T., Hobbs, P. V., Strader, S., Johnson, D., Taylor, J. P., Nielsen, K., Ackerman, A. S., Kogan, Y., Liu, Q., Albrecht, B. A. & Babb, D. (2000) Drizzle suppression in ship tracks. *Journal of the Atmospheric Sciences,* 57**,** 2707-2728.

Field, C. B., Barros, V., Stocker, T. F. & Dahe, Q. (2012) Managing the Risks of Extreme Events and Disasters to Advance Climate Change Adaptation: Special Report of the Intergovernmental Panel on Climate Change, *Cambridge University Press*.

Flato, G., Marotzke, J., Abiodun, B., Braconnot, P., Chou, S. C., Collins, W., Cox, P., Driouech, F., Emori, S., Eyring, V., Forest, C., Gleckler, P., Guilyardi, E., Jakob, C., Kattsov, V., Reason, C. & Rummukainen, M. (2013) Evaluation of Climate Models. In: Climate Change 2013: The Physical Science Basis. Contribution of Working Group I to the Fifth Assessment Report of the Intergovernmental Panel on Climate Change. [Held, I., Pitman, A., Planton, S. and Zhao, J.-C. (Review eds.)].

Forster, P., Ramaswamy, V., Artaxo, P., Berntsen, T., Betts, R., Fahey, D. W., Haywood, J., Lean, J., Lowe, D. C., Myhre, G., Nganga, J., Prinn, R., Raga, G., Schulz, M. & Van Dorland, R. (2007) Changes in Atmospheric Constituents and in Radiative Forcing. In: Climate Change 2007: The Physical Science Basis. Contribution of Working Group I to the Fourth Assessment Report of the Intergovernmental Panel on Climate Change.

[Solomon, S., D. Qin, M. Manning, Z. Chen, M. Marquis, K.B. Averyt, M.Tignor and H.L. Miller (eds.)]. Cambridge University Press, Cambridge, United Kingdom and New York, NY, USA.

Fric, T. & Roshko, A. (1994) Vortical structure in the wake of a transverse jet. *Journal of Fluid Mechanics,* 279**,** 1-47.

Friedlander, S. K. (2000) Smoke, dust, and haze: Fundamentals of aerosol dynamics, *Oxford University Press.*

Fu, Y., Wang, T. & Gu, C. (2013) Experimental and numerical analyses of gas–solid-multiphase jet in cross-flow. *Proceedings of the Institution of Mechanical Engineers, Part G: Journal of Aerospace Engineering,* 227**,** 61-79.

Fuentes, E., Coe, H., Green, D., De Leeuw, G. & Mcfiggans, G. (2010) On the impacts of phytoplankton-derived organic matter on the properties of the primary marine aerosol – Part 1: Source fluxes. *Atmospheric Chemistry and Physics,* 10**,** 9295-9317.

George, R. C., Wood, R., Bretherton, C. S. & Painter, G. (2013) Development and impact of hooks of high droplet concentration on remote southeast Pacific stratocumulus. *Atmospheric Chemistry and Physics,* 13**,** 6305-6328.

Georgii, H. W. & Gravenhorst, G. (1977) The ocean as source or sink of reactive trace-gases. *Pure and Applied Geophysics,* 115**,** 503-511.

Ghan, S. J., Guzman, G. & Abdul-Razzak, H. (1998) Competition between sea salt and sulfate particles as cloud condensation nuclei. *Journal of the Atmospheric Sciences,* 55**,** 3340-3347.

Ghate, V. P., Albrecht, B. A., Kollias, P., Jonsson, H. H. & Breed, D. W. (2007) Cloud seeding as a technique for studying aerosol-cloud interactions in marine stratocumulus. *Geophysical Research Letters,* 34**,** L14807.

Good, P., Lowe, J. A., Collins, M. & Moufouma-Okia, W. (2008) An objective tropical Atlantic sea surface temperature gradient index for studies of south Amazon dry-season climate variability and change. *Philosophical Transactions of the Royal Society B: Biological Sciences,* 363**,** 1761-1766.

Goren, T. & Rosenfeld, D. (2012) Satellite observations of ship emission induced transitions from broken to closed cell marine stratocumulus over large areas. *Journal of Geophysical Research,* 117**,** D17206.

Govindasamy, B., Thompson, S., Duffy, P. B., Caldeira, K. & Delire, C. (2002) Impact of geoengineering schemes on the terrestrial biosphere. *Geophysical Research Letters,* 29**,** 2061.

Gray, B., Wang, Y., Gu, D., Bandy, A., Mauldin, L., Clarke, A., Alexander, B. & Davis, D. (2011) Sources, transport, and sinks of SO_2 over the equatorial Pacific during the Pacific Atmospheric Sulfur Experiment. *Journal of Atmospheric Chemistry,* 68**,** 27-53.

Gu, L., Baldocchi, D. D., Wofsy, S. C., Munger, J. W., Michalsky, J. J., Urbanski, S. P. & Boden, T. A. (2003) Response of a deciduous forest to the Mount Pinatubo eruption: Enhanced photosynthesis. *Science,* 299**,** 2035-2038.

Guemas, V., Doblas-Reyes, F. J., Andreu-Burillo, I. & Asif, M. (2013) Retrospective prediction of the global warming slowdown in the past decade. *Nature Climate Change,* 3**,** 649-653.

Haines, D. A. & Smith, M. C. (1987) Three types of horizontal vortices observed in wildland mass and crown fires. *Journal of Climate and Applied Meteorology,* 26**,** 1624-1637.

Harrison, E., Minnis, P., Barkstrom, B., Ramanathan, V., Cess, R. & Gibson, G. (1990) Seasonal variation of cloud radiative forcing derived from the Earth Radiation Budget Experiment. *Journal of Geophysical Research: Atmospheres (1984–2012),* 95**,** 18687-18703.

Hartmann, J., West, A. J., Renforth, P., Köhler, P., De La Rocha, C. L., Wolf-Gladrow, D. A., Dürr, H. H. & Scheffran, J. (2013) Enhanced chemical weathering as a geoengineering strategy to reduce atmospheric carbon dioxide, supply nutrients, and mitigate ocean acidification. *Reviews of Geophysics,* 51**,** 113-149.

Hatzianastassiou, N., Matsoukas, C., Fotiadi, A., P. W. Stackhouse, J., Koepke, P., Pavlakis, K. G. & Vardavas, I. (2007) Modelling the direct effect of aerosols in the solar near-infrared on a planetary scale. *Atmospheric Chemistry and Physics,* 7**,** 3211-3229.

Haywood, J., Donner, L., Jones, A. & Golaz, J. (2009) Global indirect radiative forcing caused by aerosols: IPCC (2007) and beyond. *MIT Press.*

Haywood, J. M., Jones, A., Bellouin, N. & Stephenson, D. (2013) Asymmetric forcing from stratospheric aerosols impacts Sahelian rainfall. *Nature Climate Change,* 3**,** 660-665.

Haywood, J. M., Osborne, S. R. & Abel, S. J. (2004) The effect of overlying absorbing aerosol layers on remote sensing retrievals of cloud effective radius and cloud optical depth. *Quarterly Journal of the Royal Meteorological Society,* 130**,** 779-800.

Heyward, C. (2013) Situating and abandoning geoengineering: a typology of five responses to dangerous climate change. *PS: Political Science & Politics,* 46**,** 23-27.

Hill, A. A., Feingold, G. & Jiang, H. (2009) The influence of entrainment and mixing assumption on aerosol-cloud interactions in marine stratocumulus. *Journal of the Atmospheric Sciences,* 66**,** 1450-1464.

Hill, S. & Ming, Y. (2012) Nonlinear climate response to regional brightening of tropical marine stratocumulus. *Geophysical Research Letters,* 39**,** L15707.

Hobbs, P. V., Garrett, T. J., Ferek, R. J., Strader, S. R., Hegg, D. A., Frick, G. M., Hoppel, W. A., Gasparovic, R. F., Russell, L. M., Johnson, D. W., O'dowd, C., Durkee, P. A., Nielsen, K. E. & Innis, G. (2000) Emissions from ships with respect to their effects on clouds. *Journal of the Atmospheric Sciences,* 57**,** 2570-2590.

Hogan, R. J., Grant, A. L. M., Illingworth, A. J., Pearson, G. N. & O'connor, E. J. (2009) Vertical velocity variance and skewness in clear and cloud-topped boundary layers as revealed by Doppler lidar. *Quarterly Journal of the Royal Meteorological Society,* 135**,** 635-643.

Huang, R. & Hsieh, R. (2002) An experimental study of elevated round jets deflected in a crosswind. *Experimental thermal and fluid science,* 27**,** 77-86.

Huang, R. F. & Hsieh, R. H. (2003) Sectional flow structures in near wake of elevated jets in a crossflow. *AIAA journal,* 41**,** 1490-1499.

Huq, P. & Dhanak, M. (1996) The bifurcation of circular jets in crossflow. *Physics of Fluids,* 8**,** 754.

IPCC (2000) Special Report on Emissions Scenarios. Nakicenovic, N. & Swart, R. (eds). *Cambrige University Press.*

IPCC (2013) Summary for Policymakers. Working Group I Contribution to the IPCC Fifth Assessment Report Climate Change 2013: The Physical Science Basis. Available: http://www.climatechange2013.org/images/uploads/WGIAR5-SPM_Approved27Sep2013.pdf [Accessed 17th October 2013].

Irvine, P. J., Ridgwell, A. & Lunt, D. J. (2011) Climatic effects of surface albedo geoengineering. *Journal of Geophysical Research,* 116**,** D24112.

Jacobs, M. (2012) The Doha climate talks were a start, but 2015 will be the moment of truth. Available: http://www.theguardian.com/commentisfree/2012/dec/10/doha-climate-talks-global-warming/print [Accessed 30th July 2013].

Jacobson, M. Z., Turco, R. P., Jensen, E. J. & Toon, O. B. (1994) Modeling coagulation among particles of different composition and size. *Atmospheric Environment,* 28**,** 1327-1338.

Jansen, E., Overpeck, J., Briffa, K. R., Duplessy, J.-C., Joos, F., Masson-Delmotte, V., Olago, D., Otto-Bliesner, B., Peltier, W. R., Rahmstorf, S., Ramesh, R., Raynaud, D., Rind, D., Solomina, O., Villalba, R. & Zhang, D. (2007) Palaeoclimate. In: Climate Change 2007: The Physical Science Basis. Contribution of Working Group I to the Fourth Assessment Report of the Intergovernmental Panel on Climate Change. [Solomon, S., D. Qin, M. Manning, Z. Chen, M. Marquis, K.B. Averyt, M.Tignor and H.L. Miller (eds.)]. Cambridge University Press, Cambridge, United Kingdom and New York, NY, USA.

Jevrejeva, S., Moore, J. & Grinsted, A. (2010) How will sea level respond to changes in natural and anthropogenic forcings by 2100? *Geophysical Research Letters,* 37.

Jiang, H., Feingold, G. & Cotton, W. R. (2002) Simulations of aerosol-cloud-dynamical feedbacks resulting from entrainment of aerosol into the marine boundary layer during the Atlantic Stratocumulus Transition Experiment. *Journal of Geophysical Research,* 107**,** 4813.

Johnson, B. T., Shine, K. P. & Forster, P. M. (2004) The semi-direct aerosol effect: Impact of absorbing aerosols on marine stratocumulus. *Quarterly Journal of the Royal Meteorological Society,* 130**,** 1407-1422.

Jones, A., Haywood, J. & Boucher, O. (2009) Climate impacts of geoengineering marine stratocumulus clouds. *Journal of Geophysical Research,* 114**,** D10106.

Jones, A., Haywood, J. & Boucher, O. (2011a) A comparison of the climate impacts of geoengineering by stratospheric SO2 injection and by brightening of marine stratocumulus cloud. *Atmospheric Science Letters,* 12**,** 176-183.

Jones, A. & Haywood, J. M. (2012) Sea-spray geoengineering in the HadGEM2-ES earth-system model: radiative impact and climate response. *Atmospheric Chemistry and Physics,* 12**,** 10887-10898.

Jones, C. R., Bretherton, C. S. & Leon, D. (2011b) Coupled vs. decoupled boundary layers in VOCALS-REx. *Atmospheric Chemistry and Physics,* 11**,** 7143-7153.

Joshi, M., Sutton, R., Lowe, J. & Frame, D. (2011) Projections of when temperature change will exceed 2°C above pre-industrial levels. *Nature Climate Change,* 1**,** 407-412.

Kazil, J., Wang, H., Feingold, G., Clarke, A. D., Snider, J. R. & Bandy, A. R. (2011) Modeling chemical and aerosol processes in the transition from closed to open cells during VOCALS-REx. *Atmospheric Chemistry and Physics,* 11**,** 7491-7514.

Keffer, J. F. & Baines, W. D. (1963) The round turbulent jet in a cross-wind. *Journal of Fluid Mechanics,* 15**,** 481-496.

Keith, D. W. (2000) Geoengineering The Climate: History and Prospect. *Annual Review of Energy and the Environment,* 25**,** 245-84.

Kelso, R. M., Lim, T. & Perry, A. (1996) An experimental study of round jets in cross-flow. *Journal of Fluid Mechanics,* 306**,** 111-144.

Khairoutdinov, M. & Kogan, Y. (2000) A New Cloud Physics Parameterization in a Large-Eddy Simulation Model of Marine Stratocumulus. *Monthly Weather Review,* 128**,** 229-243.

Khairoutdinov, M. F. & Randall, D. A. (2001) A cloud resolving model as a cloud parameterization in the NCAR Community Climate System Model: Preliminary results. *Geophysical Research Letters,* 28**,** 3617-3620.

Khalil, M. a. K. & Rasmussen, R. A. (1994) Global decrease in atmospheric carbon monoxide concentration. *Nature,* 370**,** 639-641.

Klein, R. J. T., S. Huq, F.Denton, T.E. Downing, R.G. Richels, J.B. Robinson & Toth, F. L. (2007) Inter-relationships between adaptation and mitigation. Climate Change 2007: Impacts, Adaptation and Vulnerability. Contribution of Working Group II to the Fourth Assessment Report of the Intergovernmental Panel on Climate Change. [M.L. Parry, O.F.

Canziani, J.P. Palutikov, P.J. van der Linden and C.E. Hanson (eds.)]. Cambridge University Press, Cambridge, United Kingdom, 745-777.

Klein, S. A. & Hartmann, D. L. (1993) The seasonal cycle of low stratiform clouds. *Journal of Climate,* 6**,** 1587-1606.

Köhler, H. (1936) The nucleus in and the growth of hygroscopic droplets. *Transactions of the Faraday Society,* 32**,** 1152-1161.

Korhonen, H., Carslaw, K. S., Forster, P. M., Mikkonen, S., Gordon, N. D. & Kokkola, H. (2010a) Aerosol climate feedback due to decadal increases in Southern Hemisphere wind speeds. *Geophysical Research Letters,* 37.

Korhonen, H., Carslaw, K. S. & Romakkaniemi, S. (2010b) Enhancement of marine cloud albedo via controlled sea spray injections: a global model study of the influence of emission rates, microphysics and transport. *Atmospheric Chemistry and Physics,* 10**,** 4133-4143.

Kravitz, B., Forster, P. M., Jones, A., Robock, A., Alterskjær, K., Boucher, O., Jenkins, A. K. L., Korhonen, H., Kristjánsson, J. E., Muri, H., Niemeier, U., Partanen, A.-I., Rasch, P. J., Wang, H. & Watanabe, S. (2013) Sea spray geoengineering experiments in the geoengineering model intercomparison project (GeoMIP): Experimental design and preliminary results. *Journal of Geophysical Research: Atmospheres,* 118**,** 2013JD020351.

Kuang, C., Mcmurry, P. H. & Mccormick, A. V. (2009) Determination of cloud condensation nuclei production from measured new particle formation events. *Geophysical Research Letters,* 36**,** L09822.

Lacis, A. A. & Hansen, J. (1974) A parameterization for the absorption of solar radiation in the Earth's atmosphere. *Journal of the Atmospheric Sciences,* 31**,** 118-133.

Latham, J. (1990) Control of global warming? *Nature,* 347**,** 339-340.

Latham, J. (2002) Amelioration of global warming by controlled enhancement of the albedo and longevity of low-level maritime clouds. *Atmospheric Science Letters,* 3**,** 52-58.

Latham, J., Bower, K., Choularton, T., Coe, H., Connolly, P., Cooper, G., Craft, T., Foster, J., Gadian, A., Galbraith, L., Iacovides, H., Johnston, D., Launder, B., Leslie, B., Meyer, J., Neukermans, A., Ormond, B., Parkes, B., Rasch, P., Rush, J., Salter, S., Stevenson, T., Wang, H., Wang, Q. & Wood, R. (2012a) Marine cloud brightening. *Philosophical Transactions of the Royal Society A: Mathematical, Physical and Engineering Sciences,* 370**,** 4217-4262.

Latham, J., Parkes, B., Gadian, A. & Salter, S. (2012b) Weakening of hurricanes via marine cloud brightening (MCB). *Atmospheric Science Letters*.

Latham, J., Rasch, P., Chen, C.-C., Kettles, L., Gadian, A., Gettelman, A., Morrison, H., Bower, K. & Choularton, T. (2008) Global temperature stabilization via controlled albedo

enhancement of low-level maritime clouds. *Philosophical Transactions of the Royal Society A: Mathematical, Physical and Engineering Sciences,* 366**,** 3969-3987.

Lee, L. A., Pringle, K. J., Reddington, C. L., Mann, G. W., Stier, P., Spracklen, D. V., Pierce, J. R. & Carslaw, K. S. (2013) The magnitude and causes of uncertainty in global model simulations of cloud condensation nuclei. *Atmospheric Chemistry and Physics,* 13**,** 8879-8914.

Lehahn, Y., Koren, I., Altaratz, O. & Kostinski, A. B. (2011) Effect of coarse marine aerosols on stratocumulus clouds. *Geophysical Research Letters,* 38**,** L20804.

Lenton, T. M. (2013) Can emergency geoengineering really prevent climate tipping points? (Opinion Article). *Geoengineering Our Climate Working Paper and Opinion Article Series* [Online]. Available: http://wp.me/p2zsRk-7Z [Accessed 14th January 2014].

Leon, D. C., Wang, Z. & Liu, D. (2008) Climatology of drizzle in marine boundary layer clouds based on 1 year of data from CloudSat and Cloud-Aerosol Lidar and Infrared Pathfinder Satellite Observations (CALIPSO). *Journal of Geophysical Research: Atmospheres,* 113**,** D00A14.

Lewis, E. R. & Schwartz, S. E. (2004) Sea salt aerosol production: mechanisms, methods, measurements and models—a critical review, *American Geophysical Union*.

Li, J., Ma, X., Von Salzen, K. & Dobbie, S. (2008) Parameterization of sea-salt optical properties and physics of the associated radiative forcing. *Atmospheric Chemistry and Physics,* 8**,** 4787-4798.

Lienhard, J. H. (1966) Synopsis of lift, drag, and vortex frequency data for rigid circular cylinders, *Technical Extension Service, Washington State University*.

Lilly, D. K. (1968) Models of cloud-topped mixed layers under a strong inversion. *Quarterly Journal of the Royal Meteorological Society,* 94**,** 292-309.

Liu, Q., Kogan, Y. L., Lilly, D. K., Johnson, D. W., Innis, G. E., Durkee, P. A. & Nielsen, K. E. (2000) Modeling of ship effluent transport and its sensitivity to boundary layer structure. *Journal of the Atmospheric Sciences,* 57**,** 2779-2791.

Lobell, D. B. & Gourdji, S. M. (2012) The influence of climate change on global crop productivity. *Plant Physiology,* 160**,** 1686-1697.

Lu, M.-L., Conant, W. C., Jonsson, H. H., Varutbangkul, V., Flagan, R. C. & Seinfeld, J. H. (2007) The Marine Stratus/Stratocumulus Experiment (MASE): Aerosol-cloud relationships in marine stratocumulus. *Journal of Geophysical Research: Atmospheres,* 112**,** D10209.

Lu, M.-L. & Seinfeld, J. H. (2005) Study of the aerosol indirect effect by large-eddy simulation of marine stratocumulus. *Journal of the Atmospheric Sciences,* 62**,** 3909-3932.

MacNeill, J. (n.d.) Climate Change Cloud Ship [Online]. Available: http://www.johnmacneill.com/images/Salter_Albedo2.JPG [Accessed 30 May 2013].

Mahesh, K. (2013) The Interaction of Jets with Crossflow. *Annual Review of Fluid Mechanics,* 45**,** 379-407.

Majander, P. & Siikonen, T. (2006) Large-eddy simulation of a round jet in a cross-flow. *International Journal of Heat and Fluid Flow,* 27**,** 402-415.

Mann, G. W., Carslaw, K. S., Spracklen, D. V., Ridley, D. A., Manktelow, P. T., Chipperfield, M. P., Pickering, S. J. & Johnson, C. E. (2010) Description and evaluation of GLOMAP-mode: a modal global aerosol microphysics model for the UKCA composition-climate model. *Geoscientific Model Development,* 3**,** 519-551.

Margason, R. J. (1993) Fifty years of jet in cross flow research. *In: Proceedings of the AGARD Symposium on Computational and Experimental Assessment of Jets in Cross Flow, United Kingdom,* AGARD-CP-534.

Matthews, H. D. & Caldeira, K. (2007) Transient climate–carbon simulations of planetary geoengineering. *Proceedings of the National Academy of Sciences,* 104**,** 9949-9954.

Meehl, G. A., Hu, A., Tebaldi, C., Arblaster, J. M., Washington, W. M., Teng, H., Sanderson, B. M., Ault, T., Strand, W. G. & White, J. B. (2012) Relative outcomes of climate change mitigation related to global temperature versus sea-level rise. *Nature Climate Change,* 2**,** 576-580.

Miller, S. & Garrick, S. (2004) Nanoparticle Coagulation in a Planar Jet. *Aerosol Science and Technology,* 38**,** 79-89.

Minnis, P., Heck, P. W., Young, D. F., Fairall, C. W. & Snider, J. B. (1992) Stratocumulus cloud properties derived from simultaneous satellite and island-based instrumentation during FIRE. *Journal of Applied Meteorology,* 31**,** 317-339.

Moeng, C.-H. (2000) Entrainment rate, cloud fraction, and liquid water path of PBL stratocumulus clouds. *Journal of the Atmospheric Sciences,* 57**,** 3627-3643.

Moeng, C.-H. & Rotunno, R. (1990) Vertical-velocity skewness in the buoyancy-driven boundary layer, *American Meteorological Society*.

Morrison, H., Curry, J. A. & Khvorostyanov, V. I. (2005) A new double-moment microphysics parameterization for application in cloud and climate models. Part I: Description. *Journal of the Atmospheric Sciences,* 62**,** 1665-1677.

Morrison, H., Thompson, G. & Tatarskii, V. (2009) Impact of Cloud Microphysics on the Development of Trailing Stratiform Precipitation in a Simulated Squall Line: Comparison of One- and Two-Moment Schemes. *Monthly Weather Review,* 137**,** 991-1007.

Moussa, Z., Trischka, J. W. & Eskinazi, S. (1977) The near field in the mixing of a round jet with a cross-stream. *Journal of Fluid Mechanics,* 80**,** 49-80.

Muppidi, S. & Mahesh, K. (2005) Study of trajectories of jets in crossflow using direct numerical simulations. *Journal of Fluid Mechanics,* 530**,** 81-100.

Myhre, G., Shindell, D., Bréon, F.-M., Collins, W., Fuglestvedt, J., Huang, J., Koch, D., J-F., L., Lee, D., Mendoza, B., Nakajima, T., Robock, A., Stephens, G., Takemura, T. & Zhang, H. (2013) Anthropogenic and Natural Radiative Forcing. In: Climate Change 2013: The Physical Science Basis. Contribution of Working Group I to the Fifth Assessment Report of the Intergovernmental Panel on Climate Change. Available: http://www.ipcc.ch/report/ar5/wg1/#.UnOrnBBzo4I [Accessed 1st November 2013].

NASA (2013) *GISS Surface Temperature Analysis* [Online]. Available: http://data.giss.nasa.gov/gistemp/graphs_v3 [Accessed 16th August 2013].

National Snow and Ice Data Center (2013). Available: http://nsidc.org/cryosphere/sotc/sea_ice.html [Accessed 27 May 2013].

Neukermans, A., Cooper, G., Foster, J., Gadian, A., Galbraith, L., Jain, S., Latham, J. & Ormond, B. (2014) Sub-micrometer salt aerosol production intended for marine cloud brightening. *Atmospheric Research* [Online]. Available: http://www.sciencedirect.com/science/article/pii/S0169809513003128 [Accessed 6th January 2014].

Nicholls, S. (1984) The dynamics of stratocumulus: Aircraft observations and comparisons with a mixed layer model. *Quarterly Journal of the Royal Meteorological Society,* 110**,** 783-820.

Nicholls, S. (1989) The structure of radiatively driven convection in stratocumulus. *Quarterly Journal of the Royal Meteorological Society,* 115**,** 487-511.

Nicholls, S. & Leighton, J. (1986) An observational study of the structure of stratiform cloud sheets: Part I. Structure. *Quarterly Journal of the Royal Meteorological Society,* 112**,** 431-460.

Nieuwstadt, F. T. M. & Duynkerke, P. G. (1996) Turbulence in the atmospheric boundary layer. *Atmospheric Research,* 40**,** 111-142.

O'Dowd, C. D., Smith, M. H., Consterdine, I. E. & Lowe, J. A. (1997) Marine aerosol, sea-salt, and the marine sulphur cycle: A short review. *Atmospheric Environment,* 31**,** 73-80.

Otto, A., Otto, F. E. L., Boucher, O., Church, J., Hegerl, G., Forster, P. M., Gillett, N. P., Gregory, J., Johnson, G. C., Knutti, R., Lewis, N., Lohmann, U., Marotzke, J., Myhre, G., Shindell, D., Stevens, B. & Allen, M. R. (2013) Energy budget constraints on climate response. *Nature Geoscience,* 6**,** 415-416.

Painemal, D., Garreaud, R., Rutllant, J. & Zuidema, P. (2010) Southeast Pacific Stratocumulus: High-Frequency Variability and Mesoscale Structures over San Félix Island. *Journal of Applied Meteorology and Climatology,* 49**,** 463-477.

Painemal, D. & Minnis, P. (2012) On the dependence of albedo on cloud microphysics over marine stratocumulus clouds regimes determined from Clouds and the Earth's Radiant

Energy System (CERES) data. *Journal of Geophysical Research: Atmospheres,* 117**,** D06203.

Paluch, I. R. & Lenschow, D. H. (1991) Stratiform Cloud Formation in the Marine Boundary Layer. *Journal of the Atmospheric Sciences,* 48**,** 2141-2158.

Partanen, A.-I., Kokkola, H., Romakkaniemi, S., Kerminen, V.-M., Lehtinen, K. E. J., Bergman, T., Arola, A. & Korhonen, H. (2012) Direct and indirect effects of sea spray geoengineering and the role of injected particle size. *Journal of Geophysical Research,* 117**,** D02203.

Patt, A. (2009) Communicating Uncertainty to Policy Makers. *Uncertainties in Environmental Modelling and Consequences for Policy Making.* Springer.

Peters, G. P., Andrew, R. M., Boden, T., Canadell, J. G., Ciais, P., Le Quere, C., Marland, G., Raupach, M. R. & Wilson, C. (2013) The challenge to keep global warming below 2°C. *Nature Climate Change,* 3**,** 4-6.

Petters, J. L., Jiang, H., Feingold, G., Rossiter, D. L., Khelif, D., Sloan, L. C. & Chuang, P. Y. (2013) A comparative study of the response of modeled non-drizzling stratocumulus to meteorological and aerosol perturbations. *Atmospheric Chemistry and Physics,* 13**,** 2507-2529.

Pringle, K. J., Carslaw, K. S., Fan, T., Mann, G. W., Hill, A., Stier, P., Zhang, K. & Tost, H. (2012) A multi-model assessment of the impact of sea spray geoengineering on cloud droplet number. *Atmospheric Chemistry and Physics,* 12**,** 11647-11663.

Rahmstorf, S. & Coumou, D. (2011) Increase of extreme events in a warming world. *Proceedings of the National Academy of Sciences,* 108**,** 17905-17909.

Ramanathan, V., Cess, R. D., Harrison, E. F., Minnis, P., Barkstrom, B. R., Ahmad, E. & Hartmann, D. (1989) Cloud-radiative forcing and climate: Results from the Earth Radiation Budget Experiment. *Science,* 243**,** 57-63.

Ramaswamy, V., Boucher, O., Haigh, J., Hauglustaine, D., Haywood, J., Myhre, G., Nakajima, T., Shi, G. Y., Solomon, S., Betts, R., Charlson, R., Chuang, C., Daniel, J. S., Genio, A. D., Dorland, R. V., Feichter, J., Fuglestvedt, J., Forster, P. M. D. F., Ghan, S. J., Jones, A., Kiehl, J. T., Koch, D., Land, C., Lean, J., Lohmann, U., Minschwaner, K., Penner, J. E., Roberts, D. L., Rodhe, H., Roelofs, G. J., Rotstayn, L. D., Schneider, T. L., Schumann, U., Schwartz, S. E., Schwarzkopf, M. D., Shine, K. P., Smith, S., Stevenson, D. S., Stordal, F., Tegen, I. & Zhang, Y. (2001) Radiative forcing of climate change. In: Climate Change 2001: The Scientific Basis. Contribution of Working Group I to the Third Assessment Report of the Intergovernmental Panel on Climate Change, *Cambridge University Press, Cambridge, United Kingdom and New York, NY, USA*. 349-416

Randles, C. A., Russell, L. M. & Ramaswamy, V. (2004) Hygroscopic and optical properties of organic sea salt aerosol and consequences for climate forcing. *Geophysical Research Letters,* 31**,** L16108.

Rap, A., Spracklen, D. V., Bellouin, N., Scott, C. E., Forster, P. M., Carslaw, K. S., Schmidt, A. & Mann, G. (2013) Natural aerosol direct and indirect radiative effects. *Geophysical Research Letters***,** n/a-n/a.

Rasch, P. J., Latham, J. & Chen, C.-C. (2009) Geoengineering by cloud seeding: influence on sea ice and climate system. *Environmental Research Letters,* 4**,** 045112.

Rasch, P. J., Tilmes, S., Turco, R. P., Robock, A., Oman, L., Chen, C.-C. J., Stenchikov, G. L. & Garcia, R. R. (2008) An overview of geoengineering of climate using stratospheric sulphate aerosols. *Philosophical Transactions of the Royal Society A: Mathematical, Physical and Engineering Sciences,* 366**,** 4007-4037.

Rissman, T. A., Nenes, A. & Seinfeld, J. H. (2004) Chemical amplification (or dampening) of the Twomey effect: Conditions derived from droplet activation theory. *Journal of the Atmospheric Sciences,* 61**,** 919-930.

Robock, A., Marquardt, A., Kravitz, B. & Stenchikov, G. (2009) Benefits, risks, and costs of stratospheric geoengineering. *Geophysical Research Letters,* 36**,** L19703.

Rogelj, J., Meinshausen, M. & Knutti, R. (2012) Global warming under old and new scenarios using IPCC climate sensitivity range estimates. *Nature Climate Change,* 2**,** 248-253.

Rogers, D. P. & Koracin, D. (1992) Radiative transfer and turbulence in the cloud-topped marine atmospheric boundary layer. *Journal of the Atmospheric Sciences* 49:16**,** 1473-1486.

Rosenfeld, D., Kaufman, Y. J. & Koren, I. (2006) Switching cloud cover and dynamical regimes from open to closed Benard cells in response to the suppression of precipitation by aerosols. *Atmospheric Chemistry and Physics,* 6**,** 2503-2511.

Rosenfeld, D., Wang, H. & Rasch, P. J. (2012) The roles of cloud drop effective radius and LWP in determining rain properties in marine stratocumulus. *Geophysical Research Letters,* 39**,** L13801.

Roshko, A. (1954) On the development of turbulent wakes from vortex streets. *California Institute of Technology.*

Rossow, W. B. & Schiffer, R. A. (1999) Advances in understanding clouds from ISCCP. *Bulletin of the American Meteorological Society,* 80**,** 2261-2287.

Rozendaal, M. A., Leovy, C. B. & Klein, S. A. (1995) An observational study of diurnal variations of marine stratiform cloud. *Journal of Climate,* 8**,** 1795-1809.

Rudman, M. J. (1996) Simulation of the near field of a jet in a cross flow. *Experimental Thermal and Fluid Science,* 12**,** 134-141.

Russell, L. M., Sorooshian, A., Seinfeld, J. H., Albrecht, B. A., Nenes, A., Ahlm, L., Chen, Y.-C., Coggon, M., Craven, J. S., Flagan, R. C., Frossard, A. A., Jonsson, H., Jung, E., Lin, J. J., Metcalf, A. R., Modini, R., Mülmenstädt, J., Roberts, G., Shingler, T., Song, S., Wang, Z. & Wonaschütz, A. (2013) Eastern Pacific Emitted Aerosol Cloud Experiment. *Bulletin of the American Meteorological Society,* 94**,** 709-729.

Saffman, P. & Turner, J. (1956) On the collision of drops in turbulent clouds. *Journal of Fluid Mechanics,* 1**,** 16-30.

Saide, P., Spak, S., Carmichael, G., Mena-Carrasco, M., Yang, Q., Howell, S., Leon, D., Snider, J. R., Bandy, A. R. & Collett, J. L. (2012) Evaluating WRF-Chem aerosol indirect effects in Southeast Pacific marine stratocumulus during VOCALS-REx. *Atmospheric Chemistry and Physics,* 12**,** 3045-3064.

Salter, S., Sortino, G. & Latham, J. (2008) Sea-going hardware for the cloud albedo method of reversing global warming. *Philosophical Transactions of the Royal Society A: Mathematical, Physical and Engineering Sciences,* 366**,** 3989-4006.

Sandu, I., Brenguier, J.-L., Geoffroy, O., Thouron, O. & Masson, V. (2008) Aerosol impacts on the diurnal cycle of marine stratocumulus. *Journal of the Atmospheric Sciences,* 65**,** 2705-2718.

Sandu, I., Brenguier, J.-L., Thouron, O. & Stevens, B. (2009) How important is the vertical structure for the representation of aerosol impacts on the diurnal cycle of marine stratocumulus? *Atmospheric Chemistry and Physics,* 9**,** 4039-4052.

Sandu, I. & Stevens, B. (2011) On the factors modulating the stratocumulus to cumulus transitions. *Journal of the Atmospheric Sciences*.

Sandu, I., Stevens, B. & Pincus, R. (2010) On the transitions in marine boundary layer cloudiness. *Atmospheric Chemistry and Physics,* 10**,** 2377-2391.

Savic-Jovcic, V. & Stevens, B. (2008) The structure and mesoscale organization of precipitating stratocumulus. *Journal of the Atmospheric Sciences,* 65**,** 1587-1605.

Sechrist, B., Coakley Jr, J. & Tahnk, W. (2012) Effects of additional particles on already polluted marine stratus. *Journal of the Atmospheric Sciences,* 69**,** 1975-1993.

Seidel, D. J., Feingold, G., Jacobson, A. R. & Loeb, N. (2014) Detection limits of albedo changes induced by climate engineering. *Nature Climate Change,* 4**,** 93-98.

Seinfeld, J. H. & Pandis, S. N. (2006) Atmospheric chemistry and physics: From air pollution to climate change, *John Wiley & Sons*.

Seitz, R. (2011) Bright water: hydrosols, water conservation and climate change. *Climatic Change,* 105**,** 365-381.

Shepherd, J. (2012) Geoengineering the climate: An overview and update. *Philosophical Transactions of the Royal Society A: Mathematical, Physical and Engineering Sciences,* 370**,** 4166-4175.

Skamarock, W. C., Klemp, J. B., Dudhia, J., Gill, D. O., Barker, D. M., Duda, M. G., Huang, X.-Y., Wang, W. & Powers, J. G. (2008) A description of the Advanced Research WRF Version 3. *NCAR Technical Note,* NCAR/TN-475+STR.

Slangen, A., Katsman, C., Van De Wal, R., Vermeersen, L. & Riva, R. (2012) Towards regional projections of twenty-first century sea-level change based on IPCC SRES scenarios. *Climate Dynamics,* 38**,** 1191-1209.

Smith, S. & Mungal, M. (1998) Mixing, structure and scaling of the jet in crossflow. *Journal of Fluid Mechanics,* 357**,** 83-122.

Smoluchowski, M. V. (1916) Drei Vortrage uber Diffusion, Brownsche Bewegung und Koagulation von Kolloidteilchen. *Zeitschrift fur Physik,* 17**,** 557-585.

Soldati, A. & Marchioli, C. (2009) Physics and modelling of turbulent particle deposition and entrainment: Review of a systematic study. *International Journal of Multiphase Flow,* 35**,** 827-839.

Stephens, G. L. (2005) Cloud feedbacks in the climate system: A critical review. *Journal of Climate,* 18**,** 237-273.

Stevens, B. (2010) Cloud-top entrainment instability? *Journal of Fluid Mechanics,* 660**,** 1-4.

Stevens, B., Cotton, W. R., Feingold, G. & Moeng, C.-H. (1998) Large-eddy simulations of strongly precipitating, shallow, stratocumulus-topped boundary layers. *Journal of the Atmospheric Sciences,* 55**,** 3616-3638.

Stevens, B. & Feingold, G. (2009) Untangling aerosol effects on clouds and precipitation in a buffered system. *Nature,* 461**,** 607-613.

Stevens, B., Lenschow, D. H., Faloona, I., Moeng, C. H., Lilly, D. K., Blomquist, B., Vali, G., Bandy, A., Campos, T., Gerber, H., Haimov, S., Morley, B. & Thornton, D. (2003a) On entrainment rates in nocturnal marine stratocumulus. *Quarterly Journal of the Royal Meteorological Society,* 129**,** 3469-3493.

Stevens, B., Lenschow, D. H., Vali, G., Gerber, H., Bandy, A., Blomquist, B., Brenguier, J.-L., Bretherton, C. S., Burnet, F., Campos, T., Chai, S., Faloona, I., Friesen, D., Haimov, S., Laursen, K., Lilly, D. K., Loehrer, S. M., Malinowski, S. P., Morley, B., Petters, M. D., Rogers, D. C., Russell, L., Savic-Jovcic, V., Snider, J. R., Straub, D., Szumowski, M. J., Takagi, H., Thornton, D. C., Tschudi, M., Twohy, C., Wetzel, M. & Van Zanten, M. C. (2003b) Dynamics and Chemistry of Marine Stratocumulus—DYCOMS-II. *Bulletin of the American Meteorological Society,* 84**,** 579-593.

Stevens, B., Moeng, C.-H., Ackerman, A. S., Bretherton, C. S., Chlond, A., De Roode, S., Edwards, J., Golaz, J.-C., Jiang, H., Khairoutdinov, M., Kirkpatrick, M. P., Lewellen, D. C., Lock, A., Müller, F., Stevens, D. E., Whelan, E. & Zhu, P. (2005a) Evaluation of large-eddy simulations via observations of nocturnal marine stratocumulus. *Monthly Weather Review,* 133**,** 1443-1462.

Stevens, B., Moeng, C.-H. & Sullivan, P. P. (1999) Large-eddy simulations of radiatively driven convection: Sensitivities to the representation of small scales. *Journal of the Atmospheric Sciences,* 56**,** 3963-3984.

Stevens, B., Vali, G., Comstock, K., Wood, R., Van Zanten, M. C., Austin, P. H., Bretherton, C. S. & Lenschow, D. H. (2005b) Pockets of open cells and drizzle in marine stratocumulus. *Bulletin of the American Meteorological Society,* 86**,** 51-57.

Stevens, D. E. & Bretherton, C. S. (1999) Effects of resolution on the simulation of stratocumulus entrainment. *Quarterly Journal of the Royal Meteorological Society,* 125**,** 425-439.

Stuart, G. S., Stevens, R. G., Partanen, A. I., Jenkins, A. K. L., Korhonen, H., Forster, P. M., Spracklen, D. V. & Pierce, J. R. (2013) Reduced efficacy of marine cloud brightening geoengineering due to in-plume aerosol coagulation: parameterization and global implications. *Atmospheric Chemistry and Physics,* 13**,** 10385-10396.

Stubenrauch, C. J., Chédin, A., Rädel, G., Scott, N. A. & Serrar, S. (2006) Cloud properties and their seasonal and diurnal variability from TOVS Path-B. *Journal of Climate,* 19**,** 5531-5553.

Su, L. & Mungal, M. (2004) Simultaneous measurements of scalar and velocity field evolution in turbulent crossflowing jets. *Journal of Fluid Mechanics,* 513**,** 1-45.

The Royal Society (2009) Geoengineering the climate: Science, governance and uncertainty. Shepherd, J. (eds).

Tompkins, A. M. (2001) Organization of tropical convection in low vertical wind shears: The role of cold pools. *Journal of the Atmospheric Sciences,* 58**,** 1650-1672.

Trenberth, K. E., Jones, P. D., Ambenje, P., Bojariu, R., Easterling, D., Tank, A. K., Parker, D., Rahimzadeh, F., Renwick, J. A., Rusticucci, M., Soden, B. & Zhai, P. (2007) Observations: Surface and Atmospheric Climate Change. In: Climate Change 2007: The Physical Science Basis. Contribution of Working Group I to the Fourth Assessment Report of the Intergovernmental Panel on Climate Change. [Solomon, S., D. Qin, M. Manning, Z. Chen, M. Marquis, K.B. Averyt, M.Tignor and H.L. Miller (eds.)]. Cambridge University Press, Cambridge, United Kingdom and New York, NY, USA.

Tu, C.-X. & Liu, S. (2012) Nanoparticle coagulation and dispersion in a turbulent planar jet with constraints. *Thermal Science,* 16**,** 1497-1501.

Turner, D. B. (1970) Workbook of atmospheric dispersion estimates, *US Department of Health, Education, and Welfare, National Center for Air Pollution Control*.

Twohy, C. H., Petters, M. D., Snider, J. R., Stevens, B., Tahnk, W., Wetzel, M., Russell, L. & Burnet, F. (2005) Evaluation of the aerosol indirect effect in marine stratocumulus clouds: Droplet number, size, liquid water path, and radiative impact. *Journal of Geophysical Research,* 110**,** D08203.

Twomey, S. (1974) Pollution and the planetary albedo. *Atmospheric Environment (1967),* 8**,** 1251-1256.

Twomey, S. (1977) The influence of pollution on the shortwave albedo of clouds. *Journal of the Atmospheric Sciences,* 34**,** 1149-1152.

vanZanten, M. C., Stevens, B., Vali, G. & Lenschow, D. H. (2005) Observations of drizzle in nocturnal marine stratocumulus. *Journal of the Atmospheric Sciences,* 62**,** 88-106.

Vaughan, N. & Lenton, T. (2011) A review of climate geoengineering proposals. *Climatic Change,* 109**,** 745-790.

Villarini, G. & Vecchi, G. A. (2012) Projected increases in North Atlantic tropical cyclone intensity from CMIP5 models. *Journal of Climate,* 26**,** 3231-3240.

Wang, H. & Feingold, G. (2009a) Modeling mesoscale cellular structures and drizzle in marine stratocumulus. Part I: Impact of drizzle on the formation and evolution of open cells. *Journal of the Atmospheric Sciences,* 66**,** 3237-3256.

Wang, H. & Feingold, G. (2009b) Modeling mesoscale cellular structures and drizzle in marine stratocumulus. Part II: The microphysics and dynamics of the boundary region between open and closed cells. *Journal of the Atmospheric Sciences,* 66**,** 3257-3275.

Wang, H., Feingold, G., Wood, R. & Kazil, J. (2010) Modelling microphysical and meteorological controls on precipitation and cloud cellular structures in Southeast Pacific stratocumulus. *Atmospheric Chemistry and Physics,* 10**,** 6347-6362.

Wang, H., Rasch, P. J. & Feingold, G. (2011a) Manipulating marine stratocumulus cloud amount and albedo: a process-modelling study of aerosol-cloud-precipitation interactions in response to injection of cloud condensation nuclei. *Atmospheric Chemistry and Physics,* 11**,** 4237-4249.

Wang, H., Skamarock, W. C. & Feingold, G. (2009) Evaluation of scalar advection schemes in the Advanced Research WRF model using large-eddy simulations of aerosol-cloud interactions. *Monthly Weather Review,* 137**,** 2547-2558.

Wang, M., Ghan, S., Ovchinnikov, M., Liu, X., Easter, R., Kassianov, E., Qian, Y. & Morrison, H. (2011b) Aerosol indirect effects in a multi-scale aerosol-climate model PNNL-MMF. *Atmospheric Chemistry and Physics,* 11**,** 5431-5455.

Wang, M. & Overland, J. E. (2012) A sea ice free summer Arctic within 30 years: An update from CMIP5 models. *Geophysical Research Letters,* 39.

Wang, S., Golaz, J.-C. & Wang, Q. (2008) Effect of intense wind shear across the inversion on stratocumulus clouds. *Geophysical Research Letters,* 35**,** L15814.

Wang, S., Wang, Q. & Feingold, G. (2003) Turbulence, condensation, and liquid water transport in numerically simulated nonprecipitating stratocumulus clouds. *Journal of the Atmospheric Sciences,* 60**,** 262-278.

Warren, R., VanDerWal, J., Price, J., Welbergen, J. A., Atkinson, I., Ramirez-Villegas, J., Osborn, T. J., Jarvis, A., Shoo, L. P., Williams, S. E. & Lowe, J. (2013) Quantifying the benefit of early climate change mitigation in avoiding biodiversity loss. *Nature Climate Change,* 3**,** 678-682.

Webb, M., Lambert, F. H. & Gregory, J. (2013) Origins of differences in climate sensitivity, forcing and feedback in climate models. *Climate Dynamics,* 40**,** 677-707.

Wen, F., Kamalu, N., Chung, J., Crowe, C. & Troutt, T. (1992) Particle dispersion by vortex structures in plane mixing layers. *Journal of Fluids Engineering,* 114**,** 657.

Williamson, C. (1996) Vortex dynamics in the cylinder wake. *Annual Review of Fluid Mechanics,* 28**,** 477-539.

Williamson, P., Wallace, D. W. R., Law, C. S., Boyd, P. W., Collos, Y., Croot, P., Denman, K., Riebesell, U., Takeda, S. & Vivian, C. (2012) Ocean fertilization for geoengineering: A review of effectiveness, environmental impacts and emerging governance. *Process Safety and Environmental Protection,* 90**,** 475-488.

Wood, R. (2005) Drizzle in stratiform boundary layer clouds. Part I: Vertical and horizontal structure. *Journal of the Atmospheric Sciences,* 62**,** 3011-3033.

Wood, R. (2007) Cancellation of aerosol indirect effects in marine stratocumulus through cloud thinning. *Journal of the Atmospheric Sciences,* 64**,** 2657-2669.

Wood, R. (2012) Stratocumulus Clouds. *Monthly Weather Review,* 140**,** 2373-2423.

Wood, R. & Ackerman, T. (2013) Defining success and limits of field experiments to test geoengineering by marine cloud brightening. *Climatic Change,* 121**,** 459-472.

Wood, R. & Bretherton, C. S. (2004) Boundary layer depth, entrainment, and decoupling in the cloud-capped subtropical and tropical marine boundary layer. *Journal of Climate,* 17**,** 3576-3588.

Wood, R., Bretherton, C. S., Leon, D., Clarke, A. D., Zuidema, P., Allen, G. & Coe, H. (2011) An aircraft case study of the spatial transition from closed to open mesoscale cellular convection over the Southeast Pacific. *Atmospheric Chemistry and Physics,* 11**,** 2341-2370.

Wood, R., Comstock, K. K., Bretherton, C. S., Cornish, C., Tomlinson, J., Collins, D. R. & Fairall, C. (2008) Open cellular structure in marine stratocumulus sheets. *Journal of Geophysical Research,* 113**,** D12207.

Wood, R. & Hartmann, D. L. (2006) Spatial variability of liquid water path in marine low cloud: The importance of mesoscale cellular convection. *Journal of Climate,* 19**,** 1748-1764.

Woodhouse, M. T., Carslaw, K. S., Mann, G. W., Vallina, S. M., Vogt, M., Halloran, P. R. & Boucher, O. (2010) Low sensitivity of cloud condensation nuclei to changes in the sea-air flux of dimethyl-sulphide. *Atmospheric Chemistry and Physics,* 10**,** 7545-7559.

Woodhouse, M. T., Mann, G. W., Carslaw, K. S. & Boucher, O. (2013) Sensitivity of cloud condensation nuclei to regional changes in dimethyl-sulphide emissions. *Atmospheric Chemistry and Physics,* 13**,** 2723-2733.

Yamaguchi, T. & Randall, D. A. (2008) Large-eddy simulation of evaporatively driven entrainment in cloud-topped mixed layers. *Journal of the Atmospheric Sciences,* 65**,** 1481-1504.

Yang, M., Huebert, B. J., Blomquist, B. W., Howell, S. G., Shank, L. M., Mcnaughton, C. S., Clarke, A. D., Hawkins, L. N., Russell, L. M., Covert, D. S., Coffman, D. J., Bates, T. S., Quinn, P. K., Zagorac, N., Bandy, A. R., De Szoeke, S. P., Zuidema, P. D., Tucker, S. C., Brewer, W. A., Benedict, K. B. & Collett, J. L. (2011a) Atmospheric sulfur cycling in the southeastern Pacific – longitudinal distribution, vertical profile, and diel variability observed during VOCALS-REx. *Atmospheric Chemistry and Physics,* 11**,** 5079-5097.

Yang, Q., Gustafson Jr, W. I., Fast, J. D., Wang, H., Easter, R. C., Wang, M., Ghan, S. J., Berg, L. K., Leung, L. R. & Morrison, H. (2012) Impact of natural and anthropogenic aerosols on stratocumulus and precipitation in the Southeast Pacific: a regional modelling study using WRF-Chem. *Atmos. Chem. Phys. Discuss.,* 12**,** 14623-14667.

Yang, Q., W. I. Gustafson, J., Fast, J. D., Wang, H., Easter, R. C. & Morrison, H. (2011b) Assessing regional scale predictions of aerosols, marine stratocumulus, and their interactions during VOCALS-REx using WRF-Chem. *Atmospheric Chemistry and Physics,* 11**,** 11951-11975.

Yu, M., Lin, J., Chen, L. & Chan, T. (2006) Large eddy simulation of a planar jet flow with nanoparticle coagulation. *Acta Mechanica Sinica,* 22**,** 293-300.

Yu, S., Mathur, R., Pleim, J., Wong, D., Gilliam, R., Alapaty, K., Zhao, C. & Liu, X. (2013) Aerosol indirect effect on the grid-scale clouds in the two-way coupled WRF-CMAQ: model description, development, evaluation and regional analysis. *Atmos. Chem. Phys. Discuss.,* 13**,** 25649-25739.

Yum, S. S. & Hudson, J. G. (2002) Maritime/continental microphysical contrasts in stratus. *Tellus B,* 54**,** 61-73.

Zaveri, R. A., Easter, R. C., Fast, J. D. & Peters, L. K. (2008) Model for Simulating Aerosol Interactions and Chemistry (MOSAIC). *Journal of Geophysical Research,* 113**,** D13204.

Zaveri, R. A. & Peters, L. K. (1999) A new lumped structure photochemical mechanism for large-scale applications. *Journal of Geophysical Research,* 104**,** 30387-30415.

Zelinka, M. D., Klein, S. A., Taylor, K. E., Andrews, T., Webb, M. J., Gregory, J. M. & Forster, P. M. (2013) Contributions of different cloud types to feedbacks and rapid adjustments in CMIP5. *Journal of Climate,* 26**,** 5007-5027.

Zhang, Z., Ackerman, A. S., Feingold, G., Platnick, S., Pincus, R. & Xue, H. (2012) Effects of cloud horizontal inhomogeneity and drizzle on remote sensing of cloud droplet

effective radius: Case studies based on large-eddy simulations. *Journal of Geophysical Research,* 117**,** D19208.

Zhou, C., Zelinka, M. D., Dessler, A. E. & Yang, P. (2013) An analysis of the short-term cloud feedback using MODIS data. *Journal of Climate,* 26**,** 4803-4815.

Zuidema, P., Painemal, D., De Szoeke, S. & Fairall, C. (2009) Stratocumulus cloud-top height estimates and their climatic implications. *Journal of Climate,* 22**,** 4652-4666.